

Identifying and comparing meteorological and geographical influences on high resolution climate signals in the oxygen isotope values of different environmental archives

Elisabeth Margaret Thompson
St Cross College

A thesis submitted for the degree of

Doctor of Philosophy

Trinity 2018

Abstract

This thesis explores how δ^{18}O values in horse hair relate to local meteorological observations; how Greenland ice core records relate to European terrestrial climate records; and how atmospheric changes are reflected in terrestrial and biological records. Bringing together analysis of increasingly complex palaeoenvironmental proxies, δ^{18}O measurements within atmospheric, terrestrial and biological systems are critically assessed across geographical transitions, ultimately leading to greater understanding of the utilisation of oxygen isotope data for seasonal climate analysis. Horse hair sampling and δ^{18}O analysis were conducted on horse hair from: the Icelandic Food and Veterinary Authority (MAST) in Selfoss, Iceland; the Thordale Stud in the Shetland Islands, United Kingdom; the Exmoor Pony Centre (EPC) in Somerset, UK; and the Pigeon House Equestrian centre in Oxfordshire, UK. The North Greenland Ice Core (NGRIP2) was sampled and analysed for δ^{18}O, and compared to a master tree ring dataset of compiled δ^{18}O values in the UK. The results confirm that rainfall quantity and continental effects dominate both the horse hair and ice core δ^{18}O records. The growth rates of the hair were seen to decrease with an increase in latitude; and comparison between horse hair δ^{18}O and meteorological variables clearly indicates a rainfall influence. Comparison between the ice core δ^{18}O and historical coastal temperature reconstruction shows a similar gradient to what is seen in modern temperature records. The comparison between tree ring isotopes can be interpreted as showing a similar amplitude to the historic temperatures, but with a slight dampening in regards to lower peaks values. Comparison of the tree ring and ice core values indicated a significant negative correlation, with smaller amplitude changes within the tree ring δ^{18}O results. Wavelet analysis suggested a common influence from teleconnections at several timescales in both the tree ring and ice core datasets, including the El Niño Southern Oscillation and the North Atlantic Oscillation. This study demonstrates that geographical and meteorological influences are similarly reflected within palaeoenvironmental proxies of increasing complexities. It also identifies periods of common influence from climate drivers and provides detail of the greatest effects on isotopic variation in the UK, Iceland and Greenland.

Acknowledgements

I would like to thank my supervisors, Christopher Bronk Ramsey and Joseph McConnell for all their guidance and encouragement throughout this research. Their expertise and support has been vital in the development of this thesis, and I am grateful also for the collaborative opportunities they have afforded me. I would like to thank the team at the Desert Research Institute in Reno who taught me so much about ice core sampling and analysis, including Monica Arienzo, Nathan Chellman and Audrey Yau. I am very grateful to the University of Oxford and Swansea University Dendrochronology teams, including Daniel Miles, Neil Loader, Danny McCarroll, Alexander Barnes, Giles Young, Darren Davies and Josie Duffy, for generously allowing me use of the tree ring oxygen isotope master dataset within this thesis. I would like to thank Frances Taylor at the Thordale Stud; Linzi and the other staff at the Exmoor Pony Centre; Sigríður Björnsdóttir at the Icelandic Food And Veterinary Authority; Sarah Hill at Pigeon House Equestrian; and especially thank all the ponies that provided tail hair samples for me to analyse. I would like to thank my examiners, Julia Lee-Thorp, Richard Staff, Elizabeth Jeffers, Adam Csank and Rick Schulting for the all the counsel and direction they provided. The expertise and technical support of Peter Ditchfield was invaluable and I would like to especially thank him for the advice he provided during the horse hair analysis.

I would like to thank all my RLAHA, Institute and St Cross friends, including but not limited to Danielle McLean, Steven Crabb, Eleanor Farber, Patrick Roberts, Emma Loftus, Robyn Mason, Charlotte Diffey, Jessica Dunham, Hannah Ringheim, Margaret Veall, Catherine Farfan, Victoria Sainsbury, Rebecca O'Sullivan and most especially Maciej Wencel for their friendships and support. I would like to thank Gregory Chatfield, Margaret Worrall, Tracy Worrall, Lester Thompson and Amy Thompson for their unyielding patience and encouragement. I would also like to acknowledge the invaluable faith and support of the late James Thompson.

Finally, I would like to acknowledge the funding provided by the School of Archaeology, St Cross College, American Geophysical Union, European Geosciences Union and International Union for Quaternary Research, which allowed me to attend conferences and participate in research both nationally and internationally.

Contents

1 Introduction **1**
- 1.1 Case studies . . . 3
- 1.2 Stable isotope use in a climatological context . . . 5
- 1.3 Thesis structure . . . 9

2 Climate and Isotopes **11**
- 2.1 Global circulation . . . 11
- 2.2 Introduction to isotope analysis . . . 14
- 2.3 Isotopic measurement . . . 17
- 2.4 Isotopes in ice cores . . . 18
- 2.5 Isotopes in tree rings . . . 21
- 2.6 Isotope analysis within keratin . . . 24

3 Background **31**
- 3.1 Location introductions . . . 31
  - 3.1.1 Greenland . . . 33
  - 3.1.2 Iceland . . . 35
  - 3.1.3 Shetland Islands . . . 36
  - 3.1.4 Southern Britain . . . 39
- 3.2 Climatology and Hydrology . . . 42
  - 3.2.1 1850 A.D. to present . . . 42
  - 3.2.2 1400 A.D. to 1850 A.D. . . . 58
  - 3.2.3 950 A.D. to 1400 A.D. . . . 59
  - 3.2.4 1250 B.C. to 950 A.D. . . . 61
- 3.3 Horse ecology . . . 61

4 Methodology **65**
- 4.1 Horse hair . . . 66

4.1.1 Samples . . . 66
4.1.2 Analytical methods . . . 72
4.1.3 Data calibration . . . 75
4.1.4 Quality control . . . 79
4.1.5 Research methodology . . . 82
4.2 Ice core . . . 84
4.2.1 Samples . . . 84
4.2.2 Analysis method . . . 88
4.3 Tree rings . . . 90
4.3.1 Samples . . . 90
4.3.2 Analysis method . . . 94
4.4 Modern observational data . . . 94
4.5 Statistical methodology . . . 97

5 Horse Hair Latitudinal Study 101
5.1 Results . . . 101
5.1.1 Proof of concept . . . 101
5.1.2 Data preparation and precision . . . 105
5.1.3 Oxfordshire . . . 120
5.1.4 Exmoor . . . 127
5.1.5 Shetland Islands . . . 136
5.1.6 Iceland . . . 143
5.1.7 Statistical inter-comparison . . . 150
5.2 Discussion . . . 167

6 Ice Core and Dendroclimatological Research Study 171
6.1 Results . . . 171
6.1.1 NGRIP2 . . . 172
6.1.2 NGRIP2 comparison to existing ice core records . . . 174
6.1.3 Tree ring record . . . 180
6.1.4 Tree ring comparison to NGRIP2 . . . 181
6.1.5 Comparison of century averages . . . 186
6.1.6 Tree ring comparison to NGRIP compilation . . . 190
6.1.7 Medieval Climate Anomaly and the Little Ice Age . . . 206
6.1.8 Solar and volcanic forcings . . . 209
6.1.9 Wavelet analysis . . . 211
6.2 Discussion . . . 223

7 Conclusions 227
7.1 Statistical uncertainty . . . 228
7.2 Applications . . . 229

7.3 Conclusion 231

8 References **235**

List of Figures

1.1 Oxygen isotope schematic, detailing the environmental processes of δ^{18}O depletion and enrichment. 6
1.2 Schematic of the processes from which source moisture δ^{18}O is transferred to the North Greenland Ice Core, tree rings and horse hair (based on Young et al., 2015). 8

2.1 The Hadley circulation of the equatorial region, including solar radiation; areas of high and low pressure; the easterly trade winds; and direction of air movement. 12
2.2 Global surface air circulation, including the equatorial trade winds; subtropical westerly winds; polar easterly winds; as well as high and low pressure belts. 13
2.3 Schematic showing relationship between temperature (degrees Celsius) and δ^{18}O, sourced from Jouzel et al. (1994). 17
2.4 Schematic showing the transport of oxygen isotopes evaporated from sea water, through the hydrological cycle and into the North Greenland Ice Core, including stages at which ^{18}O is enriched and depleted. 19
2.5 Schematic showing the evaporative transport of oxygen isotopes from the ocean, over the Greenland Ice Sheet, including the decreasing δ^{18}O values toward the summit, based on Dansgaard et al. (1973). 19
2.6 Schematic showing the transport of oxygen isotopes evaporated from sea water, through the hydrological cycle and into tree ring cellulose, including stages at which ^{18}O is enriched and depleted (based on Young et al. 2015). 21
2.7 Evapotranspiration process resulting in the ^{18}O enrichment of leaf water, and without fractionation within capillary flow. 23

2.8 Schematic showing the transport of oxygen isotopes evaporated from sea water, through the hydrological cycle and into horse hair keratin, including stages at which ^{18}O is enriched and depleted. 25

3.1 Map of the Atlantic region and Greenland. [Map image is the intellectual property of Esri and is used herein under license. Copyright ©2017 Esri and its licensors. All rights reserved]. 32
3.2 Map of Greenland showing the location of the North Greenland Ice Core [NGRIP], the summit of the ice sheet, and the Dye-3, GRIP and GISP2 ice cores (sourced from Johnsen et al., 2001). 34
3.3 Map of Iceland with a red marker showing the location of Selfoss. [Map image is the intellectual property of Esri and is used herein under license. Copyright ©2017 Esri and its licensors. All rights reserved]. . . 36
3.4 a) Map of the Atlantic region showing the location of the United Kingdom inset into a map of the UK, indicating the location of Shetland, and b) Map of Shetland Islands with a red marker showing the location of the Thordale Stud. [Map image is the intellectual property of Esri and is used herein under license. Copyright ©2017 Esri and its licensors. All rights reserved]. 38
3.5 Map of the United Kingdom including a red box indicating the Leverhulme Project sampling area; and red markers indicating the locations of the Exmoor Pony Centre and the Pigeon House Equestrian Centre. [Map image is the intellectual property of Esri and is used herein under license. Copyright ©2017 Esri and its licensors. All rights reserved]. . . 40
3.6 Distribution map of British oxygen isotope ratios (Image sourced from Pellegrini et al., 2016, and originally derived from Darling and Talbot, 2003). 41
3.7 Map of ocean circulation within the North Atlantic and Nordic Seas, including the East Greenland Current (EGC), the East Icelandic Current (EIC), Irminger Current (IC), West Greenland Current (WGC), North Atlantic Current (NAC) and the Norwegian Atlantic Current (NwAC) (Sourced from Miettinen et al., 2015). 42
3.8 Diagram of major hydrological features of the Greenland Ice Sheet, including precipitation and snow accumulation, firn layer and ice layer, as well as a) supraglacial lakes, b) englacial channels, and c) subglacial cavities (Based on Chu, 2014). 47
3.9 United Kingdom daily mean temperature in °C by season, sourced from Jenkins et al. (2008). 54
3.10 United Kingdom average total precipitation in millimetres by season, sourced from Jenkins et al. (2008). 55

3.11 Diagram of the proxy inferred impact pattern of the Medieval Climate Anomaly on the North Atlantic Ocean, including Northern Africa, Europe, the United Kingdom, Iceland, Greenland, North America, South America, and the eastern Pacific Ocean (Sourced from Trouet et al., 2009, page 80). 60

4.1 Photograph of a horse tail hair, with red boxes indicating two areas of different thickness. 67
4.2 Horse Hair sampling locations from north to south: (a) Icelandic Food and Verterinary Authority, Iceland; (b) Thordale Stud, Shetland; (c) Pigeon House Equestrian, Oxfordshire; and (d) Exmoor Pony Centre, Exmoor. [Map image is the intellectual property of Esri and is used herein under license. Copyright ©2017 Esri and its licensors. All rights reserved]. 69
4.3 Visual example of hair sampling procedure including (a) clean hair for sampling, (b) 1mm hair segments that have been measured and weighed, and (c) the silver capsule within the metal disc capsule holder. 73
4.4 Calibration procedure using the linear method, including raw values, measured versus certified plotted values, linear equation and final calibrated values. 78
4.5 Image of the SerCon Reprocessor software, including the three carbon monoxide mass peaks and the yellow integration boundaries. 80
4.6 Example of a quality controlled machine run, with measurement errors highlighted within the red box. 81
4.7 NGRIP2 core sampling plan, showing a representation of the 3.3cm columns that were removed for sampling from the larger ice core. Sections a, b and c were returned to the archive freezer for future anaylsis. . 85
4.8 Topographic elevation map of the Greenland ice core locations including B16-23 and B26-30, NEEM, NGRIP, GRIP and Dye3, with respect to Danmarkshavn, Upernavik, Ilulissat, Tasiilaq, Nuuk, Narsarsuaq and Qaqortoq. 88
4.9 Ice core melt analysis system, sourced from McConnell et al. (2014). . . 89
4.10 Leverhulme Project sampling locations within the United Kingdom, sourced from the UK Oak Project (2019). 91
4.11 GNIP UK sampling locations described in Table 4.13. [Map image is the intellectual property of Esri and is used herein under license. Copyright ©2017 Esri and its licensors. All rights reserved]. 96
4.12 Visual representation of a Fourier transform, sourced from Fugal (2009). 98
4.13 Visual representation of a Wavelet transform, sourced from Fugal (2009). 99

5.1 Daily total rainfall measurements in millimeters, observed 9:00am to 9:00am from 02.01.2013 to 24.09.14, plotted with the approximate average rate of horse hair growth of West et al. (2004). 102
5.2 Daily mean Temperature in degrees Celsius, observed 9:00am to 9:00am from 02.01.2013 to 24.09.14, plotted with the approximate average rate of horse hair growth of West et al. (2004). 103
5.3 δ^{18}O values, expressed in ‰ with respect to V-SMOW, plotted against the sequentially sampled position along the length of the hair (in millimeters) for *Percy* and *Rama*. 104
5.4 δ^{18}O values, expressed in ‰ with respect to V-SMOW, plotted against the sequentially sampled position, alternated with carbon sampling, along the length of the hair (in millimeters) for *Periwinkle*, *Roger* and *Chaffinch*. 104
5.5 Analysis data results shown within the data preparation procedural process. 106
5.6 Plot of the δ^{18}O values of all hairs without USGS42 included with a 3-point moving average smoothing, expressed in ‰ with respect to V-SMOW. 107
5.7 Plot of the δ^{18}O values of all hairs with USGS42 included with a 3-point moving average smoothing, expressed in ‰ with respect to V-SMOW. . 107
5.8 Non-interpolated versus interpolated Z-score δ^{18}O data for *Fudge* hair 1, expressed in ‰ with respect to V-SMOW. 109
5.9 Example of Matlab peak finding script result for Oxfordshire Pony *Gem 3*. 110
5.10 3-point moving average of the final δ^{18}O values of all four hairs from the Exmoor pony *Robbie* sampled in 2015 and 2016, expressed in ‰ with respect to V-SMOW. 116
5.11 3-point moving average of the final normalised δ^{18}O values of all for hairs from the Exmoor pony *Robbie* sampled in 2015 and 2016, expressed in ‰ with respect to V-SMOW. 117
5.12 3-point moving average of the final normalised δ^{18}O values of the two hairs from the Exmoor pony *Robbie* sampled in 2016, expressed in ‰ with respect to V-SMOW. 117
5.13 δ^{18}O results for the Oxfordshire ponies, expressed in ‰ with respect to V-SMOW. 119
5.14 δ^{18}O result for the Oxfordshire ponies, including an introduced telogen phase correction for the ponies *Tonto* and *Dessi*, expressed in ‰ with respect to V-SMOW. 120
5.15 Wallingford δ^{18}O measurements within precipitation from 1979 to 2015. 121
5.16 Wallingford precipitation totals from 1979 to 2015. 121
5.17 Wallingford annual mean δ^{18}O values from 1979 to 2015. 122

5.18 Monthly mean Wallingford δ^{18}O values, using data from 1979 to 2015, including ± 1 standard deviation 123
5.19 Z-scores for the δ^{18}O values of Oxfordshire Ponies. 123
5.20 3-point averaged Z-scores for the δ^{18}O values of Oxfordshire Ponies. . . 124
5.21 Minimum, maximum and mean temperature for the meteorological station at Brize Norton, United Kingdom. 125
5.22 Rainfall data from the meteorological station at Brize Norton, United Kingdom. 125
5.23 Z-scores for Oxfordshire horse hair plotted against z-scores for mean temperature from Brize Norton, United Kingdom. 126
5.24 Wallingford GNIP data plotted with the Oxfordshire horse hair data. . . 127
5.25 Z-scores for the δ^{18}O values of Exmoor Ponies against the median centimetre date. 128
5.26 3-point averaged Z-scores for the δ^{18}O values of Exmoor Ponies against the median centimetre date. 129
5.27 3-point averaged δ^{18}O values for the two Exmoor Pony *Fudge* hairs against the median centimetre date, expressed in ‰ with respect to V-SMOW. 130
5.28 3-point averaged δ^{18}O values for the Exmoor Ponies, against the median centimetre date, expressed in ‰ with respect to V-SMOW. Plot a) shows the *Robbie 1* hair which was analysed without USGS42 and b) shows the *Rama 1*, *Robbie 2*, *Fudge 1* and *Fudge 2* hairs, which were analysed using the USGS42 standard. 131
5.29 Minimum, maximum and mean temperature for the meteorological station at Liscombe, United Kingdom. 132
5.30 Z-scores for Exmoor horse hair plotted against z-scores for mean temperature from Liscombe, United Kingdom. 133
5.31 Daily rainfall at Liscombe, Exmoor with a) the total rainfall from 0900-0900 from the 01/01/2013 to the 25/02/2015 and b) the total rainfall from 0100-2400 from the 25/02/2015 to the 31/03/2016. 134
5.32 Wallingford GNIP data plotted with the Exmoor horse hair data. 135
5.33 Z-scores for the δ^{18}O values of Shetland Ponies. 137
5.34 3-point averaged Z-scores for the δ^{18}O values of Shetland Ponies. . . . 137
5.35 [3-point averaged δ^{18}O values for the Shetland ponies, against the median centimetre date, expressed in ‰ with respect to V-SMOW. Plot a) shows the *Silver 2* hair which was analysed without USGS42 and b) shows the *Silver 1*, *Storm*, *Taktur 1* and *Taktur 2* hairs, which were analysed using the USGS42 standard]. 139
5.36 Total daily rainfall in millimetres at Lerwick, Shetland Islands. 140

5.37 Minimum and mean temperature for the meteorological station at Lerwick, Shetland Islands, United Kingdom. 141
5.38 Z-scores for Shetland horse hair plotted against z-scores for mean temperature from Lerwick, United Kingdom. 141
5.39 Altnabreac GNIP data for the available time period of 1981-1982, plotted against the Shetland horse hair δ^{18}O for 2014-2016. 143
5.40 Monthly mean Reykjavík δ^{18}O measurements, from data compiled from monthly measurements from 1962 to 2015, including ± 1 standard deviation. 144
5.41 Annual mean Reykjavík δ^{18}O measurements by year. 145
5.42 3-point averaged Z-scores for the δ^{18}O values of Icelandic Horses. . . . 145
5.43 3-point averaged δ^{18}O measurement of Icelandic Horses, expressed in ‰ with respect to V-SMOW. Plot a) shows the Jódís 2 hair which was analysed without USGS42 and b) shows the *Granis*, *Jódís 1* and *Kaeti* hairs, which were analysed using the USGS42 standard. 146
5.44 Maximum and minimum temperature at the Eyrarbakki meteorological station, Iceland. 147
5.45 Z-scores for Iceland horse hair plotted against z-scores for monthly mean temperature from Eyrarbakki, Iceland. 148
5.46 Precipitation at the Eyrarbakki meteorological station, Iceland. 149
5.47 Reykjavík GNIP data plotted with the Icelandic horse hair data. 150
5.48 δ^{18}O Boxplot results from Iceland, Shetland, Exmoor and Oxfordshire horse hairs, expressed in ‰ with respect to V-SMOW. Plot a) shows the final calibrated and smoothed data b) shows the interpolated data. 151
5.49 δ^{18}O boxplot results from Iceland, Shetland, Exmoor and Oxfordshire horse hairs divided by the inclusion or exclusion of the USGS42 standard, expressed in ‰ with respect to V-SMOW. 154
5.50 δ^{18}O boxplot results from Iceland, Shetland, Exmoor and Oxfordshire horse hairs using a one year cycle only, expressed in ‰ with respect to V-SMOW. 155
5.51 Boxplot showing the δ^{18}O values (horizontal axis) for each horse, expressed in ‰ with respect to V-SMOW. 159
5.52 Average δ^{18}O values of hair (horizontal axis), expressed in ‰ with respect to V-SMOW, for each location plotted against the average annual rainfall totals for each location (vertical axis). The bar lines show the 95% confidence intervals for the δ^{18}O of horse hair for each location. . . 160

5.53 Average δ^{18}O values (horizontal axis), expressed in ‰ with respect to V-SMOW, for each location plotted against the temperature ranges for each location, including markers for the minimum and maximum temperatures (vertical axis). The bar lines show the 95% confidence intervals for the δ^{18}O of horse hair for each location. 161
5.54 Average local GNIP δ^{18}O values (horizontal axis), expressed in ‰ with respect to V-SMOW, for each location plotted against the average horse hair δ^{18}O values for each location (vertical axis). The bar lines show the 95% confidence intervals for the δ^{18}O of horse hair for each location. . . 162
5.55 Results of the fast Fourier transform conducted on the Icelandic Horse data for *Kaeti*. 164
5.56 Results of the horse hair carbon and nitrogen isotope analysis, expressed in ‰ 166
5.57 Mean carbon and nitrogen values, expressed in ‰ 166

6.1 Full NGRIP2 ice core δ^{18}O dataset plotted against year (A.D.). 173
6.2 Sampling sites for the Greenland ice cores, adapted from Vinther et al. (2008); Kaufman et al. (2009); Seierstad et al. (2014); Weißbach et al. (2016). 174
6.3 Sampling sites for the Greenland ice cores showing the average δ^{18}O values for each sampling location, adapted from Vinther et al. (2008); Kaufman et al. (2009); Seierstad et al. (2014); Weißbach et al. (2016). . 176
6.4 The difference between NGRIP2 and NGRIP1 ice cores between 1235B.C. to 1262A.D. 178
6.5 100 year moving average δ^{18}O values for the full NGRIP record, with the Medieval Climate Anomaly within the red section and the Little Ice Age shown by the yellow section. 179
6.6 100 year moving average δ^{18}O values from 900A.D.-1900A.D. within the NGRIP record, with the Medieval Climate Anomaly within the red section and the Little Ice Age shown by the yellow section. 180
6.7 Full tree ring δ^{18}O values plotted against Year (A.D.). 181
6.8 Tree ring and NGRIP boxplots of δ^{18}O values over the full data records. 182
6.9 Comparison between the δ^{18}O United Kingdom tree ring master record and the North Greenland Ice Core 2, during the overlapping period from 1200-1261, expressed in ‰ with respect to V-SMOW. 183
6.10 Comparison between the δ^{18}O United Kingdom tree ring master record and the North Greenland Ice Core 2 with a 2 year lead relative to its original values, during the overlapping period from 1200-1261, expressed in ‰ with respect to V-SMOW. 184

6.11 Comparison between the δ^{18}O United Kingdom tree ring master record and the North Greenland Ice Core 2 with a 3 year lead relative to its original values, during the overlapping period from 1200-1261A.D., expressed in ‰ with respect to V-SMOW. 185
6.12 Difference in the δ^{18}O values of the tree ring and NGRIP2 records during the overlapping 1200-1262A.D. time period. 186
6.13 Averages for each century for the full NGRIP 1 and 2 δ^{18}O compilation, with the red region indicating the MCA and the yellow indicating the LIA. 188
6.14 Averages for each century for GRIP δ^{18}O, with the red region indicating the MCA and the yellow indicating the LIA. 189
6.15 Averages for each century for the UK tree ring δ^{18}O, with the red region indicating the MCA and the yellow indicating the LIA. 189
6.16 Dual y-axis plot showing the tree ring δ^{18}O on the right and the NGRIP compilation δ^{18}O on the left, from 1200A.D.-2012A.D. 191
6.17 Dual y-axis plot showing the tree ring δ^{18}O on the right and the NGRIP compilation δ^{18}O on the left, from 1200A.D.-1350A.D. 192
6.18 10 year moving average. 193
6.19 50 year moving average. 194
6.20 100 year moving average. 195
6.21 Northern Hemisphere temperature anomalies sourced from Moberg et al. (2005). 196
6.22 Northern Hemisphere temperature anomalies sourced from Mann et al. (2009). 196
6.23 CRU TS4.01 global historical near-surface temperatures from the University of East Anglia's Climate Research Unit. 198
6.24 Historic temperature compared to tree ring δ^{18}O. 200
6.25 Historic temperature compared to converted temperature from tree ring isotopes. 201
6.26 Historic Greenland temperature compared to NGRIP δ^{18}O. 202
6.27 Historic temperature compared to converted temperature from NGRIP isotopes. 203
6.28 NGRIP δ^{18}O compared to source water values converted from UK tree rings. 205
6.29 NGRIP δ^{18}O compared to source water values converted from UK tree rings 20 year running averages. 205
6.30 NGRIP δ^{18}O compared to source water values converted from UK tree rings 100 year running averages. 206
6.31 Data sourced from Kobashi et al. (2017) detailing the volcanic forcing (W/m^2) from 1300B.C. to 2000A.D. 210
6.32 Full wavelet analysis for tree ring and NGRIP ice core data. 212

6.33 Wavelet plot for ice core oxygen isotopes 1200-1973 A.D. 213
6.34 Wavelet analysis for tree ring and NGRIP ice core data from 1200A.D. . 215
6.35 Wavelet plot for tree ring oxygen isotopes 1200-2012 A.D. 216
6.36 Wavelet plot for ice core oxygen isotopes 1200-1973 A.D. 216
6.37 Wavelet plot for tree ring oxygen isotopes 1200-2012 A.D. 217
6.38 Wavelet plot for ice core oxygen isotopes 1200-1973 A.D. 218
6.39 Cross wavelet plot of tree rings and NGRIP compilation from 1200-1973 A.D. 219
6.40 Wavelet coherence plot of tree rings and NGRIP compilation from 1200-1973 A.D. 221
6.41 Wavelet coherence Pplot of UK historic temperatures versus tree rings from 1901-1973 A.D. 222
6.42 Wavelet coherence plot of Greenland historic temperatures versus NGRIP compilation from 1901-1973 A.D. 223

List of Tables

3.1 Approximate latitude and longitude locations for the ice core, tree ring and horse hair sampling sites (in °N, °W). 33
3.2 Locations, elevation, surface temperature, accumulation rates and values from the NGRIP and GRIP ice core sampling sites (in °N, °W, metres above sea level, metres ice equivalent accumulation, and ‰, respectively). 35
3.3 Monthly climatology - Danmarkshavn, Greenland. 49
3.4 Monthly climatology - Qaqortoq, Greenland. 49
3.5 Normalized Icelandic δ^{18}O data from Axford et al. 2011. 51
3.6 Monthly climatology - Eyrarbakki, Iceland. 52
3.7 Monthly climatology - Lerwick. 53
3.8 Monthly climatology - Liscombe. 57
3.9 Table describing the prevailing wind and wave conditions in relevant coastal regions of the United Kingdom (data sourced from Geos, 2001). 57

4.1 This table details the individual horse information from the March 7th 2016 sampling population. It describes the location, name of the horse, age as of 07.03.2016, breed of horse, and the approximate size of the horse in hands. Measurements marked by $*$ denote where exact horse height measurements for the Exmoor ponies and Iceland horses were not available and an average of the breed height was used for comparison (& Árnason and Bjarnason, 1994; Baker et al., 2000). 70

4.2 This table details the analysis information from the March 7th 2016 horse sampling exercise. It describes the location, name of the horse, the number of hairs analysed for that horse, the number of individual samples sequentially taken along the length of the hair, the number of usable samples that were analysed for that hair, and the length of hair sampled in whole centimetres. Several anomalous values were discounted due to machine or sampling errors. 71
4.3 Carbon stable isotope reference standards, with respect to $\delta^{13}C_{\ VPDB}$ (Alanine, Seal and Cow) and $\delta^{13}C_{\ VPDB-LSVEC}$ (USGS40 and 41), USGS40 and 41 sourced from United States Geological Survey (2011a); United States Geological Survey (2011b). 74
4.4 Nitrogen stable isotope reference standards, with respect to $\delta^{15}N_{\ AIR}$, USGS40 and 41 sourced from United States Geological Survey (2011a); United States Geological Survey (2011b). 74
4.5 Oxygen stable isotope reference standards, with respect to $\delta^{18}O_{\ VSMOW-SLAP}$ (USGS42 and 43) and $\delta^{18}O_{\ VSMOW}$ (EMA-P1, EMA-P2, IAEA-601 and IAEA-602), sourced from Meier-Augenstein (2009); Elemental Microanalysis (2010); United States Geological Survey (2011c); United States Geological Survey (2011d). 75
4.6 Calibration step 1. 77
4.7 Calibration step 2 - stretch factor calculation. 77
4.8 Calibration step 3 - Adjustment. 77
4.9 Data correction standards used. 79
4.10 This table details the core length, elevation (in metres above sea level) and time span for the supplementary cores from Weißbach et al. (2016). 87
4.11 Leverhulme Project sample dates and locations. 91
4.12 This table details the Meteorological variables provided by the UK Meteorological Office. 95
4.13 This table details the oxygen isotope precipitation data from the International Atomic Energy Agency (2018). 96

5.1 Sample of interpolated data, first 10 centimetres of the hair from 'Granis', Iceland, including the interpolated Z-scores (I.Z-score) and moving averages (M.A.). 108
5.2 Example of peak results, from *Gem 1* and *Gem 3*, found using the Matlab script, 'findpeaks(y,x)'. Data includes centimetre position of peak, $\delta^{18}O$ value at peak, centimetre distance between peaks, and growth rate calculate using the centimetre distance. 111
5.3 Growth rates of individual horse hairs calculated using distances between annual peaks and troughs. 112

5.4 *Rama* precision testing data with three samples from the first 8 centimetres and four samples from the second 8 centimetres of hair. 114
5.5 Picarro oxygen measurements for two troughs (A and B) in the Horse paddocks of Exmoor, expressed in ‰ with respect to V-SMOW. 136
5.6 Altnabreac monthly mean δ^{18}O measurements, data compiled from monthly measurements from 1981 and 1982. 142
5.7 Horse hair δ^{18}O data, expressed in ‰ with respect to V-SMOW, analysed by location, not separated into two populations by the use of the USGS42 standard. This table includes the mean δ^{18}O, standard deviation, normalised minimum value, normalised maximum value and sample size for each location. 151
5.8 Horse hair δ^{18}O results, expressed in ‰ with respect to V-SMOW, for all samples separated by use of USGS42 or I601 reference standards, including number of samples, minimum, maximum, mean and standard deviation. 152
5.9 Horse hair δ^{18}O results, expressed in ‰ with respect to V-SMOW, by location for data corrected using USGS42 reference standards and data corrected not using USGS42 reference standards, including mean δ^{18}O and standard deviation. 153
5.10 Horse hair δ^{18}O results by horse name, expressed in ‰ with respect to V-SMOW, for data corrected using USGS42 reference standards, including minimum, maximum, mean and standard deviation. 156
5.11 Horse hair δ^{18}O results by horse name, expressed in ‰ with respect to V-SMOW, for data corrected not using USGS42 reference standards, including minimum, maximum, mean and standard deviation. 157
5.12 Mean δ^{18}O measurements per horse, expressed in ‰ with respect to V-SMOW. 158
5.13 Annual mean meteorological variables at the station closest to each location. 158
5.14 P-value comparison between individual horse hair locations. 163
5.15 Frequency signals within the FFT looped horse hair, in centimetres/cycle, and the day conversion. 165

6.1 NGRIP2 data. 174
6.2 Ice core record comparisons from (1) Kaufman et al. (2009), (2) Vinther et al. (2010) and (3) Weißbach et al. (2016), listed geographically from north to south. 175
6.3 Tree ring data. 181
6.4 Correlation comparison between tree ring δ^{18}O and ice core δ^{18}O at a 0 year lag, 2 year lag and 3 year lag, from 1200-1261 A.D. 185
6.5 NGRIP compilation and tree ring century averages. 187

6.6 Tree ring data divided into time periods, including number of samples within the time period (A.D.), minimum, maximum, and mean δ^{18}O with respect to VPDB, as well as standard deviation. 207
6.7 Record average comparison. 208
6.8 Ice core and tree ring comparison during different time periods, including the Little Ice age from 1250-1850A.D. and the Medieval Climate Anomaly from 950-1249 A.D. 208
6.9 Ice core and tree ring comparison during different time periods, including the Little Ice age from 1300-1850A.D. and the Medieval Climate Anomaly from 950-1299 A.D. 209
6.10 Time periods (A.D.) of strong and weak solar forcing within the last 800 years, data sourced from Kobashi et al. (2013). 210

Acronyms

- **AMO** - Atlantic Multidecadal Oscillation
- **AO** - Arctic Oscillation
- **ANOVA** - Analysis of Variance
- **BP** - Before Present (1950)
- **CLIMAT** - World Meteorological Organisation international climate monitoring
- **COI** - Cone of Influence
- **CRU TS** - Climatic Research Unit Time-Series
- **DRI** - Desert Research Institute
- **DMI** - Danish Meteorological Institute
- **EIC** - East Icelandic Current
- **EGC** - East Greenland Current
- **EMA** - Elemental Microanalysis Ltd.
- **ENSO** - El Nño Southern Oscillation
- **EPC** - Exmoor Pony Centre
- **FSC** - Faroe-Shetland Channel
- **FT** - Fourier Transform
- **FFT** - Fast Fourier Transform
- **GISP** - Greenland Ice Sheet Project
- **GNIP** - Global Network of Isotopes in Precipitation
- **GPS** - Global Positioning System
- **GRIP** - Greenland Ice Core Project
- **HT** - High Temperature
- **HTEA** - High Temperature Elemental Analyser
- **IAEA** - International Atomic Energy Agency
- **IC** - Irminger Current

- **ICP-MS** - Inductively Coupled Plasma Mass Spectrometer
- **IOD** - Indian Ocean Dipole
- **IRMS** - Isotope Ratio Mass Spectrometer
- **ITCZ** - Intertropical Convergence Zone
- **LAIA** - Late Antique Ice Age
- **LIA** - Little Ice Age
- **MAST** - Icelandic Food and Veterinary Authority
- **MCA** - Medieval Climate Anomaly
- **MCDW** - Monthly Climatic Data for the World
- **NAC** - North Atlantic Current
- **NAO** - North Atlantic Oscillation
- **NEEM** - North Greenland Eemian Ice Drilling project
- **NGRIP** - North Greenland Ice Core Project
- **NwAC** - Norwegian Atlantic Current
- **PDO** - Pacific Decadal Oscillation
- **RWP** - Roman Warm Period
- **SMOW** - Standard Mean Ocean Water
- **SPSS** - Statistical Package for the Social Sciences
- **USGS** - United States Geological Survey
- **V-SMOW** - Vienna Standard Mean Ocean Water
- **WGC** - West Greenland Current
- **WISER** - Water Isotope System for Data Analysis, Visualization and Electronic Retrieval
- **WMO** - World Meteorological Organisation
- **WT** - Wavelet Transform

1. Introduction

With a current political focus on the impacts of climate change on vulnerable communities and ecosystems, palaeoclimate research has become a highly relevant field of study. The need to improve information regarding comparable historical changes in climate is imperative. This research examines the overarching question of how oxygen isotopic ratios (δ^{18}O) are recorded among palaeoenvironmental archives with different levels of fractionation complexity. Small differences in the weight and bond strength of oxygen isotopes, affected by the climate system, are revealed in the fluctuations of the ratio between the heavier [^{18}O] to lighter isotope [^{16}O]. This thesis examines how this ratio of δ^{18}O is affected by local climate, and is therefore used to reconstruct palaeoclimate. This is conducted using two case studies: firstly exploring how climate signals in ice core and tree ring records affect oxygen isotope values, during historical periods of extreme climate variability; and secondly, examining the relationship of oxygen isotopes within horse hair to latitude and climate. The purpose of these case studies is to enable researchers to improve comparisons of climate data from different environmental records; learn more about the mechanisms of past climate changes; and subsequently to

enhance what is known about possible future climate changes.

This research fills a gap in understanding the differences between modern U.K. oxygen isotope values in precipitation and those during periods of extreme climate. These time periods include the warm period from 950 A.D. to 1250 A.D. known as the Medieval Climate Anomaly (MCA)(Mann et al., 2009), and the cold period known as the Little Ice Age (LIA), which occurred at different times depending on location, within a period from 1200 A.D. to 1850 A.D. (Ogilvie, 2005). Key research questions in need of scientific exploration are:

- how Greenland ice core records relate to European terrestrial climate records; and
- how atmospheric changes are independently reflected in terrestrial tree ring and biological horse hair records.

This knowledge is important when using ice core data to glean information about European climate.

Bringing together the results of both case studies, this thesis critically evaluates ^{18}O measurements between different climate systems (atmospheric and terrestrial) and latitudes (horse hair); as well as contribute to a greater understanding of the utilisation of oxygen isotope data for seasonal climate analysis. Ultimately, this thesis aims to improve what is known about the relationship between oxygen isotopic ratios, geography and climate, as well as meteorological variables such as air temperature and rainfall. It consequently has the potential to improve the development of important new methodologies in relation to understanding changes in climate.

1.1 Case studies

The first case study specifically focuses on addressing the two key scientific research questions through a comparison of the δ^{18}O values within two historical periods of extreme climate, as well as on a direct comparison as to how the NGRIP2 ice core and a network of tree rings in the United Kingdom differ in the recording of climate signals within δ^{18}O. The study also utilises new high-resolution δ^{18}O values from the North Greenland (NGRIP2) ice core, collected for the period of 1250B.C. to 1250A.D.; NGRIP 20yr mean δ^{18}O values from 1250A.D. to 1980A.D. (NGRIP members, 2004); as well as values from a new comprehensive network of U.K. δ^{18}O oak tree data across the United Kingdom, spanning the past 1200 years.

The research explores whether oxygen isotopic ratios during the Little Ice Age reflect decreased δ^{18}O in tree rings in the same way as they do in ice core records of the same period. How does the data compare to modern values, and in turn compare with δ^{18}O values during the Medieval Climate Anomaly? Specifically, this case study aims to look at whether there is a lag between the isotopic signals within ice core and tree ring data. It also examines how changes in temperature and rainfall are reflected in tree ring and ice core records, which can be representative of terrestrial and atmospheric δ^{18}O information, respectively.

The second case study analyses whether the Rayleigh distillation process latitude effect of depleted precipitation isotopes toward the poles (Bierkens et al., 2008) can be observed within horse hair. This case study incorporates an analysis and comparison of modern horse hair from Iceland, Shetland [U.K.], Exmoor [U.K.] and Oxfordshire [U.K.]. Modern horse hair is readily available from pony centres around the globe and

provides location and dietary information that is temporally resolved over the lifetime of the horse.

Changes within oxygen isotope measurements of the horse hair over time can offer insight into seasonal fluctuations in atmospheric conditions (Sharp and Cerling, 1998; Sharp et al., 2003; Jones et al., 2007). This study specifically explores how changes in δ^{18}O values in horse hair directly reflect regional changes. This provides useful baseline findings for comparative analysis against other research. For example, the sampling sites and the pony breeds used in this study provide additional information to the increasing network of isotopic horse hair data. A comparison of these breeds with those already studied in Burnik Šturm et al. (2015) improves understanding of the intra-species variation within the δ^{18}O values of horse hair.

Investigation of the latitudinal comparison of δ^{18}O values within horse hair is unique, as is the examination of the subsequent relationship between those δ^{18}O values and local meteorological variables. Horses are useful for this type of analysis because of their wide geographic and temporal range, and the strong relationship in the data to precipitation, due to the high turnover rates compared to that of other species that retain water from leaves (van Dam and Reichart, 2009). By directly correlating the meteorological variables to δ^{18}O variations, I can also explore the effect of specific weather events at different latitudes.

Using the aforementioned data and methodology, this thesis tests several hypotheses. The first, is:

> 'there is a common component of the climate signal which is recorded (albeit at different amplitudes) in both the atmospheric and terrestrial isotope records'.

The second hypothesis to be tested is:

> 'lower [higher] temperatures of the Little Ice Age [Medieval Climate Anomaly] are reflected in the ^{18}O values of both the terrestrial and atmospheric isotope archives'.

This study also explores the hypotheses that:

> 'the temperature gradient from central England to Iceland is reflected in the oxygen isotope ratios of horse hair', and
>
> 'the amplitude of the seasonal temperature cycle is reflected in the oxygen isotope variation within horse hair'.

Analysing oxygen isotope values at different geographical positions, we can track the relationship with latitude and regional climate features. This contributes to firmer understanding of how to compare climate records from different locations.

1.2 Stable isotope use in a climatological context

The relationship between oxygen isotope ratios and temperature is determined by the difference in reaction rates and bond strengths of atoms within different weights. Heavier isotopes are less reactive due to lower vibrational frequencies and have stronger covalent bond strength. Increases in temperature cause faster vibrational energy and result in a reduction in differences of reaction rate within isotopes of varying weight (Pearson, 2012). There is a positive correlation between the $\delta^{18}O$ of precipitation and temperature, which increases with latitude toward the polar region (Dansgaard, 1964).

The effect of weight and bond strength on isotopes manifests throughout the climate system via changes in the ratio of heavier to lighter isotopes. One-way kinetic fractionation can occur when the reactant vapour is blown away from the initial site of equilibrium (Kendall and McDonnell, 1998). This study specifically examines the ratio of ^{18}O to ^{16}O. ^{16}O preferentially evaporates into cloud water vapour. The subsequent ratio of ^{18}O to ^{16}O in condensing water vapour is determined by the ambient temperature and therefore latitude. The heavier [^{18}O] oxygen isotope will condense out of the moisture first, with greater amounts of the lighter isotope [^{16}O] remaining as the air mass travels further from the source water to higher latitudes. Thus, glaciers and ice sheets, or horse hair, at higher latitudes, experience an enrichment in ^{16}O and depletion in ^{18}O in comparison to that of the oceanic source (see Figure 1.1).

Figure 1.1: Oxygen isotope schematic, detailing the environmental processes of $\delta^{18}O$ depletion and enrichment.

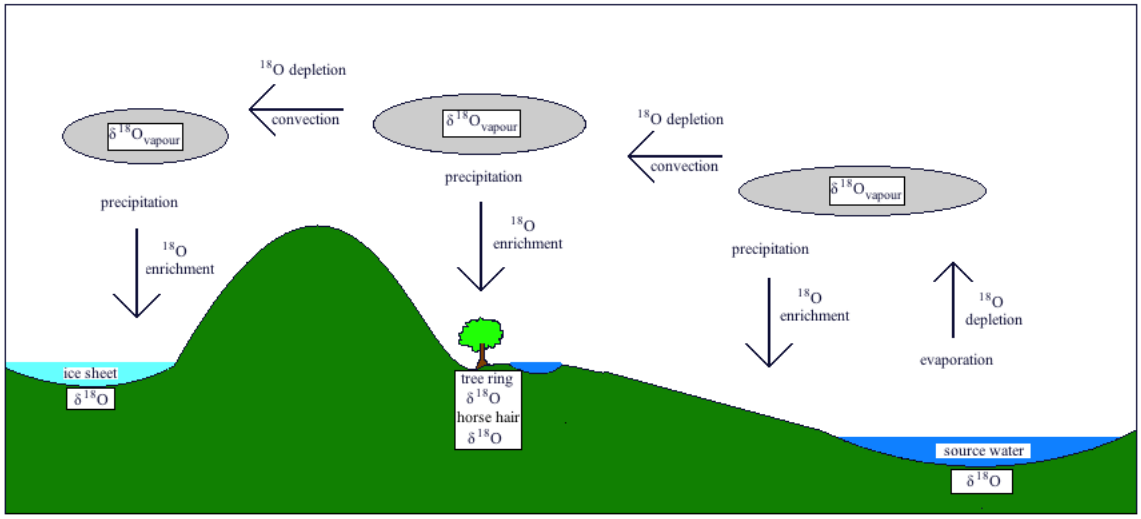

The oxygen isotope ratio within atmospheric water is primarily affected by fractionation processes associated with latitude and temperature (Dansgaard, 1964). When sequentially comparing environmental records to meteorological data, specific signals can be

isolated and de-constructed. Through this process, stable oxygen isotopic analysis is used to determine fluctuations in temperature and precipitation. Changes within the oxygen isotope measurements over time can offer insight into prevailing climatic conditions.

There are several factors which contribute to oxygen isotope distributions, specifically affecting the δ^{18}O of precipitation. These include the source effect, the amount effect, continent effect, and the altitude effect (Baker, 2014). The source effect is associated with the measure of distance from the source of the atmospheric moisture. The further the air mass has travelled from the moisture source, the isotopically depleted in ^{18}O it becomes (Dansgaard, 1964). Additionally, increased precipitation recycling in the temperature and lower latitudes due to increased evaporation and evapotranspiration associated with higher temperatures leads to isotopically lighter atmospheric moisture in comparison to evaporative effects in oceanic regions (Eltahir and Bras, 1996; Cole et al., 1999; Baker, 2014).

The amount effect relates to the quantity of precipitation from the air mass. Increased precipitation has been shown to deplete ^{18}O, as a result of water vapour recycling (Bony et al., 2008; Risi et al., 2008). Tropical and monsoonal regions are highly influenced by the amount effect, where seasonal precipitation is predominant (Dansgaard, 1964). The continent effect is similar to the source effect, where rainout during transport inland results in a depletion in ^{18}O (Rozanski et al., 1993; Baker, 2014). Finally, the altitude effect is associated with orographic or adiabatic uplift. This is where air masses are lifted due to vertical circulation or topographic features, and rainout occurs (Baker, 2014). The altitude effect also results in a depletion of ^{18}O.

Stable isotopic composition analysis is a technique commonly used within archaeolog-

ical science for palaeodiet and palaeoclimate studies. The study of isotopes is useful for examining a range of environmental factors such as diet and water source (Pang et al., 2004; West et al., 2004). Atmospheric processes of evaporation and precipitation have a calculable impact on the stable isotope ratios of oxygen and hydrogen (Dansgard, 1964). By examining the changes in stable isotopic composition of a continuous dataset over time, insight can be gained into the influence of the atmospheric conditions (Johnsen et al., 2001; Pang et al., 2004). Figure 1.2 details the transport and fractionation influences that the global circulation of δ^{18}O experiences from the moisture source [sea water], through to the δ^{18}O values of the North Greenland Ice Core record, tree ring δ^{18}O values, and the δ^{18}O values within horse keratin. This also demonstrates the increasing complexity of fractionation influences that the δ^{18}O values have undergone within these different environmental records.

Figure 1.2: Schematic of the processes from which source moisture δ^{18}O is transferred to the North Greenland Ice Core, tree rings and horse hair (based on Young et al., 2015).

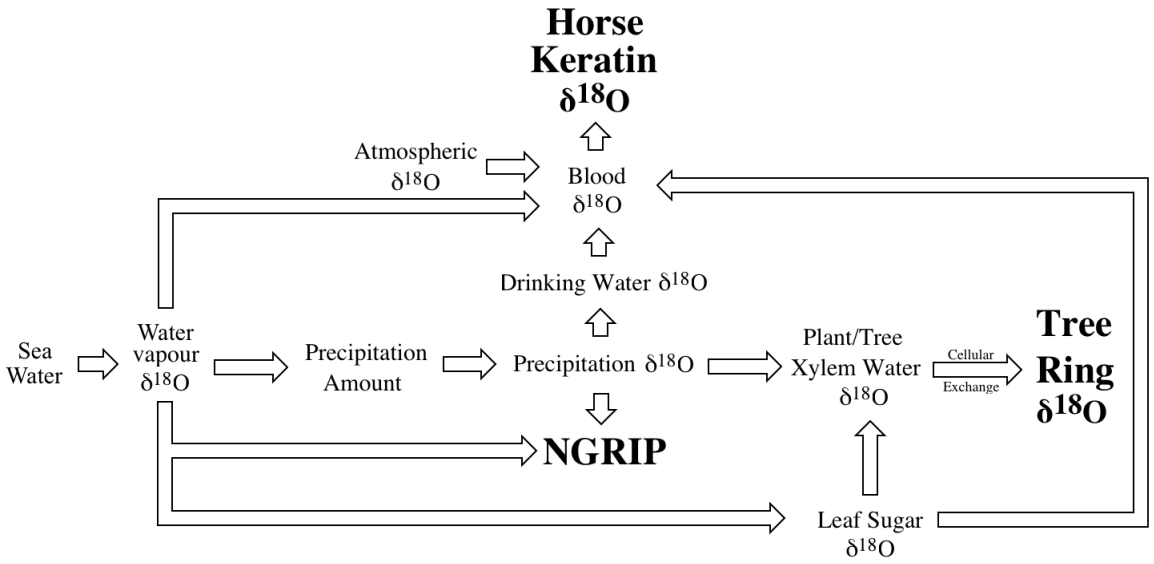

1.3 Thesis structure

This thesis is comprised of seven chapters. Chapter 2 focusses on the foundations of global circulation, and introduces isotope analysis. It goes on to examine standards of isotopic measurement and notation, stable isotopes in the biosphere as well as isotope correlation between systems. Chapter 3 details the background study location information, with geographical and geological location introductions, horse ecology, as well as climatologies during four periods of time from 1250 B.C. to 950 A.D., 950 A.D. to 1400 A.D., 1400 A.D. to 1850 A.D., and 1850 A.D. to Present.

In Chapter 4 the methodology used for the preparation and analysis of the three datasets is outlined. This includes the horse hair samples, analysis method, data calibration as well as research methodology. The chapter also details the ice core sampling and analysis method, as well as the tree ring sampling and analysis method. Finally it also describes the samples utilised from modern observational data, and the statistical methodology applied to the datasets.

Chapter 5 examines the location-based results of the horse hair latitudinal study, as well as the discussion of the results as the stand against the hypotheses. In the sixth chapter, the results and subsequent discussion of the ice core and dendroclimatology research study are explored.

The final chapter draws conclusions from the thesis, with a further discussion section, including theorised explanations for the results, as well as exploring possible statistical uncertainty. Finally, highlighting the importance of this research, Chapter 7 explores impacts of the climate on humans, as well as applications and implications of isotopic

analysis within environmental records of increasing complexity, and makes a final conclusive statement bringing together all aspects that the hypotheses have addressed.

2. Climate and Isotopes

This chapter describes the background theory and literature regarding current isotopic research. It starts by discussing global circulation (Section 2.1), and introducing isotopic theory (Section 2.2). It follows on to describe isotopic measurements and reporting practice in Section 2.3. It explores isotope research as it relates to ice core analysis in Section 2.4. Finally, in Sections 2.5 and 2.6, isotopic analysis of tree rings and keratin is examined, respectively.

2.1 Global circulation

Global circulation is driven foremost by solar radiation. Increased solar radiation at the equator increases surface air temperatures, which decreases the air density and leads to the air mass rising toward the upper atmosphere. As these air parcels rise, an area of low

pressure is created, which draws in air to replace that which has been lost upward. This creates the circulation process in Figure 2.1, known as the Hadley circulation (Tribbia, 1991; Marshall and Plumb, 2007).

Figure 2.1: The Hadley circulation of the equatorial region, including solar radiation; areas of high and low pressure; the easterly trade winds; and direction of air movement.

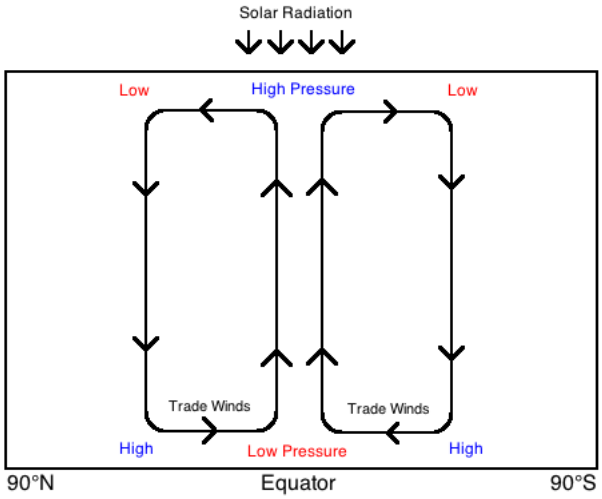

The spinning of the Earth, known as the Coriolis Force, causes a deflection in the direction of air mass movement (Persson, 1998). This movement of deflected air from high to low pressure results in south easterly [north easterly] trade winds of the Southern Hemisphere [Northern Hemisphere]; subtropical westerly winds; and the polar easterly winds shown in Figure 2.2 (Garrison, 2007).

Figure 2.2: Global surface air circulation, including the equatorial trade winds; subtropical westerly winds; polar easterly winds; as well as high and low pressure belts.

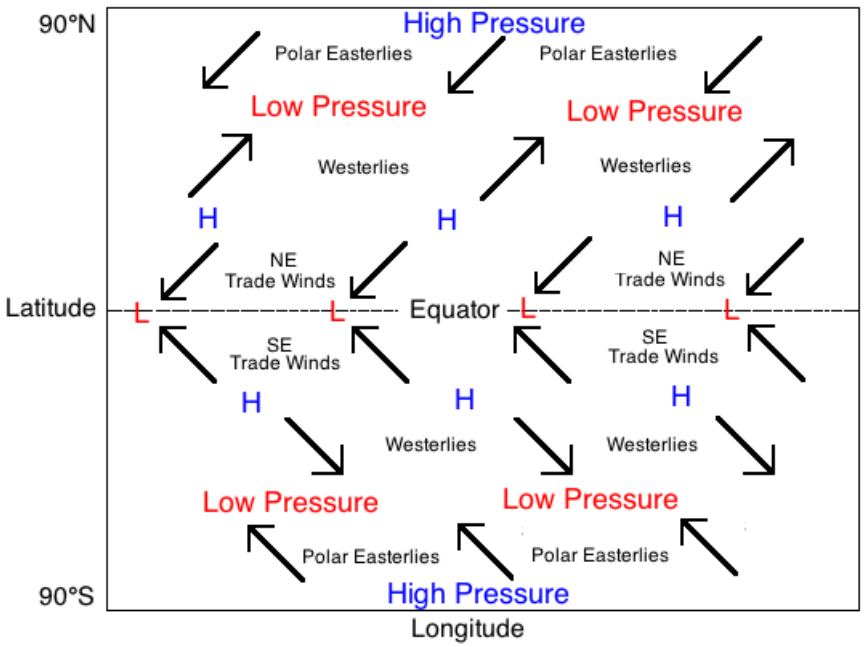

The belt of trade wind convergence around the equator is referred to as the intertropical convergence zone (ITCZ) and is associated with increase cloud and rainfall. The tilt (obliquity) of the Earth combined with the elliptical movement of the Earth around the Sun means that the maximum solar radiation does not always fall directly over the equator. This means that the band of equatorial convergence (ITCZ), shown in Figures 2.1 and 2.2, shifts northward during the Northern Hemisphere summer, and south during the Southern Hemisphere summer (Wallace and Hobbs, 2006). Areas of high solar radiation with low cloud cover experience high levels of evaporation. Evaporation occurs when solar heating of liquid water causes a water vapour phase change (Brutsaert, 1982). This water vapour is then carried by the winds and lifted by further heating or topographic uplift. As moist air rises it becomes supersaturated, and water vapour condenses onto

cloud nuclei, forming cloud droplets (Wallace and Hobbs, 2006). When these droplets get too large and heavy, they fall as precipitation.

2.2 Introduction to isotope analysis

Isotopes are atoms of the same element with different numbers of neutrons. The most abundant (99.76%) isotope of Oxygen, ^{16}Oxygen has only 8 neutrons, but ^{18}Oxygen has 10 neutrons (Ellsworth, 2012). As two variations of the same element, these isotopic atoms should have equal chemical and physical characteristics. However with high resolution accurate measurements, minute changes in the chemical and physical behaviour are observed, such as preferential evaporation. This difference between theoretically equal atoms is called isotopic fractionation (Mook, 2006). These differences manifest in two ways: heavier atoms [^{18}O] are less mobile and therefore lighter atoms [^{16}O] react faster to transitional changes; and heavier isotopes [^{18}O] require higher kinetic energy in order to change phase, which means that they do not evaporate as easily. Transitional changes can include changes between solid, liquid and gaseous states, and compound transitions, such as incorporation into biological systems. Another example of thermodynamic and biological effects on isotope fractionation is enzyme discrimination against the heaver isotope within biochemical reactions. These changes in ratio between lighter [^{16}O] and heavier [^{18}O] isotopes present within systems (horse hair/tree rings/ice cores) can be therefore traced within biological tissues and environmental records back to the causative environmental fractionation process such as temperature change, evaporation and rainfall (Koch, 1998; Gat and Airey, 2006; Sharp, 2007; Hoefs, 2009; Roberts, 2016).

The effect of weight and bond strength on isotopes manifests throughout the climate system via changes in the ratio of heavier to lighter isotopes. This study specifically examines the ratio of ^{18}O to ^{16}O. ^{16}O preferentially evaporates into cloud water vapour. The subsequent ratio of ^{18}O to ^{16}O in condensing water vapour is determined by the ambient temperature and therefore latitude. The heavier [^{18}O] oxygen isotope will condense out of the moisture first, with greater amounts of the lighter isotope [^{16}O] remaining as the air mass travels further from the source water to higher latitudes. Thus, glaciers and ice sheets, or horse hair, at higher latitudes, experience an enrichment in ^{16}O and depletion in ^{18}O in comparison to that of the oceanic source.

The oxygen isotope ratio within water is affected by fractionation processes associated with latitude and temperature (Dansgaard, 1964). When sequentially comparing environmental records to meteorological data, specific signals can be isolated and deconstructed. Through this process, stable oxygen isotopic analysis is used to determine fluctuations in temperature and precipitation. Changes within the oxygen isotope measurements over time can offer insight into prevailing climatic conditions.

Stable isotopic composition analysis is commonly used within archaeological science for palaeodiet and palaeoclimate studies (Pang et al., 2004; West et al., 2004). Atmospheric processes of evaporation and precipitation have a calculable impact on the stable isotope ratios of oxygen and hydrogen (Dansgard, 1964). By examining the changes in stable isotopic composition of a continuous dataset over time, insight can be gained into the influence of atmospheric conditions (Johnsen et al., 2001; Pang et al., 2004).

A pioneering study by Dansgaard (1964) examined the link between stable isotopes and precipitation. This research discusses the relationship between oxygen isotopes and precipitation, condensation temperature, and evaporation; as well as the differences in

fresh water and sea water oxygen isotope values. It introduces the idea that the heavy isotope concentration of an air mass decreases with increasing altitude and latitude. Isotopic ratios are impacted particularly by the rate and degree of evaporation, and heavy precipitation events can result in the distribution of large amounts of isotopically light water over large regions (Dansgaard, 1964). The effects of the evaporative preference toward the lighter isotope results in depleted $^{18}0$ meteoric water when compared to surface and soil waters (Gat and Airey, 2006).

δ^{18}O and δ^{2}H have been shown to exhibit seasonal variability within atmospheric water vapour, and consequently precipitation (Araguas et al., 1996). Mid and high latitude areas exhibit depleted isotope concentrations in winter, and in summer exhibit enriched stable isotope concentrations.

Figure 2.3 shows the direct positive correlation between the annual δ^{18}O values of precipitation and annual temperature (in degrees Celsius), within the observed present day climate system, obtained from polar measurements as well as the International Atomic Energy Agency (IAEA) isotope measurement network (Jouzel et al., 1994). As temperature increases, the oxygen isotope ratio is also seen to increase.

Figure 2.3: Schematic showing relationship between temperature (degrees Celsius) and δ^{18}O, sourced from Jouzel et al. (1994).

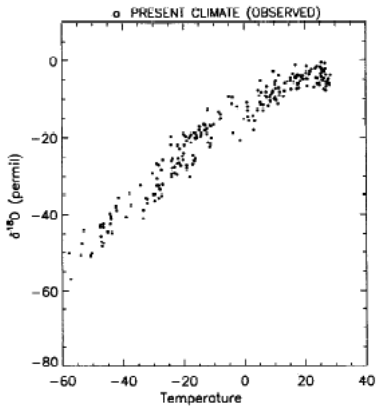

Water isotope analysis is particularly useful for studies of air mass mixing, water vapour, and determining oceanic sources of precipitation events (Froehlich et al., 2002). Values derived from water vapour measurements can be used as tracers for the diurnal and vertical patterns within atmospheric moisture, as well as to model evaporative enrichment (Lai and Ehleringer, 2011).

2.3 Isotopic measurement

Isotope ratios are defined by the abundance of the rare isotope, divided by the abundance of the abundant isotope and represents the chances of whether the abundant isotope has been replaced by the rare (Mook, 2006).

Molecular differentiation between heavier and lighter isotope atoms, causing fluctuations in the ratio of ^{18}O to ^{16}O mean that, by comparing internationally standardised values of natural water (Standard Mean Ocean Water), oxygen isotope ratios can be used to extrapolate temperature curves. In other words, deviations from baseline condi-

tions can be used as a tracer of the influx values. Oxygen isotope ratios measured within samples are referred to as the deviation from this standard, and are otherwise known as δ^{18}O values (Kendall and Caldwell, 1998). δ^{18}O values are calculated by the following equation, and are reported in units of parts per thousand (‰), and referred to as a value 'per mil':

$$\delta^{18}O = \left(\frac{^{18}O/^{16}O_{Sample} - ^{18}O/^{16}O_{Standard}}{^{18}O/^{16}O_{Standard}} \right) \times 1000$$

(Meier-Augenstein, 2009)

Comparisons can be made by referring to high versus low; more or less positive and more or less negative; heavier versus lighter (heavier having a higher δ value); and enriched versus depleted - with reference to the comparative datum, for example 'enriched in ^{18}O relative to the previous 10 years' (Kendall and Caldwell, 1998).

2.4 Isotopes in ice cores

Isotopic analysis within ice cores is particularly useful as it provides continuous chronological evidence of climatological changes through direct atmospheric deposition. The water isotope concentration of ice contained within the Greenland Ice Sheet is influenced by the isotopic values of the deposited precipitation; as well as surface diffusion fractionation with atmospheric water vapour within the top 60 metres of ice (Johnsen et al., 2000). Figures 2.4 and 2.5 show the changes in oxygen isotope values during the transport and deposition of the precipitation contained within the North Greenland Ice Core, as well as the distribution of oxygen isotope ratio change from the ocean into the

Greenland Ice Sheet, respectively.

Figure 2.4: Schematic showing the transport of oxygen isotopes evaporated from sea water, through the hydrological cycle and into the North Greenland Ice Core, including stages at which ^{18}O is enriched and depleted.

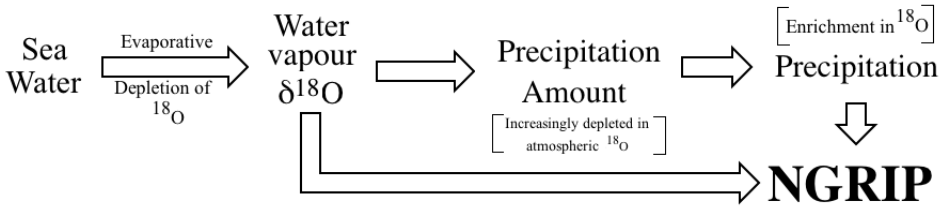

As air masses travel across the ice sheet, away from the oceanic source, the ^{18}O precipitation ratio becomes more negative. During winter this ratio depletion becomes more pronounced as the air mass approaches the summit of the ice sheet.

Figure 2.5: Schematic showing the evaporative transport of oxygen isotopes from the ocean, over the Greenland Ice Sheet, including the decreasing $\delta^{18}O$ values toward the summit, based on Dansgaard et al. (1973).

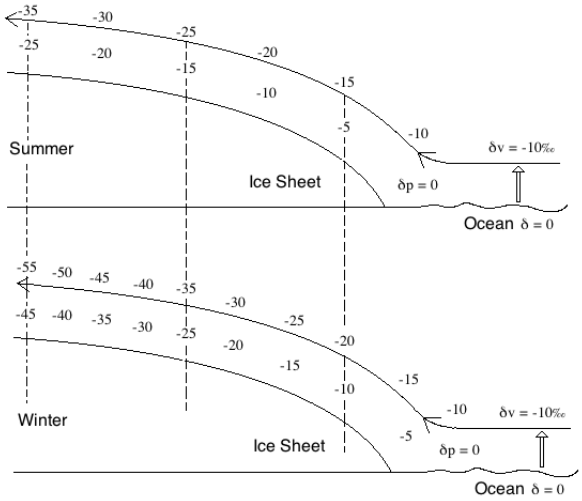

Greenland ice cores are well correlated to North Atlantic climate and are frequently used as a North Atlantic climate proxy (Walker et al., 2001). Vinter et al. (2003) extracted the

North Atlantic Oscillation signature from the winter isotope values of seven Greenland ice cores. This was done by calculating the mean winter δ^{18}O values, and completing principal component analyses on the results to isolate regional signals. These winter Greenland ice core oxygen isotope ratios produced by Vinther et al. (2003) correlated to North Atlantic Oscillation at the ninety-five percent confidence level.

Water isotope records in central Greenland site are used to describe the process of evaporative and phase change fractionation (Hoffmann and Jouzel, 2001). Using mixed cloud isotope models, researchers have also been able to interpret surface temperature variations from the oxygen and deuterium isotope values, and subsequently interpret the influence of the Little Ice Age and the Medieval Warm Period.

δ^{18}O values were analysed to produce a continuous record for two central Greenland ice cores, in order to examine changes in past climate over a 250-kyr ice core record (Dansgaard et al., 1993). A common assumption in ice core analysis is that the stratigraphy of the ice has remained undisturbed. Any folding or movement of the ice would result in a discontinuous annual profile, although visual analysis can account for such movements and the broad context of the profile is still valid (Dansgaard et al., 1993).

Regional climate changes were discovered to be a dominant influence on variations in oxygen isotopes within ice cores(Johnsen et al., 2001). Isotopic data from six Greenland sites were analysed to produce palaeotemperature estimates. High resolution Holocene profiles were produced by correlating volcanic events to δ^{18}O changes and annual layer counting (Johnsen et al., 2001).

2.5 Isotopes in tree rings

Tree ring analysis has a well established role within stable isotope research. The biological process of annual lamination of wood enables patterns within individual trees to be cross-checked over a much wider region (McCarroll and Loader, 2004). The width of these rings also provide an indication of favourable growth conditions, and subsequently favourable climatological factors. Stable isotope analysis of tree rings provides information about precipitation through soil water and summer humidity (McCarroll and Loader, 2004), and in turn about temperature and source air-mass variation (Sidorova et al., 2013).

The two determining factors in the oxygen isotope composition of tree xylem water and tree ring cellulose is determined by: the isotopic values of the inputs, including atmospheric exchange and source water root uptake; as well as the biochemical fractionation effects within the plant, including leaf water enrichment due to transpiration, as seen in Figure 2.6 (Gonfiantini et al., 1965; Yakir, 1992; Yakir, 1998; Csank, Fortier and Leavitt, 2013).

Figure 2.6: Schematic showing the transport of oxygen isotopes evaporated from sea water, through the hydrological cycle and into tree ring cellulose, including stages at which ^{18}O is enriched and depleted (based on Young et al. 2015).

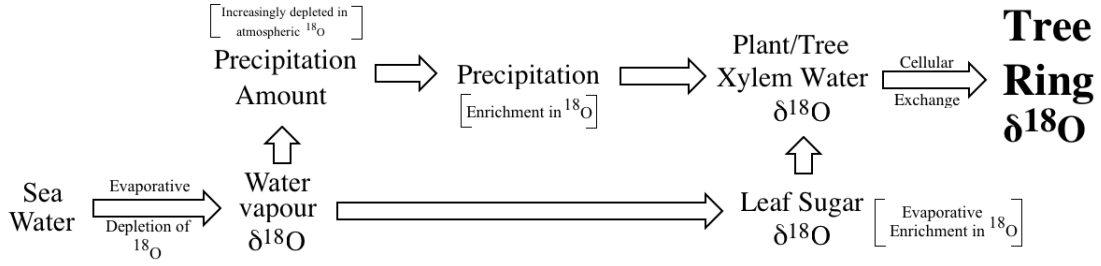

The stem and roots of a plant accurately represent available source water as there are

no fractionation effects during uptake from surrounding soil (Walker and Richardson, 1991; Thorburn and Mensforth, 1993). Deep ground water contains a smoothed signal that represents a long term average oxygen isotope signal from locally precipitated water (Flanagan, Comstock and Ehleringer, 1991). A second source of available plant water, is recent precipitation, which gives a higher resolution indication of locally precipitated δ^{18}O. Shallow rooted trees, which are most likely to access recent precipitation at the soil surface are more sensitive to annual precipitation signals; whereas deep-rooted trees that have better access to deep underground reservoirs are more sensitive to evaporative-enrichment signatures (McCarroll and Loader, 2004).

There are two evapotranspiration fractionation effects at the leaf of a plant (Figure 2.7). The first is due to the liquid to vapour phase change of water at the leaf-air boundary, which is referred to as an equilibrium effect; and the second is a result of the unequal rate of diffusion between the heavier (^{18}O) and light isotope (^{16}O), which is the kinetic effect (Flanagan and Ehleringer, 1991). Vapour pressure and relative humidity are dominant controls of evaporative enrichment during transpiration (Helliker and Ehleringer, 2002; McCarroll and Loader, 2004). The diffusion rate of ^{16}O/^{18}O has been found to equal 1.0285 (Merlivat, 1978).

Figure 2.7: Evapotranspiration process resulting in the ^{18}O enrichment of leaf water, and without fractionation within capillary flow.

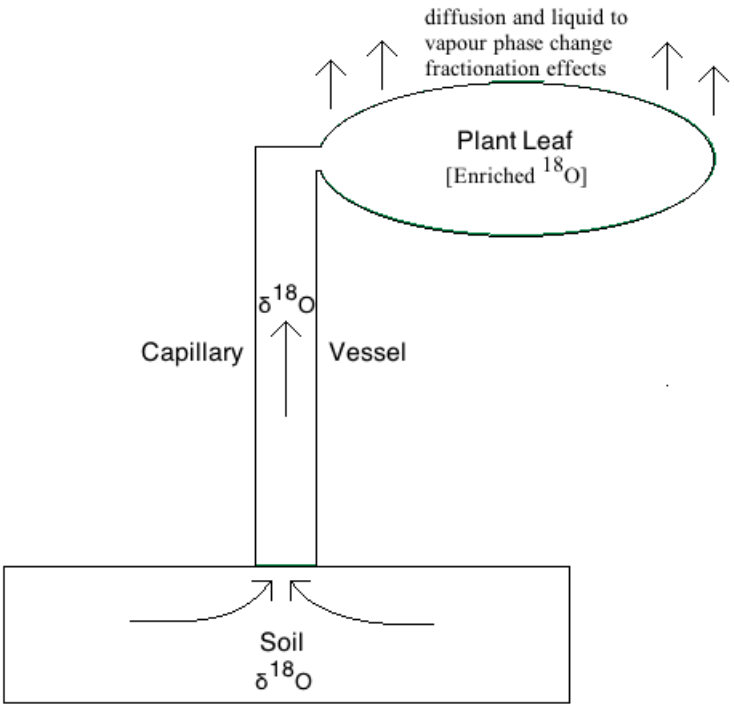

Carbon, hydrogen, nitrogen and oxygen are the dominant elements within wood and thereby provide an excellent dataset for stable isotope analysis and palaeoclimate reconstruction (McCarroll and Loader, 2004). Woodborne et al. (2015) developed a South African proxy record of rainfall, which contained centennial and decadal signals, from Baobab trees using carbon isotope analysis. Local rainfall records were used to correlate the accuracy of the proxy δ^{13}C record.

Oxygen isotopes within tree rings record changes in meteoric water, with decreasing ^{18}O values during atmospheric transport inland over continents (Saurer, 2003). Reynolds-Henne et al. (2007) also demonstrated that δ^{18}O variability in oak and pine is related to

large-scale atmospheric circulation.

Temperature variability in the Russian Altai during the June, July and August months, and the frequency of observed drought events appear to be well recorded in tree ring width and stable isotope chronologies (Sidorova et al., 2013). Fifteen samples from living trees were sampled for stable isotope analysis, and compared against local and regional climate records. Linear regression techniques were applied to the dendrochronological analysis and stable isotope data to produce the palaeoclimate reconstruction (Sidorova et al., 2013). This research found that in addition to using δ^{18}O variability to reconstruct July precipitation, it can provide a record of source air-mass variations.

δ^{18}O within tree ring cellulose is dependent on the input water isotopes, and therefore on water availability, precipitation, temperature and humidity, during the summer growth season (Saurer et al., 2000; Reynolds-Henne et al., 2007). Saurer et al. (2008) demonstrated that high temperature and low precipitation results in an increase in ^{18}O and Young et al. (2015) also found that warm and dry summers result in enriched ^{18}O, whereas wet and cooler summers show a depletion. Changes in snow isotopes can also result in depleted tree rings isotopes due to a decrease in the soil water isotopes (Saurer, 2003).

2.6 Isotope analysis within keratin

The isotopic analysis of hair has been increasingly used in climate research. Biologically inactive post-formation, and degradation resistant, keratin is a fast and continuously growing material; which makes it an excellent temporally high-resolution dataset (Zazzo et al., 2015). Hair keratin is a 'hard' keratin, comprised of a group of approx-

imately 100 proteins, made of amino acids, as well as water, lipids, pigment and trace elements (O'Connell et al., 2001; Bhushan, 2008). Specifically, the composition of hair typically includes Nitrogen, Sulfur, Histidine, Lysine, Arginine, Cystine, Tyrosine, Tryptophane, Phenylalanine and Glycine (Block, 1939).

Hair keratin is more complex than tree ring and ice cores, and has a number of additional biochemical fractionation influences. Isotopic signals within horse hair are affected by evaporative depletion of ^{18}O within water vapour relative to source sea water and the precipitation amount effect, with increasing depletion of ^{18}O within the source air mass relative to the precipitated water. Keratin isotopes are also affected by enrichment in precipitation ^{18}O relative to source air mass and evaporative ^{18}O enrichment of ground-lying surface drinking water (Figure 2.8).

Figure 2.8: Schematic showing the transport of oxygen isotopes evaporated from sea water, through the hydrological cycle and into horse hair keratin, including stages at which ^{18}O is enriched and depleted.

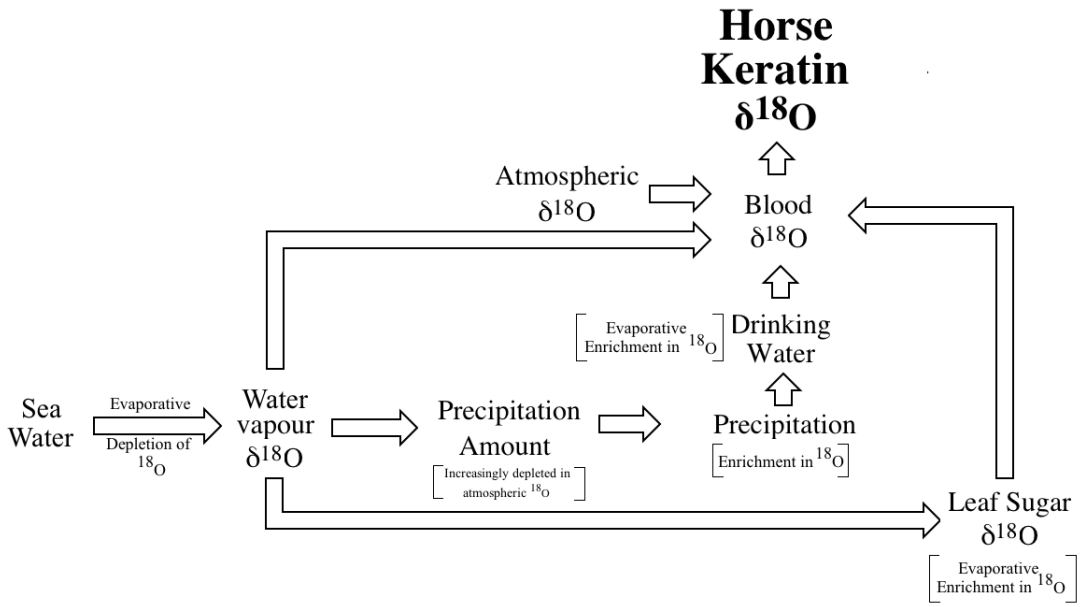

Cellular diffusion occurs within the lungs, transporting atmospheric water vapour and atmospheric oxygen into the blood. Fractionation occurs during the digestion of leaf sugars, with food water diffusion into the blood. The residence time of isotope transport within blood plasma is between two and seven days, and the response time of body water δ^{18}O to a change in isotopic drinking water inputs for a human is approximately 10-14 days (O'Connell, 1996; Sharp and Cerling, 1998). With a greater mass, a horse would have a longer complete turnover time than the 10-14 days in humans, but other studies have shown that the initial 'half-life' response within hair keratin to a change in δ^{18}O input would occur at a 0.5-4 day time scale, and would therefore still provide detail of high-resolution changes in drinking water (Sharp and Cerling, 1998; Ayliffe et al., 2004; Cerling et al., 2007).

Therefore, the isotopic ratio of hair keratin provides a record of the inputs of oxygen from food, atmospheric water vapour and atmospheric; as well as local meteoric drinking water (Fricke et al., 1998; Hoppe, 2006), which has been shown to be notably analogous to δ^{18}O values within keratin (Bryant and Froelich, 1995; Ehleringer et al., 2008; O'Grady et al., 2010; Mant et al., 2016). Changes within the oxygen isotope measurements of horse hair over time can therefore offer insight into source drinking water fluctuations, and subsequently, seasonality in atmospheric conditions (Sharp et al., 2003).

Studies of human hair have confirmed that water source has a significant influence on stable oxygen and hydrogen isotope ratios in keratin (Ehleringer et al., 2008). Tap water and hair samples were analysed from 18 states within the United States of America, to track the geographical variation of oxygen and hydrogen stable isotope variation. The result of this research was that more than eighty-five percent of model variation

was explained by the isotopic ratios of drinking water, bulk diet and dietary protein. It showed that dietary, drinking water and atmospheric oxygen all contribute to the variation in hydrogen and oxygen isotopes within body water (Ehleringer et al., 2008). Oxygen isotopes within the keratin of domestic cows showed a significant correlation with meteoric oxygen isotopes in a study by Chen et al. (2017). Associated secondary contributions to this relationship came from feed moisture, temperature and atmospheric moisture. Bowen et al. (2009) conducted hydrogen and oxygen isotope analysis on one hundred and twenty-three samples from the mid-20th century. The results showed that within indigenous populations with local dietary consumption, environmental water has a dominant impact on the variation in protein-based hydrogen and oxygen isotopic ratios.

Sheep wool provides a good proxy for seasonal climate, as it exhibits seasonality with depletion of ^{18}O values in winter and enrichment during the summer months (Zazzo et al., 2015). Although the hydrogen signal was not as clear as that within the oxygen isotope values, hydrogen isotope analysis also provided a seasonal climate pattern within the sheep wool. Differentiating examinations of oxygen, hydrogen, carbon and nitrogen stable isotopes within keratin have provided information about environmental driven seasonal changes in diet and physiology (Zazzo et al., 2015). Oxygen isotopes were also analysed in rodent hair, which found fluctuations related to drinking water and therefore meteoric water and seasonal rainfall (Kirsanow and Tuross, 2011).

A recent study that modelled non human primate hydrogen and oxygen isotope ratios, demonstrated that the isotopic composition of body water was exchangeable with the gut when estimating the δ^{18}O values of hair (O'Grady et al., 2012). This study validated the accuracy of semi-mechanistic isotopic composition model for hydrogen and oxygen,

developed by Ehleringer et al. (2008).

Although this thesis does not examine hydrogen isotopes, the links between climate and hydrogen have been well established (Reynard and Hedges, 2008). However, hydrogen analysis and its comparison to climate and meteoric water is further complicated by a strong relationship with tropic level, with a greater influence from dietary input (Birchall et al., 2005; Schulting et al., 2018).

One study examined the stable hydrogen isotope concentrations of a 370 year old Incan mummy and a Woolly Mammoth from Siberia (Sharp et al., 2003). This research showed that within the Incan mummy hair, the majority of hydrogen originated from the food, as opposed to around one third isotopically derived from the drinking water. However, it does describe the potential for deuterium (δ^2H) to provide daily to weekly isotopic representations of food and water consumption within mammals (Sharp et al., 2003).

Isotope values within keratin reflect the dietary intake of animals of difference species, with keratin carbon and nitrogen isotopes typically enriched relative to diet isotopic values (O'Connell, 1996). According to data from Minson, Ludlow and Troughton (1975); DeNiro and Epstein (1978); Jones et al. (1981); Tieszen et al. (1983); Tieszen and Boutton (1988); Katzenberg and Krouse (1989); Hare et al. (1991) the difference between δ^{13}C isotope values within keratin and the dietary input of cows, mice, gerbils, cattle and pigs ranges from -0.3 to 3.4 ‰. Rats and mice have shown a difference between the δ^{13}C of diet proteins and keratin that ranges from -2.2 to 3.2 ‰ (Nakagawa et al., 1985; Ambrose and Norr, 1993; Tieszen and Fagre, 1993.

Carbon isotopes provide information on the dietary proteins of an animal, and specif-

ically the variation in C3 and C4 plant consumption and marine versus terrestrial food sources (Stevens and Hedges, 2004). Changes in δ^{15}N reflect soil type and nitrogen availability, and is primarily used to examine tropic levels (Loftus et al., 2016). This study uses carbon and nitrogen values in order to briefly examine whether there are significant dietary differences between individual horses at the four locations, which could influence the oxygen isotope comparison.

Cerling et al. (2006) conducted an isotopic examination of African elephants over a six year period. This study collected and analysed tail hair to show the dietary and migration patterns of thirty-five elephants. This study shows that although there may be variation up to thirty percent within the growth rate of different hairs of the same animal, the growth rate within one hair appears to be constant over time. By correlating the carbon and nitrogen isotope values within the hair against GPS radio collars, Cerling et al. (2006) demonstrated the value of stable isotope analysis for dietary and geographical movement tracking.

West et al. (2004) examined the dietary changes of horses using carbon isotope analysis. This study produced isotope chronologies tracking dietary changes on 1-day, 3-day and 7-day timescales. The maximum resolution limitations of horse hair analysis lies within the analytical constraints, as opposed to biological constraints (West et al., 2004). This issue lies in length of hair required to achieve a desired sample mass required for the isotopic analysis. It is suggested that multiple hairs can be combined in one sample to increase resolution, but this relies on the acceptance of an accurate temporal and spatial alignment. Diagenesis effects, a common concern within isotopic analysis of bone, are not relevant for the biologically inactive and degradation-resistant hair keratin (O'Connell, 1996).

3. Background

This chapter examines the background climatology and geography of the study locations within this thesis. This chapter will introduce the geography and topography of the four study locations in Section 3.1; the climatology and hydrology of the locations during the four time periods of interest to this research, from 1850 A.D. to present day, 1400 A.D. to 1850 A.D., 950 A.D. to 1400 A.D., and 1250 B.C. to 950 A.D. in Section 3.2; as well as the ecological backgrounds at the horse sampling locations in Section 3.3.

3.1 Location introductions

There are four sampling locations used within this study. The Greenland Ice Sheet was the source of the ice core dataset used in this research and is the northernmost study location. Horse samples were obtained from a 13° latitudinal range from approximately

64° N in Iceland, 60° N in the Shetland Islands, as well as two southern locations between 51-52° N within the United Kingdom. The United Kingdom, in central-southern England, was also the location for extensive tree ring sampling by the 'New Tools for Science-based Archaeology: Isotope-supported Dendrochronology' project, the data from which is examined in this thesis.

Figure 3.1: Map of the Atlantic region and Greenland. [Map image is the intellectual property of Esri and is used herein under license. Copyright ©2017 Esri and its licensors. All rights reserved].



Table 3.1: Approximate latitude and longitude locations for the ice core, tree ring and horse hair sampling sites (in °N, °W).

	Latitude	Longitude
NGRIP	75.10	42.32
Tree rings	50.96-52.78	2.75-0.00
Iceland	63.92	21.00
Shetland	60.24	1.65
Oxfordshire	51.81	1.39
Exmoor	51.06	3.59

3.1.1 Greenland

Greenland boasts unique geographical and climatological setting, encompassing nearly 24 degrees of latitudinal extent. Of the 2.2 million square kilometres of land surface, the Greenland Ice Sheet makes up more than 80 percent (DMI, 2016). The main factors of Greenland morphology and climate is snow deposition and ice mass balance. Cold central Greenland snow falls during winter result in the compaction of snow into ice and the outward spreading of the ice sheet, through internal deformation due to mass increase (Lindbäck, 2015).

Figure 3.2: Map of Greenland showing the location of the North Greenland Ice Core [NGRIP], the summit of the ice sheet, and the Dye-3, GRIP and GISP2 ice cores (sourced from Johnsen et al., 2001).

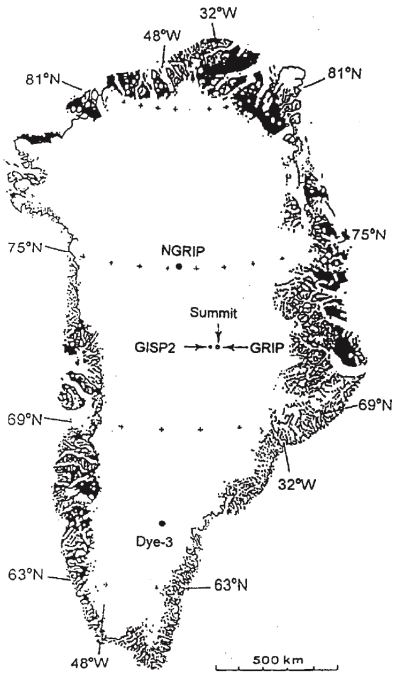

The North Greenland Ice Core Project sampled a column of the ice sheet north of the summit, centrally located between the eastern and western coastlines. In comparison, the GRIP core was obtained close to the ice sheet summit, south-east of the NGRIP location.

Table 3.2 (Guillevic et al., 2013) describes the specific characteristics of the NGRIP and GRIP sampling sites:

Table 3.2: Locations, elevation, surface temperature, accumulation rates and values from the NGRIP and GRIP ice core sampling sites (in °N, °W, metres above sea level, metres ice equivalent accumulation, and ‰, respectively).

	NGRIP	GRIP
Latitude	75.10	72.58
Longitude	42.32	37.64
Elevation	2917	3238
Surface Temperature	-31.5	-31.7
Accumulation rate	0.19	0.23
$\delta^{18}O_{ice}$	-35.5	-34.9

3.1.2 Iceland

Iceland is an island with extensive volcanic activity, approximately 103,000 square kilometres in area with a coastline around 6,000km long (Jónsson and Valdimarsson, 2005), consisting of glaciers, lakes, bays and deep fjord-like inlets (Muir, 1915). Iceland is situated in an active region of North Atlantic climatological significant, in the path of the North Atlantic Current it is heavily influenced by oceanographic surface water currents. Specifically this region is influenced by water exchange across the two local sub-marine ridges, the Mid-Atlantic Ridge and the Greenland-Scotland Ridge (Jónsson and Valdimarsson, 2005).

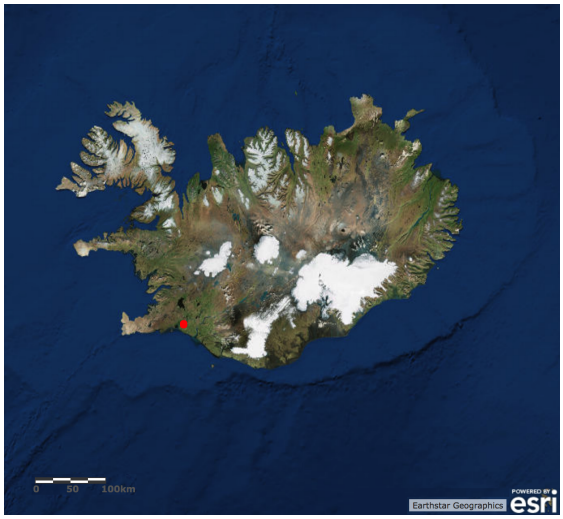

(a)

Figure 3.3: Map of Iceland with a red marker showing the location of Selfoss. [Map image is the intellectual property of Esri and is used herein under license. Copyright ©2017 Esri and its licensors. All rights reserved].

This research utilises horse hair data obtained from a location south of the capital Reykjavík, on the south-west coast of Iceland, in Selfoss. The area surrounding Selfoss is particularly flat, only tens of metres above sea level, and lies south of the typical winter sea-ice limit (Ogilvie, 2005). Selfoss sits on the southern boundary of the West Volcanic zone, in the South Iceland Seismic Zone. The Hengill volcano sits close by, to the north of Selfoss, and there is also a group of volcanoes to the south-east, which includes Hekla, Vatnafjöll, Katla, Eyjafjallajökull, and Tindfjallajökull (Gundmundsson and Andrew, 2007).

3.1.3 Shetland Islands

The Shetland Islands are part of the United Kingdom, situated north of the Scottish mainland; between the North Sea, Norwegian Sea, and the North Atlantic ocean. The

Shetland Islands sit at a latitude approximately level with the southern tip of Greenland (Golledge et al., 2008). The Shetland Islands span approximately 1° 21' of latitude and are a geologically similar to the Scottish Highlands, with igneous and metamorphosed rocks, largely resistant to marine erosion. The highest point of the Shetland archipelago, comprised of more than 100 islands, is the 450m tall Ronas Hill in the north-west of the Mainland island, although there are few tracts of flat ground (O'Dell and Walton, 1962). The Tingwall Valley is composed of metamorphic limestone, which enables fertile soil and has historical evidence of ice sheet movement, with patchy moraines. This evidence includes the north-south graining of the country, with westward moving ice suggested within the cross-cut valley at Quarff. Despite the wet climate and extensive peat cover, there is sufficient sloping and topographic variation for the prevention of bogs (O'Dell and Walton, 1962). As the highest latitude of the British Isles, the Shetland Islands are the closest to continuous daylight at midsummer. However agriculture is limited by salt encroachment via strong gales and summer fog. Fishing remains an important feature of the diet and economy. The remote oceanic location, means that the climate of the Shetland Islands is heavily influenced by ocean circulation and maritime air masses. This study uses data collected from the central western section of the mainland island, at a latitude of approximately 60.25°N and 1.65°W, which is exposed to the direct impacts of the North Atlantic Current.



(a)

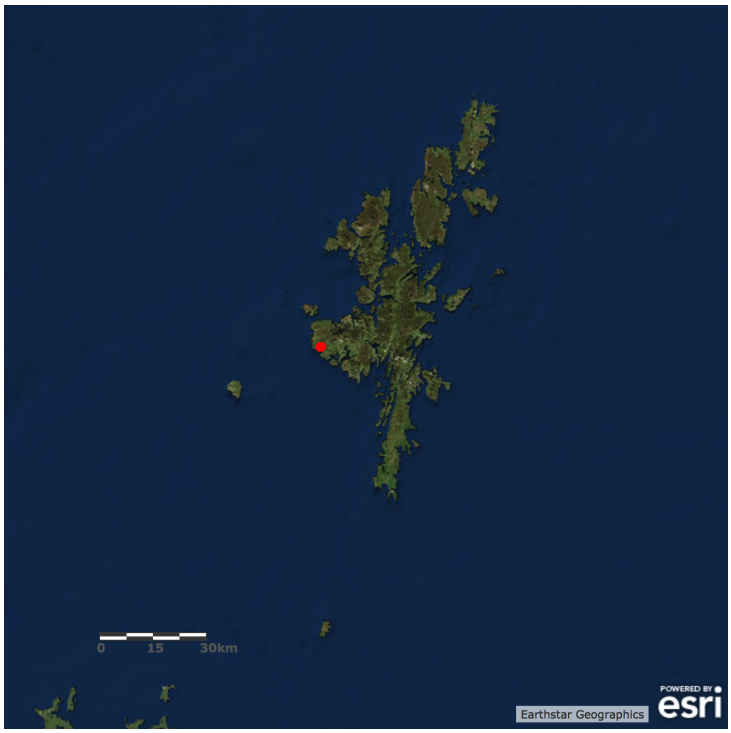

(b)

Figure 3.4: a) Map of the Atlantic region showing the location of the United Kingdom inset into a map of the UK, indicating the location of Shetland, and b) Map of Shetland Islands with a red marker showing the location of the Thordale Stud. [Map image is the intellectual property of Esri and is used herein under license. Copyright ©2017 Esri and its licensors. All rights reserved].

3.1.4 Southern Britain

The United Kingdom is land mass of approximately 244,110 square kilometres situated in the North Atlantic ocean, off the coast of the European mainland (United Kingdom, 1995). No location within the United Kingdom is further than 121 kilometres from the ocean, which plays a large part in the climate of the country. The Shetland Islands and United Kingdom received comparably warmer water than the Greenland coastline, from the southerly North Atlantic Current (see previous Figure 3.9). The circulation of the North Atlantic Gyre, the Icelandic low pressure pattern and the gulf stream all contribute to the warmer, wetter conditions in the United Kingdom. The Gulf Stream and the North Atlantic Current transport warm Atlantic waters to the United Kingdom, making it significantly milder than its western Atlantic latitudinal counterparts (Chafik, 2012). To the north, the area between the Shetland Islands and the Faroe Islands, known as the Faroe-Shetland Channel (FSC) is an important North Atlantic bottle-neck, funnelling the warmer southerly waters into the Norwegian Sea and the Artic (Chafik, 2012).

Tree ring and horse hair datasets were obtained from Oxfordshire in central-southern United Kingdom, from a longitudinal range of 0 to 2.75°W and a latitudinal range of 50.96 to 52.78°N (see Figure 3.5). The geology of the Oxfordshire county is known for its chalk and clay sediment. The Exmoor National Park, in Devon, in the south-west of England, was also a focus for horse hair sampling, being the home of the Exmoor Pony Centre. The Exmoor region is significantly less populated than the Oxfordshire region, with the total area consisting of approximately 265 square miles of forest and moorland. A plateau lies in the centre of Exmoor; the source of two main rivers, the Exe and Barle, with the highest point at approximately 520m; Dunkery Beacon. Primarily

Devonian rock, the soil of Exmoor is of two types: wet and peaty in higher moorland, and freely-draining loamy in the valleys (Burton, 1978).

Figure 3.5: Map of the United Kingdom including a red box indicating the Leverhulme Project sampling area; and red markers indicating the locations of the Exmoor Pony Centre and the Pigeon House Equestrian Centre. [Map image is the intellectual property of Esri and is used herein under license. Copyright ©2017 Esri and its licensors. All rights reserved].

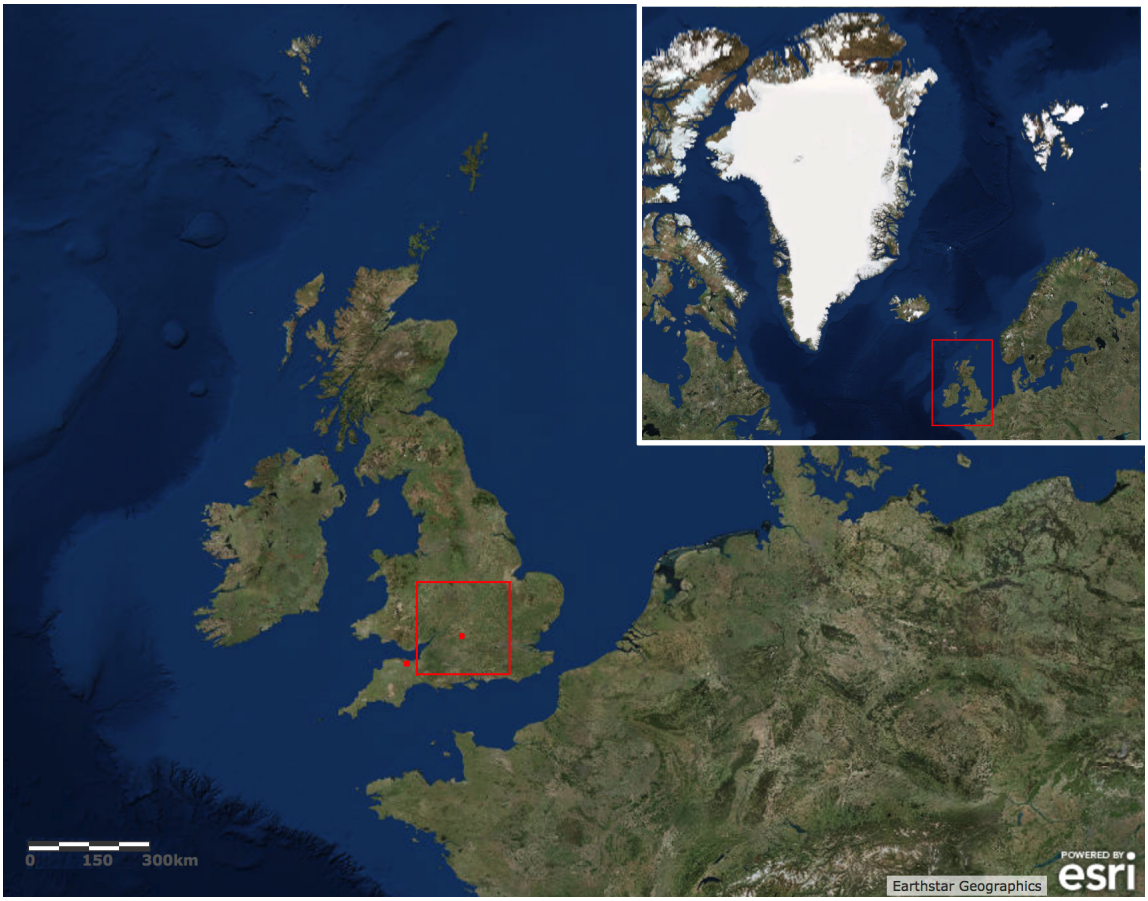

South-eastern England hydrology is centred on the Thames river and the subsequent drainage of the Thames basin, with a water catchment area of approximately 6,437 square kilometres. The origin of the Thames lies in the Cotswolds, from which it travels over the Oxford clay and the Goring Gap chalk. Oxfordshire is relatively flat, with

only low hill ranges, and contains more than 70 streams. Most of these streams are small, with the exception of the Thames (and its Windrush, Evenlode, Cherwell, Isis and Thame tributaries); the Avon tributary, the Stour; and the Great Ouse (House, 1870).

Source water in the United Kingdom is obtained from wells, adits, boreholes, reservoirs, lakes and rivers (United Kingdom, 1995). High soil moisture and low evaporation during winter in Southern Britain results in a gradual replenishment of groundwater levels, peaking in spring prior to an increase in evaporation during summer. However, if the groundwater is positioned below an impermeable soil layer, the seasonal variations are dampened (National Hydrological Monitoring Programme, 2017).

Figure 3.6: Distribution map of British oxygen isotope ratios (Image sourced from Pellegrini et al., 2016, and originally derived from Darling and Talbot, 2003).

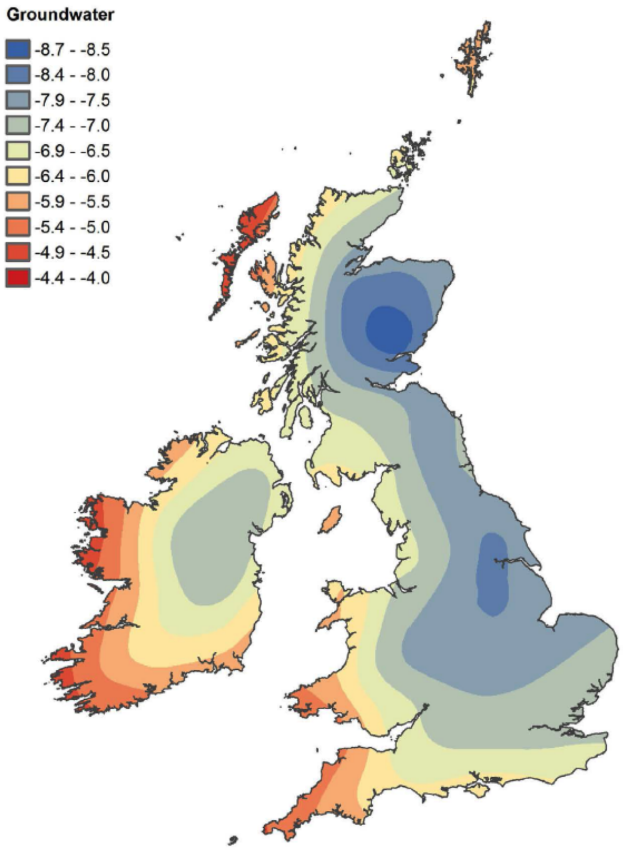

3.2 Climatology and Hydrology

3.2.1 1850 A.D. to present

The locations used within this study are all within the North Atlantic Ocean and the surrounding seas. This means that the ocean circulation and hydrological cycle of each location are interconnected and should demonstrate similar climatological drivers, albeit in different temporal scales. Figure 3.7 shows the specific circulation from the North Atlantic Current, past the United Kingdom and the Shetland Islands, dividing to the east and west around Iceland. This western branch of the current to the south of Iceland, now the Irminger Current, transports cooler waters westward around the southern coast of Greenland.

Figure 3.7: Map of ocean circulation within the North Atlantic and Nordic Seas, including the East Greenland Current (EGC), the East Icelandic Current (EIC), Irminger Current (IC), West Greenland Current (WGC), North Atlantic Current (NAC) and the Norwegian Atlantic Current (NwAC) (Sourced from Miettinen et al., 2015).

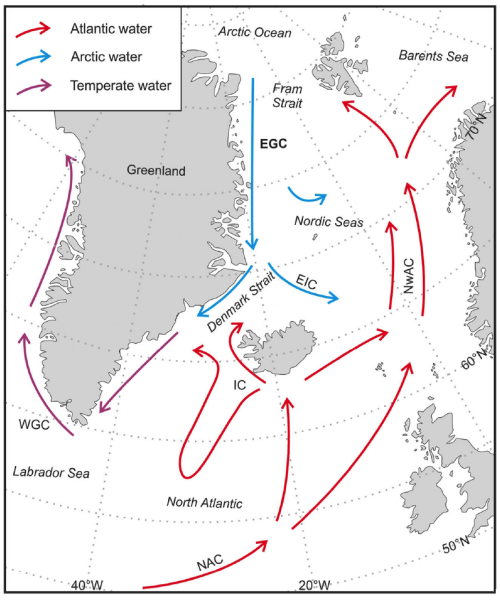

Climate drivers

The primary drivers of European and eastern North American climate consist of the North Atlantic Oscillation (NAO), the Atlantic Multidecadal Oscillation (AMO) and the Arctic Oscillation (AO). Oscillations such as the NAO, AMO, AO, the Pacific Decadal Oscillation (PDO) and the El Niño Southern Oscillation (ENSO) consist of large atmospheric or oceanic mass transfers across oceanic regions [between the Arctic and subtropical Atlantic for the NAO], and are measured by surface pressure changes (Jones et al., 1997; Hurrell et al., 2001).

The NAO is a meridional oscillation in the atmosphere that is characterised by low pressure anomalies over Iceland, and the AMO is an approximately 50-year signal associated with north Atlantic sea surface temperature (SST). The index of the Atlantic Multidecadal Oscillation, also referred to as the Atlantic Multidecadal Variability, is calculated using the difference between north Atlantic SSTs and global mean SSTs (Sutton et al., 2018). The NAO index is calculated by the sea level pressure gradient between Iceland and Portugal (Hurrell and Loon, 1997; Visbeck et al., 2001), and the AO index is calculated using the sea level pressure gradient between the polar regions and the mid-latitudes (Baez et al., 2013).

The negative phase of the AMO is characterised by enhanced oceanic heat loss over the Irminger sea and leads to a deepening of convection and cooler SSTs over the region (Sutton et al., 2018). This expansion of a cool subpolar gyre is conducive to the development of positive NAO conditions. A positive NAO has a deeper Iceland low with strong westerly winds dominating, and a strong stratospheric vortex during the winter (Visbeck et al., 2001; Beranova and Kysely, 2012). The positive phase of the AMO shows

a warming of regional SST and strengthening of the Atlantic Meridional Overturning Circulation, which results in an increased northward heat transport and can lead to the development of negative NAO conditions (Sutton et al., 2018). The greatest impact of the AMO on European air temperature appears to occur during summer (Gamiz-Fortis et al., 2011).

The positive phase of the NAO typically results in warm, wetter weather in Iceland and the U.K., especially to the north, with regional surface warming. Conversely, positive NAO phases show cold conditions with lower precipitation in Greenland (Trigo et al., 2002). The negative phase of the NAO is characterised by a weakening of the Icelandic low and subtropical high, with cold and dry conditions over Europe and Iceland, as well as higher rates of precipitation with warmer temperatures over Greenland (Trigo et al., 2002).

Winter NAO conditions have a direct influence on temperature, storm tracks and precipitation in Europe and Greenland (Ortega et al., 2015). Hurrell and Loon (1997) used 40 years of winter rainfall data to calculated correlation coefficients between the NAO and precipitation in Iceland and Lerwick for the December to March season, of 0.48 and 0.49, respectively. They also calculated a difference in precipitation rate between winters of positive and negative NAO phases, which were 0.9 and 0.8mm per day, respectively (at the 1% significance level). London showed no significant change in rainfall, and Ivigtut in south-western Greenland had a negative correlation coefficient of -0.31 with a change in rainfall of -0.9mm per day, to the 5% significance level (Hurrell and Loon, 1997).

Spring and summer can be also be prognosticated from the previous winter NAO index data (Hubálek, 2016). During the winter positive phase of the NAO the subpo-

lar jet stream of westerly winds is shifted north across the North Atlantic, with strong south-westerly winds bringing wet air masses toward the United Kingdom and Iceland (Woollings et al., 2010). However, during a negative NAO winter, these strong westerlies remain further to the south, moving across southern Europe, with precipitation also shifting toward the north of the Greenland ice sheet (Hanna et al., 2013).

Baez et al. (2013) showed that mean annual SSTs and winter SSTs in southern Europe were related to the mean autumn NAO of the previous year, and that the mean autumn AO was related to the mean summer SSTs the following year. This one-year delay in the NAO and AO relationship to SST is thought to be related to the amount of accumulated snow, which has an impact on salinity and upwelling in local oceanic waters, and subsequently can result in higher SST (Baez et al., 2013).

The El Niño phase of ENSO is thought to result in colder temperatures over north-eastern Europe, with a southward shift of the Atlantic depression. The La Niña phase shifts the Atlantic storm track north and brings warm, wet conditions to northern Europe, similar to the effects of a positive NAO phase (Gamiz-Fortis et al., 2011).

The teleconnections influencing the Atlantic Ocean are highly cyclic, with ENSO cycles in the Pacific Ocean and North Atlantic Oscillation cycles in the Atlantic at 3-5 and 6-10 year time scales (Hurrell and Loon, 1997; Tsonis et al., 2002); Pacific Decadal Oscillation periodicity from 20-30 years and 50-70 years (Mantua and Hare, 2002; McGowan et al., 2009); and Atlantic Multi-decadal Oscillation cycles from 50-90 years (Enfield and Cid-Serrano, 2010; Ólafsdóttir et al., 2013).

Impacts of climate drivers on oxygen isotopes

ENSO has been shown to impact the oxygen isotopes in precipitation and plant water, with El Niño years showing increased δ^{18}O values in regions where the amount of precipitation decreases (Welp et al., 2011).

Within the UK, the oxygen isotope ratios in tree ring cellulose increases during warm summers with low precipitation and humidity, as a result of higher precipitation δ^{18}O. Conversely, wet summers that are dominated by westerly air flow lower δ^{18}O (Young et al., 2015).

Field (2010) demonstrated that the NAO index shows a correlation with monthly precipitation δ^{18}O, particularly during winter. He also demonstrated that higher precipitation δ^{18}O values in Europe are related to the presence of a pressure dipole. This dipole of low pressure in the north and high pressure in the south results in enhanced south-westerly winds and is associated with a northward shift in the storm track (Field, 2010). Shifts in the storm track and westerly winds such as this are characteristics of a positive NAO phase. Baldini et al. (2008) also showed that positive NAO winters result in higher δ^{18}O over the European mid-latitudes, due to the increased westerly winds, carrying warmer ^{18}O enriched moisture from the North Atlantic Ocean.

Greenland

The midnight sun greatly reduces the latitudinal temperature change during the Northern Hemisphere summer, but due to the vast land mass and latitudinal span, the winter temperature and length varies significantly from north to south. Additionally, dry, warm winds referred to as Foehn winds are common for this region and can temporarily raise

winter temperatures up to 30 °C (DMI, 2016).

The southward flowing East Greenland Current transports cold Arctic water, and the now cold water originating from the North Atlantic Current, along the eastern coast of Greenland and into the Denmark Strait (Miettinen et al., 2015). Warm Atlantic water joins with the cold Arctic current along the south east coastline of Greenland, and this temperate water (sourced also from the Labrador Sea) is transported around the southern tip along the western edge of continental Greenland (Figure 3.7).

The Greenland Ice Sheet fluctuates through mass gain in snowfall and mass loss due to iceberg calving and melt (Chu, 2014). Figure 3.8 shows the major hydrological features of the Greenland Ice Sheet, demonstrating the increase of mass associated with precipitation and outward discharge of the melt water toward the ocean.

Figure 3.8: Diagram of major hydrological features of the Greenland Ice Sheet, including precipitation and snow accumulation, firn layer and ice layer, as well as a) supraglacial lakes, b) englacial channels, and c) subglacial cavities (Based on Chu, 2014).

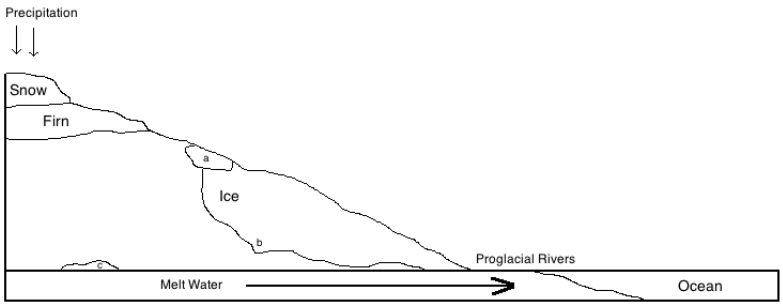

Due to the substantial mass of the Greenland Ice sheet, ice dynamics play a pivotal role in hydrological processes. Within the ablation zone, streams formed on the surface of the ice sheet feed into surface lakes, from which vertical conduits, known as moulins, can transport water to the bed of the glacier (Lindbäck, 2015). Water at the base of the ice sheet can increase movement, with lowered friction.

A hydrological study by Mernild et al. (2011) showed evidence that surface water runoff in Greenland fluctuated during climate periods such as the Medieval Climate Anomaly, the Little Ice Age, as well as the Roman Warm Period. Higher runoff was modelled during the Medieval Climate Anomaly, with lower runoff during the Little Ice Age, in comparison to present day Greenland runoff levels.

The Greenland Ice Sheet provides an excellent site for the study of historical climatological fluctuations, using cores. It was chosen for the depth of ice and flat topography of the base of the ice sheet, so as to ensure the deepest, least disturbed record as possible (NGRIP members, 2004).

Danmarkshavn, on the central eastern coastline, experiences temperatures ranging from an average daily mean of -24.3°C in February, to 3.7°C in July. Rainfall in Danmarkshavn is relatively consistent over the year, with the highest average monthly precipitation totals recorded in March, closely followed by July, August and December. On the southern tip of the Greenland coastline, around the western edge, the Qaqortoq meteorological station records much warmer temperatures, higher precipitation, and a larger range within the monthly average precipitation totals compared to its north-eastern counterpart. Qaqortoq has average daily mean temperatures that range from -5.5°C in January, to 7.2°C in July and August, with highest average monthly precipitation occurring from July to September, and a range of 46mm between the driest and wettest average monthly precipitation measurements.

Monthly precipitation and daily mean temperatures, with respect to the 1961-1990 climatology, are presented from two stations on the east [Danmarkshavn] and west [Qaqortoq] coasts of Greenland.

Table 3.3: Monthly climatology - Danmarkshavn, Greenland.

Month	Precipitation (millimetres)	Daily Mean Temperature (°C)
January	11	-23.1
February	12	-24.3
March	16	-23.4
April	9	-17.2
May	5	-6.5
June	6	0.8
July	15	3.7
August	15	2.3
September	11	-4.3
October	12	-13.7
November	12	-19.9
December	15	-21.9
Annual	141	-12.3

Table 3.4: Monthly climatology - Qaqortoq, Greenland.

Month	Precipitation (millimetres)	Daily Mean Temperature (°C)
January	57	-5.5
February	51	-5.0
March	57	-4.4
April	56	-0.6
May	56	3.3
June	75	5.2
July	97	7.2
August	93	7.2
September	92	5.0
October	72	1.2
November	78	-1.9
December	73	-4.4
Annual	858	0.6

Iceland

The western coast of Iceland, where Selfoss is located, experiences the warmer northward-bound Atlantic waters, compared with the cold northerly Arctic water of the East Icelandic Current. Temporal and spatial changes in the sea-ice extent and sea surface temperatures in surrounding waters are a strong influence on the climate of Iceland (Andrews, 2005). Additionally, the Icelandic shelf confluence of the warm saline waters brought by the Irminger Current, and the less saline, cool water from the East Icelandic Current is reflective of the broader intersection of North Atlantic currents (Figure 3.7).

The Icelandic hydrological cycle is complicated by glacial advance and retreat, with associated ice-front calving. These are indirectly linked to climate fluctuations, and influence surface water runoff and sea-leve rise (Larsen et al., 2015). A specific characteristic of the cryosphere particularly common in Iceland, is the jökulhlaup. Jökulhlaups are abrupt floods produced by the rapid draining of ice-dammed lakes, or large quantities of melted ice, beneath or within a glacier (Summerfield, 1991). Jökulhlaups can be produced when ice-dammed lakes reach their critical thresholds and the lake water begins to drain. The critical threshold is different for each lake and is dependant on the topography and ice conditions of the surrounding region (Herget, 2005). Common triggers for jökulhlaup occurrence include; subglacial volcanic activity, seismic activity, overspill, ice dam floatation, subglacial cavity formation, and subaerial dam breaches (Herget, 2005).

Table 3.9 details the results of an analysis of oxygen isotope data in a benthic core on the Icelandic shelf, from Axford et al. (2011). The data shows a peak in δ^{18}O values around 1650 A.D., with decreasing values to an available data trough at 350 A.D. Using

the generalised relationship between oxygen isotopes and temperature and rainfall, this indicates a possible warmer and/or wetter time period at 1650 A.D., with cooler and/or drier conditions up to 350 A.D.

Table 3.5: Normalized Icelandic δ^{18}O data from Axford et al. 2011.

Year	Icelandic Shelf benthic core δ^{18}O measurements
yrs A.D.	δ^{18}O benthic 328_ 1 (‰)
1850	0.64
1750	1.35
1650	1.76
1550	1.35
1450	1.23
1350	-0.19
1250	0.22
1150	-0.25
1050	-0.07
950	-0.78
850	-0.72
750	-0.07
650	-0.84
550	-1.19
450	-1.19
350	-1.25

The main weather systems that impact Iceland are the Icelandic Low and the Greenland High (Jónsson and Valdimarsson, 2005). Selfoss is warmer than the surrounding regions, with annual mean temperatures up to 14°C higher than the central highland areas (Notendur.hi.is, 2016). The meteorological stations used in this study in order to compare the δ^{18}O values in horse hair to local meteorological variables, are the Eyrarbakki and Reykjavík stations. The coldest temperatures in Eyrarbakki are recorded for January, with an average minimum of -3.61°C and an average maximum of only 2.07°C. October in Eyrarbakki is the wettest month, with an average of approximately 146 mil-

limetres of rainfall. There is an average annual range of around 61mm between the driest and wettest months.

Table 3.5 shows the average monthly maximum temperatures, minimum temperatures and rainfall climatology from 1957-2016 for Eyrarbakki, Iceland, near to the study site location, from data provided by the Icelandic Meteorological Office.

Table 3.6: Monthly climatology - Eyrarbakki, Iceland.

Month	Rainfall (millimetres)	Max. Temperature (°C)	Min. Temperature (°C)
January	133.56	2.07	-3.61
February	127.59	2.70	-2.85
March	126.90	3.67	-2.24
April	98.64	6.48	0.14
May	84.99	9.97	3.15
June	85.70	12.64	6.57
July	88.28	14.51	8.26
August	110.72	13.90	7.65
September	134.04	10.90	4.96
October	145.65	6.99	1.58
November	133.61	3.67	-1.71
December	139.78	2.26	-3.59
Annual	1409.45	7.51	1.55

Shetland Islands

South-east of Iceland, the Shetland Islands receive similar amounts of rainfall, with an average annual rainfall amount of approximately 1000-1500 millimetres per year, with respect to a 1981-2010 climatology (United Kingdom Meteorological Office, 2016a). At a lower latitude, the Shetland Islands receives warmer minimum temperatures, from the lowest minimum in February of 1.5°C to the highest minimum temperature in August of 10.2°C.

The average rainfall and temperature details for the meteorological station at Lerwick (United Kingdom Meteorological Office, 2016a) from 1981 to 2010, used for comparison to the δ^{18}O values in horse hair from the nearby Thordale Stud, are as follows:

Table 3.7: Monthly climatology - Lerwick.

Month	Rainfall (millimetres)	Max. Temperature (°C)	Min. Temperature (°C)
January	142.6	5.9	1.8
February	120.8	5.5	1.5
March	124.6	6.4	2.0
April	70.4	8.1	3.5
May	53.4	10.4	5.4
June	58.2	12.4	7.7
July	66.8	14.3	9.9
August	83.7	14.5	10.2
September	106.3	12.8	8.7
October	141.5	10.2	6.4
November	146.0	7.8	3.9
December	142.6	6.3	2.2
Annual	1256.8	9.6	5.3

Southern Britain

The climate of the United Kingdom is heavily influenced by westerly winds, driven by the North Atlantic Oscillation (Jenkins et al., 2008). Figures 3.9 and 3.10 are climatological charts from Jenkins et al. (2008), which show the average temperature and precipitation patterns over the United Kingdom. The majority of current sampling locations are in the central southern region of the United Kingdom. This area is one of the warmer regions, with spring and summer temperatures higher than 6°C, and autumn and winter temperatures in the range of 2°C to 12°C. United Kingdom rainfall predominately falls along the western coastline, with drier conditions in the central and eastern

midlands. The average total precipitation across the U.K. ranges from 100-900mm in Spring to 100-1400mm in Autumn (Jenkins et al., 2008).

Figure 3.9: United Kingdom daily mean temperature in °C by season, sourced from Jenkins et al. (2008).

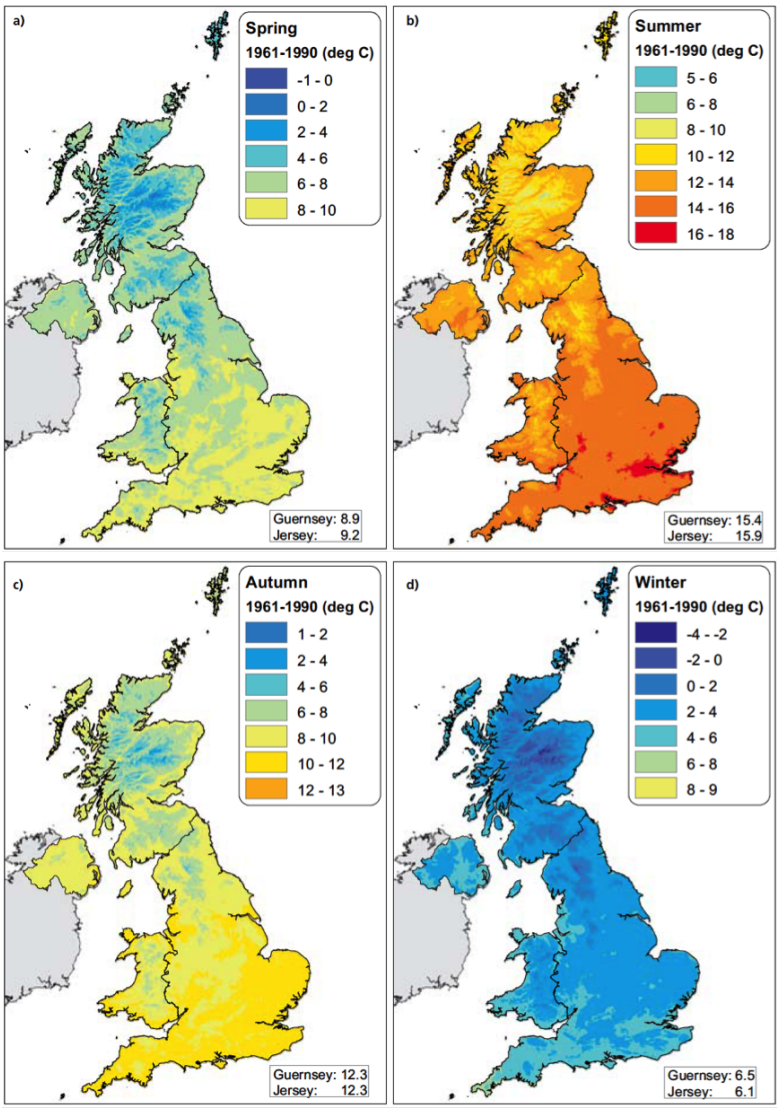

Figure 3.10: United Kingdom average total precipitation in millimetres by season, sourced from Jenkins et al. (2008).

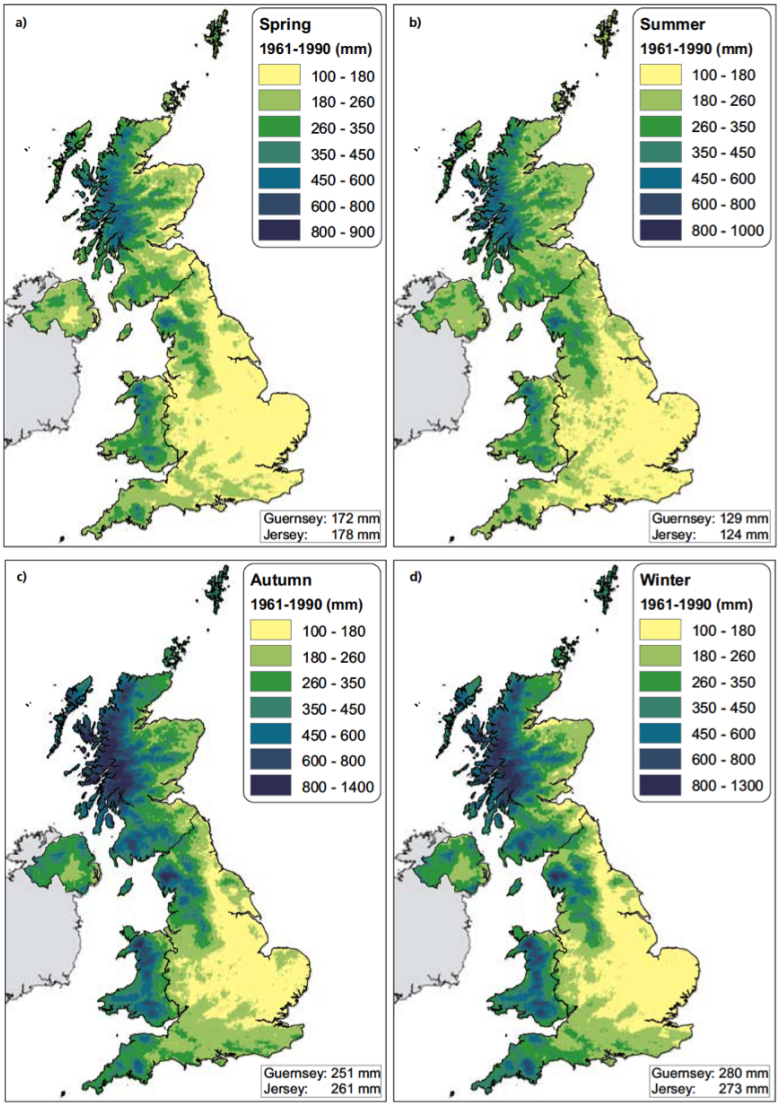

The Exmoor National Park, where the Exmoor Pony Centre (EPC) is located, is comparably wetter and colder than the surrounding region due to higher elevation. The EPC itself is approximately 308 metres above sea level, with the highest point in Exmoor reaching 521 metres. The United Kingdom Meteorological Office (2011) states that Exmoor receives up to double the rainfall of the surrounding region, with an annual average rainfall between 1381-2584 millimetres (mm), and between 161 and 198 annual average days of rain greater or equal to 1mm, with respect to 1971-2000 climatology. The average rainfall in the Exmoor region for winter is between 401-928mm, with autumn between 371-767mm, summer between 231-450mm, and spring rainfall at 241-489mm.

The temperatures in the Exmoor region range from minimum January temperatures between 0-1.8°C and minimum July temperatures of 9-11.8°C, to maximum temperatures in January between 4.7-6.9°C and between 16-20.5°C in July (UKMO, 2011).

The rainfall climatology (UKMO, 2016b) of Liscombe in the Exmoor National Park, near to the Exmoor Pony Centre, is as follows:

Table 3.8: Monthly climatology - Liscombe.

Month	Rainfall (millimetres)	Max. Temperature (°C)	Min. Temperature (°C)
January	159.2	6.1	1.5
February	112.5	6.2	1.1
March	117.6	8.5	2.5
April	88.2	10.9	3.7
May	85.4	14.1	6.4
June	79.0	16.9	9.2
July	94.4	18.6	11.2
August	103.9	18.6	11.4
September	113.1	16.4	9.4
October	161.7	12.6	7.1
November	159.0	9.1	4.1
December	171.2	6.6	1.9
Annual	1445.2	12.1	5.8

The meteorological station used in this study in order to compare the δ^{18}O values within the horse hair to local meteorological variables, is the Liscombe Station. Datasets from Liscombe, in Exmoor have been obtained from the UKMO. This includes daily rainfall, maximum temperature, minimum temperature, mean temperature and mean wind speed from the 1st January 2013 to the 31st March 2016. Hourly mean wind speed and direction has also been obtained from 1 November 2014 to 26 February 2015.

Table 3.9: Table describing the prevailing wind and wave conditions in relevant coastal regions of the United Kingdom (data sourced from Geos, 2001).

Region	Predominant Wind Directions	Predominant Wave Direction
Celtic Sea	South-West and West	West and North-West
English Channel	South-West and West	South-West and West
Irish Sea	South-West and West	South-West and West
Southern North Sea	South-West and West	North and South
West Shetland Shelf	South and South-West	South-West and West
Northern North Sea	South and South-West	North and South

3.2.2 1400 A.D. to 1850 A.D.

Although there is contention regarding exact time constraints in different areas, the period between 1400 A.D. and 1850 A.D. is characterised by large-scale hemispheric temperature declines known as the 'Little Ice Age' (Ogilvie and Jónsson, 2001). These temperature declines vary in strength, significance and temporal range at a regional scale. The cooling, most evident over Northern Hemisphere continental regions, is thought to be a result of teleconnections between the North Atlantic Oscillation and El Niño Southern Oscillation (Mann et al., 2009).

Conditions in Greenland during the Little Ice Age (LIA) were cooler than present, with lower mean tide level and relative sea level in southern Greenland during the early LIA period (Long et al., 2012). The latter part of the LIA showed decreased April sea ice concentration and increased August sea surface temperatures, with an approximate 50 year lag behind regional air temperatures (Miettinen et al., 2015). Marine cores indicate increased polar East Greenland Current water as a result of reduced impact on East Greenland from warm Atlantic water. Greenland is also thought to have contrarily experienced low sea ice cover despite below average air temperatures and surface water runoff in Greenland (Mernild et al., 2011).

Glacial fluctuations in Iceland during the LIA was due to proposed movement of the Polar Front, however there are no regionally synchronised Icelandic patterns of glacier response during this time (Chenet et al., 2010). For example, the glacial peak extent of Langjókull, Iceland, was found to have occurred between 1700 A.D. and 1930 A.D., late during the LIA (Larsen, Geirsdóttir and Miller, 2015).

Regional evidence for cool winters and dry summers in south-west Canada and south-

east Sweden from palaeoclimate reconstructions were also shown by Edwards et al. (2017). The Little Ice Age was also manifested in Britain through glacial development in the Cairngorm Mountains of Scotland (Harrison et al., 2014). Further afield, the latter part of the Little Ice Age is also thought to have influenced the thermal gradients in the Mediterranean region, causing an increase in intense storm activity (Dezileau et al., 2011).

Historical records and wind driven sand deposition in the Shetland Islands showed an increase in storminess during the Little Ice Age (Bampton et al., 2017). This was attributed to a negative phase of the NAO and increased Greenland summer ice.

Cooler conditions during the Little Ice Age, potentially due to changes in NAO or AMO phases, should show a decrease in δ^{18}O values in the ice core and tree ring records presented in this study, in the last section of the NGRIP2 and during the majority of the tree ring dataset.

3.2.3 950 A.D. to 1400 A.D.

Prior to the onset of cooler conditions during the Little Ice Age, several records exhibit an increase in temperatures known as the Medieval Climate Anomaly. During this time, it is believed that there was a northward shift in the inter-tropical convergence zone as well as an intensification of the Atlantic meridional overturning circulation. This intensification was likely to be a result of an extended positive phase of the North Atlantic Oscillation, which typical manifests as an intensification of the westerly winds (Trouet et al., 2009). These shifts in climate drivers are believe to have caused the warm and wet conditions over much of Europe. As discussed in Section 3.2.1, the positive phase

of the NAO is associated with higher δ^{18}O values over Europe, which should be seen in the latter section of the NGRIP2 and the early part of the tree ring record.

Figure 3.11: Diagram of the proxy inferred impact pattern of the Medieval Climate Anomaly on the North Atlantic Ocean, including Northern Africa, Europe, the United Kingdom, Iceland, Greenland, North America, South America, and the eastern Pacific Ocean (Sourced from Trouet et al., 2009, page 80).

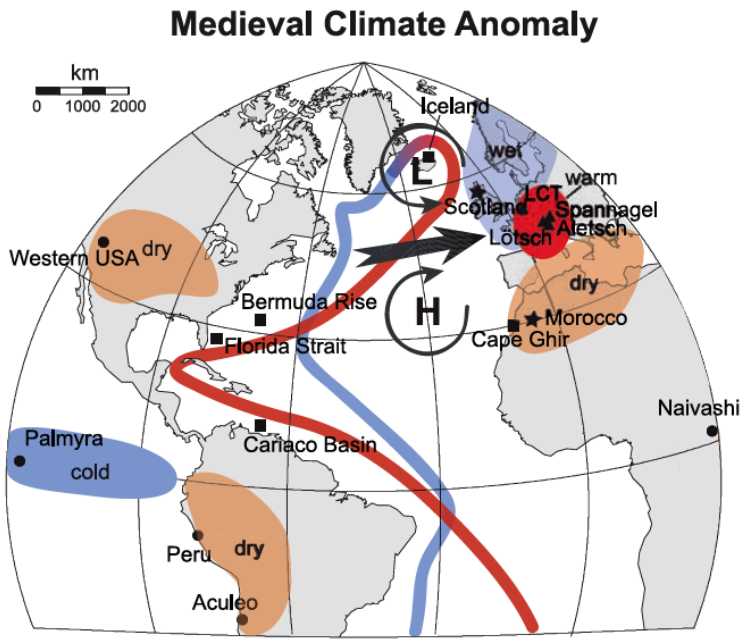

The Medieval Climate Anomaly was manifested in warm and wet conditions in Ontario, Canada, but with no discernible difference in the long term apparent carbon accumulation from present day levels (Holmquist et al., 2016). The warmest ocean surface temperatures on the south-east Greenland shelf were during the Medieval Climate Anomaly (Miettinen et al., 2015). However, just prior to and early within the Medieval Climate Anomaly, south-east Greenland had the coldest August sea surface temperatures on record, which rose to the 2900 year record warm period, by approximately 2.4°, between 1000-1050 A.D. Data from Vinter et al. (2010) indicates higher temperatures

for Greenland during the Medieval Warm Period. Reconstructions in other regions also show warm winters and wet summers in records from south-east Sweden and south-west Canada (Edwards et al., 2017).

3.2.4 1250 B.C. to 950 A.D.

Archaeological and palaeoclimatological records have suggested that the period from 750 B.C. to 550 A.D. was marked by warmer atmospheric conditions, known as the Roman Warm Period (RWP), followed by cooler conditions from 550-800 A.D., known as the Vandal Minimum (Esper et al., 2012; Wang, Surge and Walker, 2013). Similar to later periods of climate variability, the temporal constraints of the RWP are suggested to vary with geographical location. The North Sea is thought to have experienced increases in temperature from 450 B.C. to 350 A.D. (Hass, 1996), commencing later than the proposed 750 B.C. to 350 A.D. warming in the south-west of Greenland (Seidenkrantz, 2007). There is debate as to whether this RWP was geographically extensive (Esper et al., 2012). For example, north Iceland is suggested to have experienced lower temperatures as well as glacial development (Stötter et al., 1999; Jiang et al., 2002). However, areas in West Greenland, North America and Europe show relative warm sea surface and air temperatures (Lamb, 1995; Mudie et al., 2006).

3.3 Horse ecology

The Icelandic horses in Selfoss are fed with hay as well as some supplements of marine origin, and the water is sourced from the local water supply. Icelandic horses develop

thick coats over Autumn, in preparation for winter. Feed tends to consist primarily of grass during the warmer months, with hay being sufficient during winter (Míček and Schrenk, 1994).

The Thordale Stud location in the Shetland Islands is between 50-100m above sea level. The ponies at the Thordale Stud drink either from a local fresh water source or via piped water from the capital, Lerwick, further south. The feed is locally sourced south of Walls, or in the case of silage, baled from a hay field in Sandness, just four miles from the site.

The body hair or coat of the Shetland pony is shorter in summer, with a double coat consisting of rain shedding guard hairs during winter. However, the tail and mane of the Shetland pony remains long and thick regardless of season (Hodson, 1997).

The Pigeon House Equestrian centre is situated on a stream, utilising a combination of local water sources to satiate the domesticated horses. The horses eat a combination of local grasses and hay, as well as feed supplements (such as Alpha A with Oil Denge).

Exmoor pony short summer coats develop between spring and summer and the double layered winter coats develop from the end of summer into winter. Between winter and summer, guard hairs and then long winter coat hairs are shed (Baker et al., 2000). Mature male Exmoor ponies are ideally between 119.4 to 129.5 centimetres tall, with mature female ponies standing at between 116.8 to 127 centimetres tall. The wild roaming herds on Exmoor have access to a variety of food, including heather, rushes, bracken, whortleberry and grassland. More than 50% of the spring, summer and autumn free herd food consists of grasses, with approximately equal proportions of grass and gorse during winter (Baker et al., 2000). Due to high local precipitation, water supply for free

herds consists of rainfall, wet vegetation, rivers, streams, permanent bogs, or puddles. If the water has been frozen over during winter periods, the ponies have been shown to use hooves to break into the underlying water source (Baker et al., 2000).

The Exmoor Pony Centre in Exmoor National Park uses a combination of natural water sources —streams, rainwater in stone troughs, and an underground reservoir. The horses feed on a combination of local vegetation, haylage and hard feed. Pony centres keep excellent records of each individual pony's movements, which were used to confirm location and localised drinking water usage for each horse. For example:

> *Rama* was born in 2001 on Withypool Common in a wild herd. In the Autumn of 2001 he was taken to the EPC to be weaned, inspected and branded. After this, he spent time on various grazing sites in Northumberland before returning to the pony centre in autumn 2006. He spent the summer months on-site at the centre, and the winter months of 2013/14 and 2014/15 at a private home in Somerset. *Rama* retuned to the centre in February 2015 and remained there until after the sampling was conducted in March 2016.

4. Methodology

This chapter examines the methodology used for the identification and comparison of high resolution climate signals from environmental archives. This chapter will initially discuss the developement theory of this research, leading into the horse hair methodology in Section 4.1. The methodology for the ice core in Section 4.2 and dendroclimatology research is described in Section 4.3. Modern observational datasets are shown in 4.4 and the statistical methodology is explored in Section 4.5.

It is important that this study explores aspects of oxygen isotope ratio distribution and fractionation in different biological and geophysical data sources used for palaeoclimate reconstructions.

4.1 Horse hair

4.1.1 Samples

Initially, forty sets of tail hair samples were collected from the twenty-three available Exmoor ponies during two trips to the Exmoor Pony Centre, on the 29th September 2014 and the 24th September 2015. Of these samples; eight tail hairs [*Robbie*, *Periwinkle*, *Kate*, *Rama*, *Chaffinch*, *Roger* and *Percy*] were analysed for oxygen isotope data and five tail hairs [*Robbie*, *Fudge*, *Dylan*, *Walnut* and *Percy*] were analysed for carbon and nitrogen data.

Initial testing was conducted on these Exmoor pony hairs, in which correlations between meteorological variables and the oxygen isotopes were found. This initial study was conducted in order to show a proof of concept in the development of the thesis hypothesis. The following section describes the results of the preliminary work, comparing Exmoor pony hair to the temperature and rainfall observations from a local meteorological observation station.

The assumed average rate of horse hair growth for the preliminary test study is 0.72mm per day (West et al., 2004), which means that each 1cm segment of hair is indicative of just under two weeks worth of growth. Therefore approximately 2 year and 3 months worth of growth is represented in a hair that is approximately 60cm long. Initial sampling observations include variable thickness of the hair. For example: the hair sample from the horse *Fudge* gets thicker towards the middle, starting at the follicle end, reducing in thickness again right at the tail end of the hair; and *Percy* has an almost cyclic appearance of hair thickness. Figure 4.1 shows an example of a horse tail hair with a

change in thickness between two locations along the length of the hair.

Figure 4.1: Photograph of a horse tail hair, with red boxes indicating two areas of different thickness.



Visual comparison of meteorological data with the δ^{18}O values of *Percy*, *Rama*, *Periwinkle* and *Chaffinch* showed a consistent trough approximately 15 to 20cm along the length of the hair, indicative of higher rainfall and cooler temperatures. Additionally, it is proposed that the shortened wave period of *Roger's* δ^{18}O curve is a result of age-induced slower hair growth. Therefore, the visual comparison of the preliminary oxygen isotope values with corresponding points of hair growth within the meteorological data provided clear preliminary evidence of a seasonal influence.

On completion of the proof of concept analysis, further sampling was then carried out at four sites within Iceland and the United Kingdom. This secondary sampling was conducted uniformly on 7th March 2016 within a twenty-four hour period. This was achieved with the help of the managers of the participating pony centres. Similar to the previous work undertaken at Exmoor, samples were pulled straight down with enough force to remove the hair with the follicle intact. Samples were then delivered to Oxford

to undergo the isotopic analysis. Approximately five to ten samples were obtained from four to five horses residing at each location.

Four pony centre sites (see Figure 4.2) were chosen for the final horse hair sampling in order to determine whether or not there is a distinct latitudinal gradient within δ^{18}O values. The first site was the Icelandic Food and Veterinary Authority (MAST), located in Selfoss, Iceland. The second was the Thordale Stud, in Walls, to the south of the West Mainland of the Shetland Islands. Third was the Exmoor Pony Centre (EPC), located in Dulverton, Somerset. The final site was Pigeon House Equestrian, in Church Hanborough, Oxfordshire. These sites were also chosen for the overlap of available pony breeds. Icelandic horses were sampled at both the Icelandic site and the Shetland Island site; and Exmoor ponies were sampled at sites in Exmoor and Oxfordshire. Analysis of weaning foals was avoided as the values reflect a more complicated signal, including oxygen isotope influences from the mother's milk.

Tables 4.1 and 4.2 list detailed descriptions of the horses and samples that have been obtained and analysed for this research during the last 3 years.

Figure 4.2: Horse Hair sampling locations from north to south: (a) Icelandic Food and Verterinary Authority, Iceland; (b) Thordale Stud, Shetland; (c) Pigeon House Equestrian, Oxfordshire; and (d) Exmoor Pony Centre, Exmoor. [Map image is the intellectual property of Esri and is used herein under license. Copyright ©2017 Esri and its licensors. All rights reserved].



Table 4.1: This table details the individual horse information from the March 7th 2016 sampling population. It describes the location, name of the horse, age as of 07.03.2016, breed of horse, and the approximate size of the horse in hands. Measurements marked by $*$ denote where exact horse height measurements for the Exmoor ponies and Iceland horses were not available and an average of the breed height was used for comparison (& Árnason and Bjarnason, 1994; Baker et al., 2000).

Location	Horse Name	Age (years)	Breed	Size
Exmoor	*Robbie*	14	Exmoor pony	119.9cm (11.8hh) $*$
Exmoor	*Rama*	16	Exmoor pony	119.9cm (11.8hh) $*$
Exmoor	*Fudge*	18	Exmoor pony	119.9cm (11.8hh) $*$
Oxfordshire	*Nutmeg*	19	Exmoor pony	125cm (12.3hh)
Oxfordshire	*Tonto*	16	Unknown	113.8cm (11.2hh)
Oxfordshire	*Gem*	21	Welsh Mountain pony	113.8cm (11.2hh)
Oxfordshire	*Dessi*	24	Welsh Mountain pony	101.6cm (10hh)
Shetland	*Storm*	3	Shetland pony	80.3cm (7.9hh)
Shetland	*Silver*	3	Shetland pony	87.4cm (8.6hh)
Shetland	*Taktur*	6	Icelandic horse	133.1cm (13.1hh)
Iceland	*Granis*	5	Icelandic horse	133.1cm (13.1hh) $*$
Iceland	*Jódís*	7	Icelandic horse	133.1cm (13.1hh) $*$
Iceland	*Kæti*	8	Icelandic horse	133.1cm (13.1hh) $*$

Table 4.2: This table details the analysis information from the March 7th 2016 horse sampling exercise. It describes the location, name of the horse, the number of hairs analysed for that horse, the number of individual samples sequentially taken along the length of the hair, the number of usable samples that were analysed for that hair, and the length of hair sampled in whole centimetres. Several anomalous values were discounted due to machine or sampling errors.

Location	Name	No. Hairs	Hair Length (cm)	Samples per Hair	Viable Samples
Exmoor	*Robbie*	2	65, 53	52, 45	45, 44
Exmoor	*Rama*	1	75	49	48
Exmoor	*Fudge*	2	66, 53	65, 29	57, 20
Oxfordshire	*Nutmeg*	1	40	37	34
Oxfordshire	*Tonto*	1	42	29	29
Oxfordshire	*Gem*	3	44, 10, 61	21, 6, 41	19, 5, 39
Oxfordshire	*Dessi*	1	35	22	17
Shetland	*Storm*	1	36	18	17
Shetland	*Silver*	2	37, 28	15, 11	15, 11
Shetland	*Taktur*	2	14, 13	6, 4	6, 3
Iceland	*Granis*	1	37	22	22
Iceland	*Jódís*	2	46, 37	31, 23	30, 19
Iceland	*Kæti*	1	31	14	12

Additionally, samples from a second hair from the horse *Rama* were homogenised and analysed in two batches, in order to determine the sample precision and therefore accuracy as a representation of the true value of the isotopes during that time period. The first batch consisted of the first eight centimetres of the hair from *Rama*, which was ground up using mortar and pestle and separated into three silver capsules for analysis. The second batch was taken from the eighth to sixteenth centimetre position along the same hair as the first batch. This length of hair was cut into one millimetre pieces, which were shaken together to randomise and homogenise the eight centimetre section of hair. The mixed sampled was then separated into four silver capsules for the analysis. These samples were placed in various positions within the run order, in two different analysis runs, so as to also examine the machine accuracy for non-laboratory standard material

which should have minimal variation.

4.1.2 Analytical methods

Pretreatment of the horse hair for isotopic analysis included wiping each individual hair several times with methanol and allowing to oven dry overnight within an open plastic sealer bag (see Ayliffe et al., 2004; West et al., 2004; Bowen et al., 2009). It has been suggested by Bowen et al. (2005a) that it is more appropriate to vacuum-dry hair samples for six days prior to analysis, however it was thought that due to the minimal time between the post-oven sampling and machine analysis, that oven drying would be sufficient. This may have introduced small biases, but it would be a universal biases for all horse locations.

The clean hair was sequentially sampled (see Bowen et al., 2009) from the follicle end, which consists of the most recent growth. By starting the sampling process from the most recent growth, the sampling date can become a chronological marker, temporally fixing the sample information. The target sample sizes needed to be within a range of half to twice the size of the standard in order to prevent measurement drift. The target sample size for carbon and nitrogen analysis was between 0.75mg and 1.2mg. The oxygen analysis target sample size ranged between 0.50mg to 0.60mg. For the carbon and nitrogen sample weights, the target samples equated to approximately 1.5cm of the length of the full hair. The target sample weight for the oxygen analysis equated to approximately 0.8cm along the length of the hair. However, this corresponding length for each target sample weight was dependent on the thickness of the hair from each horse. The sample fragment lengths also increased during the sampling procedure for each individual, due to the hair becoming thinner towards the older keratin material at

the tip. After weighing, the carbon and nitrogen samples were cut up and placed into tin capsules, and the oxygen samples were placed into silver capsules (see Figure 4.2).

Figure 4.3: Visual example of hair sampling procedure including (a) clean hair for sampling, (b) 1mm hair segments that have been measured and weighed, and (c) the silver capsule within the metal disc capsule holder.

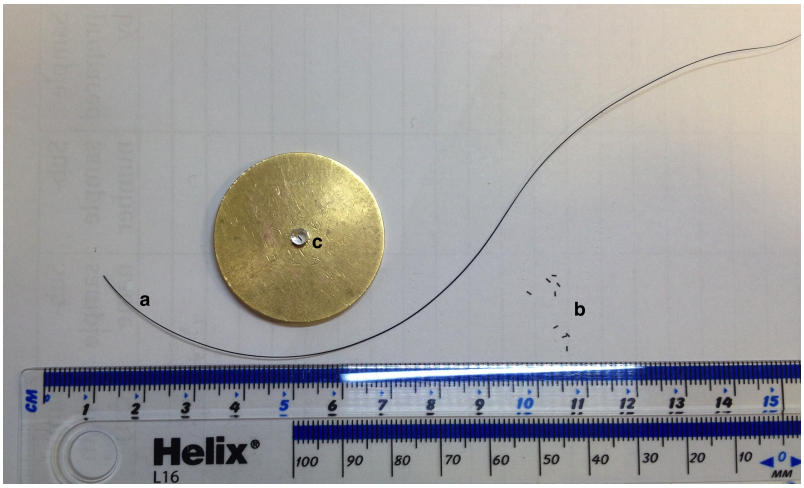

Reference material was sourced from the U.S. Geological Survey (USGS), the International Atomic Energy Agency (IAEA) and Elemental Microanalysis Ltd. (EMA). Reference standards USGS40, USGS41, alanine, seal and cow, were used for the calibration of the stable carbon and nitrogen data. These reference materials with known carbon and nitrogen values allow the user to quantify instrumental drift, as well as a correct for a number of other sampling errors including non-linearity and sample size dependency (see Coplen, 1988; Jardine and Cunjak, 2005). USGS40 and USGS41 are L-glutamic acid standards enriched in ^{13}C and ^{15}N, and the seal and cow powders were in-house bone collagen standards. stable carbon and nitrogen isotopic compositions of USGS40, USGS41, alanine, seal collagen, and modern cow bone collagen are shown in Tables 4.1 and 4.2:

Table 4.3: Carbon stable isotope reference standards, with respect to $\delta^{13}C_{\ VPDB}$ (Alanine, Seal and Cow) and $\delta^{13}C_{\ VPDB-LSVEC}$ (USGS40 and 41), USGS40 and 41 sourced from United States Geological Survey (2011a); United States Geological Survey (2011b).

Reference Material	Stable isotopic composition (‰)
USGS40	-26.39 $\pm$ 0.04
USGS41	+37.63 $\pm$ 0.05
Alanine	-26.9
Seal	-13.4
Cow	-24.28

Table 4.4: Nitrogen stable isotope reference standards, with respect to $\delta^{15}N_{\ AIR}$, USGS40 and 41 sourced from United States Geological Survey (2011a); United States Geological Survey (2011b).

Reference Material	Stable isotopic composition (‰)
USGS40	-4.52 $\pm$ 0.06
USGS41	+47.57 $\pm$ 0.11
Alanine	-1.63
Seal	+17.6
Cow	+7.76

The carbon and nitrogen samples within the tin capsules mentioned earlier were analysed using a Sercon Geo 2022 Isotope Ratio Mass Spectrometer (IRMS) coupled to Sercon Europa EA-GSL running with continuous flow mode with helium carrier gas 80 mL/min at the Research Laboratory for Archaeology and the History of Art at the University of Oxford. This machine had a precision of c. $\pm$ 0.1 ‰ for δ^{13}C and $\pm$0.3 ‰ for δ^{15} N (Jeffrey, 2016).

IAEA, USGS and EMA reference material, including USGS42, USGS43, EMA-P1, EMA-P2, IAEA-601 and IAEA-602 were used for the calibration of stable oxygen measurements within the horse hair. USGS42 consists of Tibetan human hair; USGS43 consists of Indian human hair; and EMA-P1 and EMA-P2 are finely ground stable polymers

(Elemental Microanalysis, 2010; United States Geological Survey, 2011c and 2011d). The international Benzoic acid standards IAEA-601 and IAEA-602 were also used for the correction of the horse hair samples from 7th March (Meier-Augenstein, 2009). Standards were chosen according to availability of materials and suitability for the range of expected data results.

Table 4.5: Oxygen stable isotope reference standards, with respect to δ^{18}O $_{VSMOW-SLAP}$ (USGS42 and 43) and δ^{18}O $_{VSMOW}$ (EMA-P1, EMA-P2, IAEA-601 and IAEA-602), sourced from Meier-Augenstein (2009); Elemental Microanalysis (2010); United States Geological Survey (2011c); United States Geological Survey (2011d).

Reference Material	Stable isotopic composition (‰)
USGS42	+8.56 $\pm$ 0.10
USGS43	+14.11 $\pm$ 0.10
EMA-P1	+21 $\pm$ 0.07
EMA-P2	+27 $\pm$ 1.9
IAEA-601	+23.3
IAEA-602	+71.4

The oxygen samples, within the silver capsules, were analysed using an IRMS coupled with a Sercon HTEA running at 1400 °C over glassy carbon at the Research Laboratory for Archaeology and the History of Art at the University of Oxford. This system had a precision of c. $\pm$0.2 ‰ for δ^{18}O.

4.1.3 Data calibration

The raw oxygen isotope results were drift-corrected, quality controlled and calibrated. The drift-correction was applied automatically with the Sercon Callisto system immediately after the sample analysis, reprocessing the datum to correct for any machine measurement drift during the analysis. This drift-correction is linearly applied between

reference standard pairs. The drift-corrected data were then quality controlled, removing any samples which had inappropriate values. These included values that indicated that the sample had not been fully contained within the capsule, and had subsequently recorded lower elemental composition values than appropriate to the sample weight.

Two methods of calibration were analysed within this study. The first technique will be referred to as the stretched-adjustment, and the second as the linear technique. Statistical analysis of the accuracy of each method was conducted using the full suite of standards included in each machine analysis of the samples. This analysis calibrated a random selection of datasets using both methods, with only the I601, I602 and P1 standards, and then the deviations of the measured USGS42 and USGS43 values from the certified values were compared between the two methods. As a result of this analysis, the second method, the linear technique, was chosen as the more accurate representation of the true values of the hair samples, with the assumption that as a hair standard, the USGS42 and 43 standards are a better indication of the sample value drift and measurement error. Full descriptions of both methods are as follows.

The stretched-adjustment firstly calculated the difference between the certified IAEA-601 and IAEA-602 values (+23.3 and +71.4 respectively) [referred to as the certified difference]. The difference between the results of the sampled IAEA-601 and IAEA-602 values was calculated (henceforth referred to as the measured difference). A 'stretch factor' was calculated by dividing the measured difference by the certified difference. All raw values were then multiplied by this stretch factor to calculate the stretched data. Stretched data was then adjusted by calculating the difference between the stretched mean of either the USGS42 or the EMA-P1 values, and the certified values for the USGS42 [EMA-P1] samples (referred to as the offset value). USGS42 [EMA-P1] was

chosen as the closest representative of the data values, and subsequently representative of the offset amount. This offset value was then subtracted from the stretched data to produce the calibrated values. This process was completed for all results so that deviations between certified standard values and the measured results were minimised.

Table 4.6: Calibration step 1.

Reference Material	Certified (‰)	Measured A (‰)	Measured B (‰)	Mean (‰)
IAEA-601	+23.3	+23.79	+ 24.43	+24.11
IAEA-602	+71.4	+74.87	+73.83	+74.35

Table 4.7: Calibration step 2 - stretch factor calculation.

Certified Difference (‰)	Mean Difference (‰)	Stretch factor(‰)
+48.1	+50.24	+1.04

Table 4.8: Calibration step 3 - Adjustment.

Certified Value (‰)	Stretched USGS42 Value (‰)	Adjustment factor (‰)
+8.56	+13.03	-4.47

The second method of calibration, shown in Figure 4.3, is also a two-point calibration (Coplen, 2011), utilising a linear regression technique described by Meier-Augenstein (2009), Jones et al. (2017) and Roberts et al. (2018). The measured δ^{18}O values of the reference material described in Table 4.5, specifically USGS42, IAEA-601 and IAEA-602, were plotted against the known values of these standards respectively. The plotted calibration slope and y-intercept were then used to correct the measured δ^{18}O hair sample values. For example:

Figure 4.4: Calibration procedure using the linear method, including raw values, measured versus certified plotted values, linear equation and final calibrated values.

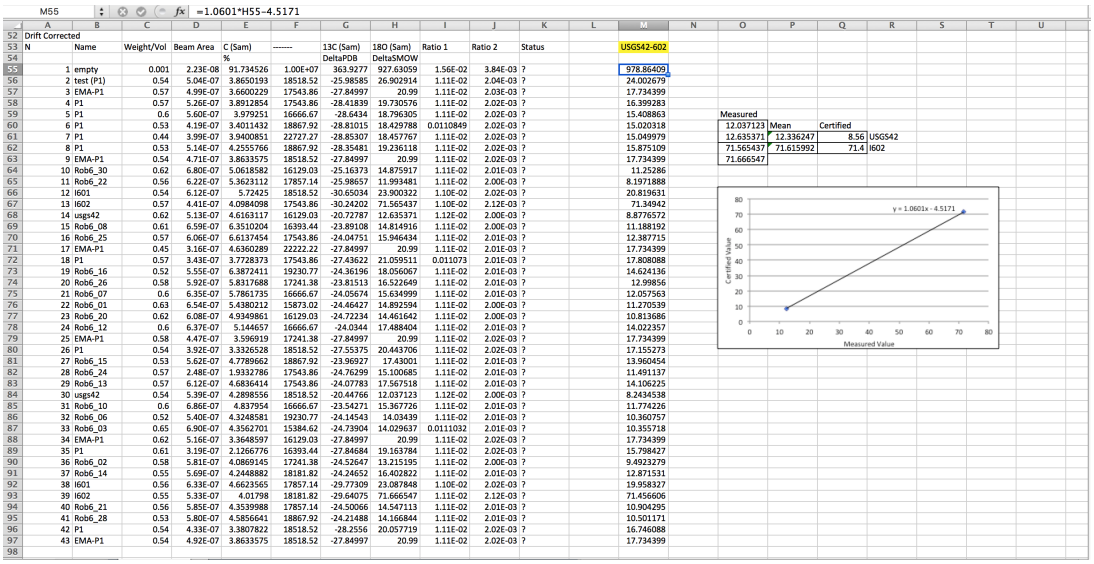

	A	B	C	D	E	F	G	H	I	J	K	L	M
52	Drift Corrected												
53	N	Name	Weight/Vol	Beam Area	C (Sam)	-------	13C (Sam)	18O (Sam)	Ratio 1	Ratio 2	Status		USGS42-602
54					%		DeltaPDB	DeltaSMOW					
55	1	empty	0.001	2.23E-08	91.734526	1.00E+07	363.9277	927.63059	1.56E-02	3.84E-03	?		978.86409
56	2	test (P1)	0.54	5.04E-07	3.8650193	18518.52	-25.98585	26.902914	1.11E-02	2.04E-03	?		24.002679
57	3	EMA-P1	0.57	4.99E-07	3.6600229	17543.86	-27.84997	20.99	1.11E-02	2.03E-03	?		17.734399
58	4	P1	0.57	5.26E-07	3.8912854	17543.86	-28.41839	19.730576	1.11E-02	2.02E-03	?		16.399283
59	5	P1	0.6	5.60E-07	3.979251	16666.67	-28.6434	18.796305	1.11E-02	2.02E-03	?		15.408863
60	6	P1	0.53	4.19E-07	3.4011432	18867.92	-28.81015	18.429788	0.0110849	2.02E-03	?		15.020318
61	7	P1	0.44	3.99E-07	3.9400851	22727.27	-28.85307	18.457767	1.11E-02	2.02E-03	?		15.049979
62	8	P1	0.53	5.14E-07	4.2555766	18867.92	-28.35481	19.236118	1.11E-02	2.02E-03	?		15.875109
63	9	EMA-P1	0.54	4.71E-07	3.8633575	18518.52	-27.84997	20.99	1.11E-02	2.02E-03	?		17.734399
64	10	Rob6_30	0.62	6.80E-07	5.0618582	16129.03	-25.16373	14.875917	1.11E-02	2.01E-03	?		11.25286
65	11	Rob6_22	0.56	6.22E-07	5.3623112	17857.14	-25.98657	11.993481	1.11E-02	2.00E-03	?		8.1971888
66	12	I601	0.54	6.12E-07	5.72425	18518.52	-30.65034	23.900322	1.10E-02	2.02E-03	?		20.819631
67	13	I602	0.57	4.41E-07	4.0984098	17543.86	-30.24202	71.565437	1.10E-02	2.12E-03	?		71.34942
68	14	usgs42	0.62	5.13E-07	4.6163117	16129.03	-20.72787	12.635371	1.12E-02	2.00E-03	?		8.8776572
69	15	Rob6_08	0.61	6.59E-07	6.3510204	16393.44	-23.89108	14.814916	1.11E-02	2.00E-03	?		11.188192
70	16	Rob6_25	0.57	6.06E-07	6.6137454	17543.86	-24.04751	15.946434	1.11E-02	2.01E-03	?		12.387715
71	17	EMA-P1	0.45	3.16E-07	4.6360289	22222.22	-27.84997	20.99	1.11E-02	2.01E-03	?		17.734399
72	18	P1	0.57	3.43E-07	3.7728373	17543.86	-27.43622	21.059511	0.011073	2.01E-03	?		17.808088
73	19	Rob6_16	0.52	5.55E-07	6.3872411	19230.77	-24.36196	18.056067	1.11E-02	2.01E-03	?		14.624136
74	20	Rob6_26	0.58	5.92E-07	5.8317688	17241.38	-23.81513	16.522649	1.11E-02	2.01E-03	?		12.99856
75	21	Rob6_07	0.6	6.35E-07	5.7861735	16666.67	-24.05674	15.634999	1.11E-02	2.01E-03	?		12.057563
76	22	Rob6_01	0.63	6.54E-07	5.4380212	15873.02	-24.46427	14.892594	1.11E-02	2.00E-03	?		11.270539
77	23	Rob6_20	0.62	6.08E-07	4.9349861	16129.03	-24.72234	14.461642	1.11E-02	2.00E-03	?		10.813686
78	24	Rob6_12	0.6	6.37E-07	5.144657	16666.67	-24.0344	17.488404	1.11E-02	2.01E-03	?		14.022357
79	25	EMA-P1	0.58	4.47E-07	3.596919	17241.38	-27.84997	20.99	1.11E-02	2.02E-03	?		17.734399
80	26	P1	0.54	3.92E-07	3.3326528	18518.52	-27.55375	20.443706	1.11E-02	2.02E-03	?		17.155273
81	27	Rob6_15	0.53	5.62E-07	4.7789662	18867.92	-23.96927	17.43001	1.11E-02	2.01E-03	?		13.960454
82	28	Rob6_24	0.57	2.48E-07	1.9332786	17543.86	-24.76299	15.100685	1.11E-02	2.01E-03	?		11.491137
83	29	Rob6_13	0.57	6.12E-07	4.6836414	17543.86	-24.07783	17.567518	1.11E-02	2.01E-03	?		14.106225
84	30	usgs42	0.54	5.39E-07	4.2898556	18518.52	-20.44766	12.037123	1.12E-02	2.00E-03	?		8.2434538
85	31	Rob6_10	0.6	6.86E-07	4.837954	16666.67	-23.54271	15.367726	1.11E-02	2.01E-03	?		11.774226
86	32	Rob6_06	0.52	5.40E-07	4.3248581	19230.77	-24.14543	14.03439	1.11E-02	2.01E-03	?		10.360757
87	33	Rob6_03	0.65	6.90E-07	4.3562701	15384.62	-24.73904	14.029637	0.011032	2.01E-03	?		10.355718
88	34	EMA-P1	0.62	5.16E-07	3.3648597	16129.03	-27.84997	20.99	1.11E-02	2.02E-03	?		17.734399
89	35	P1	0.61	3.19E-07	2.1266776	16393.44	-27.84684	19.163784	1.11E-02	2.02E-03	?		15.798427
90	36	Rob6_02	0.58	5.81E-07	4.0869145	17241.38	-24.52647	13.215195	1.11E-02	2.00E-03	?		9.4923279
91	37	Rob6_14	0.55	5.69E-07	4.2448882	18181.82	-24.24652	16.402822	1.11E-02	2.01E-03	?		12.871531
92	38	I601	0.56	6.33E-07	4.6623565	17857.14	-29.77309	23.087848	1.10E-02	2.02E-03	?		19.958327
93	39	I602	0.55	5.33E-07	4.01798	18181.82	-29.64075	71.666547	1.11E-02	2.12E-03	?		71.456606
94	40	Rob6_21	0.56	5.85E-07	4.3539988	17857.14	-24.50066	14.547113	1.11E-02	2.01E-03	?		10.904295
95	41	Rob6_28	0.53	5.80E-07	4.5856641	18867.92	-24.21488	14.166844	1.11E-02	2.01E-03	?		10.501171
96	42	P1	0.54	4.33E-07	3.3807822	18518.52	-28.2556	20.057719	1.11E-02	2.02E-03	?		16.746088
97	43	EMA-P1	0.54	4.92E-07	3.8633575	18518.52	-27.84997	20.99	1.11E-02	2.02E-03	?		17.734399
98													

Measured			
12.037123	Mean	Certified	
12.635371	12.336247	8.56	USGS42
71.565437	71.615992	71.4	I602
71.666547			

Table 4.9 specifies the standards measured and used within the calibration for each machine run.

Table 4.9: Data correction standards used.

Machine Run Number	Horses	Standards used for linear calibration
160505	*Silver 1* and *Taktur 1*	USGS42 and I602
160505A	*Storm 1* and *Taktur 2*	USGS42 and I602
160506	*Granis*	USGS42 and I602
160509	*Jódís 1*	USGS42 and I602
160510	*Kæti* and *Rama 1*	USGS42 and I602
160510A	*Rama 1*	USGS42 and I602
160511	*Jódís 1*	USGS42 and I602
160511A	*Rama 1*	USGS42 and I602
161208	*Tonto*	I601 and I602
161209	*Nutmeg*	I601 and I602
161212	*Tonto* and *Nutmeg*	I601 and I602
161212A	*Dessi*	I601 and I602
161213	*Robbie 1*	I601 and I602
161213A	*Gem 1*	I601 and I602
161214	*Robbie 1*	I601 and I602
161214A	*Robbie 1* and *Fudge 1*	I601 and I602
161215	*Fudge 1*	I601 and I602
170302	*Jódís 2*	I601 and I602
170303	*Jódís 2* and *Silver 2*	I601 and I602
170306	*Robbie 2*	USGS42 and I602
170307	*Robbie 2*	USGS42 and I602
170307A	*Fudge 1* and *Robbie 2*	USGS42 and I602
170308	*Fudge 1* and *Gem 2*	USGS42 and I602
170522	*Gem 3*	USGS42 and I602
170523A	*Gem 3* and *Rama 2*	USGS42 and I602
170523B	*Fudge 2* and *Rama 2*	USG42 and I602

4.1.4 Quality control

When examining the raw machine results, the SerCon Reprocessor software was used to check that the carbon monoxide mass peak fell within the integration windows. Figure 4.4 shows an example of the mass peak falling just outside of the ideal window, these peaks should begin to form within the integration window, to the right of the yellow bar. The data was then checked for abnormally high or low isotope values, and beam area

totals, as well as whether the values for the standards are close to expected. For example, the results from run number 170524A were discounted entirely due to a significant measurement failure, whereby there was a start failure and the samples did not drop corrected into the machine until approximately half way through the run. Figure 4.5 shows a machine run, 170524A, with the failed samples highlighted within the red box, which were subsequently removed from further analysis.

Figure 4.5: Image of the SerCon Reprocessor software, including the three carbon monoxide mass peaks and the yellow integration boundaries.

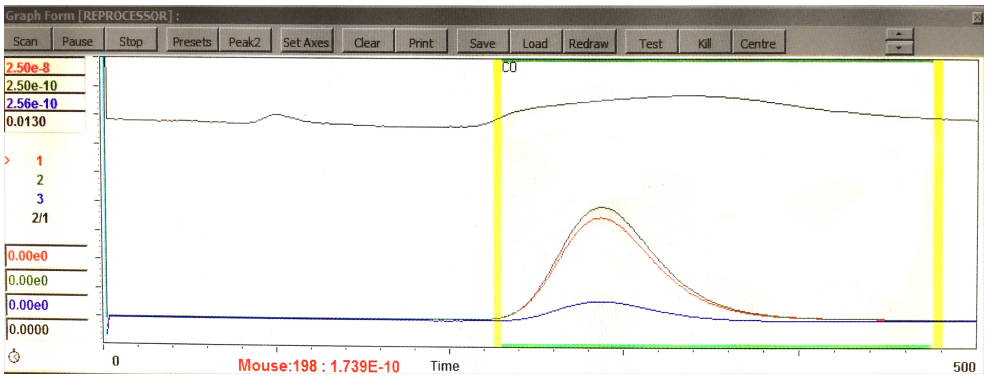

Figure 4.6: Example of a quality controlled machine run, with measurement errors highlighted within the red box.

Callisto CF-IRMS Stable Isotope Analysis System :

Project : SERCON_HT EA
Time : 08:13:36 - Date : 06-16-2017
Blank Correct : OFF
Read from : HT170524A.rec
Comment :

			<<<<<<<<<<<<CO (Sam)>>>>>>>>>>>>>>			
	Name	Weight	Total	Element	Isotope	
				C	13C	18O
		mg		%	DeltaPDB	DeltaSMOW
001	P1	0.54	4.438E-07	0.	0.00	0.00
002	P1	0.55	6.507E-07	0.	0.00	0.00
003	EMA-P1	0.51	5.196E-07	20.87	-27.85	20.99
004	USGS42	0.52	6.070E-07	4.686	-27.09	-0.22
005	F306	0.57	6.035E-07	4.251	-33.13	-4.86
006	F318	0.58	6.403E-07	4.432	-34.83	-6.26
007	I601	0.58	6.850E-07	4.742	-41.73	43.87
008	I602	0.64	6.109E-09	0.038	38.06	90.00
009	F328	0.58	6.351E-07	4.396	-36.11	-10.30
010	F304	0.55	5.736E-07	4.187	-35.76	-7.49
011	EMA-P1	0.53	6.635E-07	20.87	-27.85	20.99
012	P1	0.54	6.026E-07	3.509	-35.11	2.63
013	F303	0.56	6.453E-07	3.623	-39.12	-16.55
014	F315	0.53	6.036E-07	3.581	-40.88	-22.73
015	F307	0.55	6.005E-07	3.433	-42.96	-26.37
016	F308	0.52	5.859E-07	3.543	-43.84	-27.98
017	G311	0.75	8.248E-07	3.458	-44.49	-29.99
018	F321	0.52	5.462E-07	3.302	-45.47	-33.91
019	EMA-P1	0.57	5.187E-07	20.87	-27.85	20.99
020	P1	0.56	4.957E-07	3.56	-27.65	20.95
021	G315	0.53	5.777E-07	4.384	-23.71	13.47
022	138	0.52	5.530E-07	4.277	-22.74	11.30
023	110	0.55	5.830E-07	4.263	-22.49	10.50
024	I238	0.5	5.510E-07	4.432	-22.95	10.41
025	170	0.48	4.719E-07	3.954	-20.68	11.97
026	Z85	0.49	5.646E-07	4.634	-18.31	14.99
027	EMA-P1	0.52	4.571E-07	20.87	-27.85	20.99
028	P1	0.6	3.753E-07	2.855	-28.14	21.26
029	H258	0.5	5.061E-07	4.62	-20.84	19.80
030	Z89	0.44	4.187E-07	4.344	-21.33	17.61
031	USGS42	0.57	5.627E-07	4.506	-19.99	14.64
032	I601	0.51	5.458E-07	4.884	-29.53	25.85
033	I602	0.5	5.030E-07	4.592	-29.76	70.76
034	I45	0.48	4.865E-07	4.626	-21.23	15.23
035	171	0.5	5.054E-07	4.613	-24.18	14.67
036	P1	0.58	5.089E-07	4.005	-28.01	21.53
037	EMA-P1	0.58	4.340E-07	20.87	-27.85	20.99
038	empty	0.001	4.116E-10	1.978	-37.52	-119.45

4.1.5 Research methodology

Full associated information such as diet changes, activity and dimensions enable the modern horses to be used as a control group. By using detailed knowledge of the modern horse's activities as well as local observational climate data, physical contributions to fluctuations in oxygen isotope values can be assessed quantitatively. Darling (2004) states that the δ^{18}O values for the Exmoor region are approximately -5.5‰. These values will provide comparative information in the deconstruction of the ground water influence on the horse hair isotopic concentrations.

Subsequently, the statistical relationships between the isotopic concentrations of the horse hair and atmospheric fluctuations, compared against other environmental datasets, have the potential to improve accuracy in distinguishing seasonal climatological signals from other contributing factors within δ^{18}O measurements. It was anticipated that the δ^{18}O values of atmospheric and terrestrial palaeoenvironmental records, such as ice cores and tree rings, compared against contemporary meteorological and horse hair values, when controlling for known horse diet and activity changes, could provide a robust indicator of actual climatological fluctuations and further insight into seasonal climate information during the past.

Hair growth

Within the hair growth cycle, there are three known phases: the anagen (growth) phase; the catagen (inert) phase, and the telogen (resting) phase (Remien et al., 2014). Although there has been much discussion on the purpose and specific molecular activity of a hair follicle within the telogen phase (Geyfman et al., 2015), it is generally agreed

that the production of hair regeneration and production is inhibited during this period, prior to the shedding of the hair.

A study by Innerå et al. (2013) on equine Cushing's disease shows that there is significant variability in the percentage of hairs within the telogen versus anagen phases, with 18% of telogen rump hair follicles in spring and summer, and up to 75% of hair follicles in the telogen phase during autumn and winter. Kunz, Seifert and Tüeb (2009); LeBeau, Montgomery and Brewer (2011) state that for an adult human scalp, the normal telogen rate is between 4-24%, with July and April showing peak proportions of telogen hairs. The length of the telogen phase lasts between approximately two to four months (Krause and Foitzik, 2006; Kunz, Seifert and Tüeb, 2009; LeBeau, Montgomery and Brewer, 2011). As such, the presence of a telogen, or inactive, phase has implications for the chronology of the hair samples used in this study. Although samples were obtained with a twenty-four hour period, in order to utilise the sampling date as a chronological marker, any hairs within a telogen phase would introduce an inter-hair lag within the data. Additionally, there is evidence that Shetland ponies and other domesticated horses can still seasonally regulate metabolism function, to manage seasonal environmental stress (Brinkmann, Gerken and Riek, 2011).

Past studies have assumed a near constant hair growth rate within and between individuals of the same species (Ayliffe et al., 2004). West, Ayliffe and Cerling (2004) show that the standard error difference in growth rate was 0.03mm per day, though this mean error includes an outlier value of 0.16mm per day. Dunnett (2001) shows that a study of twenty-nine horses of varying breeds demonstrated continual, linear hair growth rate over the length of one hair during a twelve month period. Other papers also operate on the assumption that growth rate is near constant (Ayliffe et al., 2004).

A more recent study has shown that the growth rate of hair can be variable due to physiological stresses, even within an individual, but has negligible effects within this form of sampling, which incorporates a sufficient length and period of hair to even out the variation (Burnik Šturm et al., 2015). However, in order to account for any chronological mismatch that may occur between individuals with different hair growth rates, the data underwent a peak-finding process, matching the seasonal peaks and troughs to fix the chronology at each site (Burnik Šturm et al., 2015).

4.2 Ice core

4.2.1 Samples

The NGRIP2 ice core record used in this study was from Greenland, in the central plain of ice sheet, north of the summit where the Greenland Ice Core Project (GRIP) was drilled. The drilling of this core commenced in 1996, but in 1997 the machinery became frozen in place 1371 metres from the surface and could not be recovered. Drilling recommenced in 1999 twenty metres from the original site and continued until bedrock was reached in July 2003, at 3084.99 metres depth (Gfy.ku.dk, 2016). This first core drilled in 1996 is referred to as the NGRIP1 core, and the second core that spans from surface to bedrock, twenty metres from the original, is referred to as the NGRIP2. The NGRIP1 core was combined with the lower section of NGRIP2, downward from 1346m, to create the NGRIP record (Hvidberg et al., 2002). This study analysed the previously untouched section of NGRIP2, from 159.55m to 582.43m depth, which had been stored in an archive freezer.

Oxygen isotope data from the North Greenland ice core (NGRIP2) was collected for the period 1250 B.C. to 1250 A.D. Ice core data collection was conducted at the Centre for Ice and Climate (CIC), at the University of Copenhagen. To do this, the NGRIP2 ice core was taken from archive boxes within a storage freezer, where it had been kept at a temperature lower than -30°Celsius, to a working freezer kept at approximately -15°Celsius. Using an electric bench saw, a 3.33cm by 3.3cm rectangular column was cut from each 55cm long cylinder core segment (Figure 4.6). Each of these 55cm lengths of ice represented a resolution of approximately 2-3 years of data (Hoffmann and Jouzel, 2001).

Figure 4.7: NGRIP2 core sampling plan, showing a representation of the 3.3cm columns that were removed for sampling from the larger ice core. Sections a, b and c were returned to the archive freezer for future anaylsis.

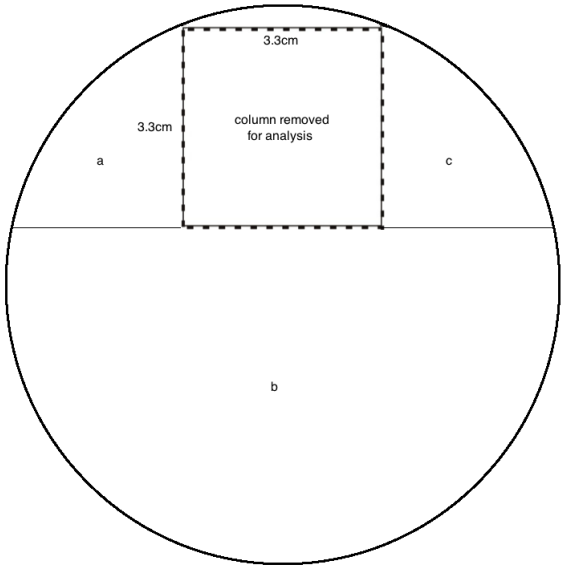

The remaining archive core pieces were re-bagged in accordance with the original archiving procedure, making sure that at no point was the core turned or flipped, as it was imperative that the sequential order of the core laminations were preserved. Dur-

ing cutting it was also important to ensure that the snow dust was continuously brushed from the ice columns, as this snow originates from different sections of the ice core and can thus contaminate the sequential ice data. This process was repeated for the thirty-six boxes, which each contained approximately 20 core segments from NGRIP2. This equated to eight hundred core segments, approximately four hundred meters of ice, and two thousand, five hundred years of data. The NGRIP2 sample segments were then shipped to the Desert Research Institute in Nevada, U.S.A., where the analysis took place. For shipping, each core segment was protected by separating layers of bubble wrap within a Styrofoam box, and kept frozen using ice packs and refrigerated shipping containers.

This study also uses existing data from the summit of the ice sheet in Central Greenland (GRIP). This 3029 metre core was drilled to the bedrock in 1992 (Iceandclimate.nbi.ku.dk, 2016). This data comprises of winter, summer and annual δ^{18}O values from 551 A.D.to 1979 A.D. (Vinther et al., 2010). Additionally, these datasets are compared with supplementary north Greenland ice cores: B16, B17, B18, B19, B20, B21, B22, B23, B26, B27, B28, B29 and B30, presented in Weißbach et al. (2016). Table 4.10 provides further details regarding the length, elevation and time period of each of these additional cores.

Table 4.10: This table details the core length, elevation (in metres above sea level) and time span for the supplementary cores from Weißbach et al. (2016).

Core	Length (metres)	Elevation (MASL)	Time period (A.D.)
B16	102.4	3040	1640-1993
B17	100.8	2820	1479-1993
B18	150.2	2508	934-1993
B19	150.4	2234	934-1993
B20	150.4	2147	1179-1994
B21	100.6	2185	1479-1994
B22	120.6	2242	1479-1994
B23	150.8	2543	1179-1994
B26	119.7	2598	1601-1995
B27	175.0	2733	1783-1995
B28	70.7	2733	1783-1995
B29	110.5	2874	1479-1995
B30	160.8	2947	1259-1995

Figure 4.7 shows the geographical position of the ice core samples relative to one another.

Figure 4.8: Topographic elevation map of the Greenland ice core locations including B16-23 and B26-30, NEEM, NGRIP, GRIP and Dye3, with respect to Danmarkshavn, Upernavik, Ilulissat, Tasiilaq, Nuuk, Narsarsuaq and Qaqortoq.

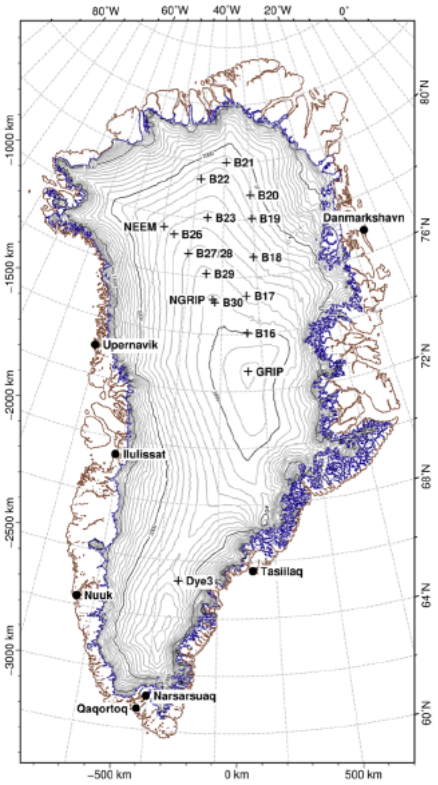

4.2.2 Analysis method

The analysis of the pre-cut core segments was conducted at the Desert Research Institute in Reno, Nevada, U.S.A (Figure 4.8). Eight-hundred core segments, making up four-hundred metres of ice, were prepared by cutting and shaving all edges to remove any possible contaminations to the outside of the ice. The cleaned ice was then loaded into an analytical ice core melt system feeding into an inductively coupled plasma mass spectrometer (ICP-MS) (see Figure 4.9, from McConnell et al., 2014).

The ICP-MS used a heated melter head to continuously melt the ice core loaded into the

Figure 4.9: Ice core melt analysis system, sourced from McConnell et al. (2014).

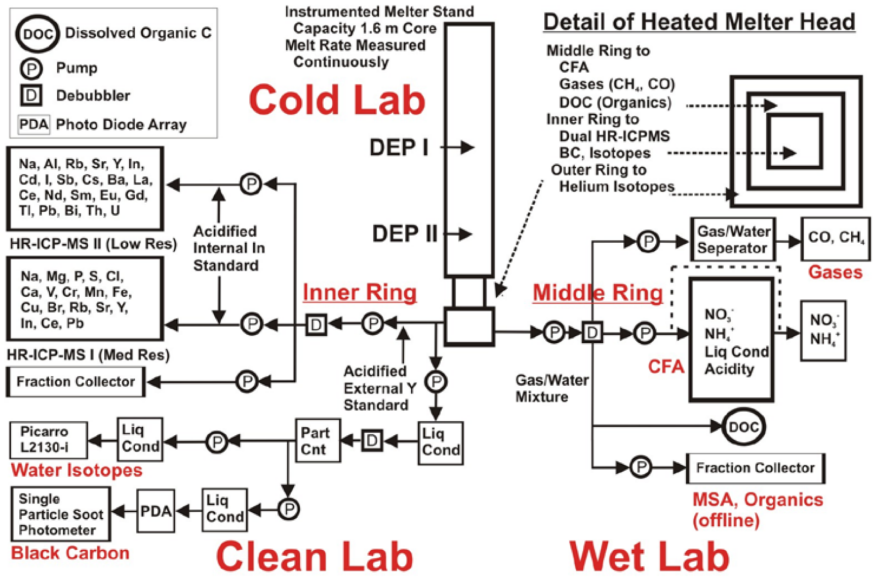

melter stand. The melter head separated the melt water into different channels, which went to different instruments through a series of peristaltic pumps and tubes in order to measure different trace elements. This system measured; oxygen and deuterium isotope ratios using a Picarro model L2130-i; as well as other trace elements that were not examined in this study, such as sodium, magnesium, sulphur, chlorine, calcium, vanadium, chromium, manganese, cobalt, copper, zinc, bromine, yttrium, indium, cerium, and lead; as well as total organic carbon, and black carbon (McConnell et al., 2002). The Picarro L2130-i Ultra High-Precision isotopic water analyzer has a typical precision of 0.011‰ and a typical maximum 24 hour drift of 0.082‰ (Picarro, 2012).

4.3 Tree rings

4.3.1 Samples

Tree ring data was provided by a Leverhulme-funded project collaboration between Swansea University and the University of Oxford, entitled 'New Tools for Science-based Archaeology: Isotope-supported Dendrochronology'. This study has developed a comprehensive dataset of δ^{18}O and δ^{13}C values from late-wood α-cellulose of oak tree samples from 1200 A.D. to 2012 A.D. The samples were obtained from a combination of building timber and living trees, evenly spread across central England. The building timbers were sub-sampled cores from the archive within the Oxford Dendrochronology Laboratory. This study will examine this master dataset of the compiled annual δ^{18}O values from the tree records sampled. The sampling locations used for the project are shown in Figures 4.10 and 4.11.

Figure 4.10: Leverhulme Project sampling locations within the United Kingdom, sourced from the UK Oak Project (2019).

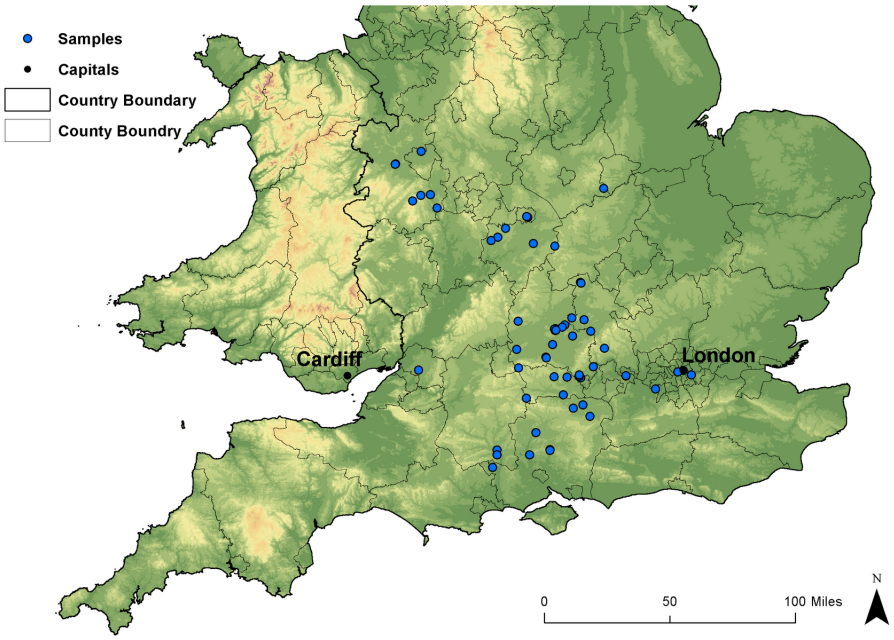

Table 4.11: Leverhulme Project sample dates and locations.

Sample	Date Range	Longitude	Latitude
WR13	1245-1200	-1.4407777	51.163311
WTB1B	1323 -1246	-2.5188583	51.524965
UC1	1367 -1324	-2.5084975	52.528376
CH11A	1469 - 1368	-2.748907	52.709595
GCT41	1512 - 1470	-1.008965	52.021849
CCPH10A	1599 - 1513	-1.248756	52.2358
BAD5B	1626 - 1600	-1.707849347	52.3412207
STW51	1690 - 1627	-1.014679992	52.02639421
MM33	1753 - 1691	-1.037905206	51.48530604
MDMH57	1800 - 1754	-1.036499	51.48439
GTH4	1288 1200	-1.0923468	51.71772
UFTN4	1372 1289	-1.4482772	52.253085
HSW4	1442 - 1373	-1.312103	51.06461
DPS61	1560 - 1443	-2.583252	52.49657
VYNE21	1620 - 1561	-1.093375647	51.30231369
NC56	1700 - 1621	-1.252414596	51.7539156

Sample	Date Range	Longitude	Latitude
SHL15	1740 - 1701	-1.183796966	51.38030917
BELL14	1800 - 1741	-2.354615535	52.45792097
SSJ1	1242 1200	-1.1650031	51.781198
LEM1b2	1342 1243	-1.1650031	51.781198
HCK1A	1399 1343	-1.3408953	51.596861
WS16	1519 - 1400	-0.1285749	51.4986
HCP67	1599 - 1520	-0.337519	51.403631
BPS39	1623 - 1600	-1.795869441	51.06376092
SCN64	1666 - 1624	-1.795869441	51.06376092
GCT72	1730 - 1667	-1.008950323	52.02185067
HN10A	1783 - 1767	-1.266890645	51.48377473
RCK5	1211 1200	-1.8376157	50.964009
WFS1	1277 1212	-1.5245268	51.363302
PEM6A	1366 1278	-1.0054757	51.321381
WCDC12	1459 - 1367	-0.607449	51.483996
WFR18	1528 - 1460	-1.501661	52.40436
RFW9	1590 - 1529		
CB011	1688 - 1591	-1.2534	51.7611
LP1A	1790 - 1689	-0.983133935	51.81033843
WTB5	1319 1200	-2.5188583	51.524965
PRC7	1399 1320	-1.5104406	52.407992
CH15	1471 - 1400	-2.748907	52.70959
BRST6	1580 - 1472	-1.096056	51.82205
BDM9	1646 - 1581	-0.782760093	52.56420801
BPS31	1710 - 1647	-1.795869441	51.06376092
NFH2	1755 - 1711	-1.023697697	51.47619685
HN15	1770 - 1756	-1.268351804	51.48427246
BAYH2	1800 - 1771	-1.189573	51.768389
MFM2	1259 -1200	-1.4979239	51.036781
WCC12	1309 -1260	-0.60734294	51.48368
AFC1	1368 -1310	-2.4156874	52.534133
MCO1	1402 -1369	-1.246665	51.75208
CCPL1	1504 -1403	-1.248756	52.2358
WAD7	1565 -1505	-1.253863	51.75482
SCN53	1649 -1566	-1.795987835	51.03678461
TWR12	1705 -1650	-0.925255413	51.74328731
DPS83	1733 -1706	-1.59479461	51.53710595
NSH21	1765 -1734	-1.846064526	52.27135771
MDMH56	1800 -1766	-1.0355	51.4848

Sample	Date Range	Longitude	Latitude
GTCX8	1265 -1200	-1.6126434	51.644161
WTB3B	1295 -1266	-2.5188583	51.524965
PEB4B	1336 -1296	-1.5967556	51.805948
OVO4	1379 -1337	-0.94246043	51.253388
TOLQ29	1507 -1380	-0.077401	51.507816
ME1	1599 -1508	-2.508494	52.78279
CCCC1	1676 -1600	-1.253922389	51.75032867
BSH10	1747 -1677	-0.905539466	51.53989475
HN14	1782 -1748	-1.268351804	51.48427246
WHM5	1269 -1200	-1.251025	51.751207
HHC4	1329 -1270	-1.7815052	52.290132
UC14	1387 -1330	-2.5084975	52.528376
WCP3	1488 -1388	-1.312861	51.060641
BOD71	1550 -1489	-1.255326	51.75393
WWB3	1578 -1551	-0.800397456	51.64496974
BAYH5	1640 -1579	-1.189573	51.768389
NC57	1670 -1641	-1.252414596	51.7539156
BOT11	1701 -1671	-1.03483554	51.49427258
SMV5	1757 -1702	-1.253877963	51.75302577
KF4	1780 -1758	-1.150307648	51.48167835
BAYH3	1800 -1781	-1.189573	51.768389
STG1S9	1234 -1200	-1.2610323	51.759363
BS16	1298 -1235	-2.7518362	52.707778
EHH23A	1352 -1299	-1.3373497	51.593478
BFDB22	1395 -1353		
ABA1	1415 -1396	-1.279846	51.66957
HCP160	1525 -1416	-0.337519	51.403631
HCP62	1599 -1526	-0.337519	51.403631
VYNE22	1651 -1600	-1.093375647	51.30231369
TWR14	1679 -1652	-0.925255413	51.74328731
BELL11	1750 -1680	-2.354615535	52.45792097
KF6	1790 -1751	-1.150307648	51.48167835
WHM8A	1280 -1200	-1.251025	51.751207
WA24A	1335-1281	-0.12853807	51.499498
WCDC2	1399 -1336	-0.607449	51.483996
CHW5	1518 -1400		
GQH14	1599 -1519	-0.003735	51.481091
WWB6	1632 -1600	-0.800397456	51.64496974
NSH31	1697 -1633	-1.846064526	52.27135771

Sample	Date Range	Longitude	Latitude
ASL1	1760 -1698	-1.59479461	51.53710595
MCO17	1800 -1761	-1.246650283	51.75208055

4.3.2 Analysis method

Oak tree rings can provide extended high resolution reconstructions of past climate when living samples are supplemented by sub-fossil and building timbers (Duffy et al., 2017). The UK Oak project conducted a thorough analysis of the isotopic ratios of latewood α cellulose within living trees and building timbers sourced from central England.

The master chronology of δ^{18}O values, used in this study, is based on measurements of homogenised latewood α cellulose of more than ten trees, which were pooled and processed prior to the cellulose isolation (Duffy et al., 2017). Latewood shavings were placed in borosilicate soxhlet extraction tubes with sodium chlorite and placed in an ultrasonic water bath at 80°C. The ultrasonic bath process was repeated, with vacuum filtration between each repetition, and followed by hot and cold washes with distilled water. After another vacuum filtration, carbohydrates were removed with sodium hydroxide baths. The first ultrasonic bath process was repeated, followed by deionised water washing, homogenisation and freeze drying of the extracted alpha cellulose (Loader et al., 1997). The cellulose samples were weighed into silver capsules for analysis in a Thermo Delta V isotope ratio mass spectrometer attached to a Flash HT elemental analyser and calibrated using in-house IAEA and SIGMA α cellulose standards. A major benefit of tree ring analysis is that confident ages can be obtained for the samples, through cross-dating of the samples, using well-established dendrochronological dating methods (Duffy et al., 2017).

4.4 Modern observational data

Meteorological data for the United Kingdom was obtained from the U.K. Meteorological Office. Liscombe is the closest meteorological station to Exmoor, less than 7 kilometres away at 51.09°N and 3.61°W, and at an altitude of 348 metres. This station provided daily data from 1st January 2013 to the 31st March 2016 hourly data was obtained, as well as hourly data from the 1st July 2014 to the 26th February 2015. The Lerwick meteorological station provided the nearest point of recorded observations for the Thordale Stud, approximately 29km away, at 60.15°N and 1.14°W at an altitude of 82 metres. The Lerwick observation data spans the period from 24th September 2015

to the 31st March 2016. The closest meteorological station to the Pigeon House Equestrian Centre in Oxfordshire, with an approximate distance of 13km is the Brize Norton station. This station is located at 51.76°N and 1.58°W, at an altitude of 62 metres, and provided observational data for the period of 1st October 2014 to 31st March 2016. Observational data from Eyrarbakki, Iceland was also obtained for the period of 1st January 2013 to the 15th September 2016, approximately 10km away from the Icelandic Food and Veterinary Authority.

Table 4.12: This table details the Meteorological variables provided by the UK Meteorological Office.

Variable	Specific measurement	Metric
Temperature	Maximum	°Celsius
	Minimum	°Celsius
	Mean	°Celsius
Humidity	hourly	%
Pressure	hourly	millibars
Precipitation	Rainfall days with >4.9	millimetres
	Rainfall days with >9.9	millimetres
	Snow fall	days
	Snow lying (0600-1800)	days
	Hail	days
Wind	Speed	knots
	Maximum gust speed	knots
	Gale	days
	Mean direction	°
Thunder	Thunder days	days
Radiation	Global total	KJ per m^2
Sunshine	Total	days

Rainfall oxygen isotope data from the International Atomic Energy Agency (IAEA) Global Network of Isotopes in Precipitation (GNIP), using the Water Isotope System for Data Analysis, Visualization, and Electronic Retrieval (WISER)), was obtained for comparison to the oxygen isotope values within the horse hair as well as the meteorological observations. The oxygen isotope data within precipitation was obtained from the locations described in Table 4.13.

Figure 4.11: GNIP UK sampling locations described in Table 4.13. [Map image is the intellectual property of Esri and is used herein under license. Copyright ©2017 Esri and its licensors. All rights reserved].

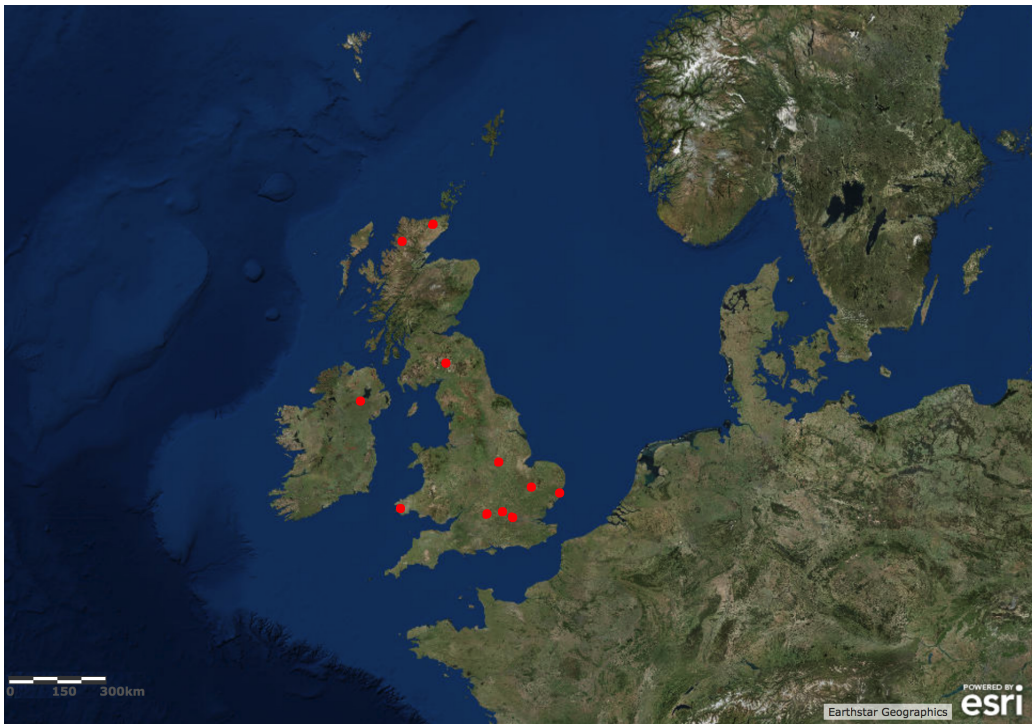

Table 4.13: This table details the oxygen isotope precipitation data from the International Atomic Energy Agency (2018).

Location Name	Country	Latitude	Longitude	Altitude (m)	Time period
Altnabreac	United Kingdom	58.38	-3.7	155	1981-1982
Armagh Observatory	United Kingdom	54.35	-6.65	64	2012-2014
Danmarkshavn	Greenland	76.77	-18.67	12	1991-2014
Fleam Dyke	United Kingdom	52.17	0.25	30	1980-1983
Godthab	Greenland	64.17	-51.75	48	1991
Groennedal	Greenland	61.22	-48.12	27	1961-1974
Inchnadamph	United Kingdom	58.15	-4.98	73	2003-2005
Keyworth	United Kingdom	52.88	-1.08	60	1985-1996
Nord	Greenland	81.60	-16.67	35	1961-1972
Prins Christians Sund	Greenland	60.03	-43.12	76	1976-1978
Reykjavík	Iceland	64.13	-21.93	14	1960-2014
Wallingford	United Kingdom	51.60	-1.1	48	1979-2011

4.5 Statistical methodology

Venegas (2001) describes a 'signal' as being a pattern in a dynamic system, of the researchers field of interest, within the dimensions of time and/or space. However, 'noise' is referred to as being all physical or instrumental factors irrelevant to the pattern of interest (Venegas, 2001). This study aims to separate the climate signals from the δ^{18}O, while removing all 'noise' associated with fractionation relating to other factors such as post-depositional processes. The data has been processed and statistically analysed using the MATLAB R2014a, R version 3.1.2, Microsoft Excel, and SPSS 22.0.0.0. software packages.

Two techniques commonly used for the analysis of climate signals are the Fourier transform (FT), shown in Figure 4.12; and the Wavelet transform (WT), shown in Figure 4.13. Raw signals are commonly representatives of amplitude and time domains, however the frequency component of a signal can also be examined using Fourier and Wavelet transforms. The frequency of a signal is the number of cycles per second, and is denoted by Hertz (Hz)(Polikar, 1996). A signal referred to as high frequency, shows rapid change, whereas a low frequency signal has a smoother/slower transition. A Fourier transform of a time domain signal uses sine and cosine base functions to convert raw signals to the frequency domain (Lau and Weng, 1995). This is shown by the representation of the Fourier pair in Figure 4.12, with the time, frequency and discrete Fourier transform operator represented by nT, $k\omega_0$ and $\mathscr{F}_d$, respectively (Kraniauskas, 1994).

$f[nT] \overset{\mathscr{F}_d}{\longleftrightarrow} F[k\omega_0]$

Figure 4.12: Visual representation of a Fourier transform, sourced from Fugal (2009).

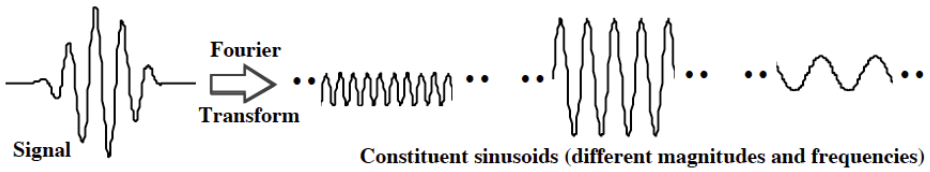

The algorithm used to compute a Fourier transform is known as a fast Fourier transform, or FFT (Cooley et al., 1969).

Further to the Fourier transform technique, a Wavelet transform produces a power spectrum; providing two-dimensional visualisation of how the amplitude of a signal evolves with time, over different frequencies (Venegas, 2001). The WT uses wavelets, or localised functions, as flexible windows through which to pass the signal between, starting with low and high pass filters (Polikar, 1996). It repeats this process, referred to as signal decomposition, progressively passing the signal through various stretched or shifted wavelet filters at different frequencies (Fugal, 2009). Each filtered signal represents the same raw signal, but within isolated frequency bands. By three-dimensionally plotting the result, the raw signal can be described by time, frequency and amplitude, and thereby shows which frequency is evident with what power at specific time intervals. Isolating the frequencies and power of the horse hair, tree ring and ice core signal in time, we can examine statistically significant common factors and determine correlations to seasonal or regional climate features.

Figure 4.13: Visual representation of a Wavelet transform, sourced from Fugal (2009).

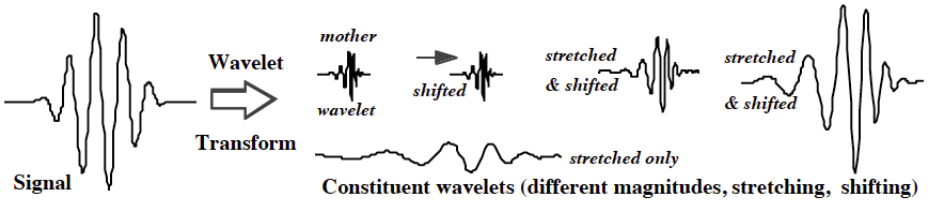

The wavelet transform enables the extraction of nonstationary signals in timeseries (Prokoph and El Bilali, 2008). Cross-wavelet analysis uses two continuous wavelet transforms (CWTs), identifying relationships and regions of common power between nonstationary signals found in the two time series (Grinsted et al., 2004; Maraun and Kurths, 2004). Cross-wavelet transforms enable the detection, extraction and reconstruction of phase shifted relationships in the time-frequency space, between signals that would otherwise appear uncorrelated during correlation or trend analysis (Prokoph and El Bilali, 2008). Furthermore, wavelet coherence shows where there is significant coherence between two time series when examining two CWTs, even if common power is low (Grinsted et al., 2004).

Cross-wavelet and wavelet coherence analysis is commonly used when examining climate teleconnections, such as the relationship between the North Atlantic Oscillation and regional air temperatures.

In addition to statistical techniques such as Fourier and wavelet transforms, several other factors need to be explored when analysing tree rings and ice core data. Changes in tree ring growth rate are a common problem when utilising tree ring chronologies (García-Suárez et al., 2009). To solve this issue, it important to standardise the data using a linear regression; filtering or smoothing; or de-trending with an age-dependant biological growth curve. Similarly, diffusion between the δ^{18}O of air and the top 60 metres of

a core, creates a smoothed ice core record (Johnsen et al., 2000). Fortunately, the effect of diffusion fractionation can be modelled and corrected using temperature and accumulation constraints (Johnson et al., 2000). To account for the changes in the isotopic signal caused by diffusion rate changes, Vinther (2006) applied two different methods of correction to the GRIP and NGRIP data, due to differences in the latitude, and subsequently summer melting differences. The traditional method of back-diffusion, or reversed diffusion, was applied to the GRIP data (Vinther et al., 2010) used within this study, re-establishing the annual oscillations using deconvolution filters (Johnsen, 1977). No correction is necessary for the NGRIP2 ice core data, as this is below 60 metres depth, where diffusion impacts are negligible.

5. Horse Hair Latitudinal Study

5.1 Results

5.1.1 Proof of concept

Five hairs from sampling undertaken during the planning stages of this study, in September of 2014 and 2015, were examined. The following section describes the results of the preliminary work, visually comparing Exmoor pony hair to the temperature and rainfall observations from a local meteorological observation station.

The assumed average rate of horse hair growth for these hairs is 0.72mm [0.072cm] per day (West et al., 2004), which means that each 1cm segment of hair is indicative of just under 14 [13.89] days worth of growth. Therefore approximately 833 days [or around 2 years and 3 months] of growth is represented in hair approximately 60cm

long. Near uniform growth of horse tail hair means that any temporal lag within the spatial comparison of the four isotopes on different sequentially sampled hairs from the same horse is thought to be negligible, and therefore an acceptable limitation (Dunnett, 2001). Sampling observations include variable thickness of the hair. For example: the hair sample from the horse *Fudge* gets thicker towards the middle, starting at the follicle end, reducing in thickness again right at the tail end of the hair; and *Percy* has an almost cyclic appearance of hair thickness.

Figure 5.1: Daily total rainfall measurements in millimeters, observed 9:00am to 9:00am from 02.01.2013 to 24.09.14, plotted with the approximate average rate of horse hair growth of West et al. (2004).

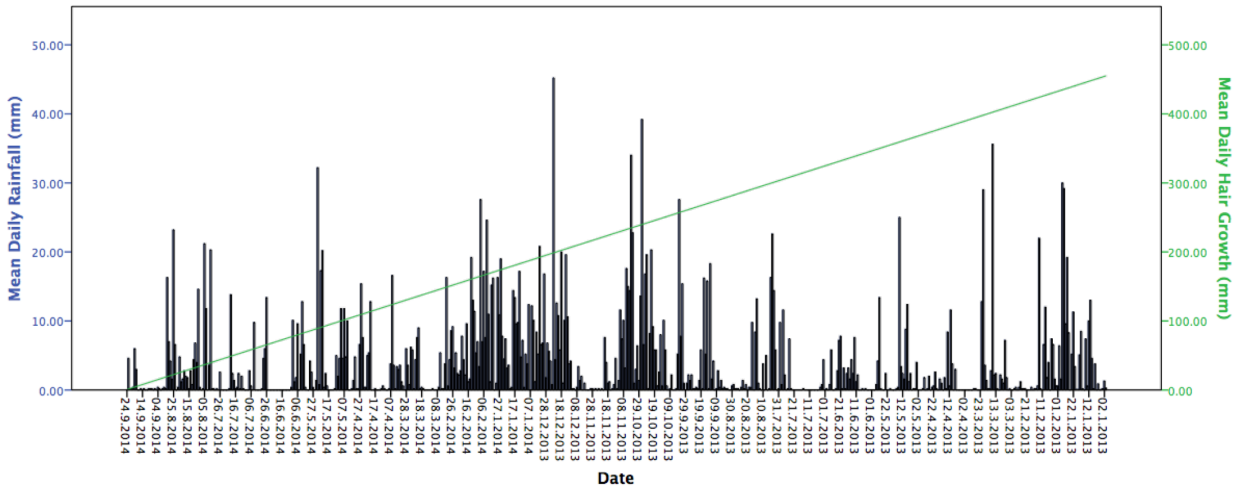

Figure 5.2: Daily mean Temperature in degrees Celsius, observed 9:00am to 9:00am from 02.01.2013 to 24.09.14, plotted with the approximate average rate of horse hair growth of West et al. (2004).

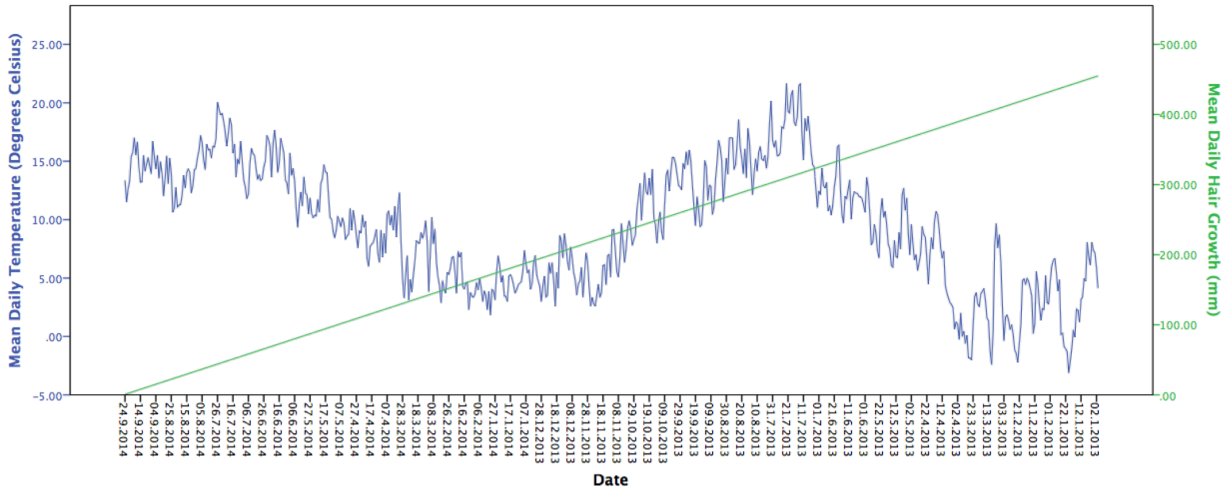

Figures 5.1 and 5.2 show a Northern Hemisphere winter period of higher rainfall and cooler average temperatures from November 2013 to March 2014 occurring approximately 15 to 20cm along the length of the hair, assuming an average horse hair growth rate of 0.72mm per day (West et al., 2004). Figure 5.3 shows the δ^{18}O values of *Percy* and *Rama* sampled sequentially along the length of one hair. However, Figure 5.4 shows lower resolution sequential oxygen sampling alternated with sample segments for carbon analysis, thereby containing less data points.

Figure 5.3: δ^{18}O values, expressed in ‰ with respect to V-SMOW, plotted against the sequentially sampled position along the length of the hair (in millimeters) for *Percy* and *Rama*.

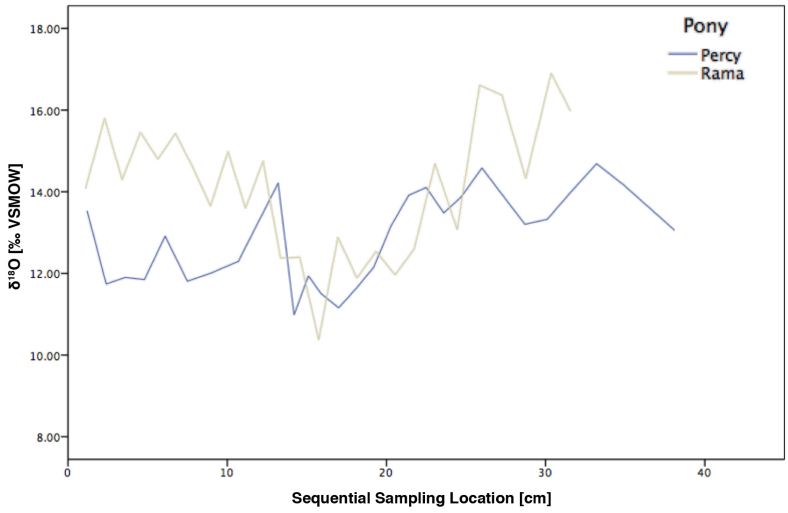

Figure 5.4: δ^{18}O values, expressed in ‰ with respect to V-SMOW, plotted against the sequentially sampled position, alternated with carbon sampling, along the length of the hair (in millimeters) for *Periwinkle*, *Roger* and *Chaffinch*.

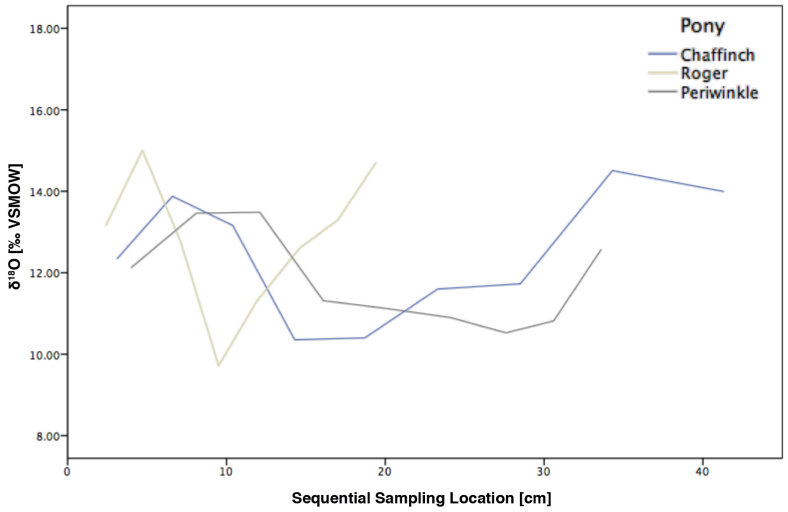

Visual comparison of the meteorological data within Figures 5.1 and 5.2 with the δ^{18}O values of *Percy*, *Rama*, *Periwinkle* and *Chaffinch* all show a trough in both curves approximately 15 to 20cm along the length of the hair, consistent with the higher rainfall and cooler temperatures. Additionally, it is proposed that the shortened wave period of *Roger's* δ^{18}O curve is a result of age-induced slower hair growth.

Visual comparison of the preliminary oxygen isotope values with corresponding points of hair growth within the meteorological data shows a seasonal influence. This evidence provided a useful starting point for the investigation.

5.1.2 Data preparation and precision

Previous sampling trips and analysis of Exmoor pony hair, prior to the setting of the sampling parameters for this study, provided a larger sample size and an excellent opportunity for uncertainty and error mapping. Figure 5.5 shows the data preparation procedure and structure of the datasets described and used for later analysis, from the samples obtained on 7th March 2016.

Figure 5.5: Analysis data results shown within the data preparation procedural process.

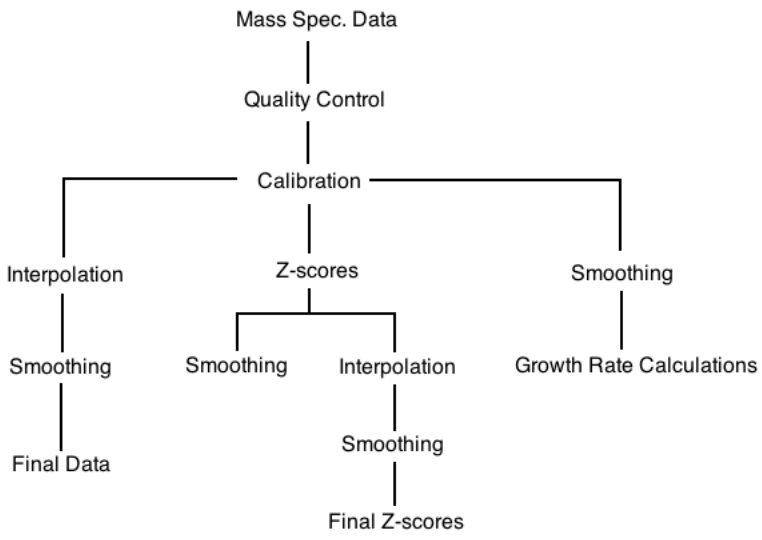

Following the quality control and calibration described in the methodology section, Z-scores were calculated by removing the average value for the hair from the sample value in question, and then dividing by the standard deviation of the hair values. For example the final calibrated value for *Gem 3* sample 3.03 was 12.90‰, the mean value for the *Gem 3* hair was 11.65‰ and the standard deviation was 1.56‰. The Z-score for *Gem3.03* was therefore: $(12.90 - 11.65)/1.56 = 0.80$. These Z-scores standardised all the horse hair values regardless of which standard was used for the analysis, and enabled cross-comparison across hairs that otherwise cannot be directly compared.

Hairs with a sufficient number of samples also had a 3-point or 5-point [for particularly long hairs] moving average applied to calibrated Z-scores and interpolated data in order to smooth noise from the curves. This also provided an alternative noise reduction technique to triplicate measurement, in order to alleviate time and machine availability pressures. Figures 5.6 and 5.7 show the smoothed data, using a 3-point moving average, split into data analysed with the USGS42 standard, and those analysed without. During

the course of this research, it was noted that a significant difference was evident for sample analyses conducted using the USGS42 standard compared to those which used I601 and I602 standards, creating a known weakness in the data. The normalisation and smoothing of the data has removed the potential error caused by the availability and use of these different standards.

Figure 5.6: Plot of the δ^{18}O values of all hairs without USGS42 included with a 3-point moving average smoothing, expressed in ‰ with respect to V-SMOW.

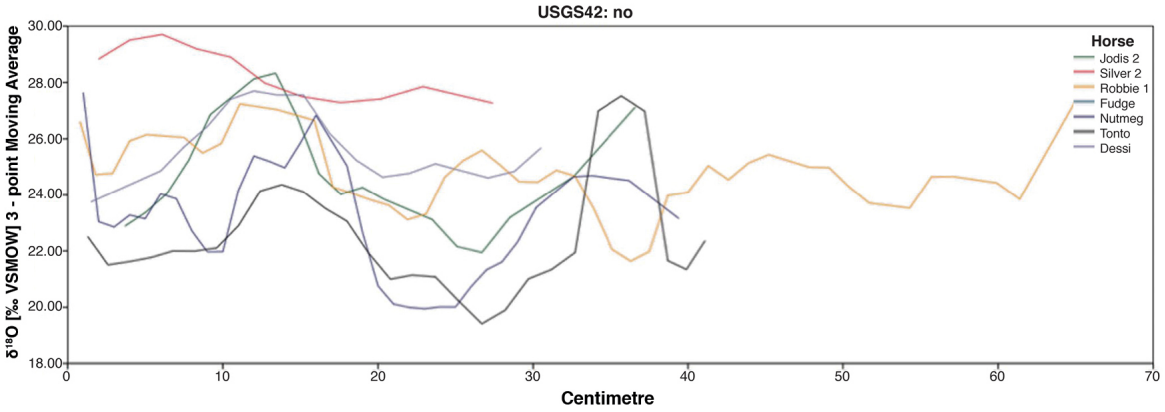

Figure 5.7: Plot of the δ^{18}O values of all hairs with USGS42 included with a 3-point moving average smoothing, expressed in ‰ with respect to V-SMOW.

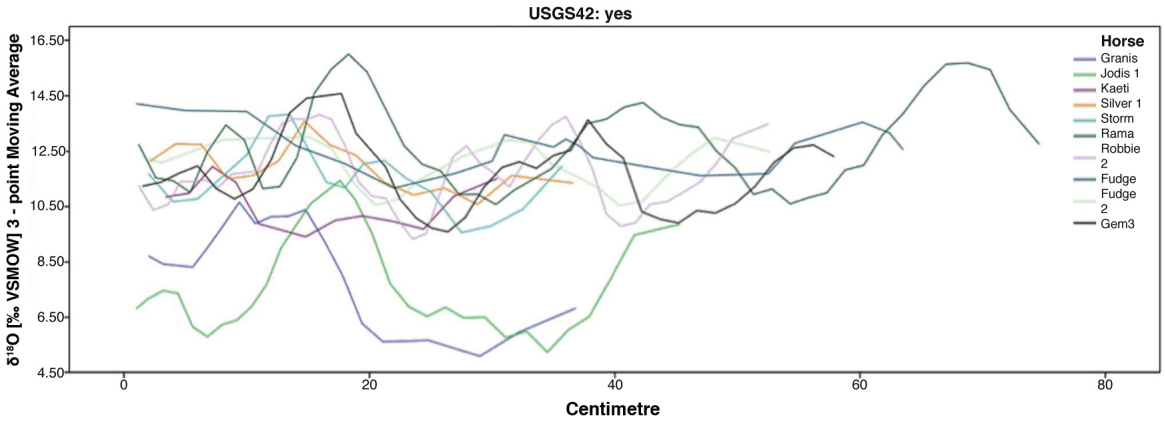

The smoothed calibrated data was used to determine the seasonal peak and trough timing and subsequently estimate the growth rate per hair, as described in detail in the following section. Due to the use of I601 and I602 standards as well as USGS42, the internal variation signal is more reliable than the absolute levels when conducting an examination of the full data record.

Using a Matlab, the horse hair data for each hair was interpolated to create a temporally regular timeseries. This was a linear interpolation, applied using the Matlab 1-Dimensional 'interp1' function, interpolating the isotopic data into increments of one centimetre (Table 5.1). Only minor differences between the peak structures of the final calibrated data and the linear interpolation of that data were evident.

Table 5.1: Sample of interpolated data, first 10 centimetres of the hair from 'Granis', Iceland, including the interpolated Z-scores (I.Z-score) and moving averages (M.A.).

Cm	Interpolated	M.A.	I.Z-score	M.A.	Days	End Date	Start Date	Middle Date
1	8.41	8.21	0.20	0.10	15.63	20/02/16	07/03/16	28/02/16
2	8.01	8.62	0.01	0.30	31.25	04/02/16	20/02/16	12/02/16
3	9.45	8.82	0.68	0.39	46.88	20/01/16	04/02/16	27/01/16
4	9.00	8.85	0.47	0.40	62.5	04/01/16	20/01/16	12/01/16
5	8.09	8.23	0.05	0.11	78.13	19/12/15	04/01/16	27/12/15
6	7.59	8.00	-0.19	0.00	93.75	04/12/15	1 9/12/15	12/12/15
7	8.31	9.13	0.15	0.53	109.38	18/11/15	04/12/15	26/11/15
8	11.50	10.12	1.63	0.99	125	03/11/15	18/11/15	10/11/15
9	10.54	10.70	1.18	1.26	140.63	18/10/15	03/11/15	26/10/15
10	10.07	10.21	0.97	1.03	156.25	02/10/15	18/10/15	10/10/15

The first hair from *Fudge* provides an example of the differences that the inclusion of USGS42 versus I601 and I602 only exhibited in the sequential results of a single hair. The *Fudge 1* hair was cleaned, prepared and weighed into silver capsules in December 2016. Two machine runs during December 2016 analysed approximately half these

samples [161214A and 161215] and the remaining samples were analysed in March 2017 [170307A and 170308]. The December 2016 analysis did not include the use of USGS42, as I601 and I602 were deemed sufficient at the time, however the March 2017 had USGS42 as an additional standard. This hair thus provides a useful comparison of the normalisation and interpolation techniques used for the development of the final dataset.

The Figure 5.8 shows the comparison between the normalised values from all the machine runs for the *Fudge* hair from 2016 and 2017, and the interpolated values, which used a linear interpolation of the 2017 to estimate the full record. The large variation between the values, from the different machine standard use, is clear within the non-interpolated data. The interpolated data appears to provide a reasonable representation of the *Fudge 1* signal, without the high variation caused by the use of different standards. Therefore the interpolated data is primarily used in the following comparisons between the individual hair records, unless it is stated otherwise.

Figure 5.8: Non-interpolated versus interpolated Z-score δ^{18}O data for *Fudge* hair 1, expressed in ‰ with respect to V-SMOW.

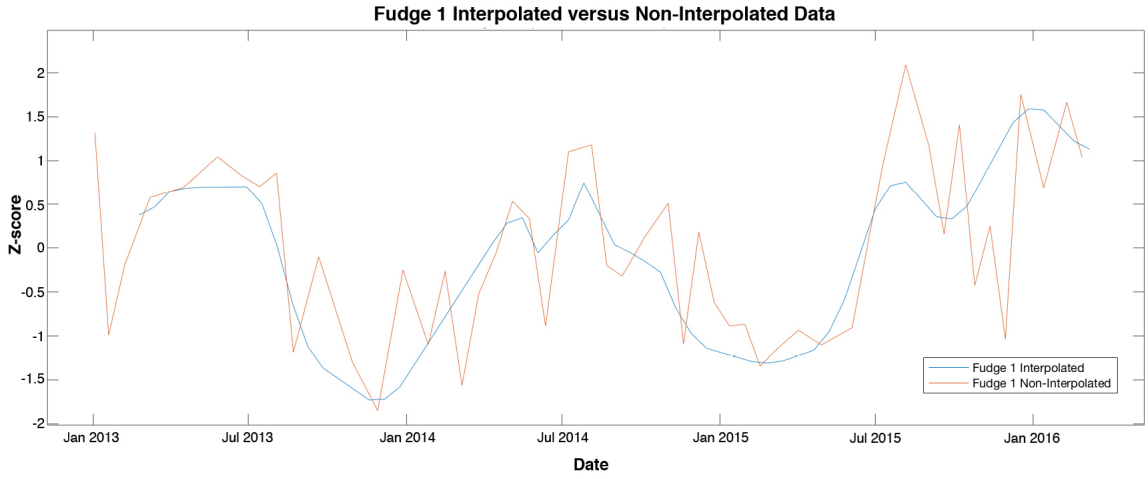

Growth Rates

In order to better compare the hairs within and between individuals of the same location, the growth rates of each hair were estimated (Table 5.3). The δ^{18}O values for each hair were plotted against the centimetre location of the associated samples. Using a combination of plotted raw calibrated values and smoothed z-score values, within Excel and Matlab, the peak and trough positions for each hair were identified, as shown in Figure 5.9 and Table 5.2.

Figure 5.9: Example of Matlab peak finding script result for Oxfordshire Pony *Gem 3*.

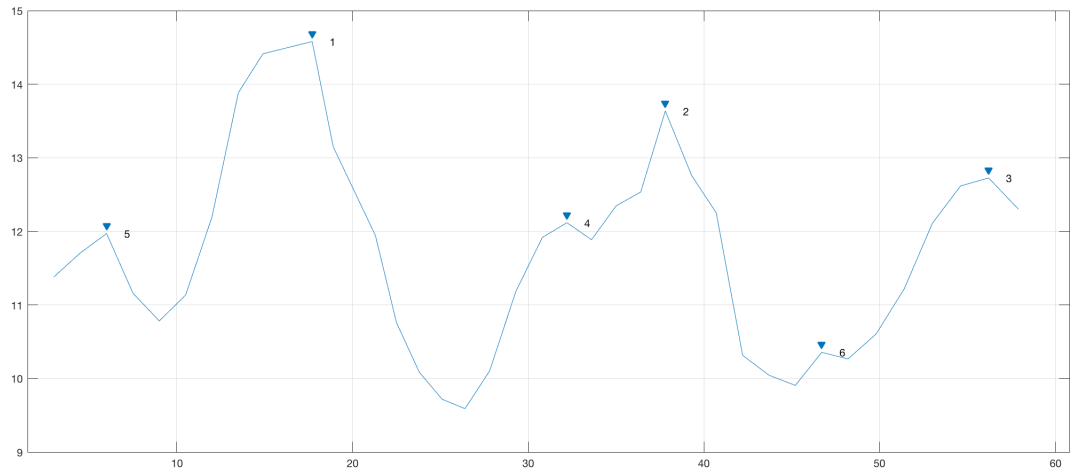

Table 5.2: Example of peak results, from *Gem 1* and *Gem 3*, found using the Matlab script, 'findpeaks(y,x)'. Data includes centimetre position of peak, δ^{18}O value at peak, centimetre distance between peaks, and growth rate calculate using the centimetre distance.

Hair	Centimetre	δ^{18}O value	Centimetre difference	Growth rate (cm/day)
Gem 1	18.5	41.48		
	37.8	42.22	19.3	0.0528
Gem 3	17.7	14.58		
	37.8	13.64	20.1	0.0550
	56.2	12.73	18.4	0.0504

The growth rate for the horse *Kæti* was calculated using the averaged growth rates from the other Icelandic ponies. Similarly, the growth rates for the two hairs from horse *Taktur* were calculated using an average of the other Shetland ponies. Although there were not enough clear peaks or trough to do an annual calculation of growth rate within the *Silver 2* and *Storm* hairs, a six month calculation was calculated by measuring the distance between the peak and the associated trough. The hair *Gem 2* growth rate was also calculated using the growth rates calculated for the other two hairs from the same pony *Gem 1* and *Gem 3*.

Table 5.3: Growth rates of individual horse hairs calculated using distances between annual peaks and troughs.

Hair	Growth rate (cm/day)
Granis	0.064
Jódís 1	0.076
Jódís 2	0.063
Kæti	0.068
Iceland Average	0.068
Standard Deviation	0.006
Silver 1	0.058
Silver 2	0.061
Storm	0.077
Taktur 1	0.066
Taktur 2	0.066
Shetland Average	0.066
Standard Deviation	0.007
Rama	0.066
Robbie 1	0.046
Robbie 2	0.051
Fudge 1	0.056
Fudge 2	0.049
Exmoor Average	0.054
Standard Deviation	0.008
Gem 1	0.053
Gem 2	0.053
Gem 3	0.053
Nutmeg	0.049
Tonto	0.06
Dessi	0.058
Oxford Average	0.054
Standard Deviation	0.004
Total Average	0.06
Total Standard Deviation	0.009

The southern horses, based at Exmoor and Oxfordshire have the same average hair growth rate at 0.054 centimetres per day. The northern horses, in Iceland and Shetland, also have similar, higher average hair growth rates at 0.068cm per day and 0.066cm

per day, respectively. These growth rates were tested for significance using the Matlab 'anova1' function and produced a non-significant p-value of 0.96.

Precision

In order to determine the homogeneity of the samples and analysis process, a hair from the Exmoor pony *Rama* was cleaned and dried using the same preparation process as the rest of the samples in this study. The first eight centimetres of this hair, from the follicle end, was homogenised by cutting and grinding within a cleaned mortar and pestle. Although this method proved ineffective in transforming the material into a powder, it did sufficiently mix the first eight centimetres of hair. This homogenised material was evenly distributed into samples labelled *Ram4.01*, *Ram4.02* and *Ram4.03*, and spread through two sets of analytical runs. Another eight centimetres (from 8-16cm along the length of the hair) was also sampled and homogenised. The second eight centimetres of hair was cut into millimetre sections, as per the sampling method of the other hairs used for this study. Instead of weighing the hair segment prior to cutting into millimetre sections for the silver capsule, these samples were cut all along the eight centimetre length first. These fragments were then shaken within a clean, sealed tube. Once mixed, the sample pieces were weighed and randomly distributed into four samples, *Ram4.04*, *Ram4.05*, *Ram4.06* and *Ram4.07*. These samples were also randomly spread through the same two sets of analysis runs as the first eight centimetres. This process was conducted in order to determine the variance and precision of the sampling procedure.

Using the growth rate of 0.066cm per day for *Rama*, calculated within the previous section, the first eight centimetres converts to a time period between the 6th November 2015

and the 7th March 2016. The second eight centimetres of samples are representative of the period between the 8th July 2015 and the 6th November 2015.

Table 5.4 shows the results of the two sets of homogenised samples, including the sample name, the δ^{18}O value, the machine analysis run name, and which segment of hair the sample originated from.

Table 5.4: *Rama* precision testing data with three samples from the first 8 centimetres and four samples from the second 8 centimetres of hair.

Sample	δ^{18}O values	Analysis Run	centimetres
Ram4.01	10.77	170523A	0-8
Ram4.02	10.30	170523A	0-8
Ram4.03	10.37	170523B	0-8
Mean	10.48		
Standard Deviation	0.254		
Ram4.04	13.96	170523B	8-16
Ram4.05	11.58	170523A	8-16
Ram4.06	12.81	170523A	8-16
Ram4.07	12.33	170523B	8-16
Mean	12.67		
Standard Deviation	0.998		

There was a greater range, 2.38‰, between the results of the second set of samples, from the 8-16 centimetre location of the hair. As there does not appear to be any association between high or low values and particular runs, the spread is not clearly a result of machine run error, though it could be a contributing factor. The 2.38‰ range is most likely to be a result of unequal mixing of fragments within the sample preparation. Although the sample pieces were randomised within the samples, it is hard to determine that the proportion of segments from locations along the eight centimetres in question were evenly distributed within the four samples analysed. This mixing of fragments by randomised mixing therefore appears to be inadequate in comparison to sample mixing

by grinding. However, these results are still useful for determining the minimum spread within homogenised samples over a period of approximately four months, during the transition of the Summer and Autumn months.

Within the ground samples, there was a range of 0.47‰. Although it is possible that the procedure of grinding was also insufficient for pure homogenisation of the sample, these results show that for the horse hair samples used within this study there should be a maximum sampling precision error of just under 0.5‰.

During previous sampling sessions, hair was extracted from several of the Exmoor ponies, later used for this study. These earlier hair samples were run in preliminary analysis prior to the sampling in March 2016. These samples were subsequently used to compare against later samples collected on the 7th March from the same horse. Four hairs from the horse *Robbie* were sampled and analysed during 2015 and 2016. The final calibrated, smoothed, and normalised data can be compared to examine the variance and precision of individual hair results.

Figure 5.10 shows all four of the calibrated and smoothed Exmoor *Robbie* hairs. These hairs include two separate lines for the same hair from 2015, 'a' and 'b', from 2015, which is shown split into the results which were analysed within runs using the USGS42 standard, and those without the USGS42 standard. Similarly, the second hair from 2016 was analysed without the USGS42 standard.

Figure 5.10: 3-point moving average of the final δ^{18}O values of all four hairs from the Exmoor pony *Robbie* sampled in 2015 and 2016, expressed in ‰ with respect to V-SMOW.

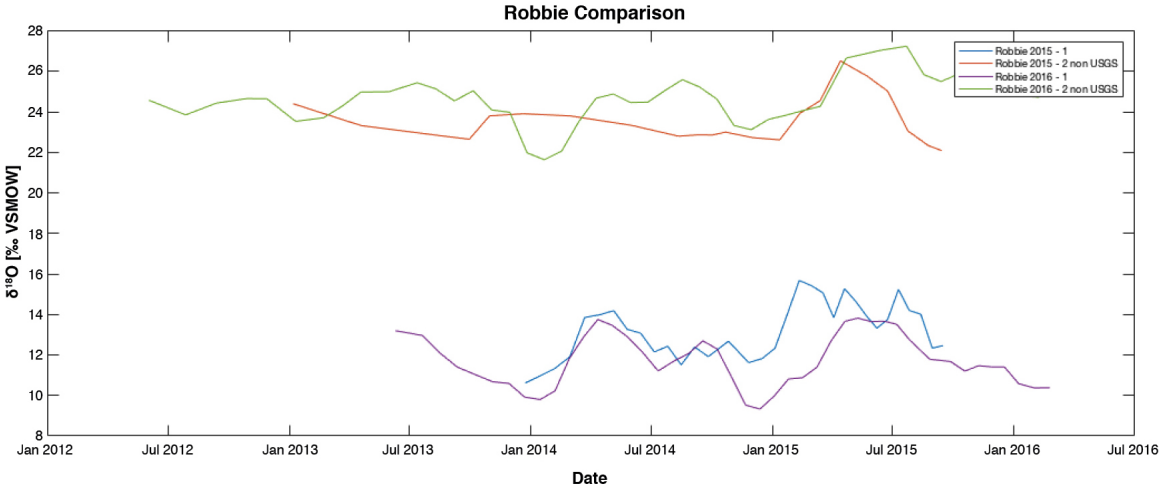

Figures 5.11 and 5.12 show the normalised values for the hairs from 2015 and 2016, respectively. Although there is clearly variability, due to inter-hair variability as well as machine and mathematical processing errors such as the use of the USGS42 standard and natural smoothing effects, there is clear alignment of all hairs across the two sampling years.

Figure 5.11: 3-point moving average of the final normalised δ^{18}O values of all for hairs from the Exmoor pony *Robbie* sampled in 2015 and 2016, expressed in ‰ with respect to V-SMOW.

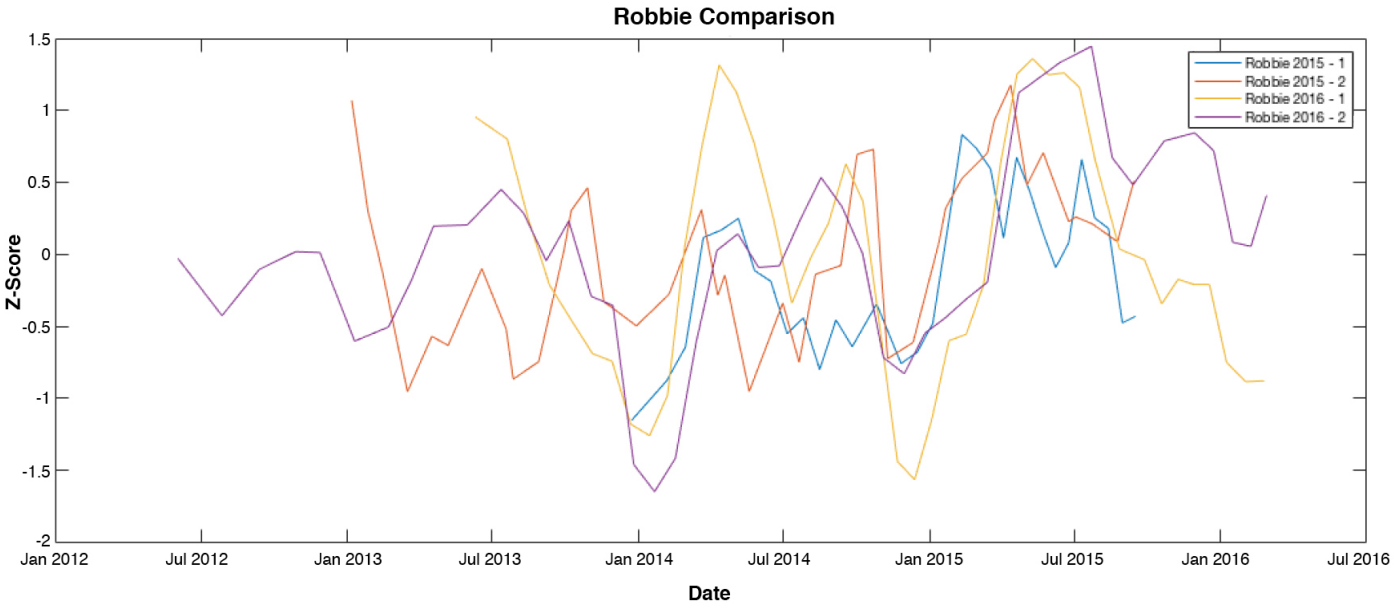

Figure 5.12: 3-point moving average of the final normalised δ^{18}O values of the two hairs from the Exmoor pony *Robbie* sampled in 2016, expressed in ‰ with respect to V-SMOW.

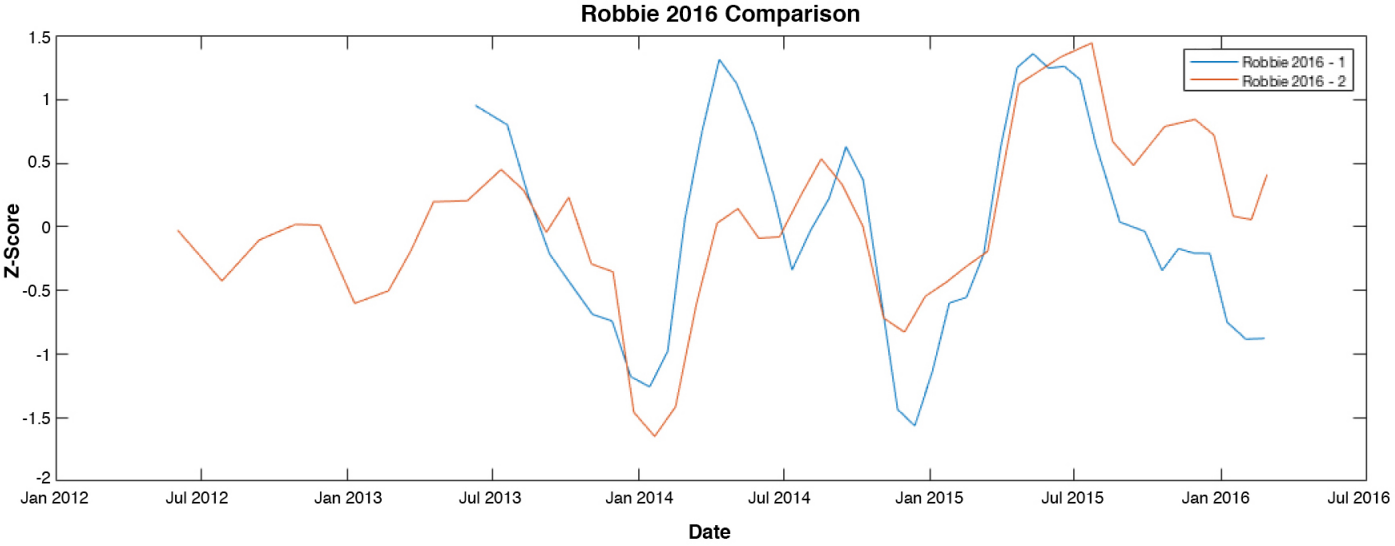

Telogen Lag

As the horses within this study were sampled on the same day, at the end of the United Kingdom meteorological winter on 7th March 2016, during a typical shedding period (Innera et al. 2013), it is proposed that a similar proportion of the samples hairs would be within a telogen phase of the hair growth cycle. However, hair with clear follicle bulbs and anterior hair ends were specifically identified (Deedrick and Koch, 2004) for sampling, due to ease of mid-sampling direction identification, in case of hair movement during sampling or later sampling of a half processed hair. With this in mind, it may be that a couple of the hairs still have a data lag, of between thirty and ninety days.

Jódís 2 was noted to include the follicle cap during sampling, and can therefore be specifically ruled out as a having been sampled during a telogen phase of growth. A three month (90 day) lag-correction, an average for the length of the telogen phase, was introduced within the hair data for *Tonto*, *Dessi* and *Kæti*, and a 60 day lag was introduced to the *Silver 1* data. This study sampled singular hairs from several locations, and therefore it is likely that there would be variation within each location. Other hairs from other horses, may also be within early stages of the telogen phase, and thus incurring a slight error within the temporal boundaries of the samples.

Figures 5.13 and 5.14 show the before and after results of the introduced lag-corrections for the two Oxfordshire ponies, *Tonto* and *Dessi*, demonstrating a trough in δ^{18}O values around November and December 2014. A corresponding peak occurs between approximately April to July 2015. Another peak is also evident across the five records from approximately March to August 2014. These peaks are consistent with seasonal winter and summer troughs and peaks, respectively. It is a reasonable assumption for this study

that these four hairs, from the nineteen hairs sampled, with sufficient temporal length are the only hairs with a significant telogen lag. This percentage, of 21.1% , is consistent with previous studies results quoting a percentage of 4-24% hair samples found to be in a telogen phase at any one time (Kunz, Seifert and Töeb, 2009; LeBeau, Montgomery and Brewer, 2011).

Figure 5.13: δ^{18}O results for the Oxfordshire ponies, expressed in ‰ with respect to V-SMOW.

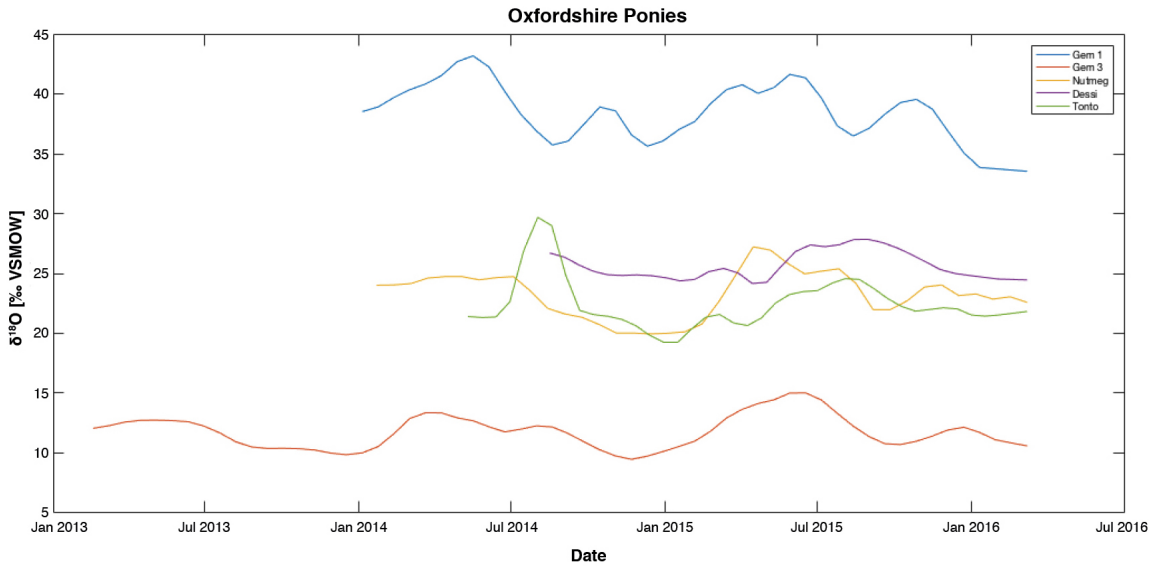

Figure 5.14: δ^{18}O result for the Oxfordshire ponies, including an introduced telogen phase correction for the ponies *Tonto* and *Dessi*, expressed in ‰ with respect to V-SMOW.

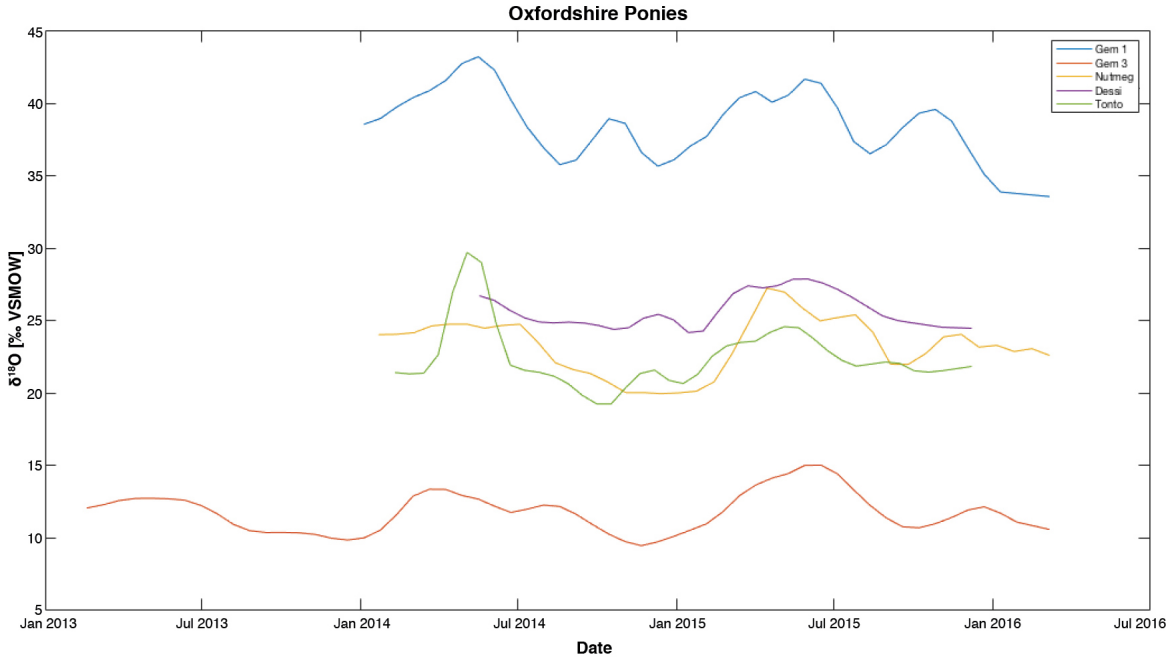

5.1.3 Oxfordshire

A nearby measurement station in Wallingford, Oxfordshire provided δ^{18}O and precipitation measurements. This station is part of a network of isotope measurements available via the International Atomic Energy Agency (IAEA) Global Network of Isotopes in Precipitation (GNIP) Water Isotope System for data analysis, visualization and electronic retrieval (WISER) database (IAEA/WMO, 2018).

The Wallingford isotope data shows that there is significant variability within the δ^{18}O values of precipitation, with a range greater than 15‰ from just above -14‰ to 2‰. The average δ^{18}O over this record is -6.74‰. When comparing the δ^{18}O of precipitation and the rainfall totals, the period between 2000 and 2004 can be seen to have had high

rainfall, with fewer above average δ^{18}O spikes.

Figure 5.15: Wallingford δ^{18}O measurements within precipitation from 1979 to 2015.

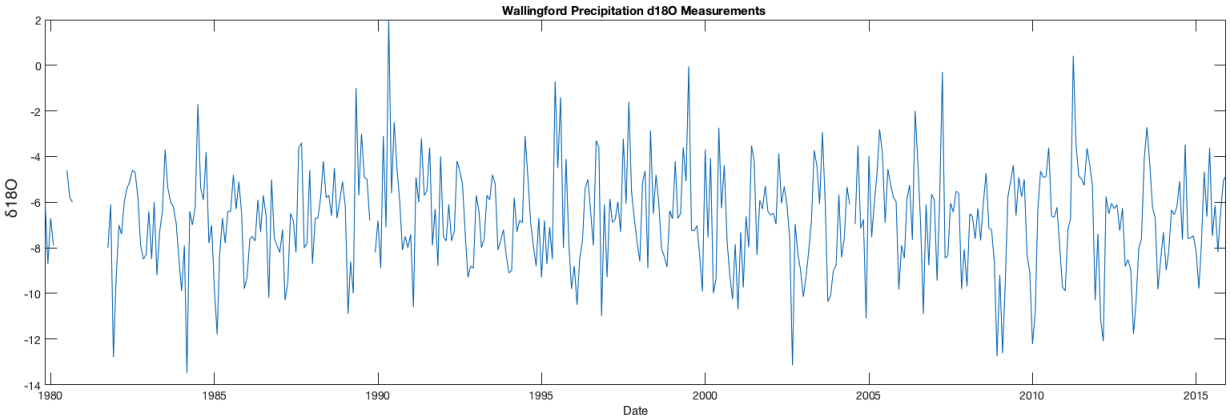

Figure 5.16: Wallingford precipitation totals from 1979 to 2015.

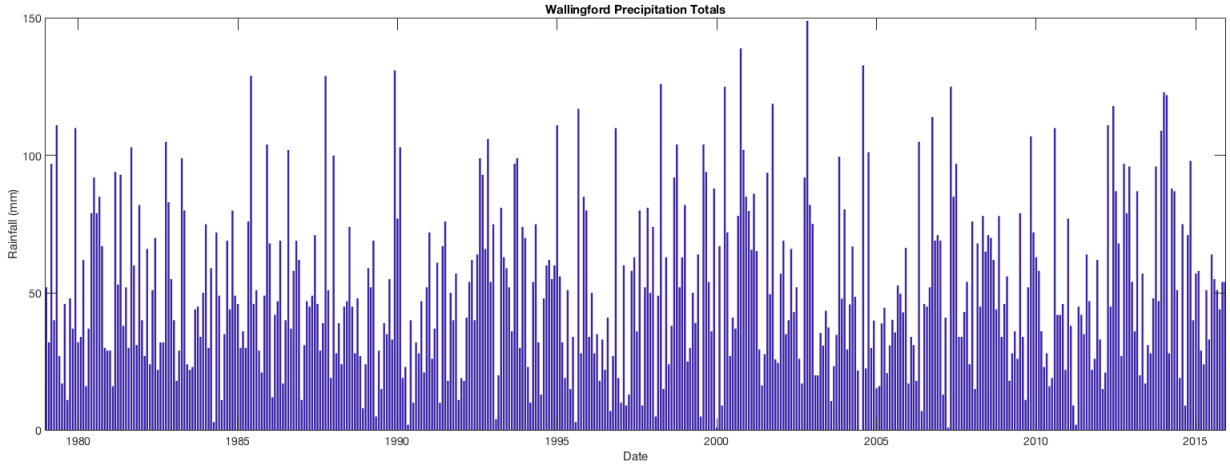

The annual mean δ^{18}O values for the same period as Figure 5.15 highlights years which had particularly low or high δ^{18}O values. 1981 particularly had a low δ^{18}O mean of nearly -9‰. 1990, 2005 and 2011 all had higher δ^{18}O, nearing -5.5‰. The period from 1988 to 1991 coincides with a prolonged period within the positive phase of the Arctic Oscillation. Cold air is confined within the polar regions by a strong polar wind

belt at approximately 55° N. Using information about the positive correlation between temperatures and δ^{18}O values, higher δ^{18}O values between 1988 to 1991 are consistent with the higher temperatures pushing further north during this positive Artic Oscillation (AO) phase. During 2010 and into 2011, there was a prolonged negative phase of the North Atlantic Oscillation (NAO). This is characterised by below normal precipitation and below normal temperatures over northern Europe. This teleconnection effect is also consistent with a peak in δ^{18}O values of precipitation. However, there is no apparent dominance of AO or NAO phase to explain the δ^{18}O peak in 2005, only a very negative spike in the Southern Oscillation Index, which did not result in an El Niño Southern Oscillation event.

Figure 5.17: Wallingford annual mean δ^{18}O values from 1979 to 2015.

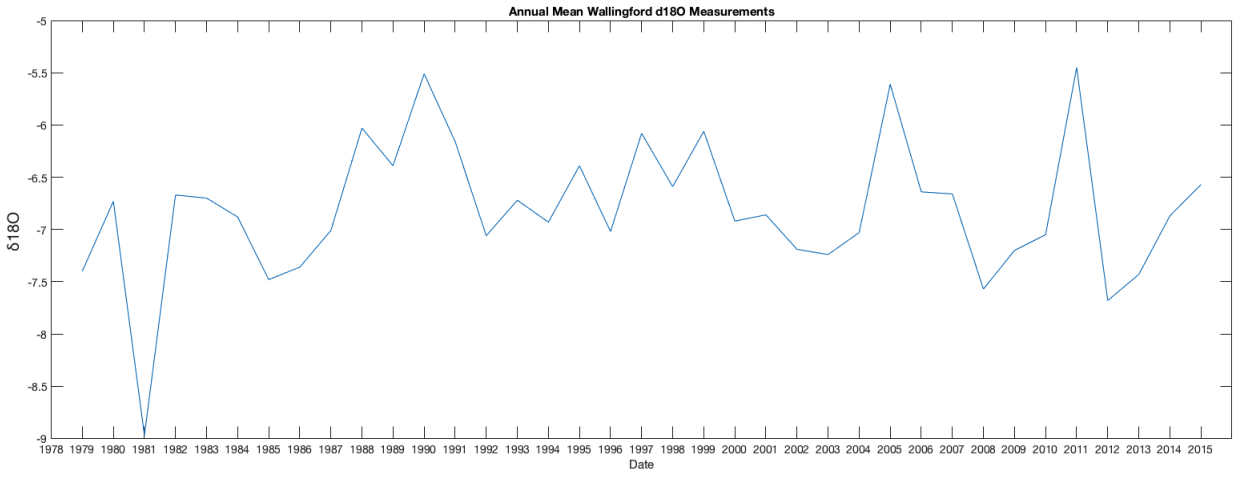

Consistent with temperature and rainfall climatologies for the Wallingford region and the relationships described in the previous sections between temperature, rainfall and δ^{18}O, the highest δ^{18}O values occur in the summer months, from June to July, and the lowest occur during winter, from December to February (Figure 5.18). The seasonal peak to peak amplitude of this Wallingford δ^{18}O data was 3.25‰ .

Figure 5.18: Monthly mean Wallingford δ^{18}O values, using data from 1979 to 2015, including ± 1 standard deviation

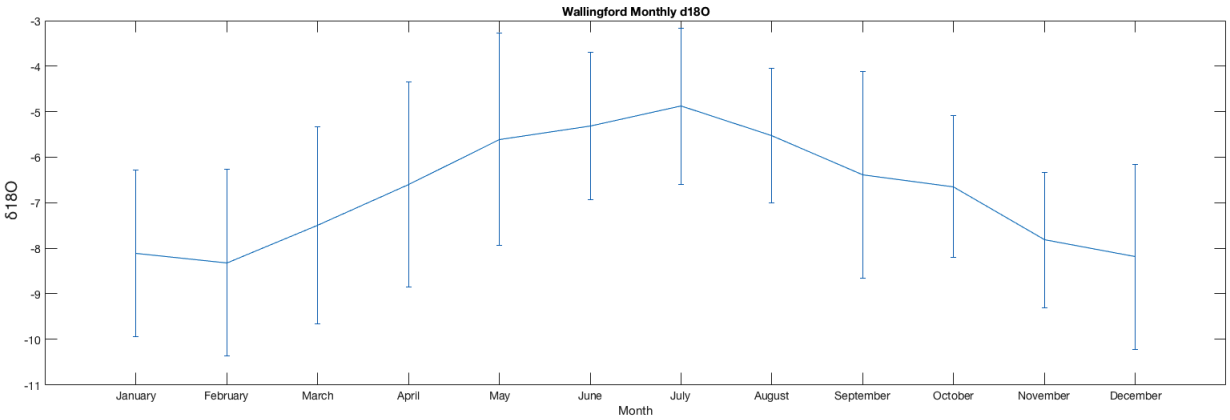

Although there is significant individual noise and variation within the horse hair δ^{18}O of the Oxfordshire ponies, two prominent peaks are clear in Figures 5.19 and 5.20. With troughs occurring just prior to January in 2014 and 2015, the δ^{18}O values sharply peak between approximately March and June [March and July during 2015]. The hair data from Oxfordshire showed a seasonal δ^{18}O amplitude of between 4‰ to 7‰ . The overall signal consistency of the individual normalised hairs in both Figure 5.19 and 5.20 is clear, despite the aforementioned noise.

Figure 5.19: Z-scores for the δ^{18}O values of Oxfordshire Ponies.

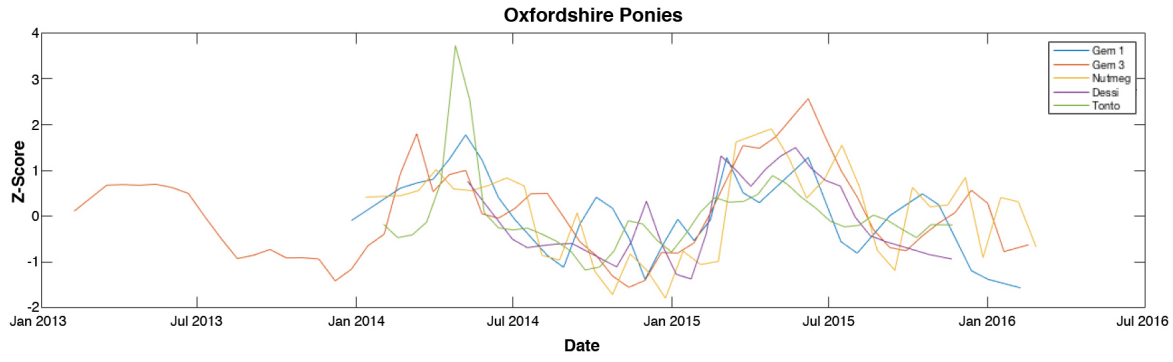

Figure 5.20: 3-point averaged Z-scores for the δ^{18}O values of Oxfordshire Ponies.

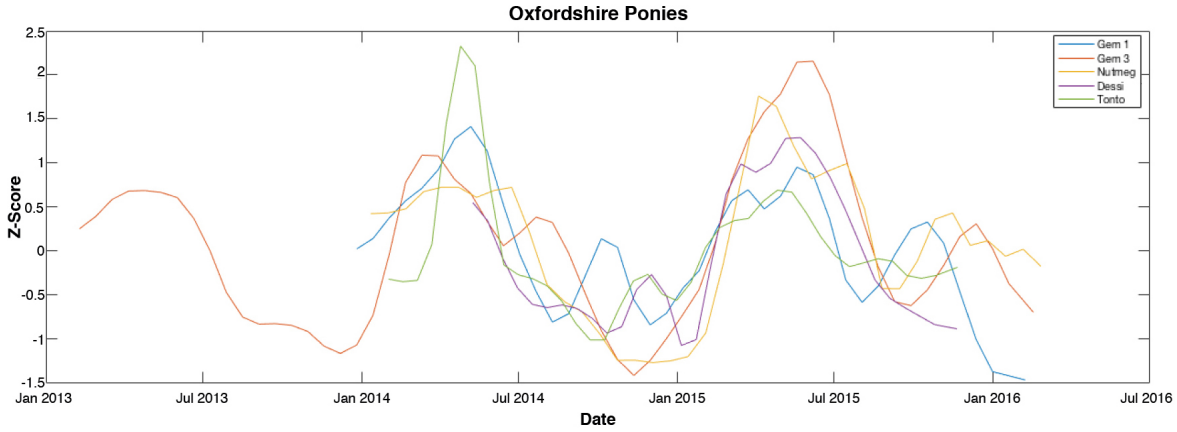

The temperature data obtained from the Brize Norton meteorological station, in Oxfordshire is shown in Figure 5.21. This data shows that the summer temperature peaks were in late July and August for the 2013-2015 years, with January 2015 and late February 2016 showing the lowest minimum temperatures. Early February 2016 saw higher minimum and maximum temperatures than expected for winter. There was also a notable warm temperature spike in the maximum temperature record at the beginning of July 2015. The mean peak amplitude for the seasonal maximum and minimum temperatures was 14.9° C and 11.2° C respectively.

Figure 5.21: Minimum, maximum and mean temperature for the meteorological station at Brize Norton, United Kingdom.

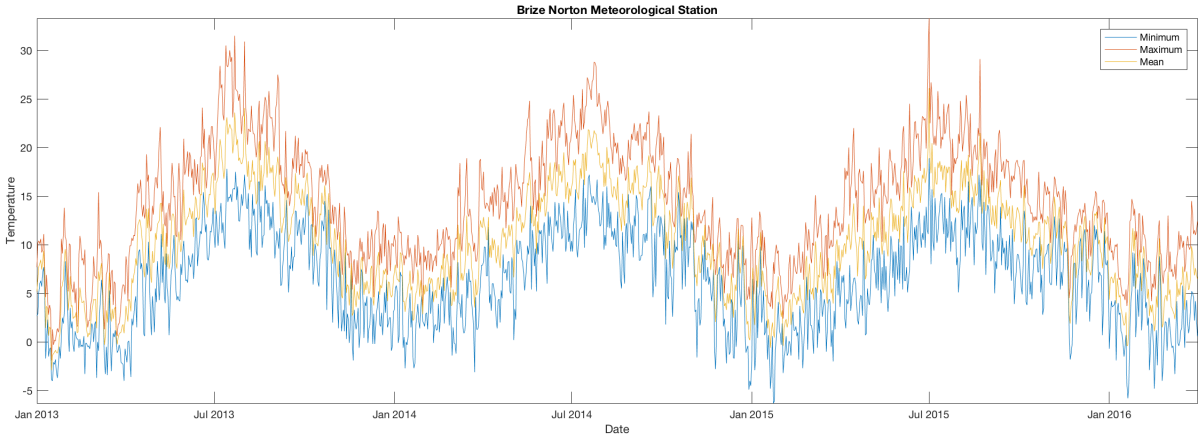

There are several peak rainfall events of note in the Brize Norton record (Figure 5.22). These high rainfall measurements were recorded on the 23rd December 2013, 6th February 2014, 25th April 2014, 25th August 2014, 24th July 2015, 30th December 2015, and the 8th March 2016.

Figure 5.22: Rainfall data from the meteorological station at Brize Norton, United Kingdom.

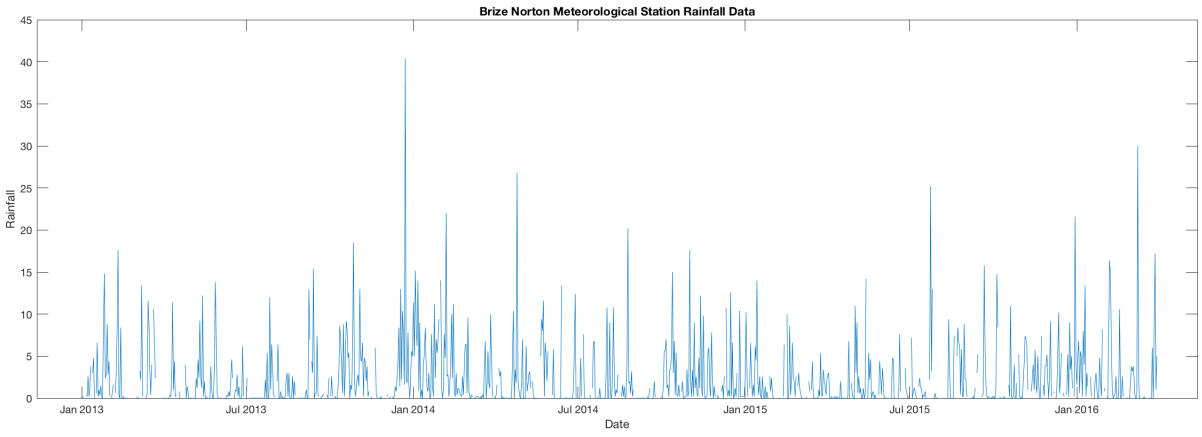

Figure 5.23 shows a comparison between the z-scores for the Oxfordshire horse hair

and z-scores calculated for the Brize Norton mean temperature record, from January 2013 to March 2016. The similarity between the seasonal temperature amplitude and the amplitude of the horse hair data is clearly shown.

Figure 5.23: Z-scores for Oxfordshire horse hair plotted against z-scores for mean temperature from Brize Norton, United Kingdom.

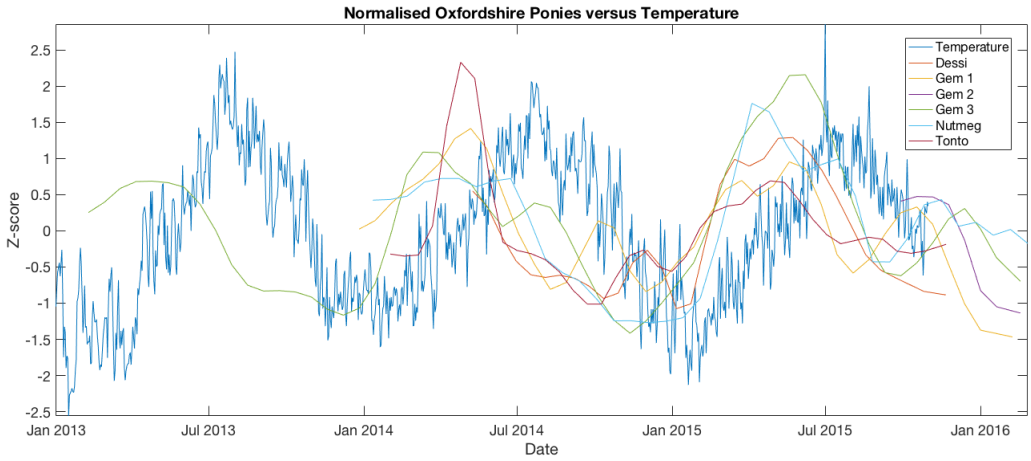

Although there is good alignment between the individual hair records and a clear seasonal signal within the δ^{18}O results, there appears to be an incongruous lead between the hair samples and the meteorological variables. This could be due to the turnover half-life of 0.5-4 days and potential full turnover time of more than 14 days for hair δ^{18}O to stop equilibrating after a major change in dietary water isotopic values, discussed in Section 2.6. As the date values were converted from sequentially sampled centimetre date ranges and as the plotted dates used are the median date within these ranges, small errors within the calculated growth rate could have been magnified further along the record. Figure 5.24 shows a comparison between the Wallingford GNIP data and the Oxfordshire pony hair. The trough minimums in the horse hair data lie between the September and December months and the peaks lie from the April to June months. The Wallingford data peaks during the summer months, with troughs during winter. Figure

5.24 shows an indication of the seasonal influence on the biological δ^{18}O values within Oxfordshire pony hair, with clear similarity in the data structures, although there appears to be a misalignment of the results with the local weather. The difference in peak and trough timing may be due to slight inaccuracies in the horse hair time scale tuning. The distance between the peaks of the horse hair data and the GNIP data is small at the start of the sampling record in early March 2016 but becomes larger toward the tail end of the hairs, in July 2013. This is indicative of a compounding effect of small growth rate inaccuracies at the start of the hair record.

Figure 5.24: Wallingford GNIP data plotted with the Oxfordshire horse hair data.

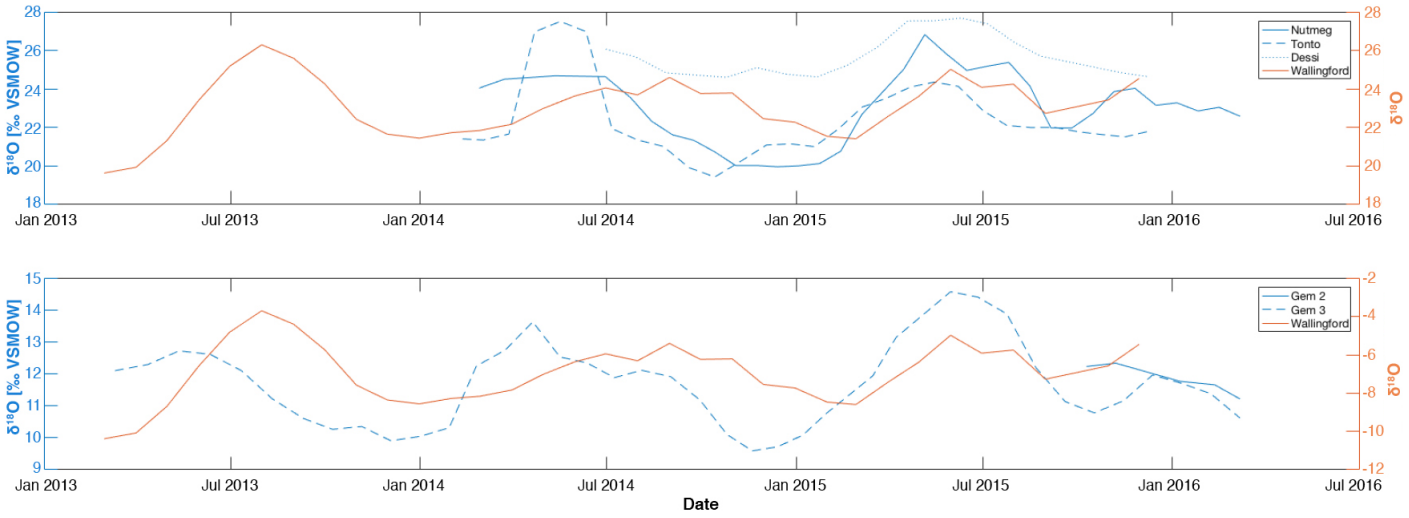

5.1.4 Exmoor

This section details the primary results of the Exmoor pony δ^{18}O values from a sequential sampling of individual hairs. As detailed earlier, the results that are being examined have been analysed, quality controlled, calibrated, interpolated, growth rate corrected and smoothed. Figure 5.25 includes the non-smoothed normalised values for all the

sampled Exmoor hairs plotted against the median date, from the middle of sample's calculated date range. *Robbie 1* was the temporally longest hair, extending approximately 4 years back to around April 2012. At 65cm this record was the third longest in centimetre length, after *Rama 1* at 75cm and *Fudge 1* at 66cm. However, with the slowest growth rate of the Exmoor ponies at 0.046cm/day, compared to *Rama* at 0.066cm/day and *Fudge 1* at 0.056cm/day, this means that it provided the longest record of all the sampled hairs. Figure 5.25 shows a spike in the *Robbie 1* hair around November 2013, in addition to the general peak shown in several hairs around July 2013. *Robbie 2*, *Fudge 1*, *Robbie 1* and *Rama 1* all show a slight double peak and trough between January and July 2014, to varying discernibility. There is also an abrupt trough after an initial peak in all of the hairs around July 2015, with a second sharp peak in *Rama 1* and *Robbie 1* around September 2015.

Figure 5.25: Z-scores for the δ^{18}O values of Exmoor Ponies against the median centimetre date.

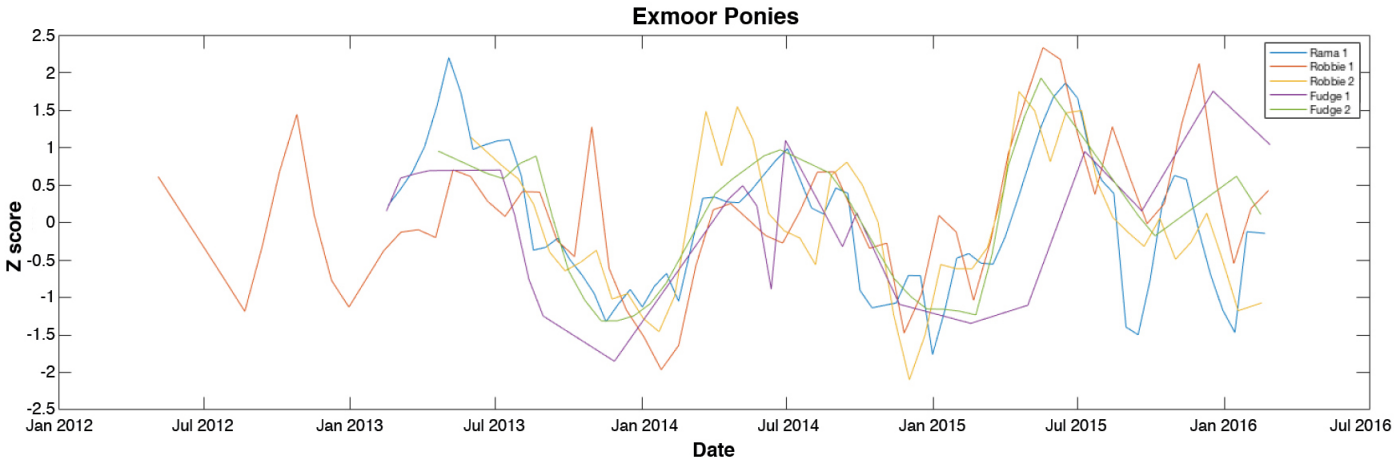

The smoothed normalised values in Figure 5.26 have removed some of the noise seen in Figure 5.25, with clearer primary features remaining. All hairs show clear seasonal

peaks and troughs occurring around July and January of each year, with the most prominent trough occurring in January 2014 and the most prominent peak occurring just prior to July 2015. There is a disturbance in this seasonal pattern, as described for Figure 5.15, in the form of a trough at around August to October 2015.

Figure 5.26: 3-point averaged Z-scores for the δ^{18}O values of Exmoor Ponies against the median centimetre date.

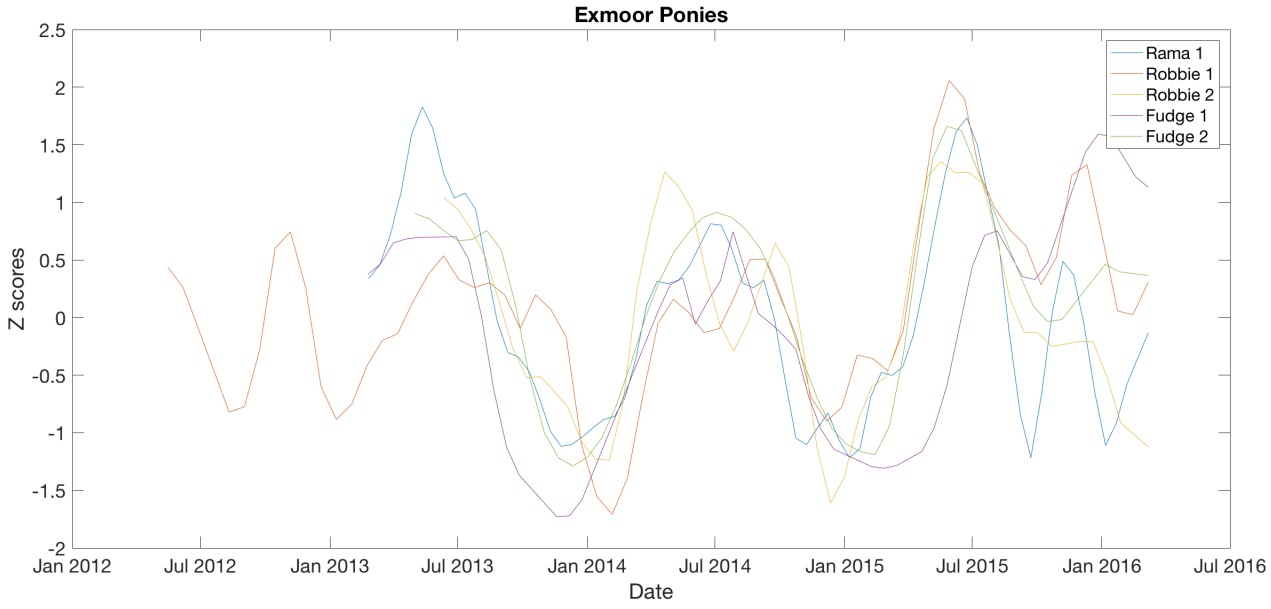

Figure 5.27 shows the smoothed values for the two *Fudge* hairs, plotted against the median date, calculated using the growth rate estimation of *Fudge* hair. Although both hairs line up well with each other, there are still obvious differences between the two records. This difference is caused by the amplification of small errors in the growth rate calculation, as well as the plotted median date representing a date range for each sample, with varying centimetre lengths. However, given that these records are representations of mean values during two different moving time ranges, these data show good potential reproducibility and application for seasonal interpretation.

Figure 5.27: 3-point averaged δ^{18}O values for the two Exmoor Pony *Fudge* hairs against the median centimetre date, expressed in ‰ with respect to V-SMOW.

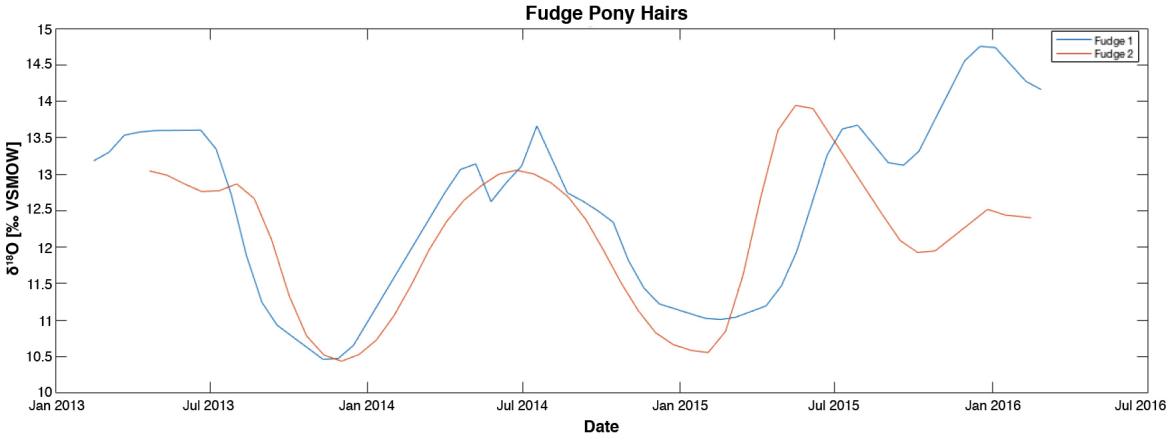

Of the five hairs sampled from Exmoor for this study, 1 and a half (all of *Robbie 1* and half the samples of *Fudge 1*) did not use the USGS42 standard samples within the machine runs. Figure 5.28 shows the smoothed values for the Exmoor ponies, with *Robbie 1* hair separated due to the lack of USGS42 standard use during analysis, to enable further comparison of the records. *Robbie 1* shows consistent troughs in January of each year, with the most pronounced trough in 2014. The other hairs also show analogous troughs in January 2014 and January 2015, as well as increased δ^{18}O values over the summer periods of each year. Also consistent with the *Robbie 1* data, as well as the earlier normalised data plots, there are deviations within the expected summer peaks during July 2014 in the *Robbie 2* record and around September 2015 in the *Rama 1* record. The approximate peak to peak amplitude of the Exmoor hairs was between 3‰ to 5.5‰ .

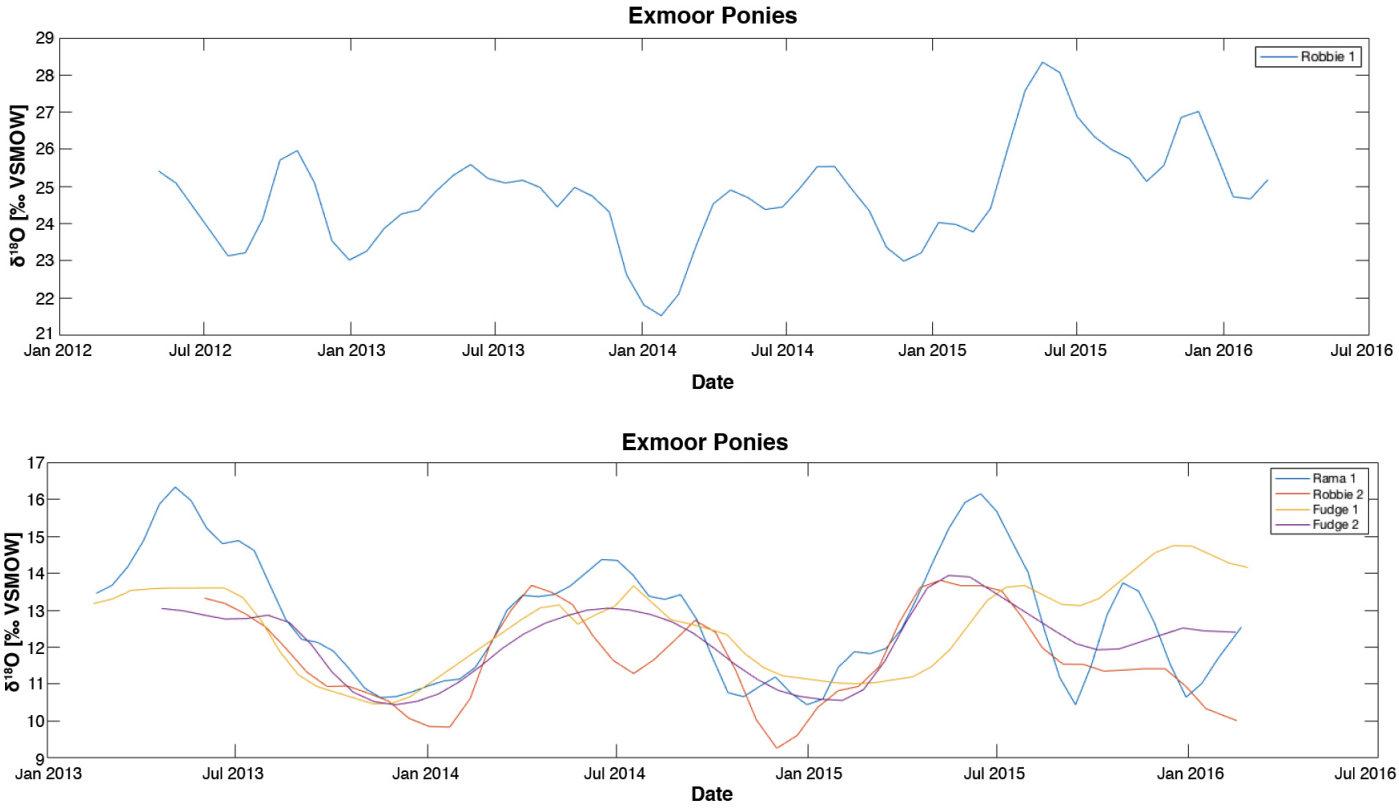

Figure 5.28: 3-point averaged δ^{18}O values for the Exmoor Ponies, against the median centimetre date, expressed in ‰ with respect to V-SMOW. Plot a) shows the *Robbie 1* hair which was analysed without USGS42 and b) shows the *Rama 1*, *Robbie 2*, *Fudge 1* and *Fudge 2* hairs, which were analysed using the USGS42 standard.

Figures 5.29 and 5.30 show the meteorological observations for the nearby Lisombe station. Visual comparison between Figures 5.25 to 5.28 and the temperature data from Liscombe show clear similarities. There are regular seasonal winter troughs in January and summer peaks in July of each year. The most prominent peak in maximum temperature occurs in the July 2013 summer. However, the highest minimum temperature peak occurs during an event in July 2015, which is shortly followed by a period of high minimum temperatures, with only small diurnal variation between minimum and maximum temperature, in December 2015. The climatological peak amplitude for Liscombe was 10.3° C for the minimum temperature and 12.5° C for the maximum temperature (Table 3.6 of Section 3.2.1).

Figure 5.29: Minimum, maximum and mean temperature for the meteorological station at Liscombe, United Kingdom.

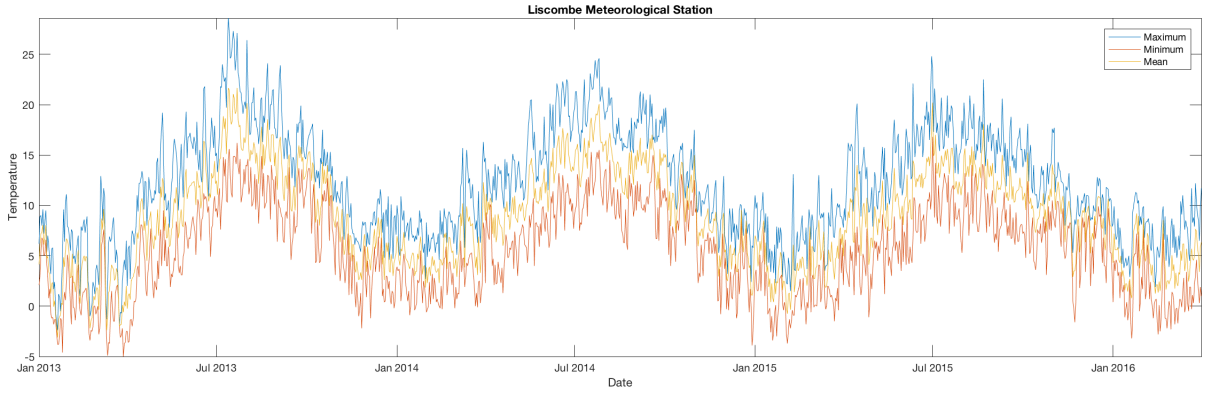

Figure 5.30 shows a comparison between the z-scores for the Exmoor horse hair and z-scores calculated for the Liscombe mean temperature record, from July 2012 to March 2016. The seasonal amplitude for the temperature and the amplitude of the horse hair data is obviously comparable.

Figure 5.30: Z-scores for Exmoor horse hair plotted against z-scores for mean temperature from Liscombe, United Kingdom.

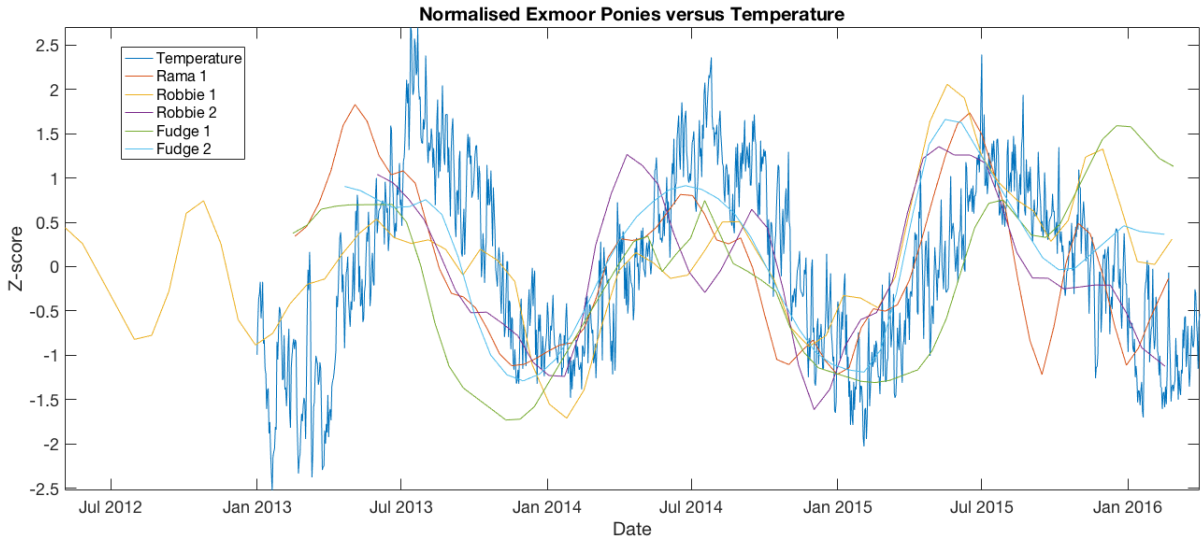

The daily rainfall values obtained from the Liscombe meteorological station show slightly lower rainfall during summer and higher rainfall during winter. Figure 5. 31 shows the total daily rainfall data for a) 0900-0900 from the 01/01/2013 to the 25/02/2015, and b) the total rainfall from 0100-2400 from the 25/02/2015 to the 31/03/2016. The data from Liscombe shows high rainfall events on:

- the 15th March 2013 and the 21st March 2013,

- the 27th October 2013 and the 03rd November 2013,

- the 23rd December 2013,

- the 24th May 2014,

- the 24th and 26th July 2015,

- the 30th November 2015, and

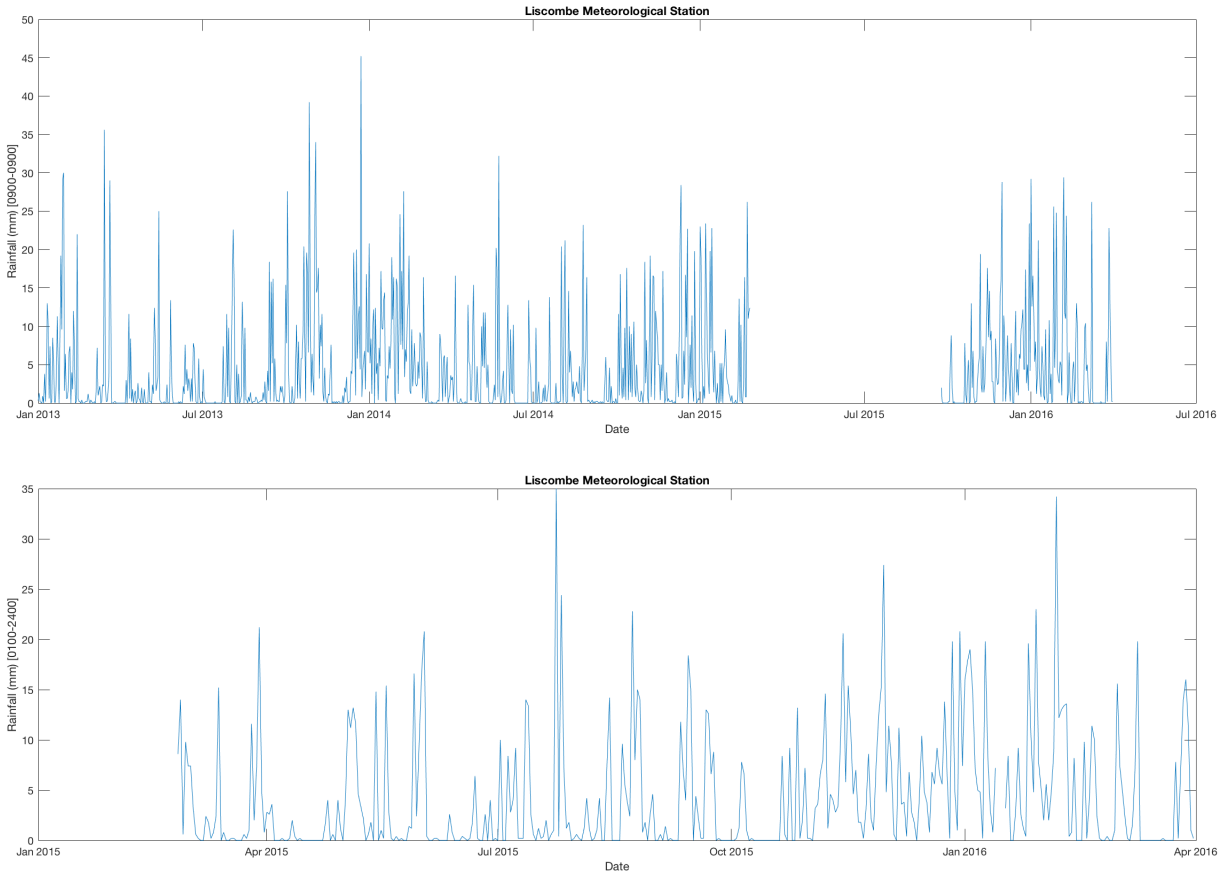

Figure 5.31: Daily rainfall at Liscombe, Exmoor with a) the total rainfall from 0900-0900 from the 01/01/2013 to the 25/02/2015 and b) the total rainfall from 0100-2400 from the 25/02/2015 to the 31/03/2016.

- the 6^{th}February 2016.

In addition to these peak rainfall days, the periods around January 2016 appeared to have been particularly wet, with a number of high rainfall days.

Comparison between the horse hair data and the meteorological observations show similarities to the temperature peaks and rainfall amounts. The deviation in the horse hair δ^{18}O values during July 2014 could be a delayed result of increased rainfall from the late May rainfall event. Similarly the fluctuating drop in δ^{18}O values between July 2015

and January 2016 could have been due to the two high rainfall days on the 24th and 26th July 2015. The January 2014 spike in the *Robbie* hairs may also correspond to the dry days just prior to January 2014 in the Liscombe rainfall record.

Figure 5.32: Wallingford GNIP data plotted with the Exmoor horse hair data.

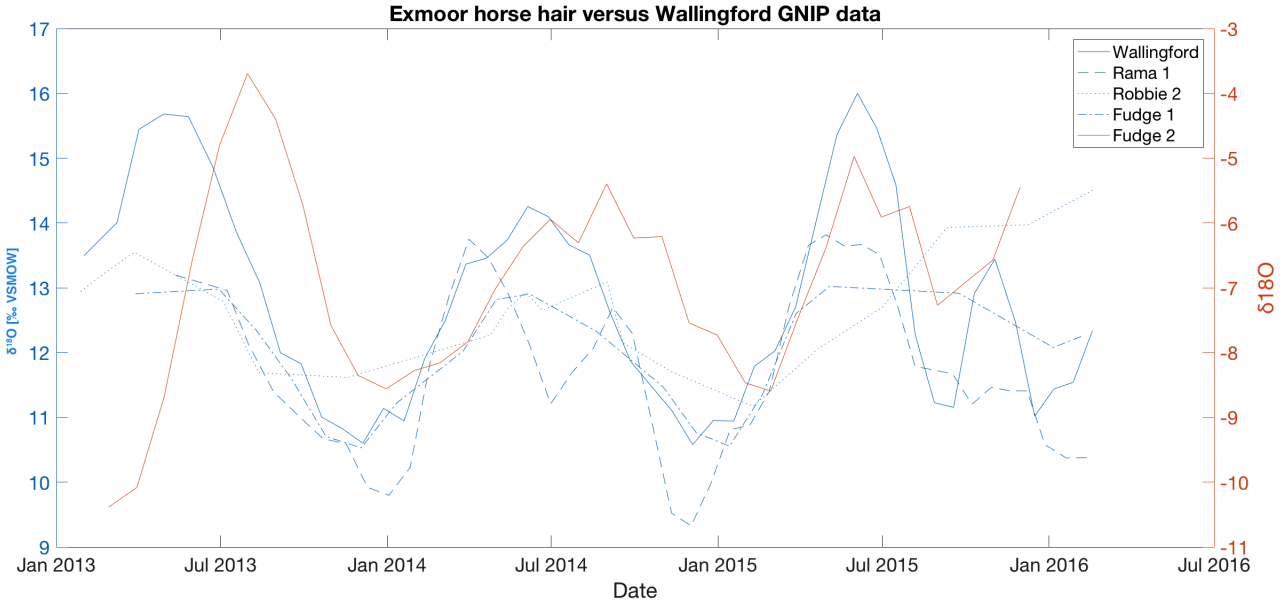

Water Samples

During one of the preceding sampling visits to the Exmoor Pony Centre in September 2015, two plastic tubes were used to sample two water troughs (A and B) in the paddocks housing the Ponies that had been sampled. These samples were left with head space, where the water was not flush with the lid and oxygen exchange is likely to have occurred between the water and the air within these tubes. However, for the sake of comparison, these samples were manually injected and measured for δ^{18}O using a Picarro L2120-i Analyzer, which has a typical precision of $<$0.2 ‰. The results from multiple injections from each sample (A and B) are shown in Table 5.5.

Table 5.5: Picarro oxygen measurements for two troughs (A and B) in the Horse paddocks of Exmoor, expressed in ‰ with respect to V-SMOW.

Trough	δ^{18}O measurement
A	-5.4
	-5.4
	-5.3
	-5.2
	-5.5
Average	-5.36
Standard Deviation	0.11
B	-5.4
	-5.3
	-5.3
	-5.2
Average	-5.30
Standard Deviation	0.08

These values fall within values likely for the Exmoor region, with Wallingford GNIP values ranging between a -4.73‰ average in July to a -7.98‰ average for December. Pellegrini et al. (2016) and Darling (2004) show the Exmoor region to lie within the -5.5‰ to -5.9‰ contours for the δ^{18}O values of groundwater. These results from previous studies also indicate that there is an approximate -1‰ difference between Wallingford groundwater and that in Exmoor. The coastal location of Exmoor is consistent with increased δ^{18}O values, when compared to Wallingford, albeit the higher altitude of the Exmoor moorland is likely to have dampened this difference.

5.1.5 Shetland Islands

The normalised values in Figure 5.33 for the Shetland Island ponies show good cohesion over the period from July 2015 to December 2015, with some variation between *Silver 2* and the other horse records after January 2016. The smoothed values in Figure 5.34

also show an analogous homogeneous trough in August 2015 and a peak during late September and October 2015. The Shetland Island hairs had the shortest centimetre lengths, with an average of 25.6 centimetres. The *Silver 1* hair was the longest record, however it also had the slowest growth rate out of the Shetland hairs, at 0.058cm/day.

Figure 5.33: Z-scores for the δ^{18}O values of Shetland Ponies.

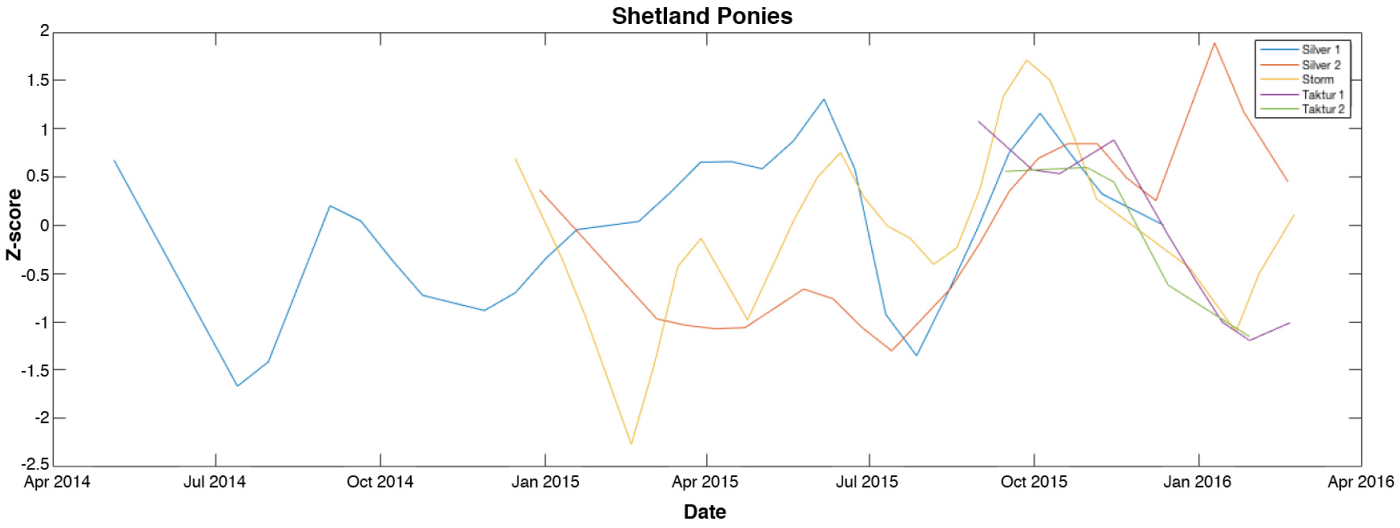

Figure 5.34: 3-point averaged Z-scores for the δ^{18}O values of Shetland Ponies.

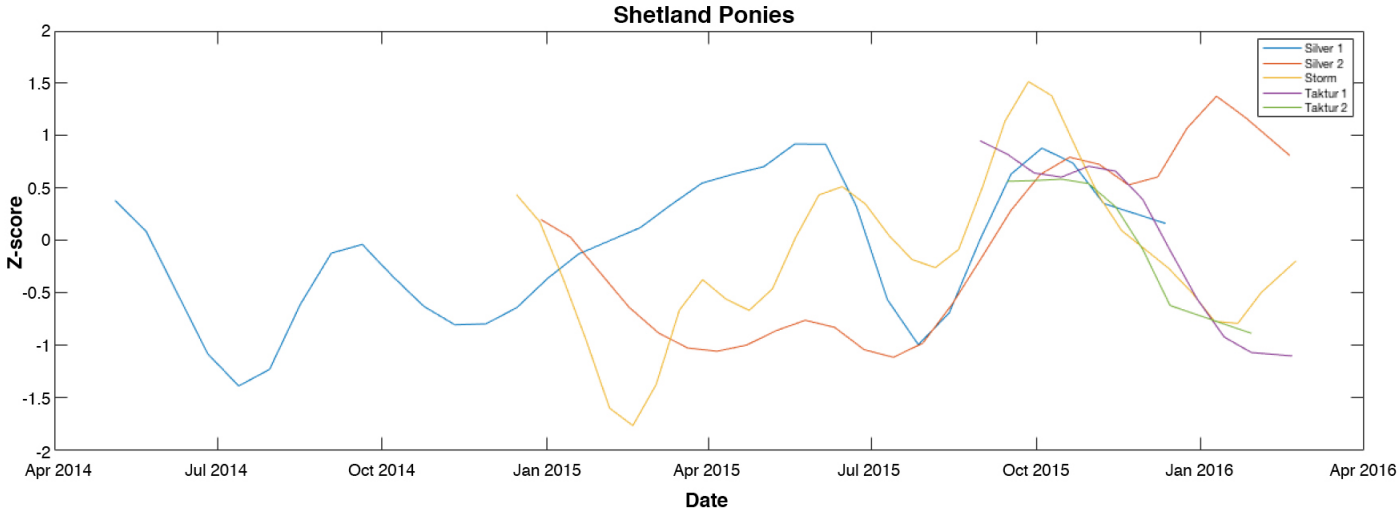

The final dataset shows the increasing difference between the *Silver 1* and *Storm* records later in the sequential record, temporally prior to July 2015. Despite the difference in absolute values of the *Silver 2* record, the relative similarities with the other hairs in regards to the peaks and troughs show that even with the use of different standards the potential inclusion of this data is valid. The Shetland Island hair showed a seasonal range of 3.5‰ to 4.5‰ .

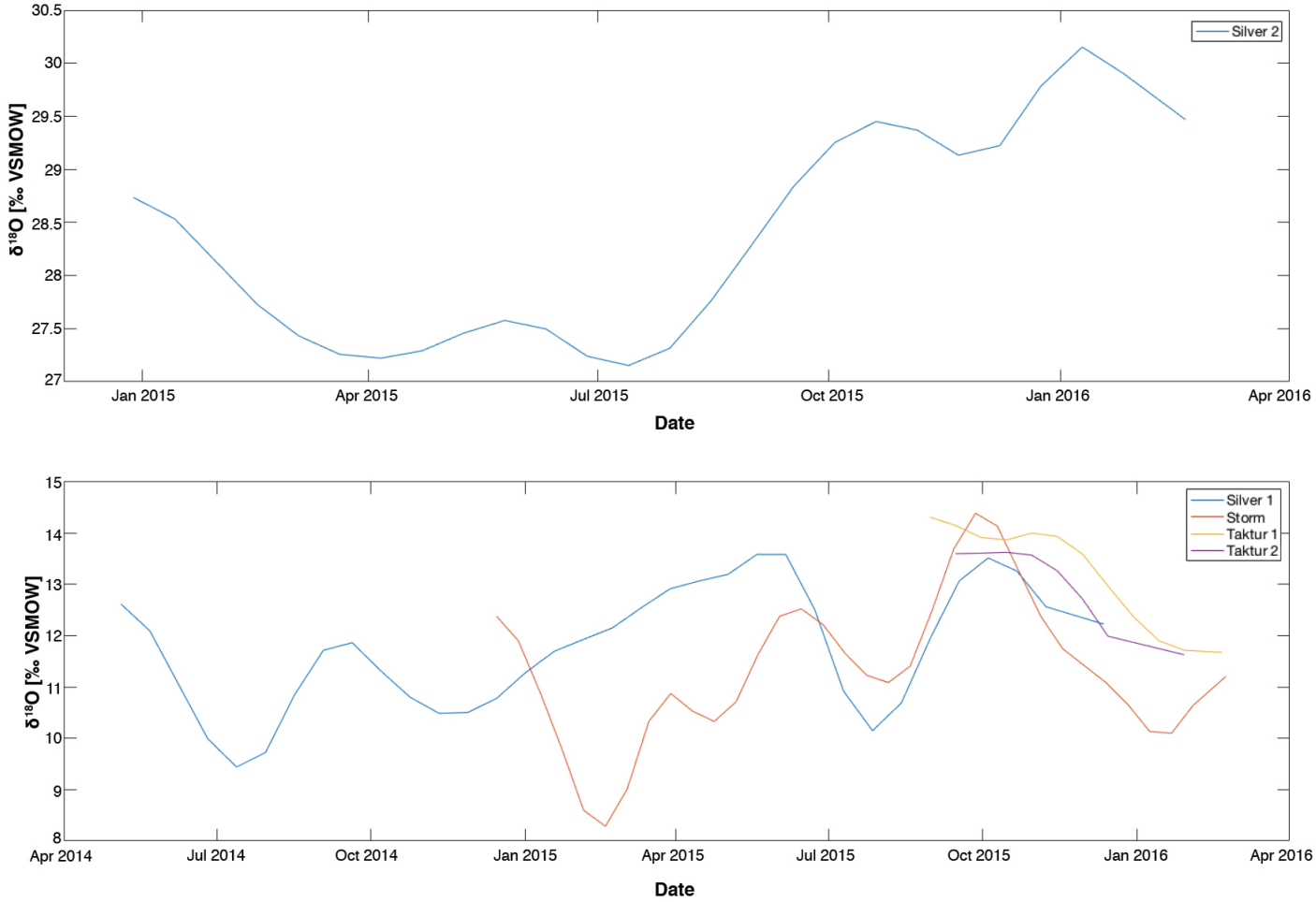

Figure 5.35: [3-point averaged δ^{18}O values for the Shetland ponies, against the median centimetre date, expressed in ‰ with respect to V-SMOW. Plot a) shows the *Silver 2* hair which was analysed without USGS42 and b) shows the *Silver 1*, *Storm*, *Taktur 1* and *Taktur 2* hairs, which were analysed using the USGS42 standard].

Figures 5.36 and 5.37 show the meteorological conditions at the Lerwick observation station, close to the Thordale Stud in the Shetland Islands for the period from July 2014 to April 2016. Climatologically, the months from October to January experiences the highest amount of rainfall in this region, with January and February exhibiting the coldest temperatures. Rainfall data from Figure 5.36 shows high rainfall events on the 9th August 2014, 13th January 2015, 14th August 2015, 15th September 2015, and 7th October 2015.

Figure 5.36: Total daily rainfall in millimetres at Lerwick, Shetland Islands.

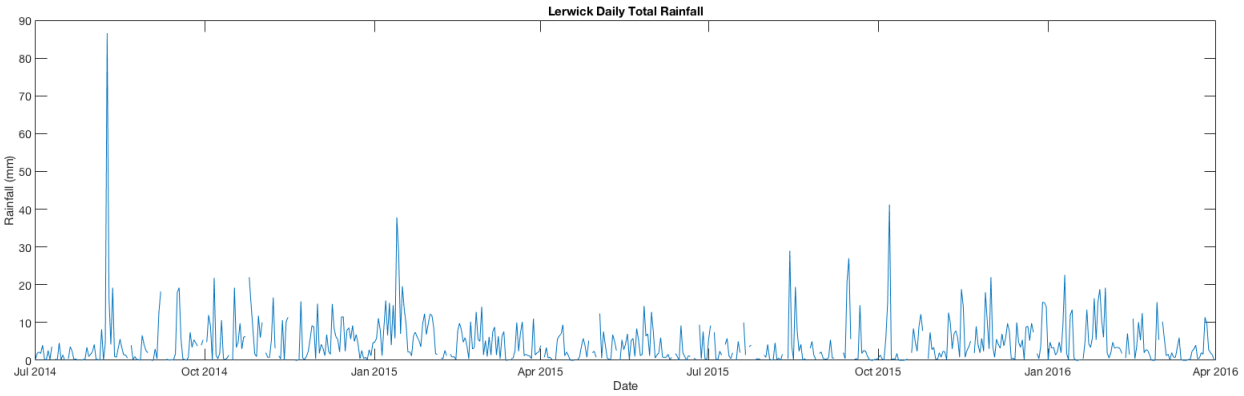

Figure 5.37 shows that the peak temperatures in 2014 and 2015 occurred slightly later than the climatological norm, toward August and September. However, lower temperatures were shown to have occurred in January and February of each year, which is consistent with the climatology of the region. Additionally, there were two anomalous periods where the minimum temperatures fell further than previous recordings, on the 17th and 18th January 2016 and 26th February 2016. There were also several periods of high minimum and mean temperatures in December 2015 to February 2016. The The seasonal amplitude of the climatological minimum temperatures was 8.7°, and 8.6°between the maximum temperatures.

Figure 5.37: Minimum and mean temperature for the meteorological station at Lerwick, Shetland Islands, United Kingdom.

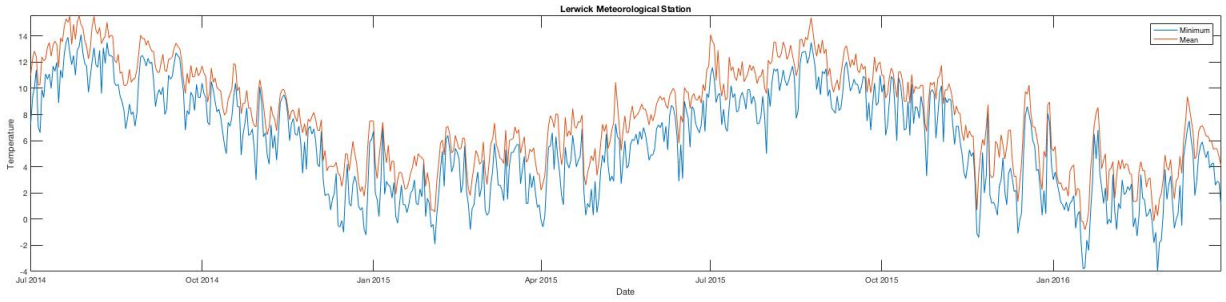

The results in Figure 5.38, show that there is a similar, although slightly reduced, amplitude in the horse hair, when a comparison of z-scores between the horse hair and the mean temperature is made.

Figure 5.38: Z-scores for Shetland horse hair plotted against z-scores for mean temperature from Lerwick, United Kingdom.

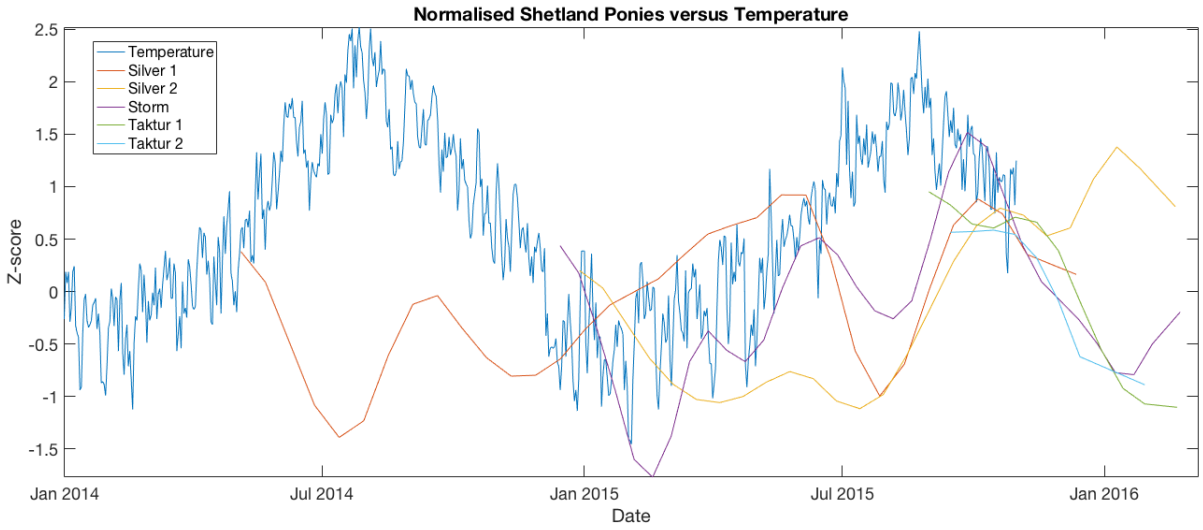

The closest IAEA GNIP WISER station for δ^{18}O measurements to Lerwick was Altnabreac, in northern Scotland (IAEA/WMO, 2018). This station is across the North Sea and a distance from the Shetland Island location, however comparison can provide

a useful indication as to the potential local δ^{18}O precipitation values. There is a larger spread within the data provided by the GNIP WISER program for Altnabreac (Table 5.6) compared to the Wallingford monthly mean δ^{18}O measurements. March contains the lowest value at -12.6‰, and the highest δ^{18}O measurements were during June and July, at -4.2‰ and -5.4‰ respectively. The range of these means within the Altnabreac GNIP data was approximately 8.4‰. The mean value for the Altnabreac record was -8.00‰, lower than the Wallingford mean of -6.74‰, which is consistent with a higher latitudinal position.

Table 5.6: Altnabreac monthly mean δ^{18}O measurements, data compiled from monthly measurements from 1981 and 1982.

Year	Altnabreac δ^{18}O (‰)
January	-8.5
February	-9
March	-12.6
April	-6.6
May	-9.1
June	-4.2
July	-5.4
August	-6.90
September	-9.5
October	-8
November	-9.7
December	-7.5

A comparison of the meteorological variables with the horse hair data from the Shetland Islands shows that contrary to the Exmoor record, the visual correlation between the datasets is not so clear. The January 2015 trough in temperature is consistent with a decline in δ^{18}O values and the peak δ^{18}O values occurs in late September, which is also consistent with the temperature data. Although the unexpected additional trough in the δ^{18}O of July 2015 does not have an evident association with a specific temperature or

rainfall event, the rainfall totals of 131.2mm for the month of May 2015 were much higher than the average of 53.4mm for May, based on a 1981-2010 climatology.

Figure 5.39 also shows an amplitude comparison, between the Altnabreac δ^{18}O values from 1981-1982, plotted against the Shetland Island horse hair δ^{18}O for 2014-2016. The amplitudes between the GNIP data and the δ^{18}O values in horse hair are also similar.

Figure 5.39: Altnabreac GNIP data for the available time period of 1981-1982, plotted against the Shetland horse hair δ^{18}O for 2014-2016.

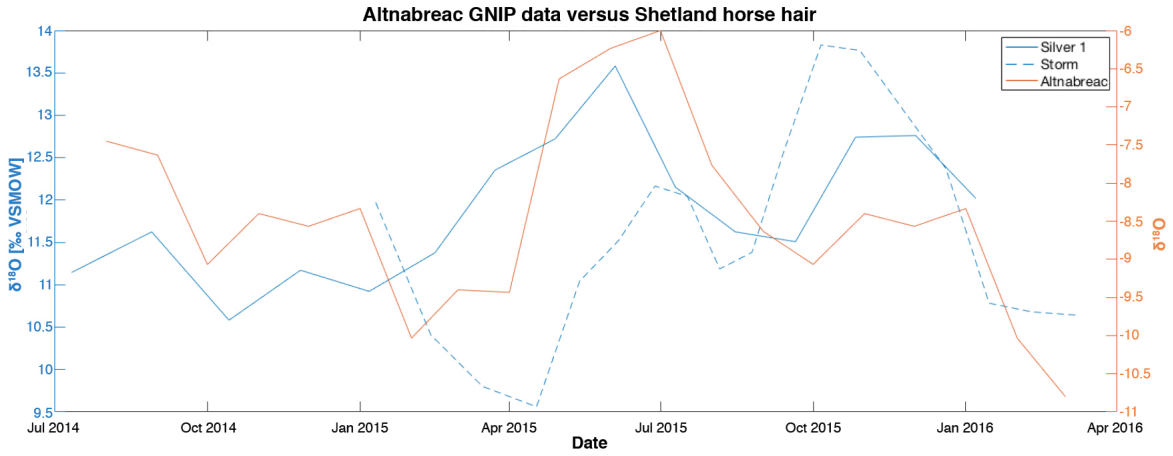

5.1.6 Iceland

According to the monthly mean Reykjavík δ^{18}O record, obtained from the IAEA GNIP WISER database, the peak in δ^{18}O values occurs in the month of May, with lower values during the winter months from November to January. The Reykjavík seasonal amplitude shown in Figure 5.40 was approximately 2.84‰ ±2.03‰.

Figure 5.40: Monthly mean Reykjavík δ^{18}O measurements, from data compiled from monthly measurements from 1962 to 2015, including ± 1 standard deviation.

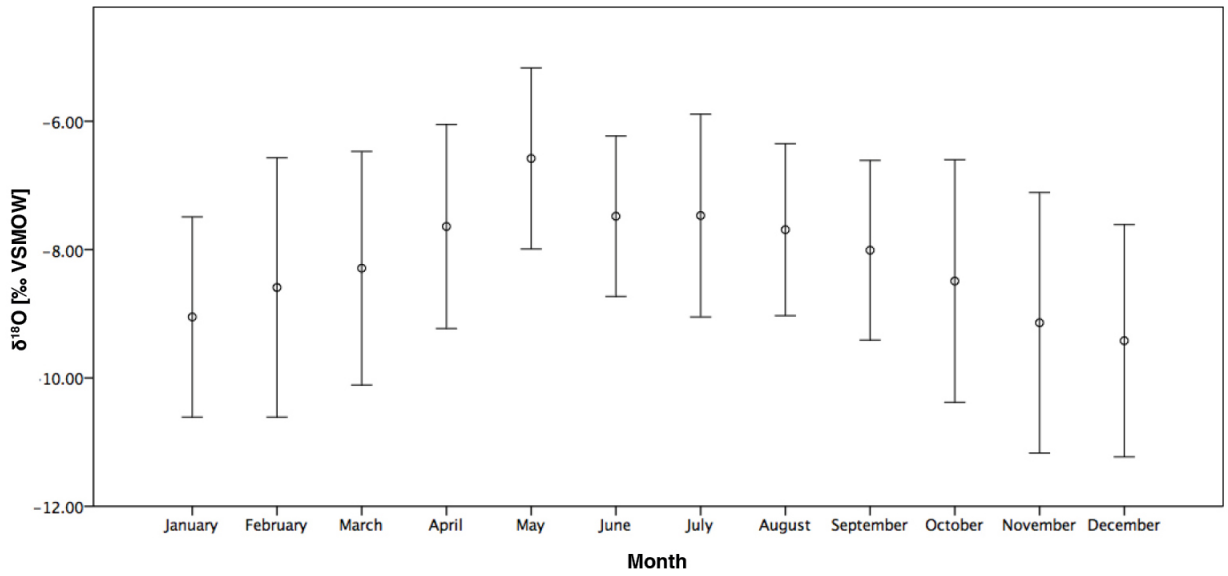

Figure 5.41 shows an apparent change in the δ^{18}O trend from the period before 1976 and to the period after 1993. Prior to 1976 the annual mean Reykjavík δ^{18}O measurements were between -7.0‰ and -8.0‰ , however after 1993 the annual mean values lay between 7.6‰ and 9.5‰. The values for the years relevant to this study for 2014 and 2015 were the lowest on record at -9.49‰ and -9.22‰ respectively.

Figure 5.41: Annual mean Reykjavík δ^{18}O measurements by year.

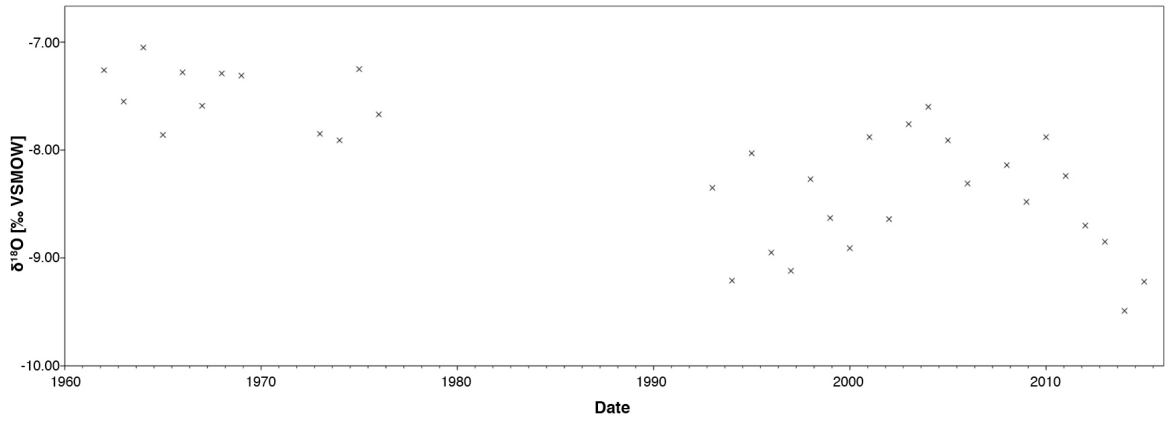

Figures 5.42 and 5.43 show the normalised comparison of Icelandic horse hairs and the final δ^{18}O values for each individual, respectively. All four hairs peak during the July to September 2015 months. All records also indicated that the values are declining from an initial peak prior to the start of the temporal record, with the *Jódís 2* and *Jódís 1* signals both showing a steep decline from this peak in particular. The *Jódís 1* and *Granis* data both indicate that there is an additional influence on the seasonal signal toward the end of December 2015 and into January of 2016. Additionally, the records all show a smaller peak and subsequent deviation within the rise in values from February to April 2015.

Figure 5.42: 3-point averaged Z-scores for the δ^{18}O values of Icelandic Horses.

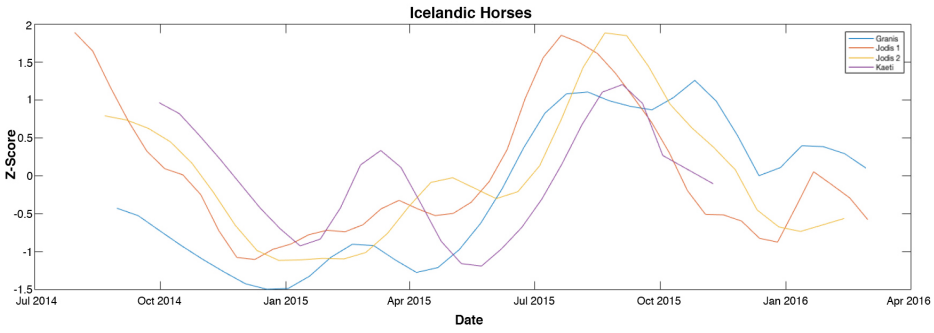

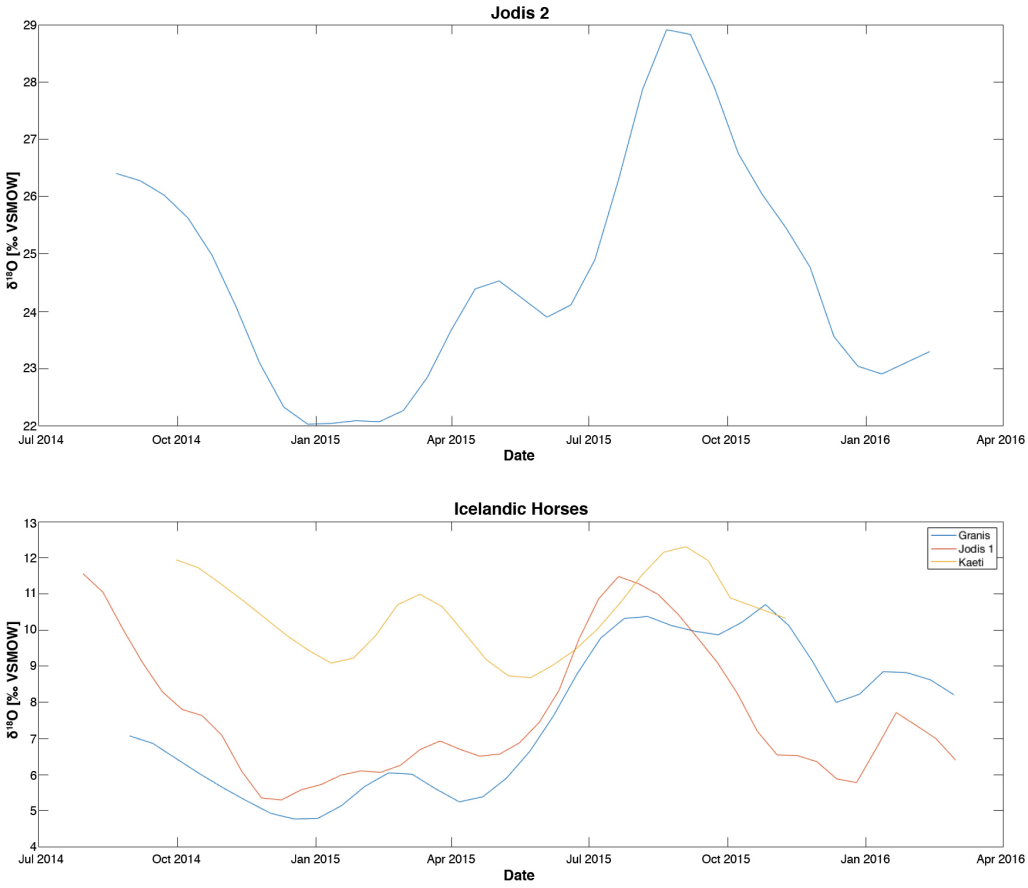

Figure 5.43: 3-point averaged δ^{18}O measurement of Icelandic Horses, expressed in ‰ with respect to V-SMOW. Plot a) shows the Jódís 2 hair which was analysed without USGS42 and b) shows the *Granis*, *Jódís 1* and *Kaeti* hairs, which were analysed using the USGS42 standard.

The seasonal range in δ^{18}O values, shown in Figure 5.43 horse hair results, was between 4‰ to 5.5‰ .

The maximum and minimum temperature data (Figure 5.44) from the nearby Eyrarbakki meteorological station show that temperatures reach a summer apex during July to September of each year. The minimum temperatures drop sharply during the winter with extended temperature troughs from October until April [May] in 2014 [2015].

Referring back to the climatological means of Table 3.5 in Section 3.2.1., the seasonal amplitude of the minimum temperatures was 11.87° C , and 12.44° C between the maximum temperatures.

Figure 5.44: Maximum and minimum temperature at the Eyrarbakki meteorological station, Iceland.

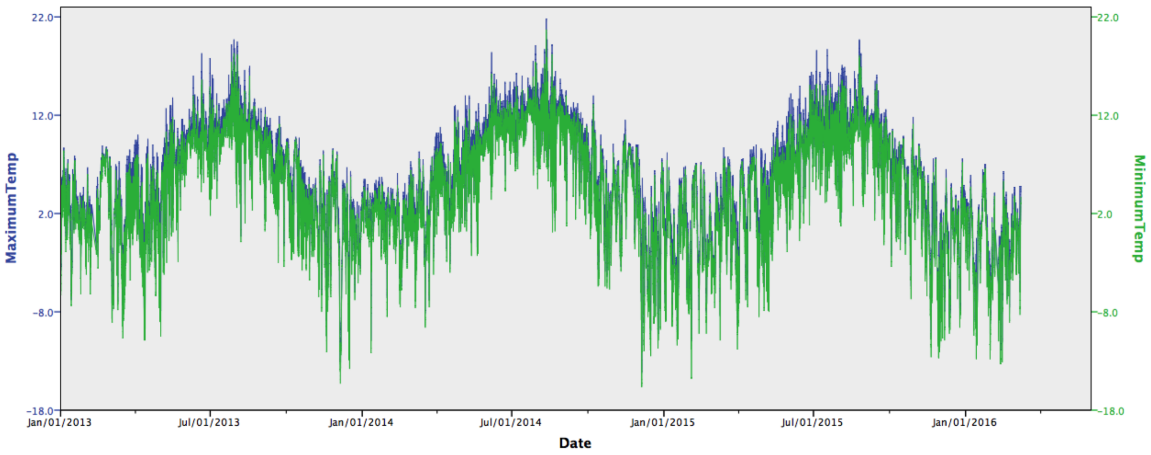

Figure 5.45 shows a comparison between the z-scores for the Iceland horse hair and z-scores calculated for the Eyrarbakki monthly mean temperature record, from July 2014 to July 2016. As with the z-score comparisons for Oxfordshire, Exmoor and Shetland, the seasonal amplitude for the temperature and the amplitude of the Icelandic horse hair data is equivalent.

Figure 5.45: Z-scores for Iceland horse hair plotted against z-scores for monthly mean temperature from Eyrarbakki, Iceland.

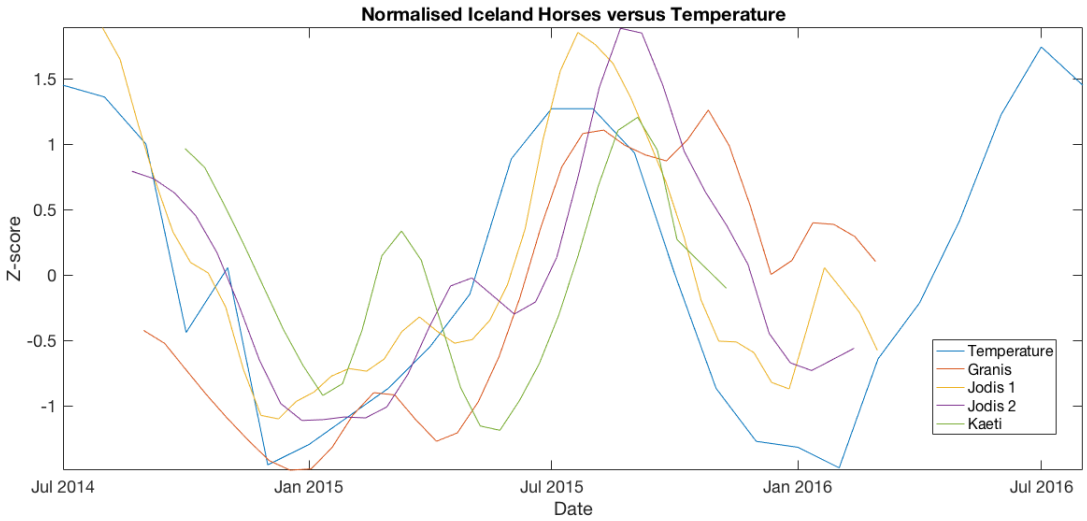

Monthly total precipitation values from Eyrarbakki are shown in Figure 5.46, from 2014 to 2016. The particularly dry months each year include August 2014 with a total of only 50.5mm, June 2015 with 23.4mm for June 2015 and only 8.1mm of precipitation in May 2016. These are all well below average rainfall for the months in question when comparing to the 1957-2016 climatology. October 2015 received the highest precipitation at 255.5mm, compared to a climatological October total of 145.65mm, but was followed by ten months of values below climatology, including the very low May 2016 value.

Figure 5.46: Precipitation at the Eyrarbakki meteorological station, Iceland.

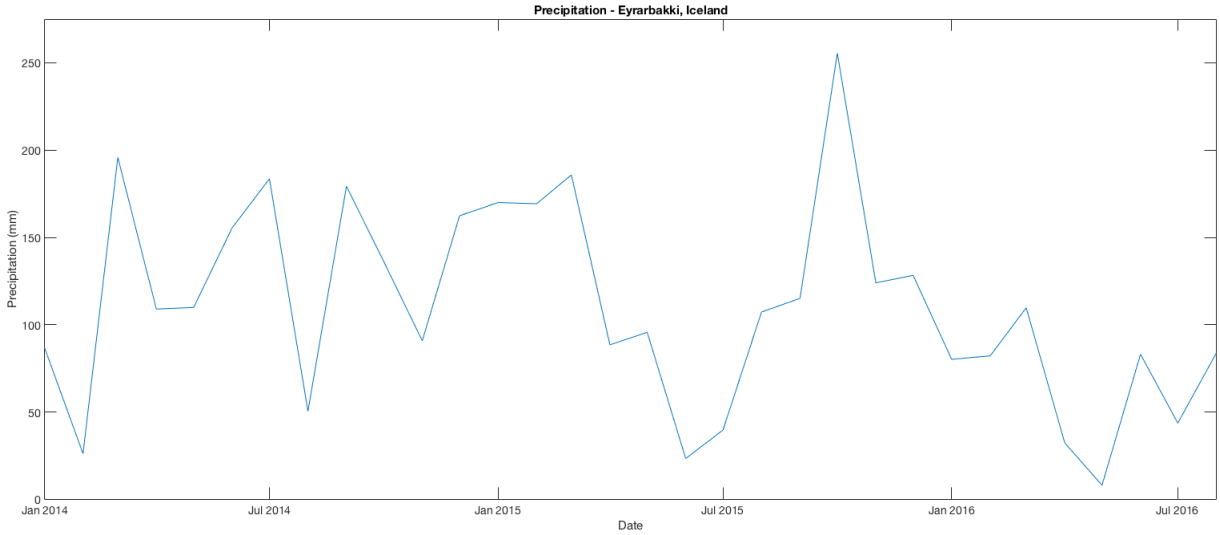

The data from Iceland show excellent consistency between the δ^{18}O within hair and the Icelandic temperature observations. Although GNIP data was not available for the Reykjavík station during 2015 and 2016, the data for 2013 and 2014 indicates that both records show annual seasonal peaks during July to September, which declines over October and into January. The May peak in monthly mean δ^{18}O values at Reykjavík is not clearly reflected within the horse hair values. The smaller peak in hair δ^{18}O coincides with a period of lower precipitation during February to April 2015. The decline in δ^{18}O values within horse hair during October is consistent with the effects of the peak rainfall event in October 2015. The subsequent deviation in the δ^{18}O decline is also consistent with drier conditions in the precipitation record from November 2015 onward, specifically the January 2016 drop in the precipitation record, which was 53.4mm drier than the January climatological average.

Figure 5.47: Reykjavík GNIP data plotted with the Icelandic horse hair data.

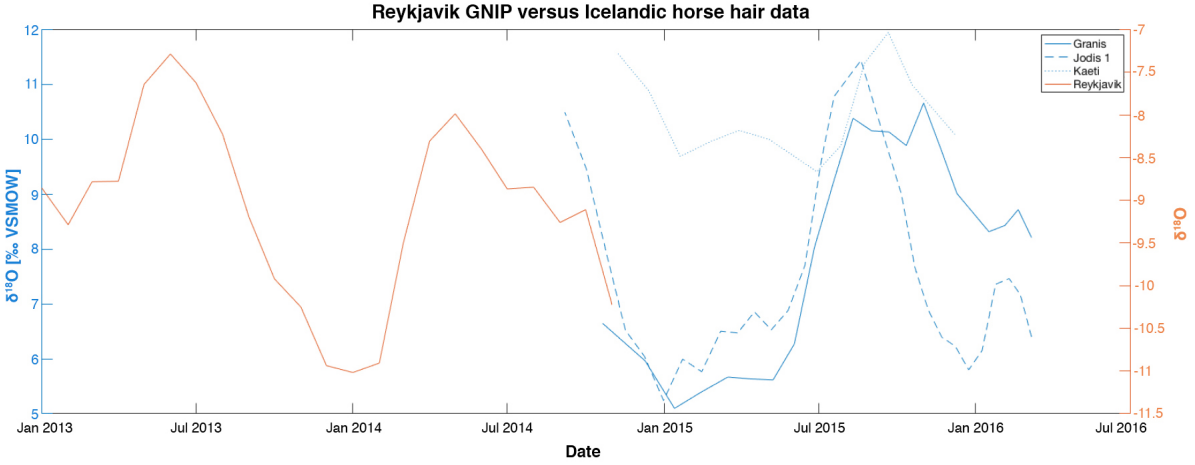

5.1.7 Statistical inter-comparison

The full results including all the final processed data shows that the Icelandic horses, had the lowest mean δ^{18}O value of 12.05‰. The ponies sampled in the Shetland Islands had an average value of 15.50‰, which was higher than the Exmoor average of 15.45‰. The Oxfordshire results had the highest average δ^{18}O at 21.79‰. A comparison of the normalised data also shows smaller data variation in the Shetland population

Table 5.7: Horse hair δ^{18}O data, expressed in ‰ with respect to V-SMOW, analysed by location, not separated into two populations by the use of the USGS42 standard. This table includes the mean δ^{18}O, standard deviation, normalised minimum value, normalised maximum value and sample size for each location.

Location	Sample Size	Mean	Standard Deviation	Min. Z-score	Max. Z-score
Iceland	82	12.05	7.28	-1.57	2.28
Shetland	52	15.50	6.99	-2.34	1.89
Exmoor	176	15.45	5.66	-2.30	2.68
Oxfordshire	143	21.79	8.77	-1.79	4.61
Total	453	16.84	8.03		

When examining the full results of the non-interpolated and interpolated data (Figure 5.48) there appears to be a δ^{18}O latitudinal gradient from Iceland to Oxfordshire, however when the use of different standards is taken into account, it is evident that this data is biased. The SPSS statistical analysis has automatically attributed the samples in the Iceland and Shetland locations without the USGS42 to be anomalous, but has not repeated this assignation to the Exmoor and Oxfordshire data (Figure 5.48a).

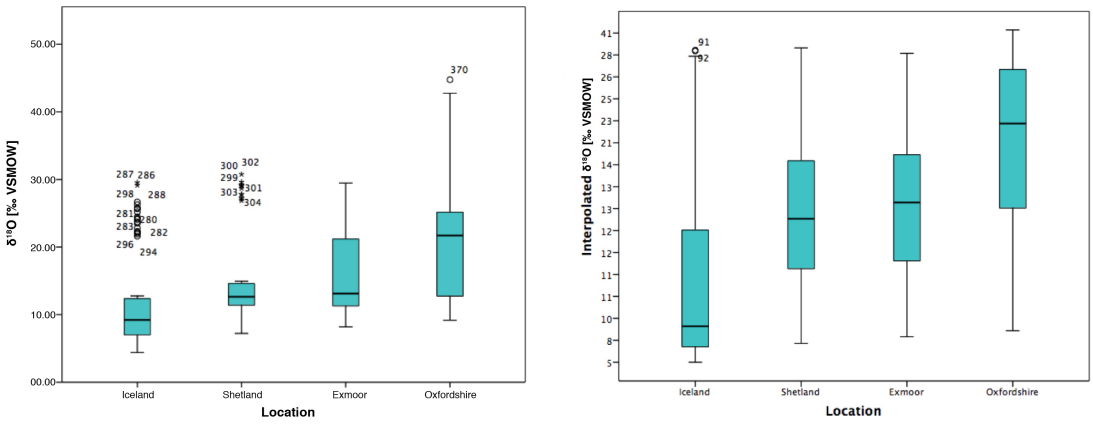

(a) (b)

Figure 5.48: δ^{18}O Boxplot results from Iceland, Shetland, Exmoor and Oxfordshire horse hairs, expressed in ‰ with respect to V-SMOW. Plot a) shows the final calibrated and smoothed data b) shows the interpolated data.

By dividing the final data into two populations, whether the USGS42 standard was used

within the analysis or not, better interpretation can be made about the δ^{18}O results. Comparison of the USGS42 versus I601 use shows a difference in the means of more than 14‰. There was also significantly more variation in the results of the samples which did not use USGS42 as a sample standard during analysis.

Table 5.8: Horse hair δ^{18}O results, expressed in ‰ with respect to V-SMOW, for all samples separated by use of USGS42 or I601 reference standards, including number of samples, minimum, maximum, mean and standard deviation.

Standard	Number samples	Minimum	Maximum	Mean	Std. Deviation
USGS42	279	4.39	17.33	11.25	2.43
I601	174	18.35	44.77	25.81	5.26

In order to examine the bias in the location data caused by the different use of standards, Table 5.9 shows the data divided into the two populations of analysis using the USGS42 or I601 standard. When comparing locations using the USGS42 population, Iceland still had the lowest mean oxygen isotope values at 8.28‰, although the Oxfordshire mean was lower than both the Shetland and Exmoor mean at 11.67‰. The population which was analysed using the I601 standard had the lowest mean in Iceland with 24.58‰, with Shetland showing the highest mean of 28.49‰.

Table 5.9: Horse hair δ^{18}O results, expressed in ‰ with respect to V-SMOW, by location for data corrected using USGS42 reference standards and data corrected not using USGS42 reference standards, including mean δ^{18}O and standard deviation.

Horse	USGS42	Mean Value	Standard Deviation
Iceland	yes	8.28	2.27
Shetland	yes	12.02	1.76
Exmoor	yes	12.30	1.68
Oxfordshire	yes	11.67	1.48
Total All	yes	11.25	2.43
Iceland	no	24.58	2.30
Shetland	no	28.49	1.20
Exmoor	no	24.62	1.81
Oxfordshire	no	26.28	6.65
Total All	no	25.81	5.26

Figure 5.49 further demonstrates the data distributions detailed in Table 5.9. Within the data calibrated using the USGS42 standard, Iceland stands out as a record that is different to the other location distributions. The other three locations appear to be fairly similar in mean and quartile ranges. The other thing to note in this plot is the large amount of variation and anomalous data within the non-USGS42 Oxfordshire data.

Figure 5.49: δ^{18}O boxplot results from Iceland, Shetland, Exmoor and Oxfordshire horse hairs divided by the inclusion or exclusion of the USGS42 standard, expressed in ‰ with respect to V-SMOW.

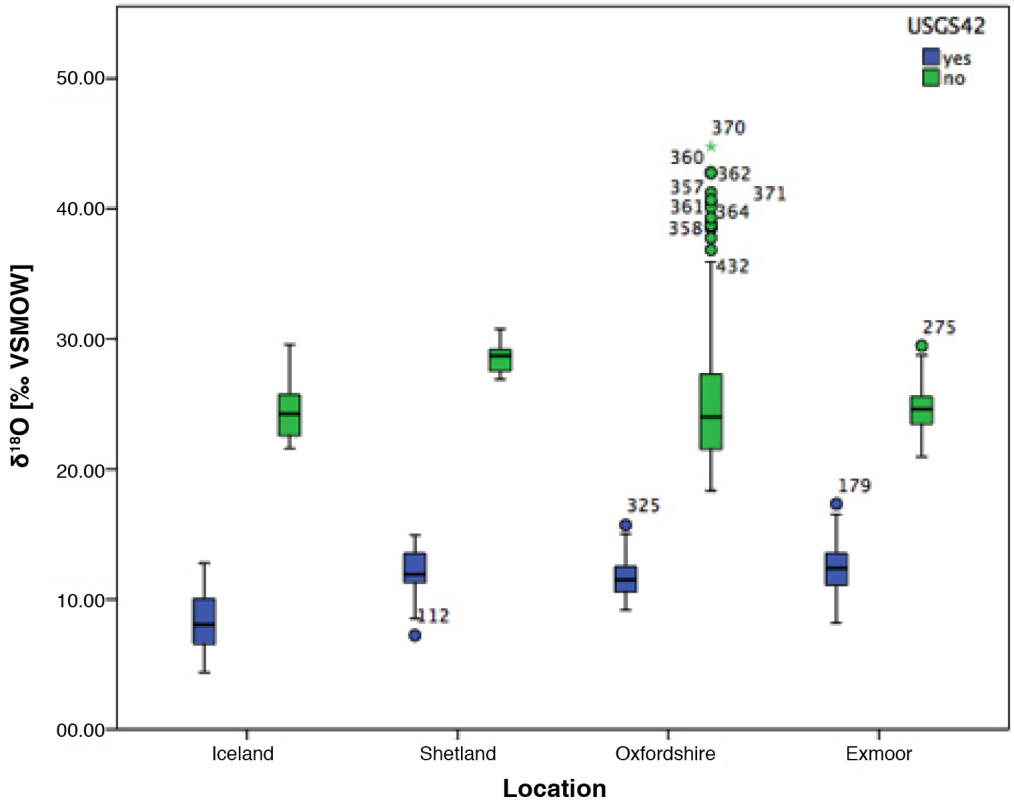

As the Figure 5.49 boxplot incorporates all of the USGS42 referenced data, the results have been biased toward the longer records in Exmoor and Oxfordshire. The Iceland data only contained one seasonal peak and trough, compared to the multiple peaks in the southern region and subsequently has under-represented Iceland within the statistical comparison. To examine the full extent of this bias, the boxplot in Figure 5.50 has been produced using only one year from each of the USGS42 referenced hairs, typically from January to January of the first year of data. The Oxfordshire data included two years of *Gem 3* data to alleviate the lack of samples referenced by the USGS42 standard.

Figure 5.50: δ^{18}O boxplot results from Iceland, Shetland, Exmoor and Oxfordshire horse hairs using a one year cycle only, expressed in ‰ with respect to V-SMOW.

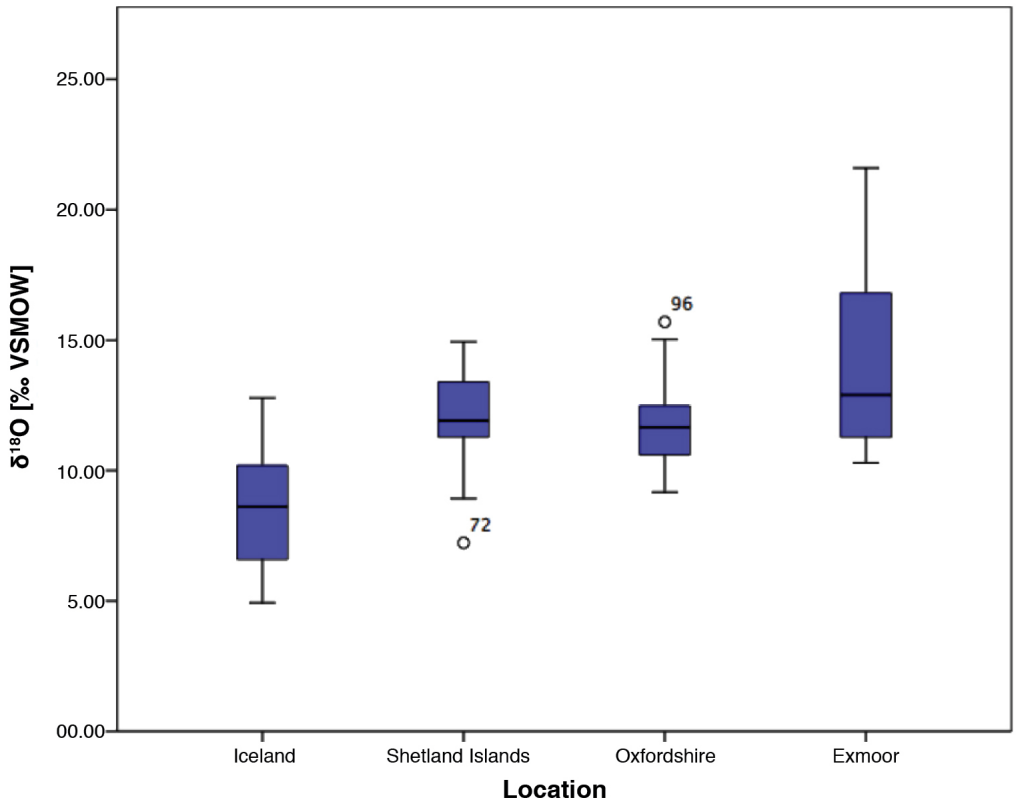

Table 5.10 shows the detailed information regarding the individual horse hair results, for USGS42 referenced data. This table also includes the age information for each horse. It is interesting to note that there is no apparent association between the age of the horse and a consistent increase or decrease in δ^{18}O. The lowest mean value was from the Icelandic horse *Granis* and the highest was from the Icelandic horse living in the Shetland Islands *Taktur*. The values within the individual horse records ranged from a minimum value of 4.39‰ to a maximum value of 17.33‰. Again, all three hair records from Iceland have lower oxygen isotope values.

Table 5.10: Horse hair δ^{18}O results by horse name, expressed in ‰ with respect to V-SMOW, for data corrected using USGS42 reference standards, including minimum, maximum, mean and standard deviation.

Horse	Age	Minimum value	Maximum Value	Mean Value	Standard Deviation
Granis	5	4.59	11.82	7.99	2.16
Jódís 1	7	4.39	12.37	7.60	2.09
Kaeti	8	8.26	12.78	10.48	1.51
Silver 1	3	8.52	14.59	11.93	1.79
Storm	3	7.23	14.94	11.57	1.86
Taktur 1	6	11.46	14.63	13.09	1.28
Taktur 2	6	11.26	13.65	12.83	1.36
Rama 1	16	8.97	17.33	12.79	1.94
Robbie 2	14	8.20	14.62	11.73	1.54
Fudge 1	18	10.30	14.97	12.70	1.29
Fudge 2	18	10.40	14.30	11.97	1.19
Gem 2	21	10.78	12.55	11.89	0.72
Gem 3	21	9.17	15.70	11.65	1.56

The horse statistics for the samples referenced with the I601 standard are shown in Table 5.11. This table includes only one Iceland, Shetland and Exmoor pony, *Jódís 2*, *Silver 2* and *Robbie 1* respectively. The remaining four horse hairs were from the Oxfordshire group, *Gem 1*, *Nutmeg*, *Tonto* and *Dessi*. The δ^{18}O values within this population ranged from 18.35‰ to 44.77‰. The I601 group also shows a far greater spread in the data than the USGS42 group.

Table 5.11: Horse hair δ^{18}O results by horse name, expressed in ‰ with respect to V-SMOW, for data corrected not using USGS42 reference standards, including minimum, maximum, mean and standard deviation.

Horse	Minimum value	Maximum Value	Mean Value	Standard Deviation
Jódís 2	21.60	29.56	24.58	2.30
Silver 2	26.89	30.77	28.49	1.20
Robbie 1	20.93	29.47	24.62	1.81
Gem 1	32.93	44.77	38.47	3.35
Nutmeg	18.71	27.58	23.00	2.40
Tonto	18.35	36.84	22.41	3.13
Dessi	23.63	28.18	25.84	1.57

As the USGS42 standard was comprised of human hair rather than benzoic acid [I601] and as calculated in Section 4.1.3, USGS42 is better representation of the true horse hair values. The following results only include values calibrated using the USGS42 standard. Table 5.12 details the mean for each horse as well as the local GNIP WISER measurement station and the respective local δ^{18}O precipitation average. The Wallingford station is the closest oxygen isotope measuring location to both the Exmoor Pony Centre and the Pigeon House Equestrian Centre in Oxfordshire and is used as a reference for both of these locations. There is a clear latitudinal difference within the GNIP measurements with the lowest values in Iceland and the highest in the southern region of the United Kingdom. These values as well as the meteorological variables summarised in Table 5.13 are used to explore the central tendencies and compare the location based hair results within the scatterplots in Figures 5.51 to 5.56.

Table 5.12: Mean δ^{18}O measurements per horse, expressed in ‰ with respect to V-SMOW.

Horse	Mean δ^{18}O (‰)	GNIP measurement location	GNIP Mean δ^{18}O value
Granis	7.99	Reykjavík	-8.13
Jódís	7.60	Reykjavík	-8.13
Kaeti	10.48	Reykjavík	-8.13
Silver 1	11.93	Altnabreac	-8.00
Storm	11.57	Altnabreac	-8.00
Taktur 1	13.09	Altnabreac	-8.00
Taktur 2	12.83	Altnabreac	-8.00
Rama 1	12.79	Wallingford	-6.74
Robbie 2	11.73	Wallingford	-6.74
Fudge 1	12.70	Wallingford	-6.74
Fudge 2	11.97	Wallingford	-6.74
Gem 2	11.89	Wallingford	-6.74
Gem 3	11.65	Wallingford	-6.74

Table 5.13 is a summary of the local meteorological variables, with Exmoor being the wettest location, on the western coast of the United Kingdom, closely followed by Iceland. The driest region by far is the inland location of Brize Norton, Oxfordshire, which is also the warmest of the four stations. The temperatures show a typical north-south gradient of colder to warmer within both minimum and maximum temperatures, although the difference between the minimum temperatures in Shetland, Exmoor and Oxfordshire is less than 1° .

Table 5.13: Annual mean meteorological variables at the station closest to each location.

Location	Measurement Station	Rainfall (mm)	Max. Temp. (°C)	Min. Temp. (°C)
Iceland	Eyrarbakki	1409.5	7.5	1.6
Shetland	Lerwick	1256.8	9.6	5.3
Exmoor	Liscombe	1445.2	12.1	5.8
Oxfordshire	Brize Norton	684.7	14.2	6.2

Figure 5.51 shows the a boxplot for each horse that was calibrated using the USGS42

standard. This plot shows and compares the central tendencies of the δ^{18}O results separated by individual horses.

Figure 5.51: Boxplot showing the δ^{18}O values (horizontal axis) for each horse, expressed in ‰ with respect to V-SMOW.

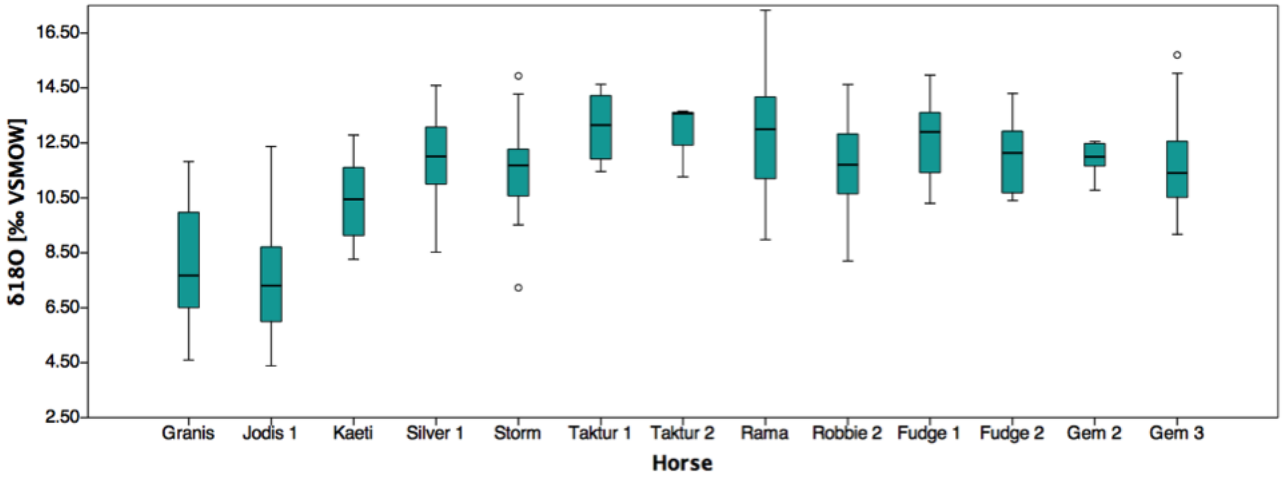

Figures 5.52, 5.53, and 5.54 show the average δ^{18}O values for each horse location plotted against the average annual rainfall totals, temperature and average local GNIP δ^{18}O values for the corresponding locations, respectively. These plots also show the 95% confidence intervals for the δ^{18}O values of the horse hair at each location. These confidence intervals were calculated by adding the mean to the t-score multiplied by the standard error for each location.

Figure 5.52: Average δ^{18}O values of hair (horizontal axis), expressed in ‰ with respect to V-SMOW, for each location plotted against the average annual rainfall totals for each location (vertical axis). The bar lines show the 95% confidence intervals for the δ^{18}O of horse hair for each location.

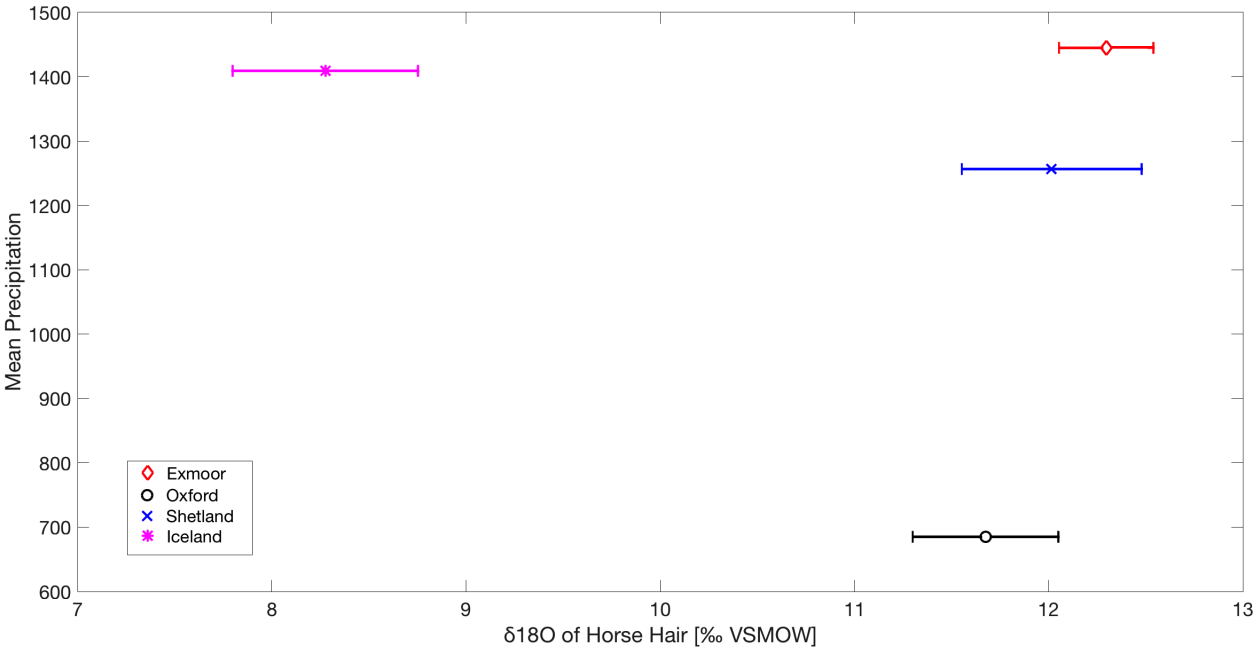

Figure 5.52 shows Iceland as an outlier, with high rainfall and the lowest δ^{18}O values, and although Oxford has similar δ^{18}O values to Shetland and Exmoor, it receives the least amount of precipitation. The scatterplot in Figure 5.53, showing minimum and maximum temperatures, again has Iceland as an outlier, with the lowest minimum temperature and lowest δ^{18}O values. examining the maximum temperature at each location. The other three locations are spread out by increasing latitude with increasing temperature, with Shetland showing higher δ^{18}O values. and a much lower average minimum temperature.

Figure 5.53: Average δ^{18}O values (horizontal axis), expressed in ‰ with respect to V-SMOW, for each location plotted against the temperature ranges for each location, including markers for the minimum and maximum temperatures (vertical axis). The bar lines show the 95% confidence intervals for the δ^{18}O of horse hair for each location.

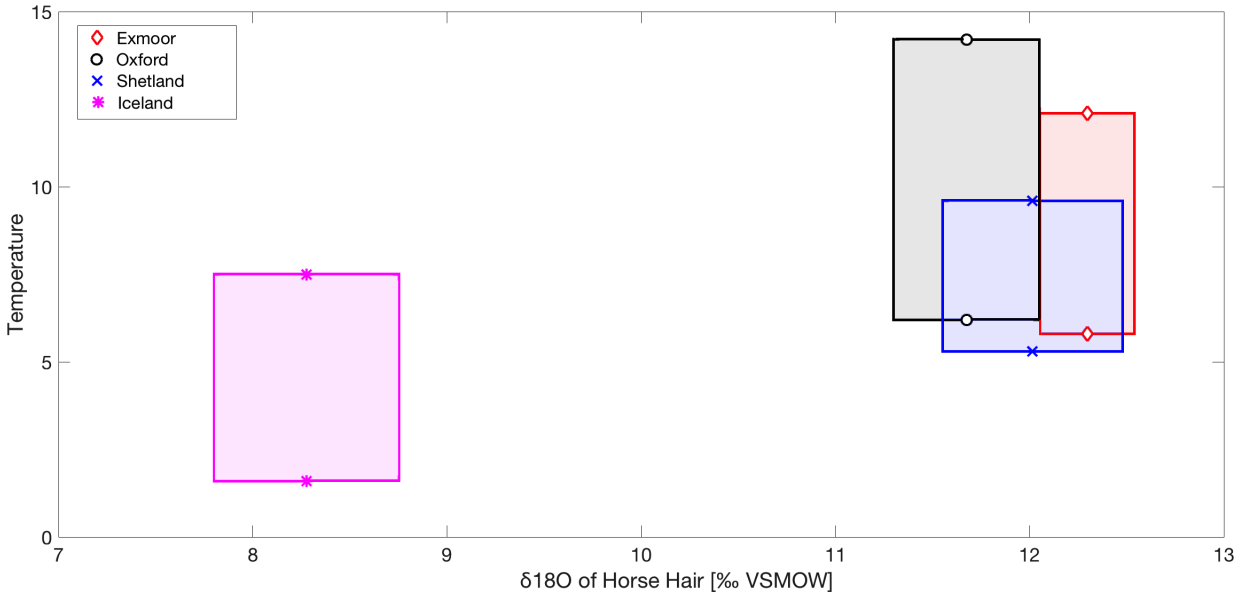

The local precipitation isotopes group Exmoor and Oxfordshire, with the lower precipitation δ^{18}O values in Shetland and Iceland, separating these locations.

Figure 5.54: Average local GNIP δ^{18}O values (horizontal axis), expressed in ‰ with respect to V-SMOW, for each location plotted against the average horse hair δ^{18}O values for each location (vertical axis). The bar lines show the 95% confidence intervals for the δ^{18}O of horse hair for each location.

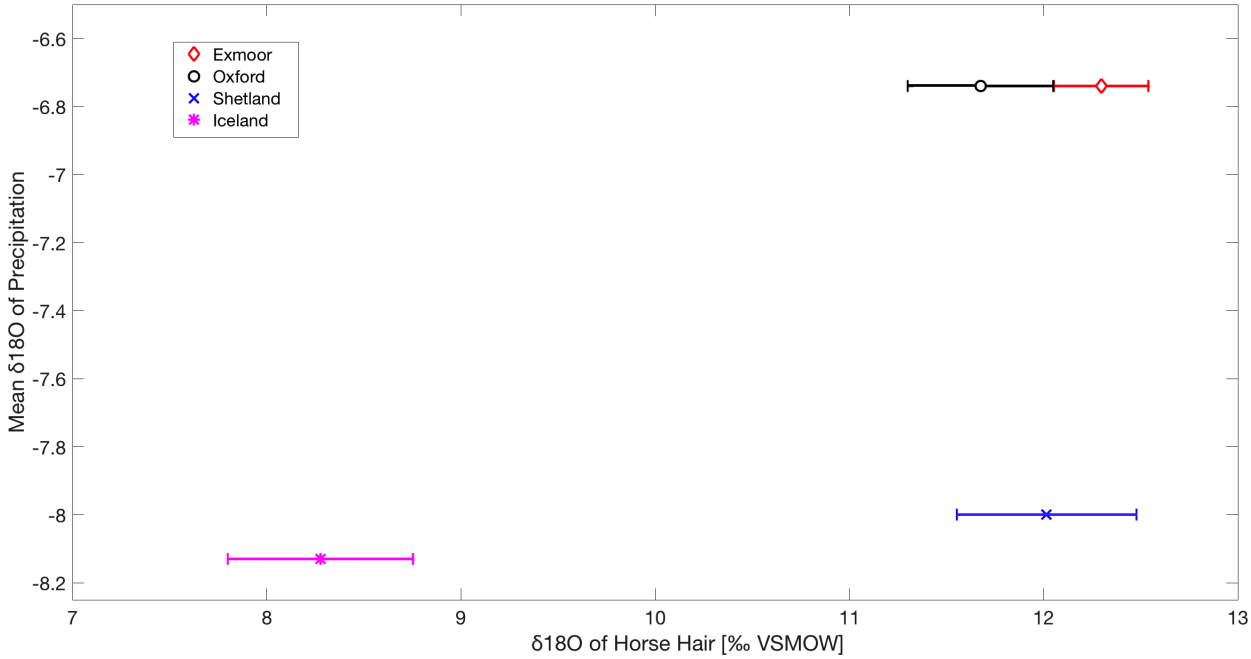

The results of an Analysis of Variance (ANOVA) statistical test, conducted in Matlab using the Tukey-Kramer significant difference procedure for the USGS42 inclusive individual horse data, showed that the mean δ^{18}O values of Iceland was statistical different to the mean values for Shetland, Oxfordshire and Exmoor, to the 99% confidence level. This means that the δ^{18}O values of horse hairs from Iceland are not part of the same statistical population, and that there is some effect on the δ^{18}O values within horse hair. Table 5.14 shows the results p-values obtained during the ANOVA testing for the individual comparisons between locations, and demonstrates the difference between the Icelandic hair population. These results are consistent with the visual analysis of the location populations shown in the Figure 5.50 boxplot.

Table 5.14: P-value comparison between individual horse hair locations.

Location 1	Location 2	P-value
Iceland	Shetland	3.7683e-09
Iceland	Oxfordshire	3.7683e-09
Iceland	Exmoor	3.7683e-09
Shetland	Oxfordshire	0.8209
Sheltand	Exmoor	0.8607
Oxfordshire	Exmoor	0.2290

Fast Fourier Transforms

Due to the short length of the horse hair records, fast Fourier transform (FFT) analysis was not feasible for determining seasonal or climate teleconnection signals. In order to lengthen the record for this analysis, this study identified the annual cycles of each hair within the previous results discussions, from using growth rate converted date data. This annual cycle was isolated for each hair and looped in order to create a ten year record. This ten year record could then be analysed using a Matlab FFT in order to examine the common frequencies within the horse hair data. The two Shetland Island Horse records for *Taktur* as well as the *Gem 2* records were too short for the identification of a full annual cycle in order to provide a looped record, and were subsequently not used for FFT analysis. Figure 5.55 shows an example of the FFT plot for the Icelandic horse *Kaeti*.

Figure 5.55: Results of the fast Fourier transform conducted on the Icelandic Horse data for *Kaeti*.

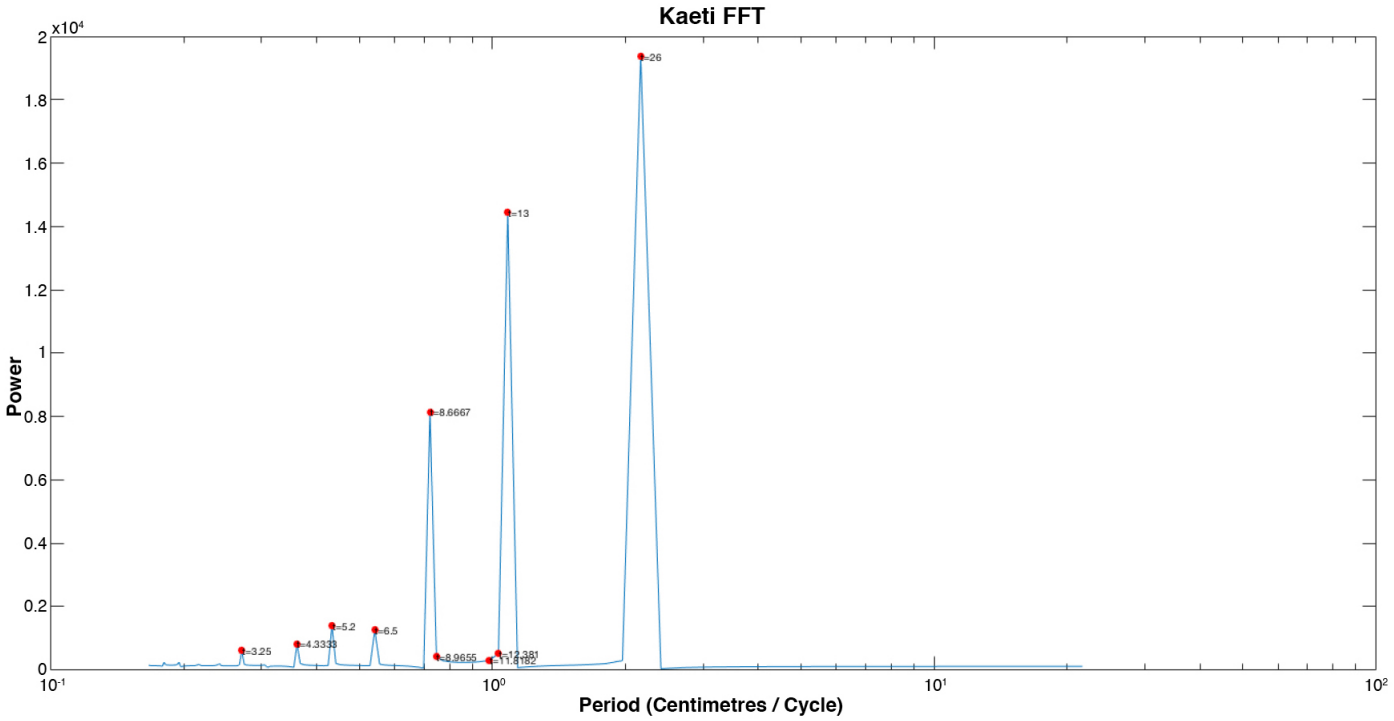

The strong common signals (with a power greater than 1) displayed by the FFT of each horse are displayed in Table 5.15, including a day/cycle conversion using the growth rate of each horse (rounded to the nearest day).

Table 5.15: Frequency signals within the FFT looped horse hair, in centimetres/cycle, and the day conversion.

Horse	Signal (cm/cycle)	Days/cycle
Granis	25.1	392
Jódís 1	15.1, 30.2	199, 397
Jódís 2	12, 24	190, 381
Kaeti	13, 26	191, 382
Silver 1	12.3, 24.6	212, 424
Silver 2	23	377
Storm	14.6, 29.2	190, 379
Rama 1	24.9	377
Robbie 2	9.9, 19.8	194, 388
Fudge 1	21.9	391
Fudge 2	18	367
Gem 1	6.7, 10, 20	126, 189, 377
Gem 3	10.5, 21	198, 396
Nutmeg	4.7, 6.4, 9.6, 17.1	96, 131, 196, 349
Tonto	5.7, 11.7, 22.3	95, 195, 372
Dessi	22.2	383

Carbon and Nitrogen

Some carbon and nitrogen analysis was conducted on Exmoor pony hair collected prior to the sampling on the 7th March. The horses sampled and analysed include *Dylan*, *Fudge*, *Percy*, *Robbie* and *Walnut*. The analysis and reference standards are described in the earlier Methodology section and the results are shown in Figures 5.56 and 5.57. The individual horse sample results group well, and the mean values provide an indication that dietary variation between individuals was minimal between the horses.

Figure 5.56: Results of the horse hair carbon and nitrogen isotope analysis, expressed in ‰ .

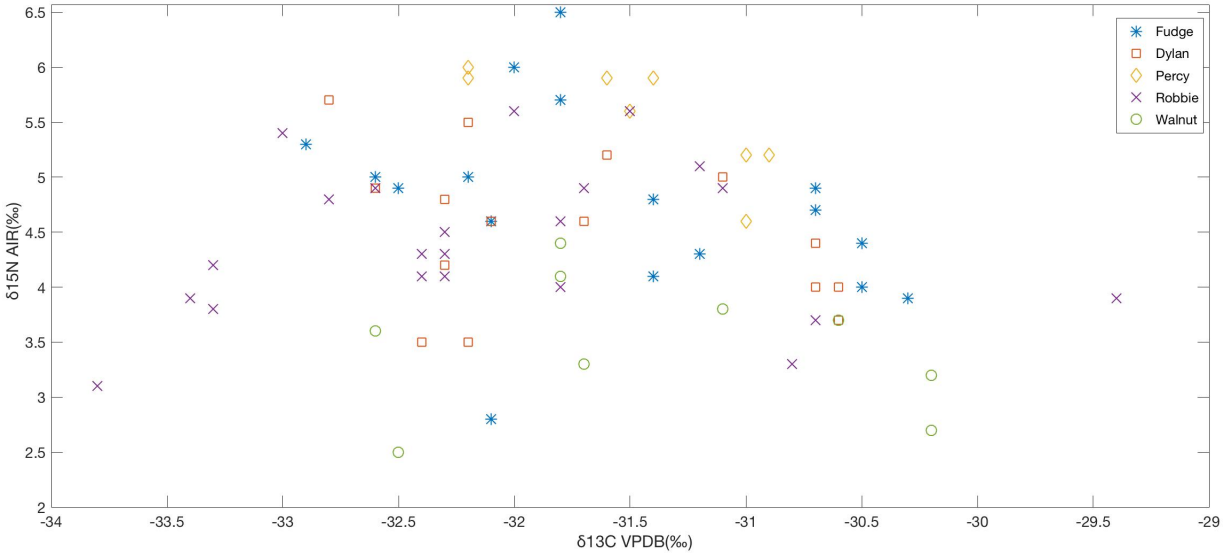

Figure 5.57: Mean carbon and nitrogen values, expressed in ‰ .

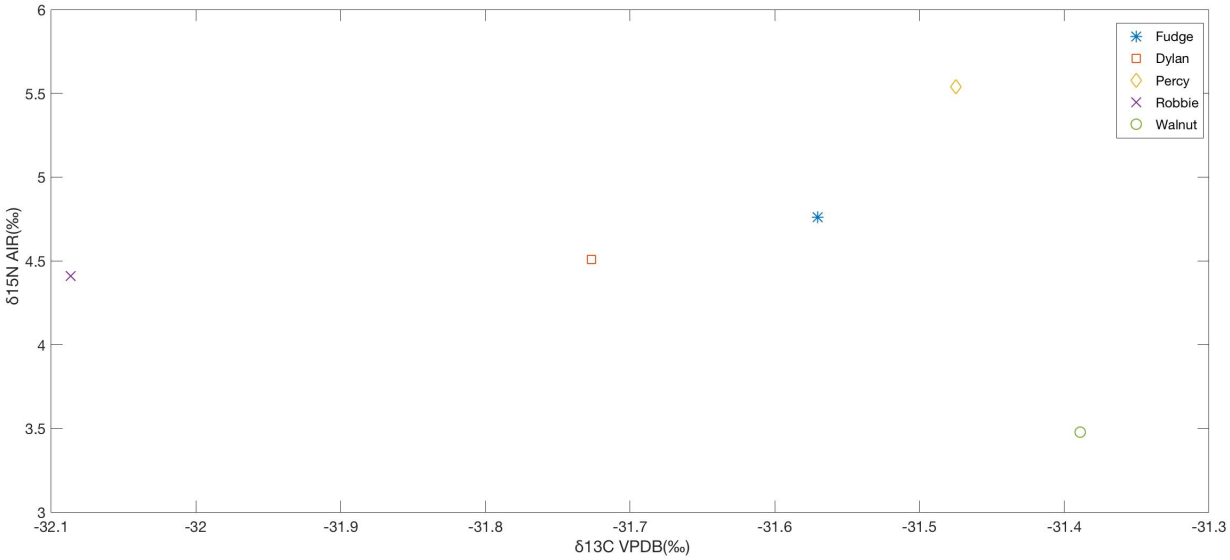

5.2 Discussion

The results from sequentially sampling horse hair from four independent pony centres in Iceland, Shetland Islands, Oxfordshire and Exmoor have been difficult to reconcile with the hypothesis that the temperature gradient and latitudinal depletion gradient of water isotopes should be evident in horse hair δ^{18}O values. The boxplots shown in Figure 5.48 show a latitudinal gradient consistent with the hypothesis, however as discussed earlier 174 samples were removed from this data pool in order to account for bias caused by changes in reference standard used during analysis.

The issue of the large spread in values associated with the use of the USGS42 and USGS43 hair standards versus the I601 and I602 benzoic acid standards has been an interesting outcome of this study. It was not expected that a disparity to the scale of 10-15‰ would occur. The values were crossed checked to examine what sample dates coincided with the difference in values, but the USGS42 exclusion was the only common factor for the higher values [around 25‰]. Corrections were initially applied to shift the higher values closer to the expected, using an average displacement calculated from the location mean, however it was thought that this would be introducing artificiality into the values, especially when then comparing differences within locations. It was therefore decided that the most appropriate method for dealing with these two distinct data populations, would be to only compare normalised data within each locations, and include on the USGS42 corrected values when comparing across the four locations.

The revised boxplot, split by the reference standard used, did not clearly demonstrate a latitudinal gradient from the southern locations in Exmoor and Oxfordshire to the Shetland Islands.

Results from the rainfall comparison with the mean δ^{18}O values in horse hair (Figure 5.52) showed Iceland as an outlier, with high rainfall and the lowest δ^{18}O values, and although Oxford has similar δ^{18}O values to Shetland and Exmoor, it receives the least amount of precipitation. Although this does not support the expected effect of a latitudinal gradient on the oxygen isotope values, these results reflect the pattern of groundwater isotope distribution shown in Figure 3.11, within the earlier discussion on the hydrology of the United Kingdom (Section 3.3.3). These results also reflect the rainfall amount effect discussed in Section 1.2. South-westerly air masses moving over the United Kingdom result in high rainfall over the western coast, including Exmoor (see Figure 3.7 within the climatology Section 3.2.1). This causes increased depletion of ^{18}O values toward the interior of the United Kingdom and the Oxfordshire region, and can be seen within the results shown. With similar values in Oxfordshire and Shetland, specifically in the revised boxplot in Figure 5.50, the data indicate similar effect of latitude and rainfall amount. The increase in latitude results in decreased values in Shetland and Iceland compared to Exmoor, however the decreased rainfall amount in Oxfordshire has resulted in similar values between Oxfordshire and the Shetland Islands.

The IAEA GNIP WISER δ^{18}O seasonal differences in mean values, the local minimum and maximum temperature amplitudes and the seasonal amplitudes in the hairs of each location were all presented in the result section. These values were examined for the purpose of exploring the hypothesis that 'the amplitude of the seasonal temperature cycle is reflected in the oxygen isotope variation within horse hair'. Comparing the amplitudes in the standardised Figures 5.23, 5.30, 5.38 and 5.45, it can be interpreted that the temperature amplitudes are similar to the horse hair amplitudes. It it clear from the rainfall comparison that there is significant influence between rainfall amount and

the δ^{18}O values of hair, which is consistent with basic isotopic theory and the literature findings discussed within the earlier chapters.

Results of the fast Fourier transform analysis on the looped horse hair data demonstrated that there are strong seasonal cycles in every hair. These results support and augment the findings of the amplitude comparison for the examination of the seasonal signals within biological δ^{18}O values in horse hair.

One hair from the Shetland Islands showed a lack of correlation with the meteorological data as the sequential sample progressed back in time. This manifested in an unexpected trough occurring in August rather than the typical winter January date. The potential cause of this difference could be interpreted to be a change in growth rate within the individual. Perhaps the pony experienced biological or environmental stress, causing temporary retardation of hair growth. or a biological cause. Additionally, all hairs are shown against the median date, within a calculated date range that was extrapolated using the individual growth rates and recorded centimetre sample location. Small changes in growth rate along the length of the hair could potentially cause errors in the date assignment of samples toward the tail end of the hair (dates furthest from the sampling date). A small error in the growth rate calculation could also potentially compound the inaccuracy of date assignments toward the tail end samples.

When considering the results of the sample precision examination, testing the homogenised samples of the *Rama* hair, the values shown have a maximum sampling error of $<0.5‰$. Examinations of multiple hairs over multiple sampling excursions, from single individuals (including *Robbie*, *Fudge*, *Gem*, *Silver* and *Jódís*) show that there is significant variation when sequentially analysing single hairs. However, when this noise is smoothed or normalised, examination of seasonal trends, meteorological influences and extreme

climate events within the hair is possible.

Another interesting and unexpected result from this study was observed when calculating the individual growth rate. A division between the northern and southern locations was evident when examining the calculated rates of hair growth. The growth rates at the two northern horse locations had a difference of only 0.002cm/day, at an average of 0.068cm/day in Iceland and an average of 0.066cm/day in the Shetland Islands. Both two southern locations in Exmoor and Oxfordshire had a calculated average growth rate of 0.054cm/day. These results have also shown that there are differences observed in the growth rates of different hairs within the same individual, which is consistent with the results of research discussed earlier, conducted by Cerling et al. (2006). With a small sample size, these values were not significant, however it would be interesting to repeat this work with a larger sample size. These result may provide for interesting further examinations into the potential effects of temperature on horse hair growth, and whether northern horse breeds naturally have faster growing hair in order to account for harsher climates.

6. Ice Core and Dendroclimatological Research Study

6.1 Results

This chapter describes the results from the new North Greenland Ice Core 2 sampling and analysis conducted in Copenhagen, Denmark and Reno, U.S.A. and the Desert Research Institute. It also compares a new dataset provided by the the Leverhulme-funded collaboration between Swansea University and the University of Oxford, entitled 'New Tools for Science-based Archaeology: Isotope-supported Dendrochronology'. This study was granted use of this unpublished master chronology dataset of δ^{18}O values for the purpose of direct comparison to the new high-resolution NGRIP2 dataset. The results of the analysis of these two new datasets is shown in the following sections.

Section 6.1.1 introduces the NGRIP2 results, with Section 6.1.2 drawing comparison between NGRIP1 and existing ice core records. Section 6.1.3 shows the results of the UK tree ring master δ^{18}O data, and Section 6.1.4 analyses the differences between the NGRIP2 and the tree ring δ^{18}O values. Section 6.1.5 explores the century averages for each dataset. Section 6.1.6 shows the comparison between the amalgamated NGRIP dataset and the tree ring values, and Section 6.1.7 delves further in the differences between these datasets during anomalous climate periods. Section 6.1.8 examines the potential influences and forcings on the tree ring and ice core δ^{18}O records, with the final Section 6.1.9 showing the wavelet analysis results for these datasets.

6.1.1 NGRIP2

Post-analysis processing of the new high-resolution NGRIP2 δ^{18}O record required agreement of the new independent age-scale chronology between the Desert Research Institute (DRI) and the Centre for Ice and Climate in Copenhagen. This chronology was developed using contemporaneously measured sulfur concentrations with the NEEM-2011-S1 volcanic record, as well as multi-parameter annual-layer counting (McConnell et al., 2018). Subsequent evaluation of the chronology was conducted by the DRI team using the ^{10}Be values of the GRIP core as well as the IntCal13 ^{14}C record.

Although NGRIP1 and NGRIP2 were parallel cores, sampled twenty meters apart, the procedure for ice core age scale determination for the past 2500 years has evolved in the time period between the analysis of NGRIP1 and NGRIP2 (Sigl et al., 2015). This means that the age scale used for NGRIP1 in the original publications is up to 7 years different to the NGRIP2 age scale used in this study (McConnell et al., 2018). Volcanically synchronised match-points were therefore used for comparisons between NGRIP2

and the NGRIP1 and GRIP ice core records within the following results.

It should be noted that although back diffusion corrections are a common stage in the analysis process of ice core research, diffusion effects do not have a significant influence beyond an annual scale. This is due to diffusion effects not occurring across the annual peak boundaries or gradient reversal. Subsequently, back diffusion corrections have not been deemed necessary for the following analysis. An additional note regarding the post-analysis processing is that the annual average data was filled by using interpolated monthly calculated values within the NGRIP2 record.

Figure 6.1 shows the results for the full annual NGRIP2 δ^{18}O record analysed for this thesis, from 1235B.C. to 1262A.D.

Figure 6.1: Full NGRIP2 ice core δ^{18}O dataset plotted against year (A.D.).

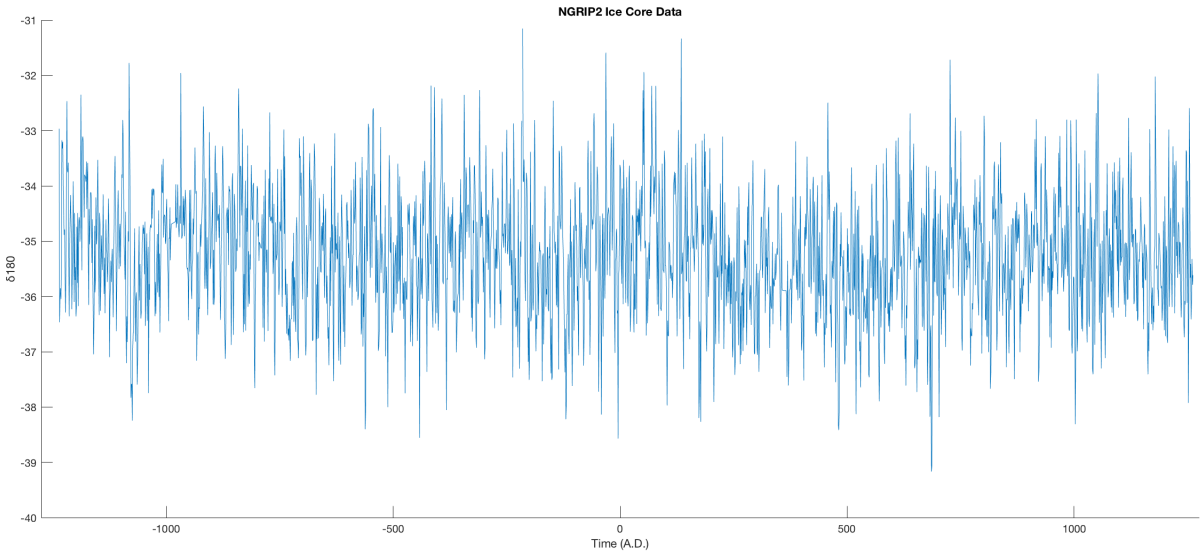

Table 6.1 details the actual values of the full annual NGRIP2 record. The standard deviation was calculated to be 1.10‰, and the total data range was 12.85‰.

Table 6.1: NGRIP2 data.

Sample Size	Min. value	Max. Value	Mean Value	Median Value	Standard Deviation
2498	-39.17	-26.32	-35.24	-35.24	1.10

6.1.2 NGRIP2 comparison to existing ice core records

The map in Figure 6.2 shows the locations of the ice cores discussed within this section (Vinther et al., 2008; Kaufman et al., 2009; Seierstad et al., 2014; Weißbach et al., 2016). The northern most core was the Agassiz A79, with Dye3 at the lowest latitude. A79 was also the western most core, and Renland was the furthest east.

Figure 6.2: Sampling sites for the Greenland ice cores, adapted from Vinther et al. (2008); Kaufman et al. (2009); Seierstad et al. (2014); Weißbach et al. (2016).

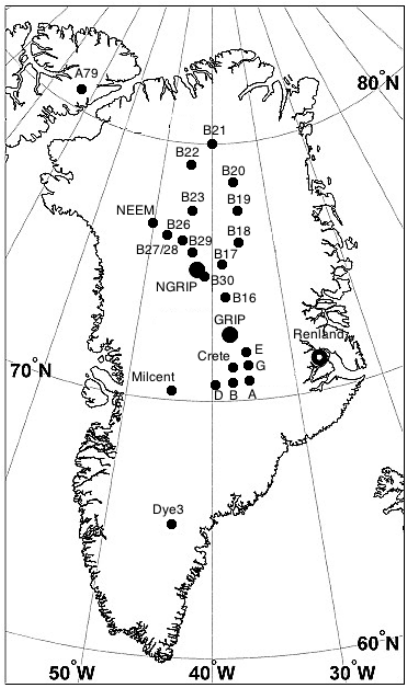

Table 6.2 shows detailed results gathered for existing ice core data, from several published datasets, including Vinther et al. (2008); Kaufman et al. (2009); Seierstad et

al. (2014); Weißbach et al. (2016). This table shows the ice core identifier, minimum δ^{18}O values, maximum δ^{18}O values, mean δ^{18}O values, standard deviations and the time period of the δ^{18}O sampling.

Table 6.2: Ice core record comparisons from (1) Kaufman et al. (2009), (2) Vinther et al. (2010) and (3) Weißbach et al. (2016), listed geographically from north to south.

Ice Core	Minimum	Maximum	Mean	Standard Deviation	Time Period
A79[1]	-31.54	-26.17	-28.30	0.87	0 - 1995A.D.
B21[3]	-38.30	-30.40	-34.51	1.27	1372 - 1994A.D.
B22[3]	-39.10	-29.80	-34.43	1.33	1372 - 1994A.D.
B20[3]	-39.40	-30.70	-35.19	1.40	775 - 994A.D.
B23[3]	-42.10	-32.20	-35.90	1.24	1023 - 1994A.D.
B19[3]	-39.40	-31.30	-35.45	1.32	753 - 1953A.D.
B26[3]	-37.20	-29.40	-33.86	1.25	1505 - 1995A.D.
B28[3]	-38.16	-30.77	-34.61	1.45	1195 - 1995A.D.
B27[3]	-38.30	-27.20	-34.43	1.27	1195 - 1995A.D.
B27/B28[3]	-38.30	-27.20	-34.47	1.24	1195 - 1995A.D.
B18[3]	-41.50	-31.80	-36.55	1.24	874 - 1993A.D.
B29[3]	-39.20	-31.60	-35.65	1.16	1471 - 1995A.D.
B17[3]	-40.10	-33.90	-37.04	1.08	1363 - 1993A.D.
NGRIP1[1]	-40.11	-30.72	-35.36	1.14	0 - 1995A.D.
B30[3]	-38.50	-31.50	-35.40	1.09	1471 - 1995A.D.
B16[3]	-40.60	-33.10	-37.07	.98	1470 - 1993A.D.
GRIP[2]	-41.24	-35.09	-38.32	1.27	551 - 1979A.D.
SiteE[2]	-43.61	-33.63	-38.28	1.99	1778 - 1970A.D.
Renland[2]	-31.24	-25.07	-28.33	1.24	1778 - 1970A.D.
SiteG[2]	-42.46	-32.43	-37.74	1.90	1778 - 1970A.D.
Crete[2]	-42.14	-33.25	-36.99	1.72	552 - 1973A.D.
SiteA[2]	-41.40	-31.86	-36.03	1.86	1778 - 1970A.D.
SiteB[2]	-41.75	-31.62	-36.29	1.73	1778 - 1970A.D.
SiteD[2]	-44.24	-31.32	-35.62	1.95	1778 - 1970A.D.
Milcent[2]	-38.57	-28.14	-32.34	1.89	1778 - 1970A.D.
DYE-3[1]	-31.68	-25.06	-27.88	0.91	0 - 1995A.D.
DYE3-71/79[2]	-31.72	-26.38	-28.91	1.08	551 - 1978A.D.
DYE3-4B[2]	-32.31	-25.24	-28.99	1.21	1551 - 1978A.D.
DYE3-18C [2]	-32.97	-26.49	-29.50	1.21	551 - 1978A.D.
DYE3-20D [2]	-33.28	-26.30	-29.37	1.19	551 - 1978A.D.

The results of Table 6.2 show that the Agassiz and DYE3 cores, from the Kaufman et al. (2009) dataset, had the least amount of variability, with standard deviations of 0.87 and 0.91 ‰ respectively. The greatest variability was found in SiteE, from the Vinther et al. (2010) data, with 1.99‰. The lowest minimum δ^{18}O value was shown in SiteD, with -44.24‰ , and the highest maximum δ^{18}O value within the DYE3 core, at -25.06‰.

The mean values for each of the cores are shown graphically in Figure 6.3. The highest averages were shown for the A79, Renland and DYE3 cores, towards the coastal areas of Greenland. GRIP and SiteE had the lowest values, toward the summit of the Greenland ice sheet.

Figure 6.3: Sampling sites for the Greenland ice cores showing the average δ^{18}O values for each sampling location, adapted from Vinther et al. (2008); Kaufman et al. (2009); Seierstad et al. (2014); Weißbach et al. (2016).

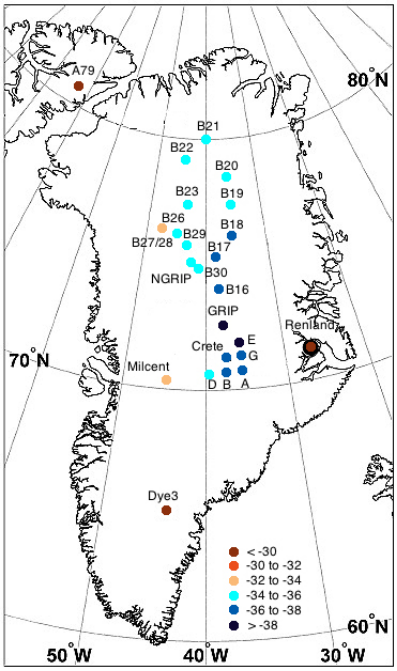

NGRIP compilation

This section details the creation of the NGRIP compilation dataset, used predominantly in the following sections for comparisons between NGRIP and other datasets. This NGRIP dataset is an amalgamation of the NGRIP1 and NGRIP2 ice core records, with NGRIP1 having been transferred and checked against the NGRIP2 age-depth scale. The amalgamation process used the NGRIP2 data up until and including 1261A.D., with NGRIP1 data used from 1262A.D. onwards. In order to confirm the correct transfer point [1262A.D.] within the NGRIP1 chronology, multiple linear regression equations between age-depth match points were used to convert the NGRIP1 data onto the NGRIP2 chronology.

Figure 6.4 shows the difference between the NGRIP1 and NGRIP2 δ^{18}O values during the time period of the NGRIP2 analysis. The two records indicate a difference of predominately less than 2‰, with only 8 events exceeding a 4‰ difference. Although the age scale has been adjusted, the differences shown in the figure are potentially a result of small differences in the NGRIP1 and NGRIP2 age scales during certain time periods.

Figure 6.4: The difference between NGRIP2 and NGRIP1 ice cores between 1235B.C. to 1262A.D.

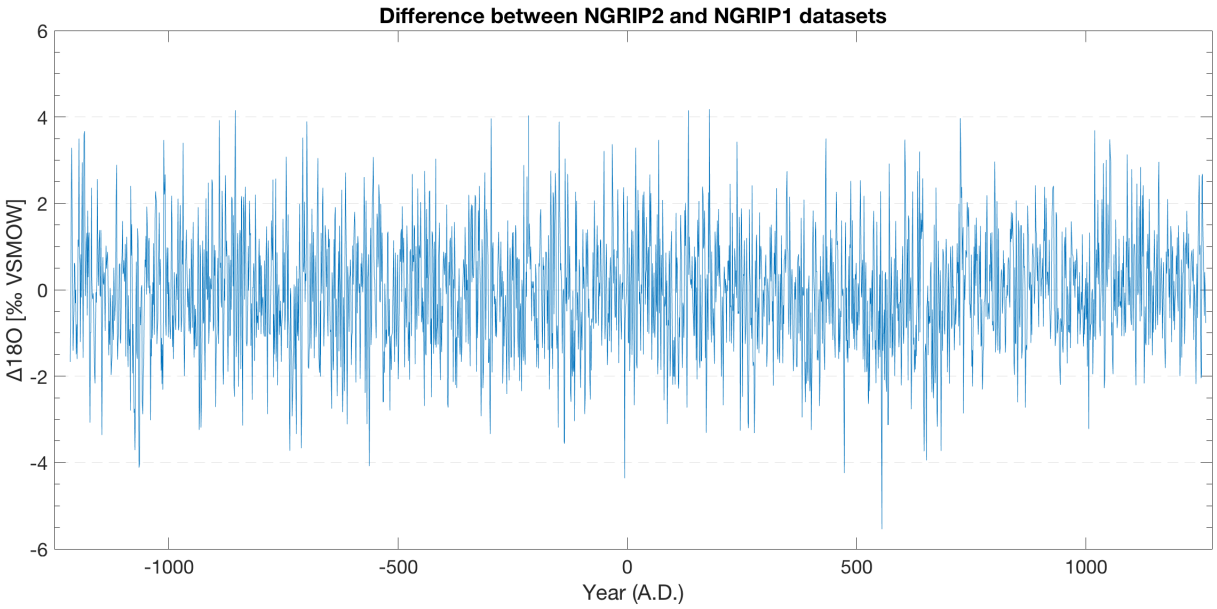

Figure 6.5 shows a 100 year moving average of the amalgamated NGRIP record.

Figure 6.5: 100 year moving average δ^{18}O values for the full NGRIP record, with the Medieval Climate Anomaly within the red section and the Little Ice Age shown by the yellow section.

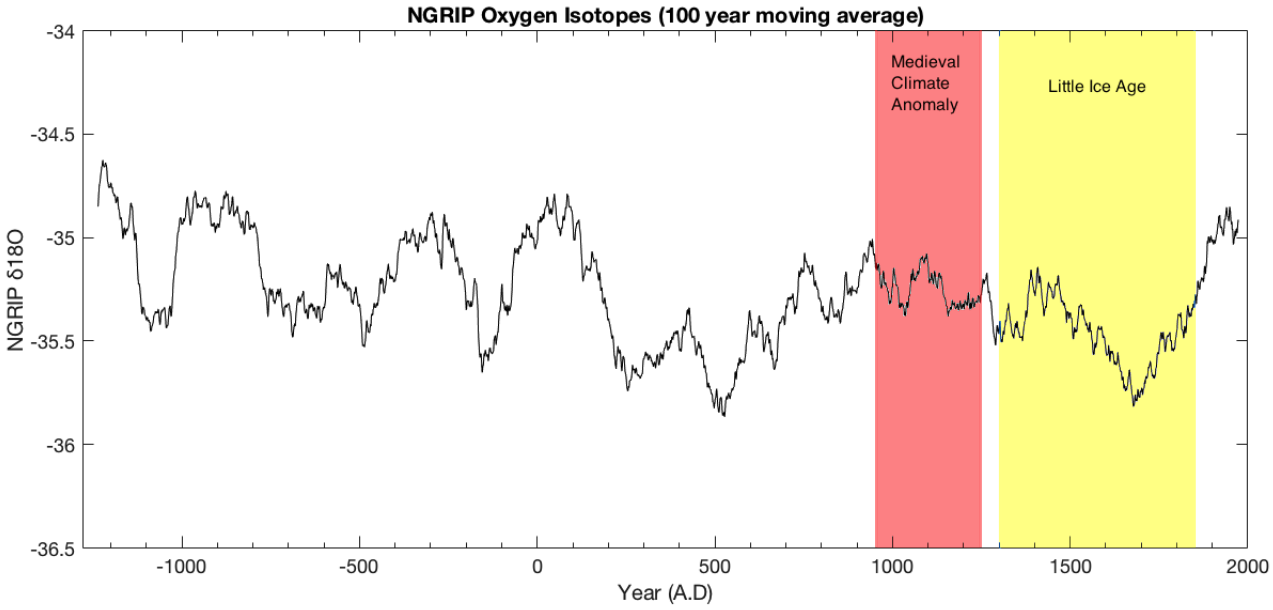

Figure 6.5 indicates that before 500A.D. there are several peaks lasting 200-300 years, which is not as evident during the later centuries. The highest values are at approximately 1200B.C. and 100 A.D., with the lowest values occurring at around 500A.D. and 1650-1700A.D.

Figure 6.6: 100 year moving average δ^{18}O values from 900A.D.-1900A.D. within the NGRIP record, with the Medieval Climate Anomaly within the red section and the Little Ice Age shown by the yellow section.

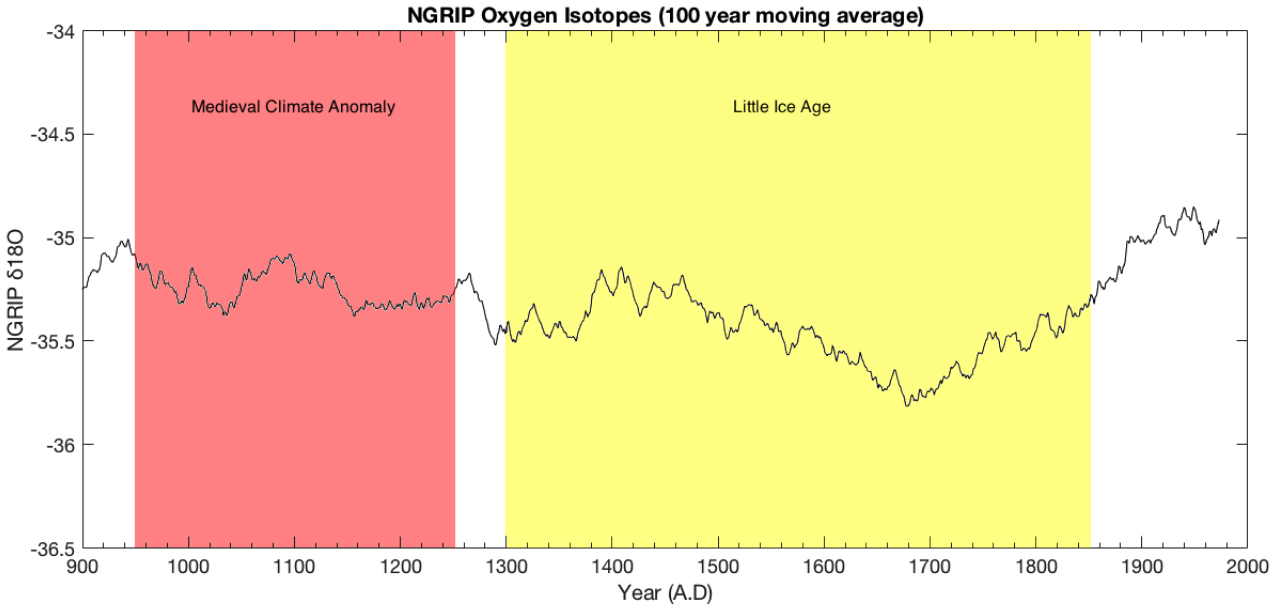

Examining the smoothed NGRIP figure for 900A.D.-1900A.D. (Figure 6.6), the trough in Figure 6.5 is shown to occur at approximately 1680A.D., and is followed by rising values into the 20th and 21st centuries. These results show higher δ^{18}O values associated with the warmer Medieval Climate Anomaly relative to the later Little Ice Age, which demonstrates a clear drop in δ^{18}O values during the 17th century.

6.1.3 Tree ring record

Figure 6.7 shows the full United Kingdom tree ring δ^{18}O record from 1200-2012A.D. This figure shows a cooling in the later part of the record, from approximately 2000A.D. There was a sharp increase at 1278A.D., to 31.60‰ with a minimum value of 27.41‰ following soon after at 1294A.D. Additionally, there was a decreasing trend from just

prior to 1600 to approximately 1630A.D.

Figure 6.7: Full tree ring δ^{18}O values plotted against Year (A.D.).

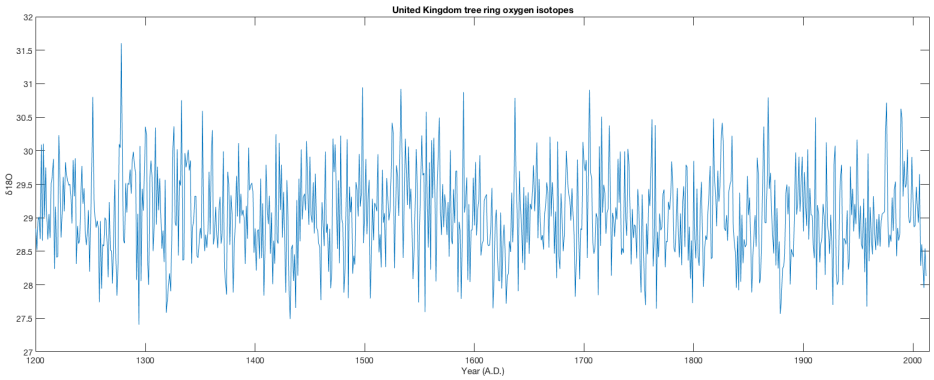

Table 6.3 details the minimum value at 1294A.D., the maximum value at 1278A.D., the average and the standard deviation. The variability in the tree ring oxygen isotope record was relatively small, with a standard deviation of 0.67‰.

Table 6.3: Tree ring data.

Minimum value	Maximum Value	Mean Value	Standard Deviation
27.41	31.60	29.04	0.67

6.1.4 Tree ring comparison to NGRIP2

The full NGRIP2 data range, including the interquartile range was much greater than that of the tree ring isotopes (Figure 6.8). Using SPSS (IBM Corporation, 2013) the tree ring isotopes show a range of 4‰, whereas the NGRIP2 record has a larger range of approximately 6‰.

Figure 6.8: Tree ring and NGRIP boxplots of δ^{18}O values over the full data records.

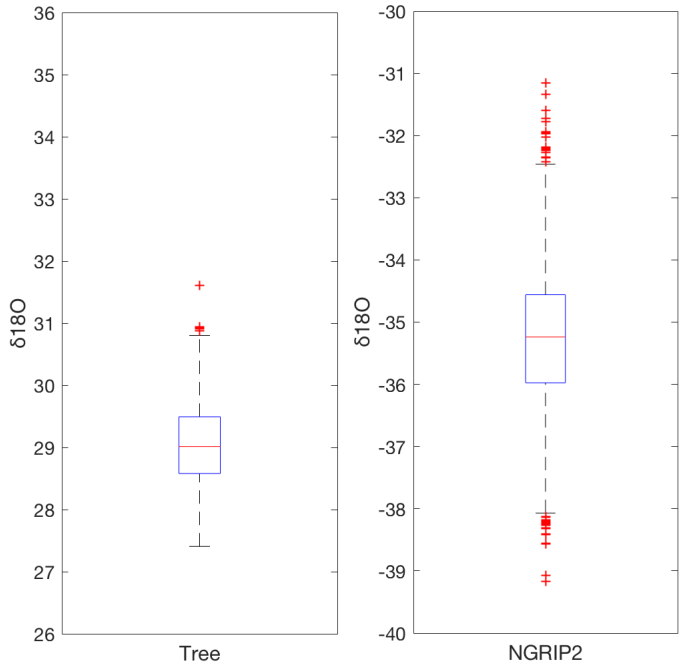

Figures 6.8, 6.9 and 6.10 compare the UK tree ring record against the NGRIP2 record during the overlapping period from 1200 to 1261A.D. Figure 6.8 shows that the data range within the tree rings was less than that of NGRIP2 during this period. The NGRIP2 data fluctuated within about 5.5‰, between -32.5‰ and -38‰, with the tree rings ranging within approximately 3‰, from 28 to 31‰.

Figure 6.9: Comparison between the δ^{18}O United Kingdom tree ring master record and the North Greenland Ice Core 2, during the overlapping period from 1200-1261, expressed in ‰ with respect to V-SMOW.

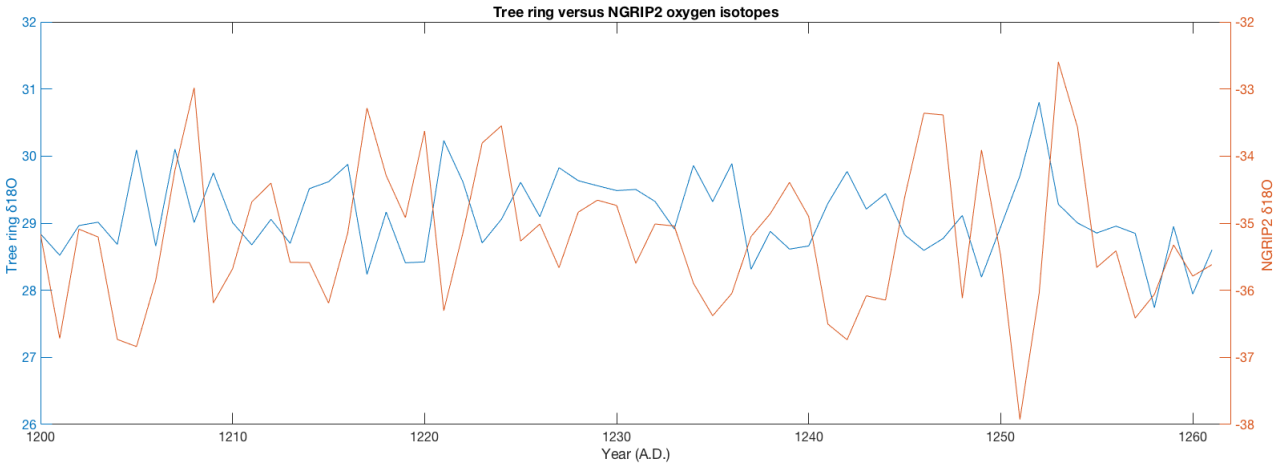

Introducing a two year offset between tree ring and ice core data, Figure 6.10 shows an increased visual cohesion between the two records. The NGRIP2 data was shifted two years prior to its original chronology to 1198-1259A.D. from 1200-1261A.D. in order to examine whether there is an atmospheric or hydrologically driven offset between the Greenland atmospheric oxygen isotopes and the United Kingdom tree ring isotope.

Figure 6.10: Comparison between the δ^{18}O United Kingdom tree ring master record and the North Greenland Ice Core 2 with a 2 year lead relative to its original values, during the overlapping period from 1200-1261, expressed in ‰ with respect to V-SMOW.

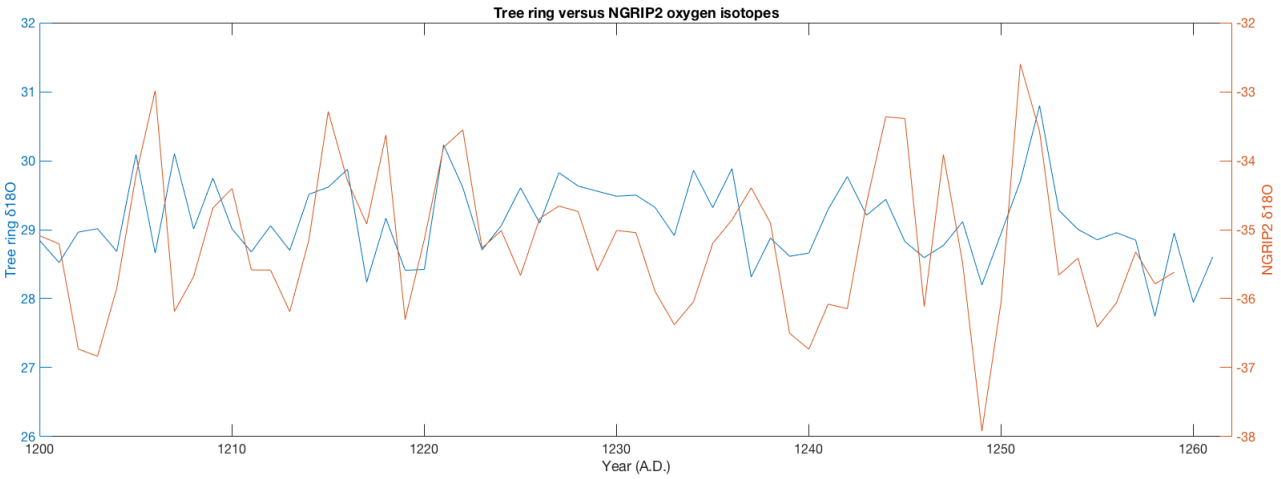

The 2 year and 3 year (Figures 6.10 and 6.11) introduced lead times show that there are similar influences on the Greenland and United Kingdom climates recorded within the atmospheric and terrestrial oxygen isotope records, though dampened and delayed within the tree ring dataset.

Figure 6.11: Comparison between the δ^{18}O United Kingdom tree ring master record and the North Greenland Ice Core 2 with a 3 year lead relative to its original values, during the overlapping period from 1200-1261A.D., expressed in ‰ with respect to V-SMOW.

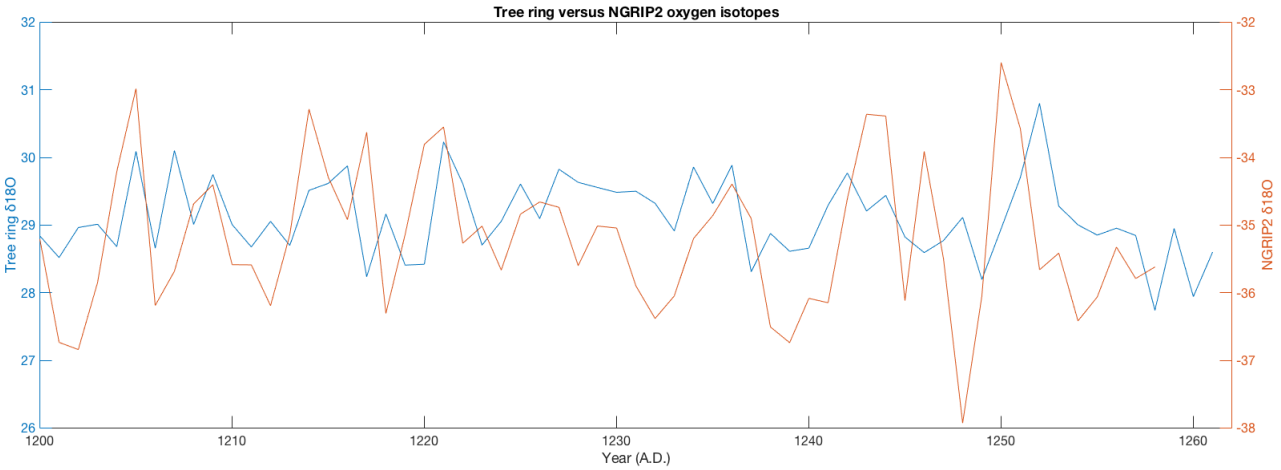

Examining Figures 6.9, 6.10 and 6.11, which compare the tree rings with the NGRIP2 ice core from 1200 to 1261 A.D., there is a general agreement in the data, which is confirmed in the correlation coefficients of Table 6.4.

Table 6.4: Correlation comparison between tree ring δ^{18}O and ice core δ^{18}O at a 0 year lag, 2 year lag and 3 year lag, from 1200-1261 A.D.

Lag time (years)	Correlation Coefficient	P-value
0	-0.3075	0.0151
2	0.3733	0.0033
3	0.2405	0.0665

The results of the correlation coefficients show that the tree ring and NGRIP2 data had the highest positive correlation at a two year lag, with 37.33% , and a P-value of 0.0033. Figure 6.12 shows the per mil (‰) difference between the NGRIP2 and the tree ring data. This was calculated by finding the mean difference between the tree ring δ^{18}O and the NGRIP2 δ^{18}O, between 1200 and 1262A.D., and then calculating the difference

from the mean for each year. The largest difference between the two records during the overlapping 62 year period occurred in 1252A.D., when depleted NGRIP2 core δ^{18}O values (-37.93‰) coincided with a slight enrichment in the δ^{18}O of the tree ring record (30.80‰).

Figure 6.12: Difference in the δ^{18}O values of the tree ring and NGRIP2 records during the overlapping 1200-1262A.D. time period.

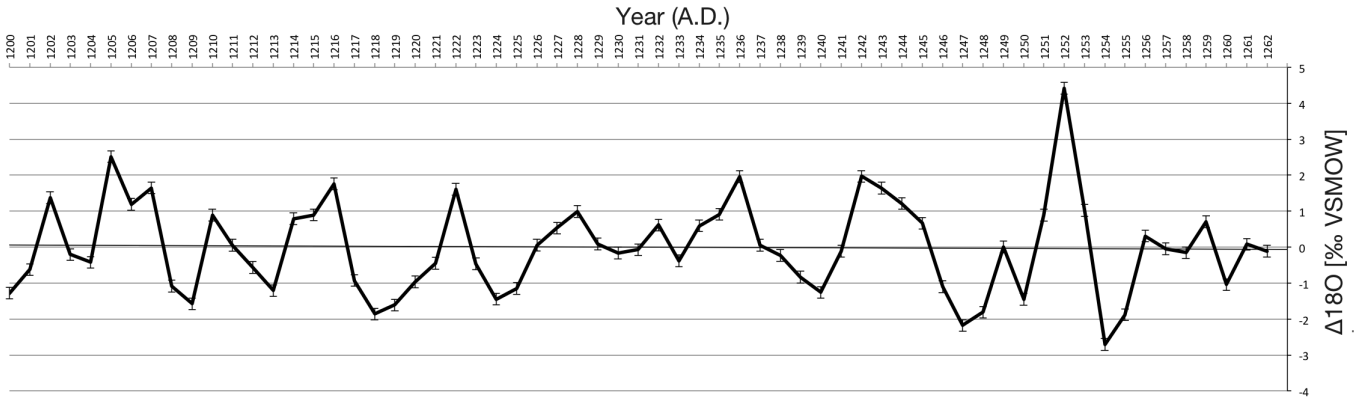

6.1.5 Comparison of century averages

The following section examines the averages for the NGRIP, GRIP and tree ring records by century. This identifies the centuries that exhibit higher or lower δ^{18}O values, and by inference, periods of anomalous average climate. Table 6.5 shows the mean δ^{18}O values to two decimal places for each century, in per mil (‰). Values marked with '# ' indicate higher δ^{18}O and values marked with '*' indicate less depleted δ^{18}O totals.

Table 6.5: NGRIP compilation and tree ring century averages.

Century (A.D.)	NGRIP δ^{18}O	GRIP δ^{18}O	Tree δ^{18}O	Century (B.C.)	NGRIP δ^{18}O	GRIP δ^{18}O
2000	-	-	28.78 #	0	-35.06	-34.95
1900	-34.85 *	-35.00	29.03	100	-35.57	-35.05
1800	-35.34	-35.12	29.00	200	-35.01	-34.73
1700	-35.56	-35.05	29.03	300	-34.96	-34.80
1600	-35.67 #	-35.27	28.96	400	-35.33	-34.85
1500	-35.45	-34.92	29.19 *	500	-35.2	-34.48 *
1400	-35.26	-35.08	28.96	600	-35.34	-34.76
1300	-35.44	-35.39 #	29.09	700	-35.27	-34.91
1200	-35.28	-35.02	29.11	800	-34.88	-34.78
1100	-35.3	-35.39 #	-	900	-34.85 *	-34.71 *
1000	-35.27	-35.16	-	1000	-35.34	-34.91
900	-35.08	-34.80	-	1100	-34.95	-34.89
800	-35.36	-35.18	-	1200	-34.82 *	-34.98
700	-35.17	-34.72 *	-			
600	-35.46	-35.01	-			
500	-35.73 #	-35.16	-			
400	-35.56	-35.02	-			
300	-35.57	-34.95	-			
200	-35.66	-35.07	-			
100	-35.16	-35.06	-			
0	-34.81 *	-34.73 *	-			

The centuries which showed the highest δ^{18}O values in the NGRIP record, and subsequently may indicate warmer and/or wetter conditions, were 1900A.D., 0A.D., 900B.C. and 1200B.C. In comparison, lowest values [most depleted in ^{18}O] were shown during 1600A.D. and 500A.D. within the NGRIP record, which are indicative of cooler and/or drier environments. The GRIP record had the lowest values during 1300A.D. and 1100A.D., with the highest values earlier in the temporal record. These higher values, which potential indicate warm/wet conditions, are shown for 700A.D., 0A.D., 500B.C. and 900B.C. This data demonstrates that during the 0A.D. and 900B.C. centuries, there appears to be wide-scale warming across Greenland, with higher values within both the

NGRIP and GRIP records at this time.

In comparison, the tree ring data shows a peak in high δ^{18}O values within the 16th century, and contrarily lower values during the 21st century A.D. There are slightly higher values within the 13th century A.D. coinciding with the Medieval Climate Anomaly (MCA) and prior to declining δ^{18}O into the Little Ice Age (LIA). The remainder of the tree ring record shows a lower range of variability than the ice cores, with reasonably consistent values within approximately 0.15‰ .

Figure 6.13: Averages for each century for the full NGRIP 1 and 2 δ^{18}O compilation, with the red region indicating the MCA and the yellow indicating the LIA.

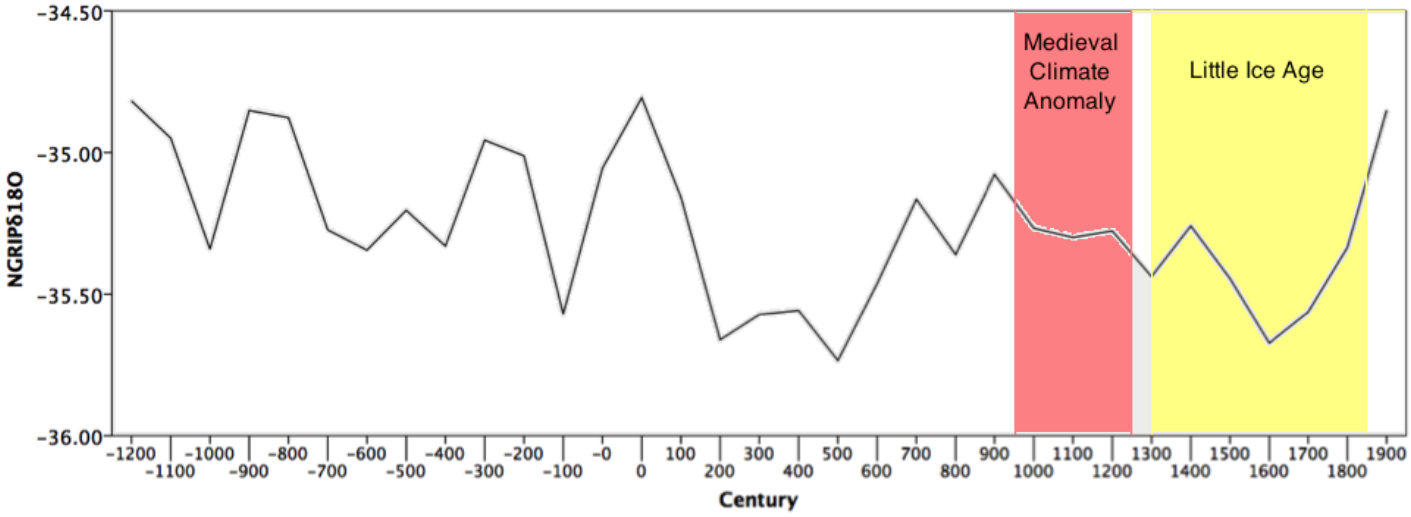

Figure 6.14: Averages for each century for GRIP δ^{18}O, with the red region indicating the MCA and the yellow indicating the LIA.

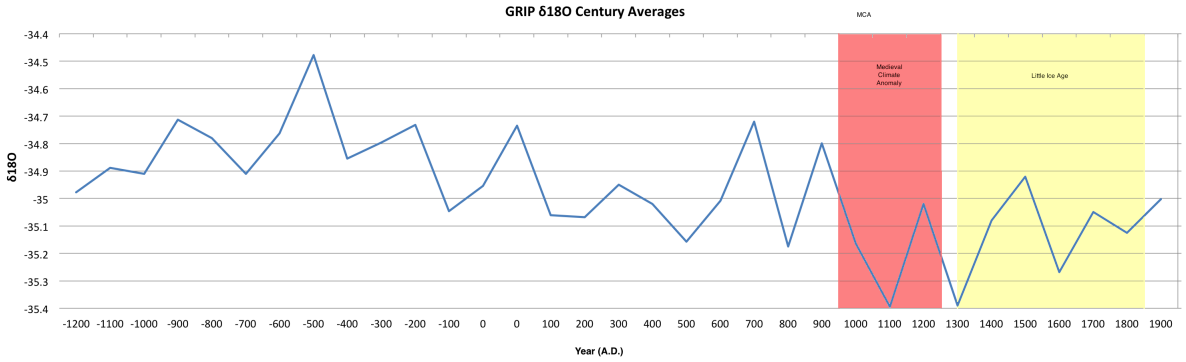

Figure 6.15: Averages for each century for the UK tree ring δ^{18}O, with the red region indicating the MCA and the yellow indicating the LIA.

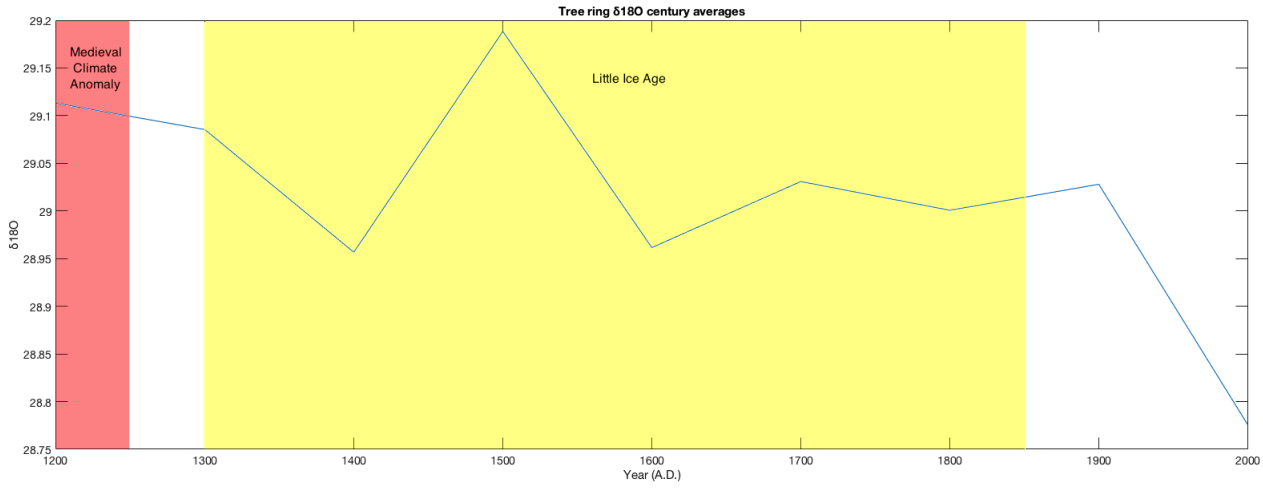

Lower values in the NGRIP record during 1600A.D. fall inside of the Little Ice Age temporal boundaries, with the subsequent sharp rise in δ^{18}O values to 1900A.D. consistent with the modern period of warming. The Medieval Climate Anomaly is less clear than the LIA within the century averages, only shown by a small plateau of average to slightly higher than average values (-35.27‰). Warming within the MCA was not evident within the GRIP record, with the lowest δ^{18}O value at 1100A.D. The other equal

lowest value of the GRIP data heralded the start of the LIA period, at 1300A.D. Within the tree ring averages, declining values coming out of the MCA and into the LIA are broken by the 16th century δ^{18}O peak. However, the tree ring comparison is limited by the lack of data for the entire MCA period. It is interesting to note again that the 21st century shows the lowest δ^{18}O values, which may indicate cooler and/or drier conditions within the central southern United Kingdom area of sampling.

6.1.6 Tree ring comparison to NGRIP compilation

This section compares the NGRIP data amalgamation to the tree ring oxygen isotopes. Figure 6.16 shows these two records from 1200A.D. to 2012A.D., with the NGRIP δ^{18}O y axis in blue on the left, and the tree δ^{18}O y axis in orange on the right. Although there is greater variation within NGRIP and an overall correlation coefficient of -0.0675 for 1200-1973A.D. (p-value=0.06), the two records do indicate that there is an interrelationship during certain time periods.

Figure 6.16: Dual y-axis plot showing the tree ring δ^{18}O on the right and the NGRIP compilation δ^{18}O on the left, from 1200A.D.-2012A.D.

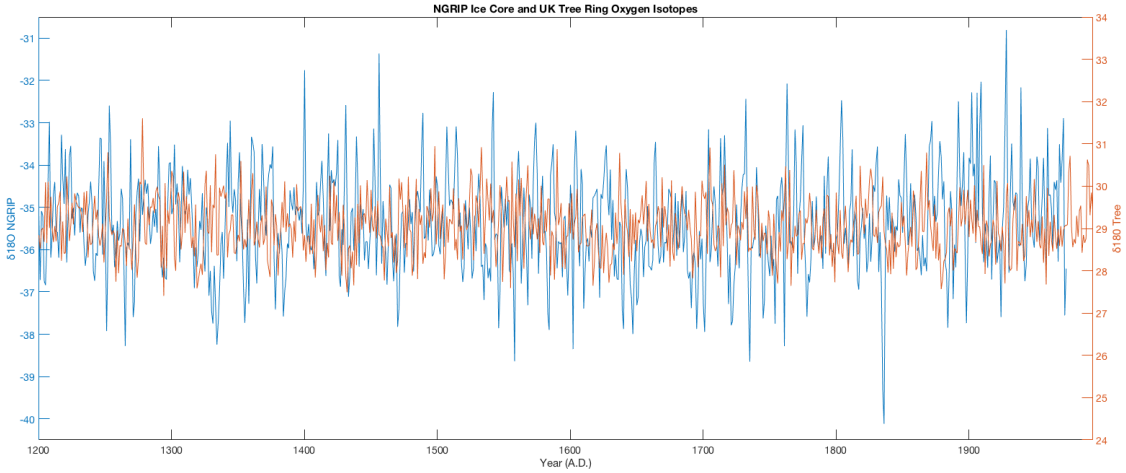

Zooming into the time period from 1200A.D. to 1350A.D., Figure 6.17 shows several instances where both records are less depleted in ^{18}O, for example around 1225A.D., 1275A.D. and 1310A.D. Another example of the cohesion between these two records is the pattern of peaks and troughs at approximately 1335A.D.

Figure 6.17: Dual y-axis plot showing the tree ring δ^{18}O on the right and the NGRIP compilation δ^{18}O on the left, from 1200A.D.-1350A.D.

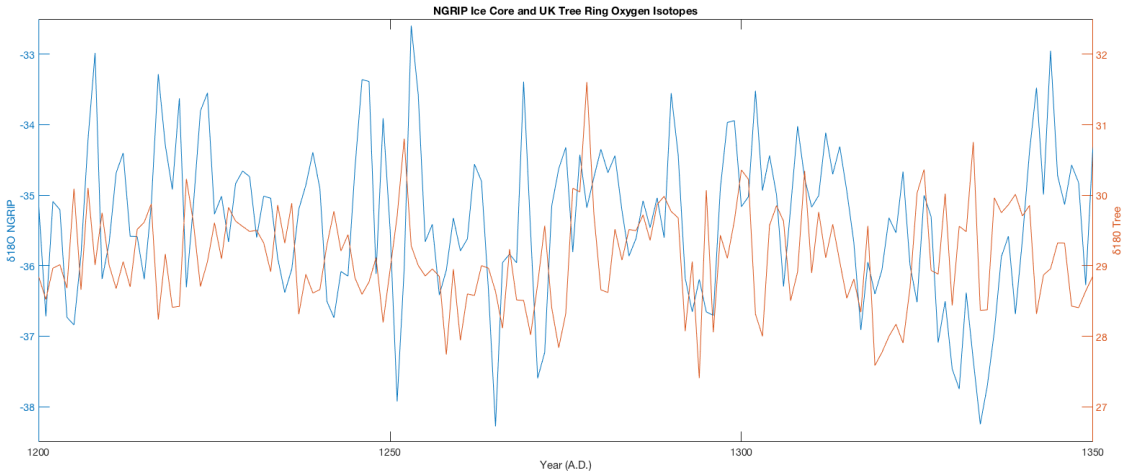

Figure 6.18 shows the same records as Figures 6.16 and 6.17 with a 10 year running average applied to the data. This process produces a smoothed record with reduced noise. The results of this 10 year moving mean indicates that there is excellent agreement during the first 100 years of data, but there is a division around 1310A.D. After this date, the records appear to fluctuate out of phase with each other. This was confirmed by an negative correlation coefficient of -0.2127 (p-value=0.06). It is important to note that correlation coefficients were conducted on discrete 10 year averages, as correlation coefficients of smoothed data are biased toward the low frequency relationship. There are also long periods in which the data shows a negative correlation, such as around 1325-1550A.D. and 1600-1650A.D.

Figure 6.18: 10 year moving average.

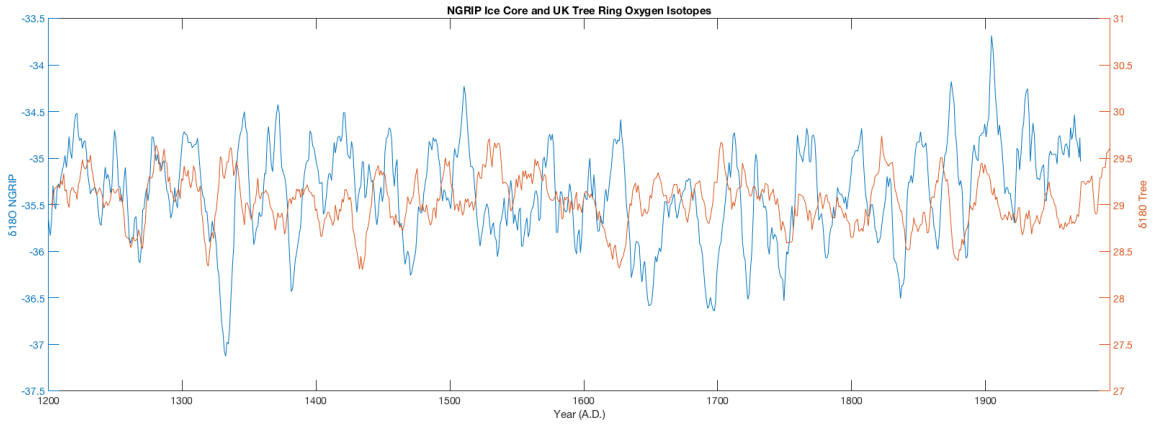

The 50 year moving average (Figure 6.19) clearly shows a cohesive period from 1200-1300A.D., as well as similarity in the two records from approximately 1450-1500A.D. Other than these two periods, the NGRIP and tree ring oxygen isotopes also appear to be antiphased within the 50 year running means. Additionally, the NGRIP record shows a temporary hiatus within the rising oxygen isotope values from 1675-1973A.D., just after the turn of the 19th century. The correlation coefficient of -0.4678 (p-value=0.07) confirmed that the signals on longer time scales have a similar impact on both records, with the two records negatively correlated.

Figure 6.19: 50 year moving average.

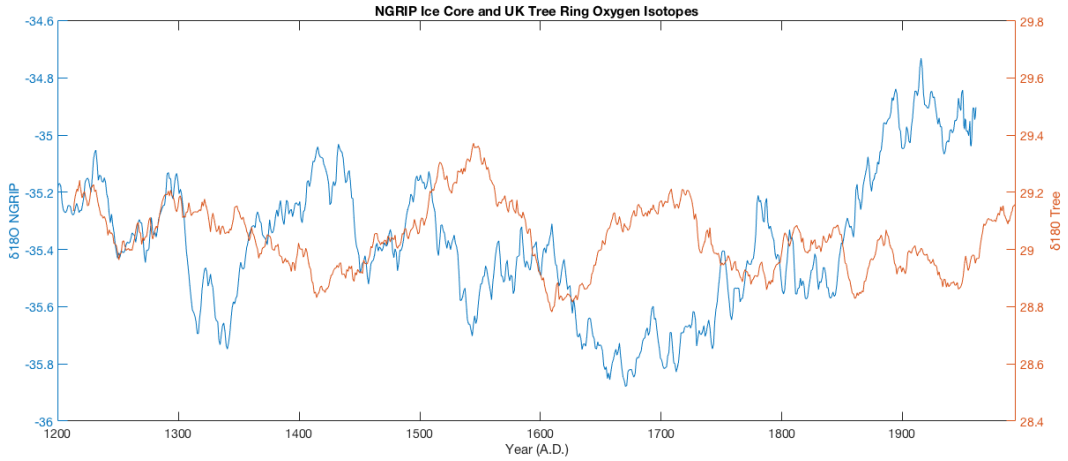

The 100 year running mean plot in Figure 6.20 shows a steep increasing trend within the NGRIP record from just prior to 1700A.D. through to the 20th century. However, the tree ring δ^{18}O values do not reflect this trend. The tree ring record also has a smaller data range in comparison to the NGRIP record. The tree ring record also shows two δ^{18}O peaks from approximately 1500-1575A.D. and 1675-1750A.D. The 100 year moving average produced the poorest correlation, with a coefficient of -0.003 (p-value=0.99), as the number of discrete averages were insufficient.

Figure 6.20: 100 year moving average.

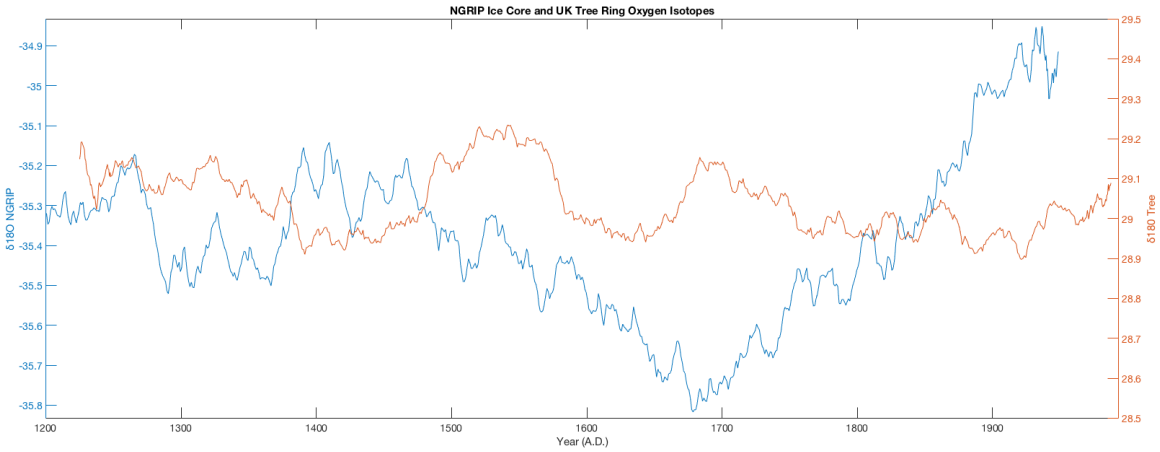

Historic Temperatures

The Moberg et al. (2005) Northern Hemisphere temperature reconstruction incorporates summer temperatures from the Agassiz core, GRIP borehole temperatures, tree ring data and other proxies from around the Northern Hemisphere. This historic Northern Hemisphere temperature profile shows that the period from 1400 to approximately 1720A.D. was anomalously cool. The temperature signal trend from 1600A.D. to 2000A.D. is similar to that seen within the NGRIP 50 year moving average within the previous section (Figure 6.19), including the previously discussed hiatus.

Figure 6.21: Northern Hemisphere temperature anomalies sourced from Moberg et al. (2005).

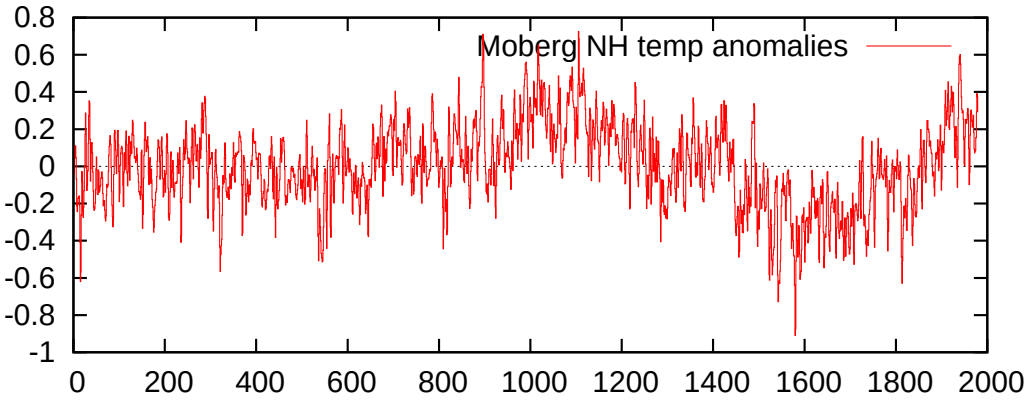

Figure 6.22 also shows a Northern Hemisphere temperature reconstruction, from Mann et al. (2009). Although this dataset also shows the rising temperature anomalies from approximately 1600, the hiatus and other broad features are not as clear.

Figure 6.22: Northern Hemisphere temperature anomalies sourced from Mann et al. (2009).

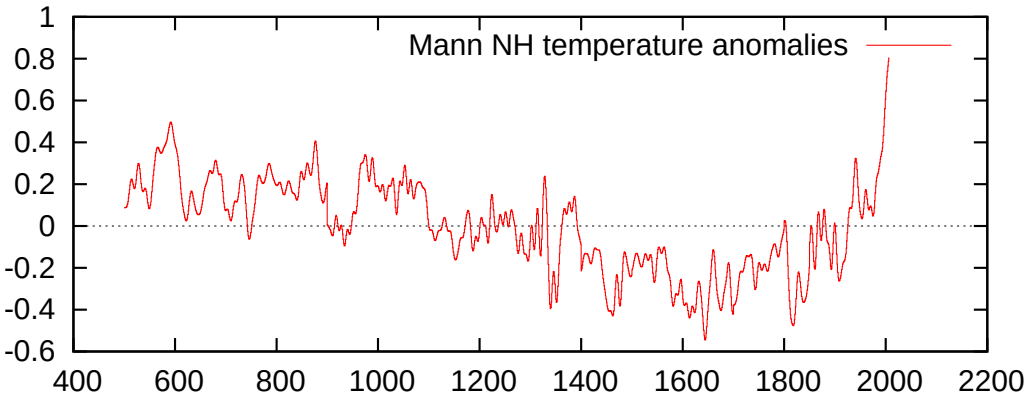

The CRU TS4.01 data is shown in Figure 6.23. This data was obtained from the Natural Environmental Research Council Centre for Environmental Data Analysis (Harris and Jones, 2017), and plotted using the Panoply program (Schmunk, 2018). The first image

(Figure 6.23a) shows the global near-surface temperature for January 1901, and the second (Figure 6.23b) shows the near-surface temperatures for July 1963. Figure 6.23 demonstrates that Greenland ice cap temperatures fluctuate between approximately -38°C and -12°C, whereas average United Kingdom temperatures fluctuate from around 1°C to 17°C.

(a) January 1901.

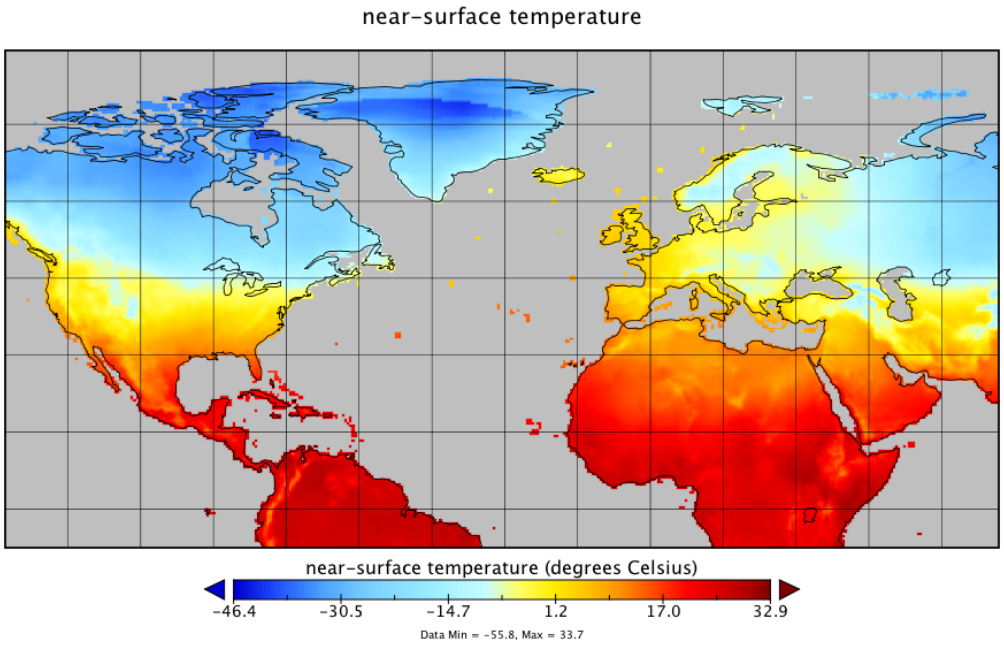

(b) July 1963.

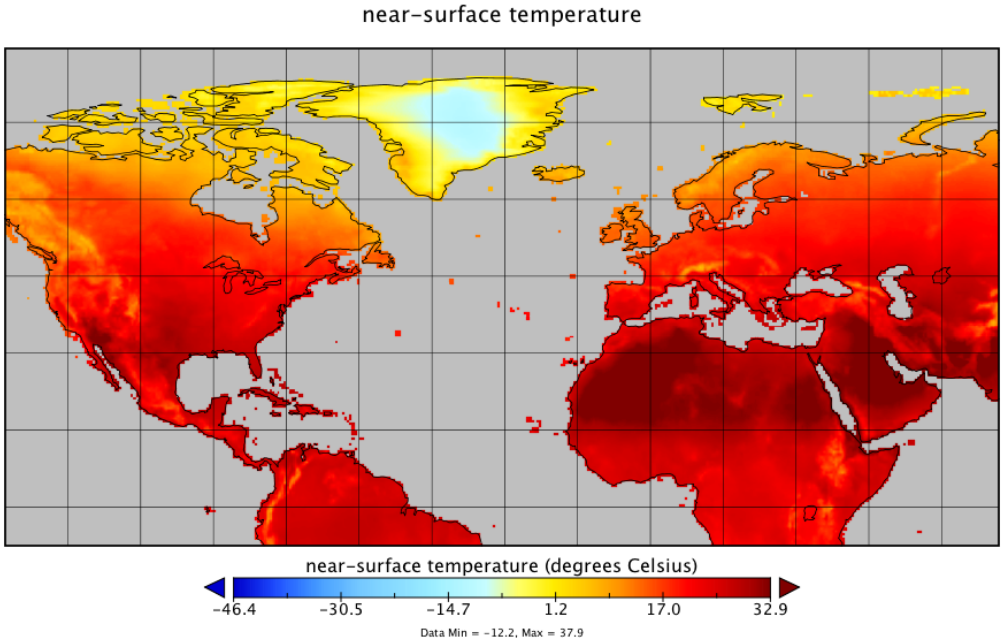

Figure 6.23: CRU TS4.01 global historical near-surface temperatures from the University of East Anglia's Climate Research Unit.

Historic temperature data was also used for further comparisons against the δ^{18}O results from the UK tree rings and the NGRIP compilation datasets. The data used, the CRU TS2.1 Global Climate Dataset, was produced by the University of East Anglia's Climatic Research Unit (Mitchell and Jones, 2005), and downloaded from the World Bank (Sdwebx.worldbank.org, 2018). It consists of 0.5°grids interpolated from observational station data, climatologies from 1961-1990 and long term historical measurements. The temperature station observation records that produced the CRU TS2.1 were primarily sourced from Jones (1994), Jones and Moberg (2003), Peterson et al. (1998), New et al. (2000), Hahn and Warren (1999) as well as the World Meteorological Organization official international climate monitoring (CLIMAT) and Monthly Climatic Data for the World (MCDW) data.

Figure 6.24 shows the CRU TS2.1 United Kingdom historical temperature dataset, annually averaged and plotted against the tree ring oxygen isotopes from 1900 to 2012A.D. This figure shows excellent agreement between the historical mean temperature in the United Kingdom and the UK tree ring δ^{18}O values. Despite greater variability within the oxygen isotope values, the majority of the features are temporally aligned. However, there is questionable agreement in the early part of the record, from 1900A.D. to 1920A.D. These datasets both show increased temperature and δ^{18}O values from around 1990A.D. to 2010A.D., as well as a spike at around 1975A.D.

Figure 6.24: Historic temperature compared to tree ring δ^{18}O.

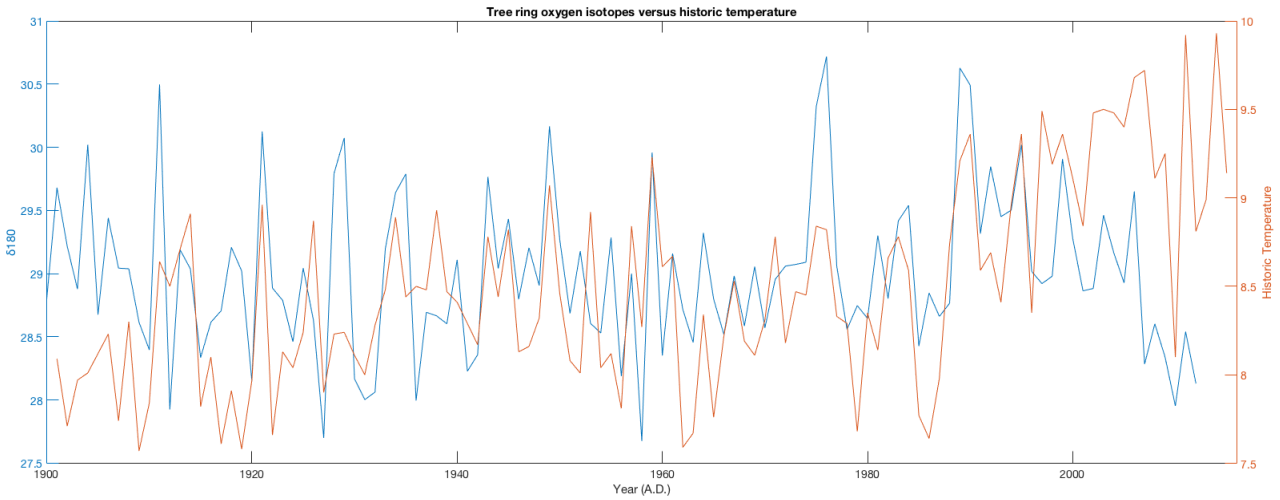

The next stage in the comparison between the tree ring oxygen isotope results and the historical temperature observations compares the isotope record after it has been converted to temperature. This tree ring δ^{18}O conversion to temperatures was conducted using the equation from Burk and Stuiver (1981), as follows:

Temperature = (δ^{18}O - 22.97) $\div$ 0.41

Figure 6.25 shows the results of the temperature conversion, plotting tree ring temperatures against historic mean temperature observations. Due to the linear relationship between the oxygen isotopes and temperature, the relationship shown in Figure 6.25 is broadly similar to that seen in Figure 6.24.

Figure 6.25: Historic temperature compared to converted temperature from tree ring isotopes.

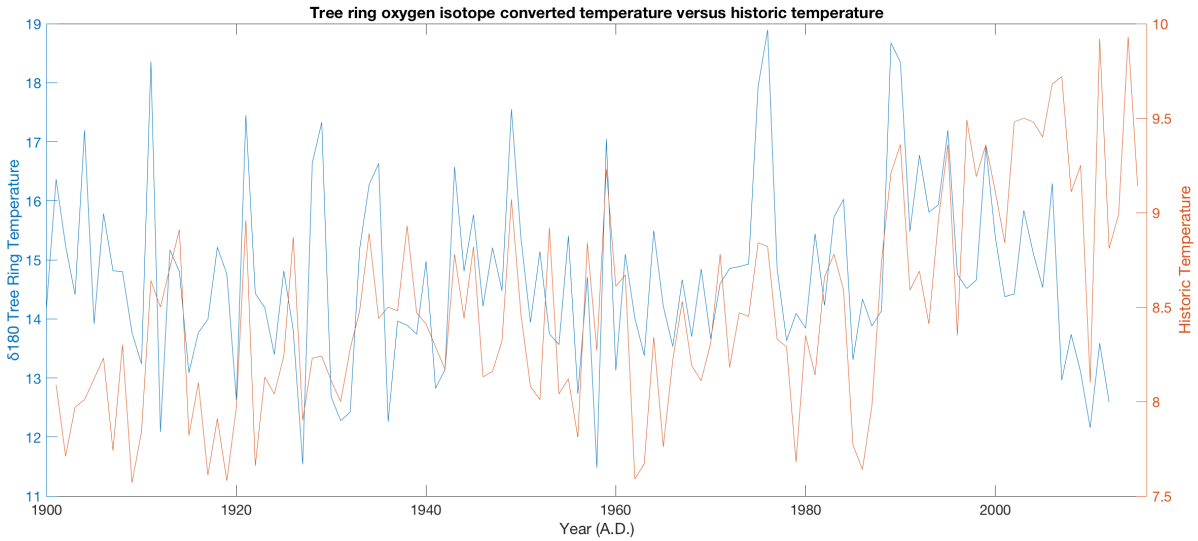

Comparing Greenland historical temperatures with the NGRIP oxygen isotope record (Figure 6.26) also shows good agreement between the annual variation of the two time series. Specifically, the period from 1920 to 1950A.D. demonstrates cohesion in the peaks and troughs of the two records. There is an increasing trend from 1920 to 1930A.D. in the historical temperature records, as well within the δ^{18}O values.

Figure 6.26: Historic Greenland temperature compared to NGRIP δ^{18}O.

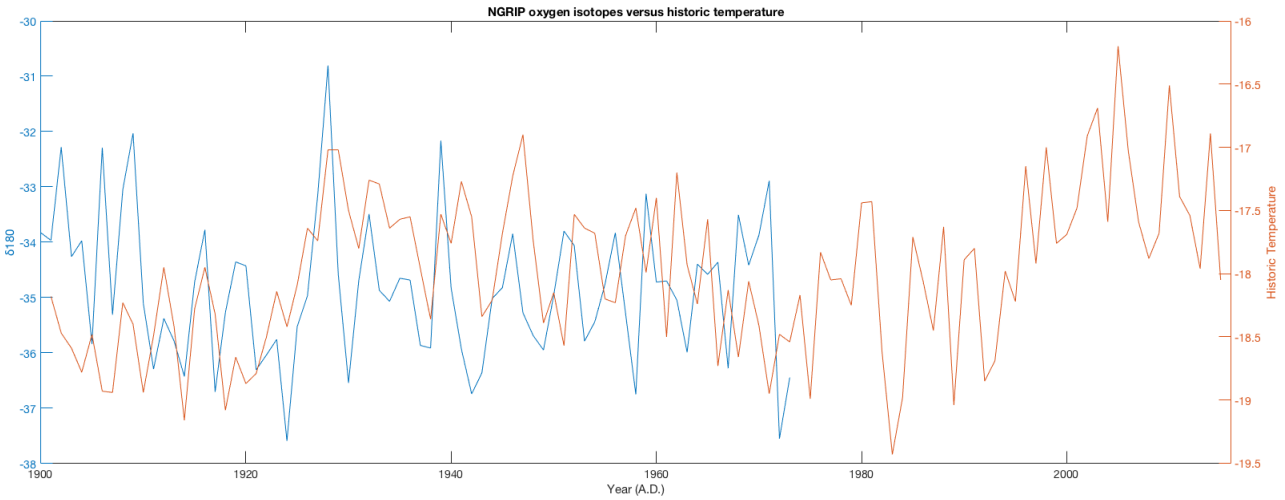

As for Figure 6.25, Figure 6.27 shows the temperatures converted from oxygen isotope values, albeit from the NGRIP ice core. The equation used for the conversion between ice core δ^{18}O and temperature was obtained from Dansgaard (1964):

Temperature = (δ^{18}O + 13.7) ÷ 0.67

As with Figure 6.25, the linear relationship between temperature and δ^{18}O means that Figures 6.26 and 6.27 are broadly similar. The δ^{18}O values converted to temperature are consistent with the NGRIP surface temperature measurements from Guillevic et al. (2013) in Section 3.1.1 (Table 3.1). Due to the gridded interpolation of the historical temperatures, the actual temperature values do not match the NGRIP isotope converted temperatures. However, re-examining Figure 6.23 shows a large temperature difference between the coastal regions of Greenland, where the meteorological observation stations are based, and the NGRIP location in the central region of the ice sheet. This temperature gradient equals approximately 13-14°C, which is consistent with the temperature difference between the historical record and the NGRIP isotope converted temperatures.

Figure 6.27: Historic temperature compared to converted temperature from NGRIP isotopes.

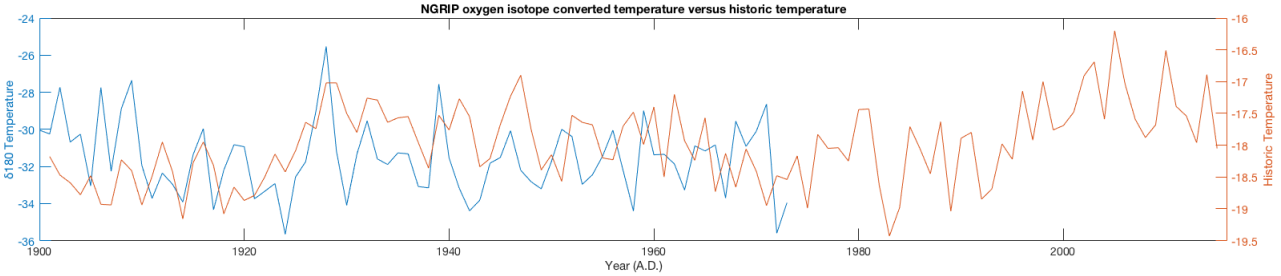

A comparison of the UK historical data with the Greenland historical temperatures resulted in a correlation of 0.26 (p-value=0.01). This conflicts with the negative correlation shown earlier, however may indicate the same temperature and depletion gradient effect from the coastal region of Greenland to the interior of the ice sheet, as described earlier.

Source water isotopes

This section explores several comparative plots of the NGRIP ice with the oxygen isotope values from the UK tree rings, which have been converted to precipitation source water. This conversion was conducted using the Anderson et al. (2002) equation, solving for source water δ^{18}O from cellulose δ^{18}O. Anderson et al. (2002) developed this model by reversing the combined cellulose and leaf-water models from Flanagan et al. (1991) and Roden et al. (2000). The equation is as follows:

$$\delta^{18}O_{sourcewater} \approx \delta^{18}O_{cellulose} - (1-f)(1-h)(\alpha+\alpha_k) - \epsilon_o$$

f is the dampening factor related to the re-exchange of xylem water with source water

[average value of 0.44 calculated from Allison, Gat and Leaney (1985); Saurer et al. (1997); Roden et al. (2000); Anderson et al. (2002); Barbour et al. (2002); Treydte et al. (2014)]. The south-east England summer average relative humidity was used [23%] (h), and α represents the liquid-vapour equilibrium fractionation coefficient for water [9.95‰, calculated using the Treydt et al. (2014) model]. α_k is the liquid-vapour kinetic fractionation coefficient for water [16‰, from Dongmann (1974)], and ϵ_o is the biological fractionation of water [27‰, from Hook et al. (2015) and Csank, Fortier and Leavitt (2013)].

Figure 6.28 shows the NGRIP δ^{18}O values plotted against the tree ring oxgyen isotopes from cellulose converted to atmospheric source water δ^{18}O. There is good cohesion within the variation of each time series. This can be specifically seen at 1300A.D., 1400A.D., as well as 1800A.D. The approximate 26‰ difference between the summer United Kingdom tree ring source water record and the winter NGRIP record is close to the difference between the measurements of -35.5‰ from Guillevic et al. (2013) in Section 3.1.1 (Table 3.1), and the Pellegrini et al. (2016) UK groundwater isotope values, from -7 to -8‰ (Figure 3.11 of Section 3.3.3), as well as the Wallingford GNIP δ^{18}O values which ranged between -14‰ and 2‰ (shown in Figure 5.16 of Section 5.1.3).

Figure 6.28: NGRIP δ^{18}O compared to source water values converted from UK tree rings.

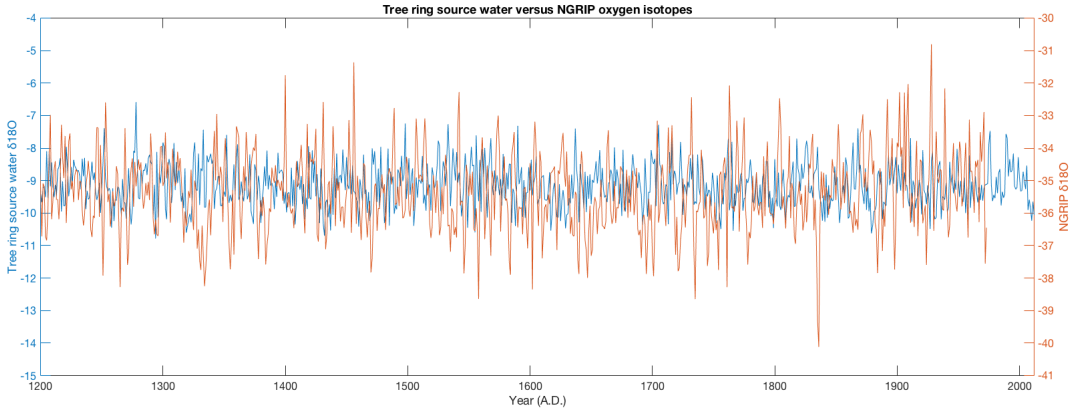

Figure 6.19 shows the 20 year running mean totals for the tree ring source water δ^{18}O against NGRIP δ^{18}O. The relationship between these two time series is well aligned for the first 300 years, albeit with three large antiphased deviations in the NGRIP core at 1300A.D., just prior to 1400A.D., and just after 1450A.D. The records then appear to be antiphased until approximately 1850A.D.

Figure 6.29: NGRIP δ^{18}O compared to source water values converted from UK tree rings 20 year running averages.

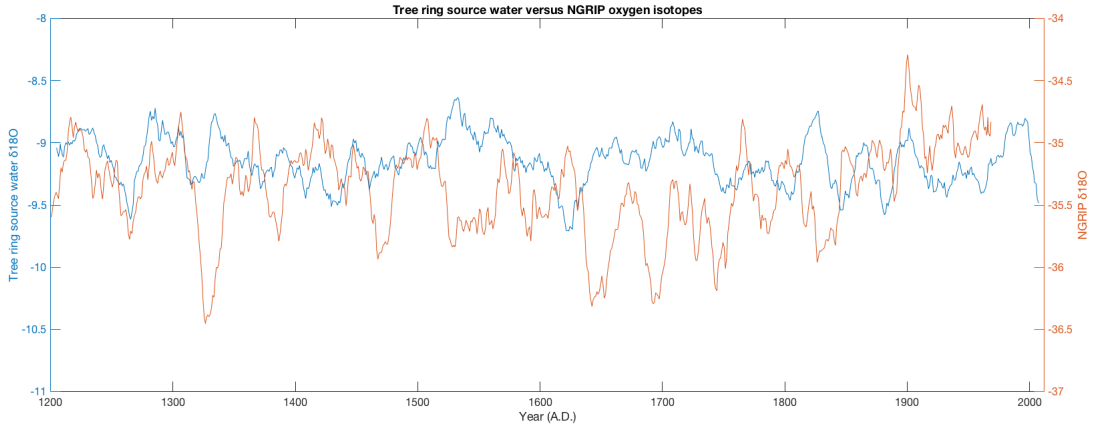

Figure 6.30 shows the 100 year moving average for the source water δ^{18}O from the UK

tree rings and the NGRIP δ^{18}O. The two records are well aligned within this figure until approximately 1375A.D., with apparent antiphased trends from 1375A.D. to 1475A.D., and 1550A.D. to 1750A.D. The increasing trend in the NGRIP data is the dominant feature from approximately 1675A.D., whereas an increasing trend in the source water values is not evident until around 1925A.D.

Figure 6.30: NGRIP δ^{18}O compared to source water values converted from UK tree rings 100 year running averages.

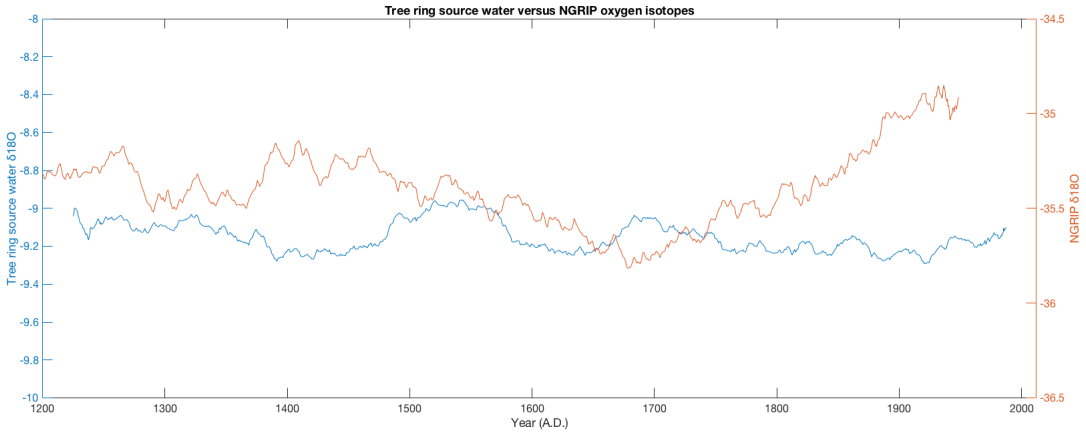

6.1.7 Medieval Climate Anomaly and the Little Ice Age

This section examines the desciptive statistics of the tree ring, NGRIP1, NGRIP2, NGRIP compilation and GRIP datasets in regards to the Medieval Climate Anomaly (MCA) and the Little Ice Age (LIA).

Table 6.5 shows the tree ring δ^{18}O values divided into four periods of time, including: post-LIA [1850-2011 A.D.], LIA [1400-1850 A.D.], the earlier LIA period [from 1250-1400 A.D.], and the MCA [1200-1250 A.D.]. There is no apparent cooling within the maximum or mean δ^{18}O during the LIA or 1250-1400A.D. periods as may have

been expected. However, the minimum δ^{18}O results show the early LIA period from 1250-1400A.D. as well as the LIA to have the lowest values, at 27.41 and 27.49‰ respectively. The MCA period had the highest mean δ^{18}O value at 29.15‰, despite having a much smaller data pool of 50 years.

Table 6.6: Tree ring data divided into time periods, including number of samples within the time period (A.D.), minimum, maximum, and mean δ^{18}O with respect to VPDB, as well as standard deviation.

Time Period (A.D.)	n	Min. δ^{18}O	Max. δ^{18}O	Mean δ^{18}O	Std. Dev.
1850-2012	162	27.57	30.79	28.99	.65
LIA [1200-1850]	450	27.49	30.94	29.03	.67
1250-1400	150	27.41	31.60	29.08	.73
MCA [950-1250]	50	28.20	30.23	29.15	.53

Table 6.6 shows the comparison between the tree ring, NGRIP1 and NGRIP2 δ^{18}O values for sectioned time periods. The first row of each record shows the results for the full record in question, which is 1200-2012A.D. for the tree ring record, 1236B.C.-1973A.D. for the NGRIP1 record, and 1235B.C.-1261A.D. for the NGRIP2 record. The second row for each record is the Little Ice Age [1200-1850A.D.], and the third is the Medieval Climate Anomaly [950-1250A.D.]. The NGRIP1 record is the only dataset to show decreased values during the LIA period at -35.44‰ . The total averages for the three time periods of NGRIP2 differed by only 2‰ overall. As with the previous table, the LIA period showed slight depletion in comparsion to the MCA, within the tree ring δ^{18}O.

Table 6.7: Record average comparison.

Record	Time Period	Average δ^{18}O
Tree	1200-2012A.D.	29.04
	1200-1850A.D.	29.05
	1200-1250A.D.	29.15
NGRIP1	1236B.C.-1973A.D.	-35.27
	1200-1850A.D.	-35.44
	950-1250A.D.	-35.38
NGRIP2	1235B.C.-1261A.D.	-35.24
	1200-1261A.D.	-35.22
	950-1250A.D.	-35.23

Table 6.7 compares the compiled NGRIP record, with the GRIP ice core as well as the tree rings already discussed. Within this table, the LIA is shown to have depleted δ^{18}O means in comparison to the post 1850A.D. time period within the NGRIP and GRIP records, as well as compared to the MCA within the tree ring and NGRIP records. The minimum δ^{18}O values appear to be the most depleted during the LIA compared with other time periods within the NGRIP and GRIP datasets.

Table 6.8: Ice core and tree ring comparison during different time periods, including the Little Ice age from 1250-1850A.D. and the Medieval Climate Anomaly from 950-1249 A.D.

Time Period	Record	No. of Samples	Minimum	Maximum	Mean	Standard Deviation
>1850	Tree	162	27.57	30.79	28.99	0.66
	NGRIP	124	-37.85	-30.81	-34.99	1.28
	GRIP	91	-37.49	-32.45	-35.05	1.00
LIA	Tree	601	27.41	31.6	29.05	0.69
	NGRIP	600	-40.12	-31.37	-35.47	1.17
	GRIP	254	-38.19	-32.93	-35.13	0 .78
MCA	Tree	50	28.2	30.23	29.15	0.53
	NGRIP	300	-38.31	-31.97	-35.23	1.04
	GRIP	117	-36.58	-32.74	-35.13	0.75
<949	NGRIP	2186	-39.17	-26.32	-35.24	1.11
	GRIP	762	-37.22	-32.69	-34.90	0.77

The final table within this section shows the same data as the previous Table 6.7, but with the LIA and MCA date border changed to 1300A.D., so 1300-1850A.D. and 950-1299A.D. respectively. This change was implemented to explore the results of sections 6.1.5 and 6.1.6, which showed that 1300A.D. was a key change point within the century averages and the alignment between the NGRIP and tree ring records. This table shows that the records with lower minimum δ^{18}O values for the LIA were still the NGRIP and GRIP; lower maximum δ^{18}O values in the GRIP and tree rings; as well as lower δ^{18}O means in the NGRIP and tree ring records.

Table 6.9: Ice core and tree ring comparison during different time periods, including the Little Ice age from 1300-1850A.D. and the Medieval Climate Anomaly from 950-1299 A.D.

Time Period	Record	No. of Samples	Minimum	Maximum	Mean	Standard Deviation
LIA	NGRIP	550	-40.12	-31.37	-35.48	1.17
	GRIP	233	-38.19	-32.93	-35.13	0.79
	Tree	551	27.49	30.94	29.04	0.67
MCA	NGRIP	350	-38.31	-31.97	-35.25	1.06
	GRIP	138	-36.58	-32.74	-35.12	0.75
	Tree	100	27.41	31.6	29.11	0.68

6.1.8 Solar and volcanic forcings

This section presents the solar and volcanic forcings that may have had an influence on the NGRIP and tree ring datasets. Figure 6.33 shows the volcanic forcing (W/m^2) for 1300B.C. to 2000A.D., sourced from Kobashi et al. (2017). This data shows two peaks in volcanic activity from 1263-1264A.D. of -30.72 and -11.30 W/m^2 respectively. Other major peaks occurred in 682A.D., 628A.D. and 38B.C., with values of -4.97W/m^2, -8.19W/m^2 and -17.77 W/m^2 respectively. However, it is important to note that Kobashi et al. (2017) used an earlier ice core age scale, which could have a difference from the

NGRIP2 age scale of up to seven years, prior to 1258A.D.

Figure 6.31: Data sourced from Kobashi et al. (2017) detailing the volcanic forcing (W/m^2) from 1300B.C. to 2000A.D.

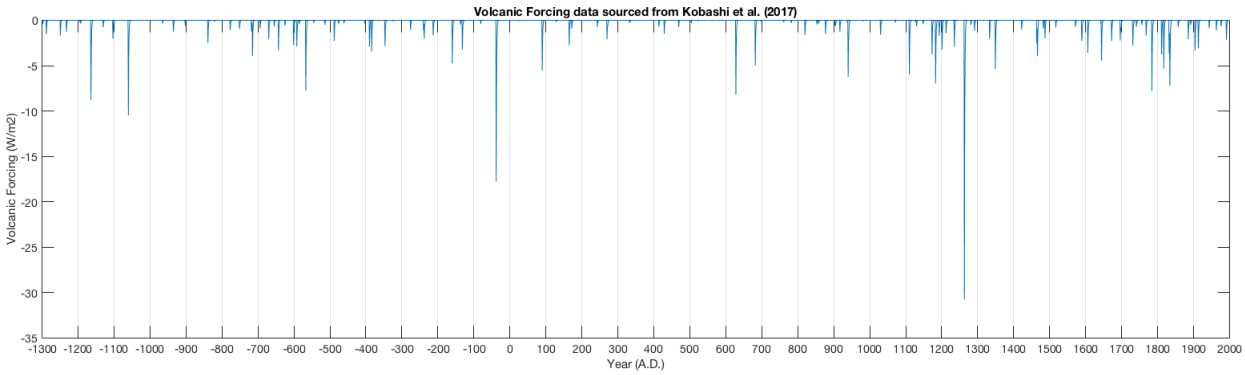

Table 6.9 shows solar forcing data, sourced from Kobashi et al. (2013). This data shows periods of strong or weak solar activity from 1200A.D. to 2000A.D. When compared to the 100 year running average oxygen isotopes for the NGRIP and tree rings in Figure 6.20, the strong period of solar activity from 1597 to 1624A.D. coincides with the break in antiphased agreement between the two records.

Table 6.10: Time periods (A.D.) of strong and weak solar forcing within the last 800 years, data sourced from Kobashi et al. (2013).

Strong Solar Activity (A.D.)	No. of Years	Weak Solar Activity (A.D.)	No. of Years
1826 - 2000	175	1800 - 1825	26
1740- 1799	60	1625 - 1739	115
1597 - 1624	28	1396 - 1596	201
1345 - 1395	51	1270 - 1344	75
1200 - 1269	70		

6.1.9 Wavelet analysis

This section examines the results of the wavelet analysis on the UK tree ring record, NGRIP compilation dataset, as well as cross wavelet analysis against the respective local historical temperature records. Figures 6.32 a and b show the results of wavelet analysis on the tree ring and NGRIP compilation datasets. The dashed line indicates the "cone of influence", outside of which is influenced by the edge effects, and the solid black contour lines enclose the areas with greater than 95% confidence (Torrence and Compo, 1998). The main features to note in the tree ring analysis are the regions of strong power at 20-30 year, 25-60 year and 45-75 year periodicities between 1250-1500A.D., 1760-1920A.D. and 1250-1375A.D. respectively. The NGRIP data shows a region of strong power with a 300-600 year periodicity from 750B.C. to 500 A.D.

(a) Wavelet plot tree ring 1200-2012 A.D.

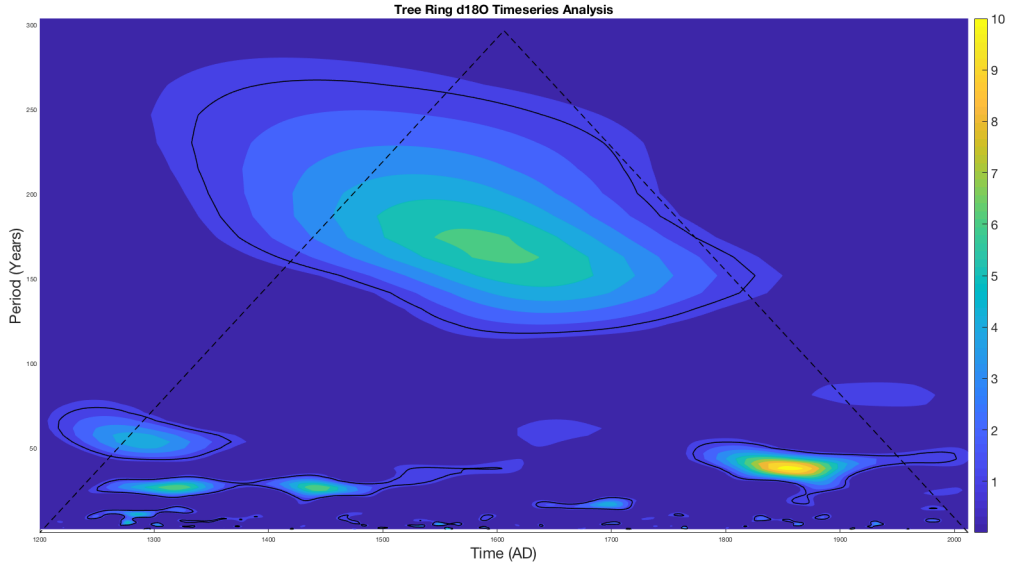

(b) Wavelet plot ice core 1236 B.C.-1973 A.D.

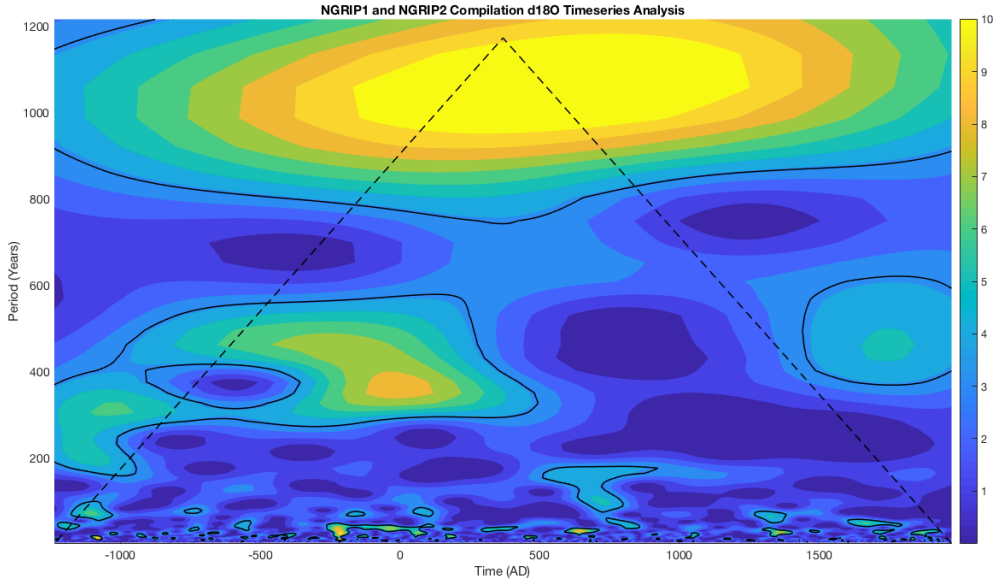

Figure 6.32: Full wavelet analysis for tree ring and NGRIP ice core data.

Zooming into the NGRIP compilation results within Figure 6.33 there are several regions of similar periodicity to the tree ring record, centred on 40 and 75 years. This includes a 50-100 year region at approximately 1100B.C., 70-80 year at 750B.C., 65-75 year at 200B.C., 60-80 year at 100A.D., and 45-75 at 1300A.D. From approximately 200B.C. to 100A.D. there appears to be a large amount of activity in the NGRIP wavelet results. It is interesting that the end of this period of greater power coincides with a change point of the NAO, with Olsen et al. (2012) and Drake (2017) claiming that there was a shift around this period towards the positive phase.

There is also a region with a periodicity of 70-180 years between 500-1000A.D., as well as a region with high power at approximately 250B.C. with a periodicity of around 5-50 years.

Figure 6.33: Wavelet plot for ice core oxygen isotopes 1200-1973 A.D.

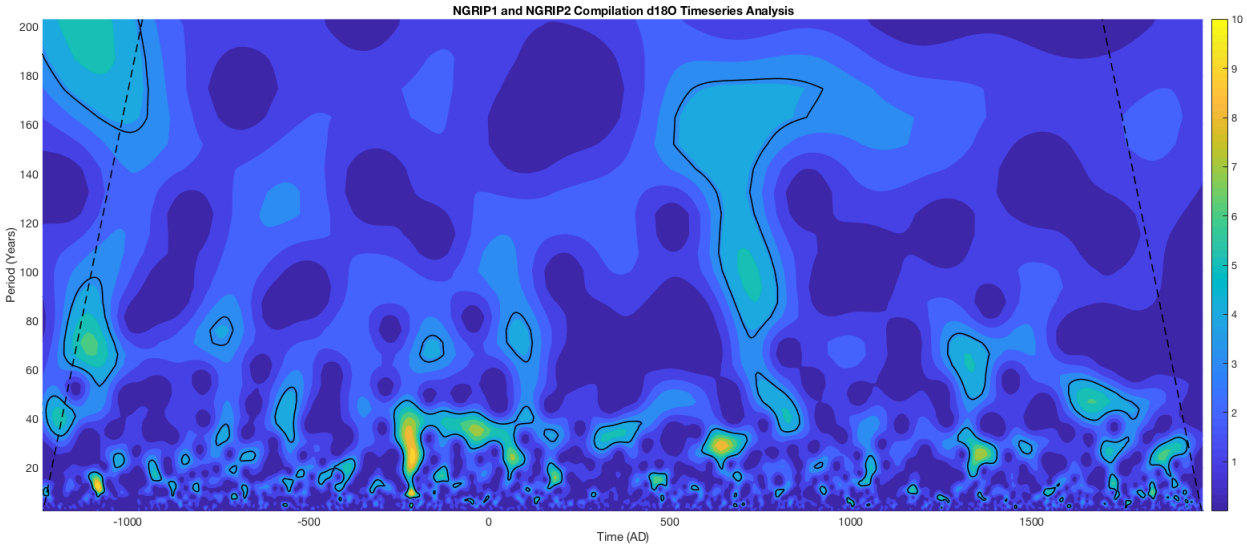

Figure 6.34 shows the wavelet analyses of the tree ring and ice core dataset from 1200A.D., zoomed into a 0-200 year periodicity. Both records show regions of high

power at 20-40 and 50-80 year periodicities. For the tree ring record these regions both occur from 1250-1370A.D., whereas the NGRIP record shows the 20-40 year region from 1300A.D. to 1400A.D., and the 50-80 year region from 1270A.D. to 1390A.D.

Olsen et al. (2012) states that at 1300A.D., at the beginning of LIA, the NAO changed phase, from predominately positive to fluctuating negative conditions. In Section 3.2.1 the features of typical AMO phases were discussed in relation to the instigation of NAO phases. For example, regional warming of SSTs and strengthening of the Atlantic Meridional Overturning Circulation, associated with the positive phase of the AMO, is conducive to the development of negative NAO conditions. With the strong influence of the Atlantic ocean on both the Greenland and United Kingdom climate and meteoric isotopes, it is not surprising for there to be an AMO influence prior to 1300A.D. in both the records.

(a) Wavelet plot for tree ring oxygen isotopes 1200-2012 A.D.

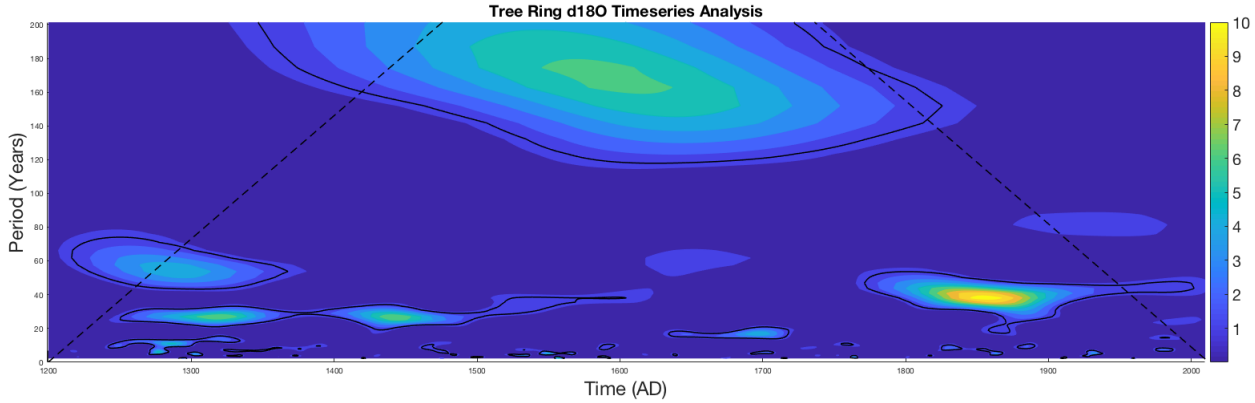

(b) Wavelet plot for ice core oxygen isotopes 1200-1973 A.D.

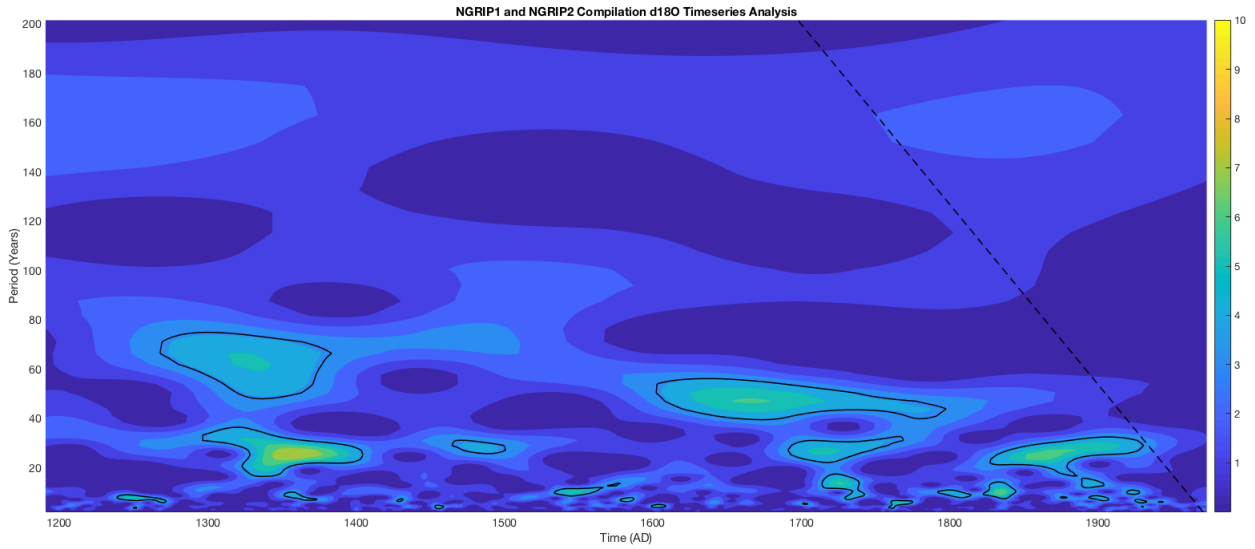

Figure 6.34: Wavelet analysis for tree ring and NGRIP ice core data from 1200A.D.

Figure 6.35 shows the tree ring wavelet analysis zoomed into a maximum 50 year periodicity. The region with the strongest power had a periodicity centred at 40 years, from approximately 1790-1950A.D. The tree ring record had two pulses of 25 year periodicity centred at approximately 1300A.D. and 1430A.D.

Figure 6.35: Wavelet plot for tree ring oxygen isotopes 1200-2012 A.D.

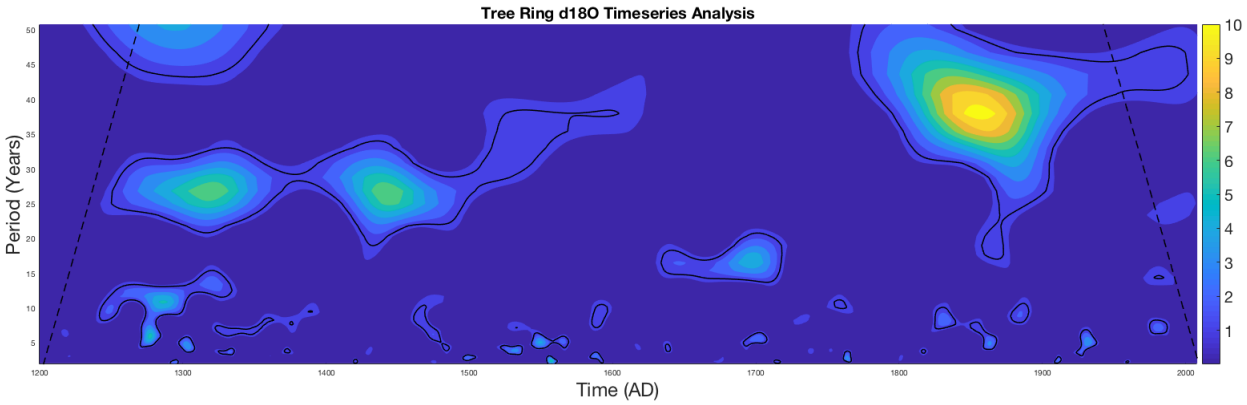

Figure 6.36 shows the NGRIP wavelet analysis zoomed into a maximum 50 year periodicity. The NGRIP results show four regions of 25 year periodicity centred at approximately 1350A.D., 1490A.D., 1710A.D. and 1890A.D.

Figure 6.36: Wavelet plot for ice core oxygen isotopes 1200-1973 A.D.

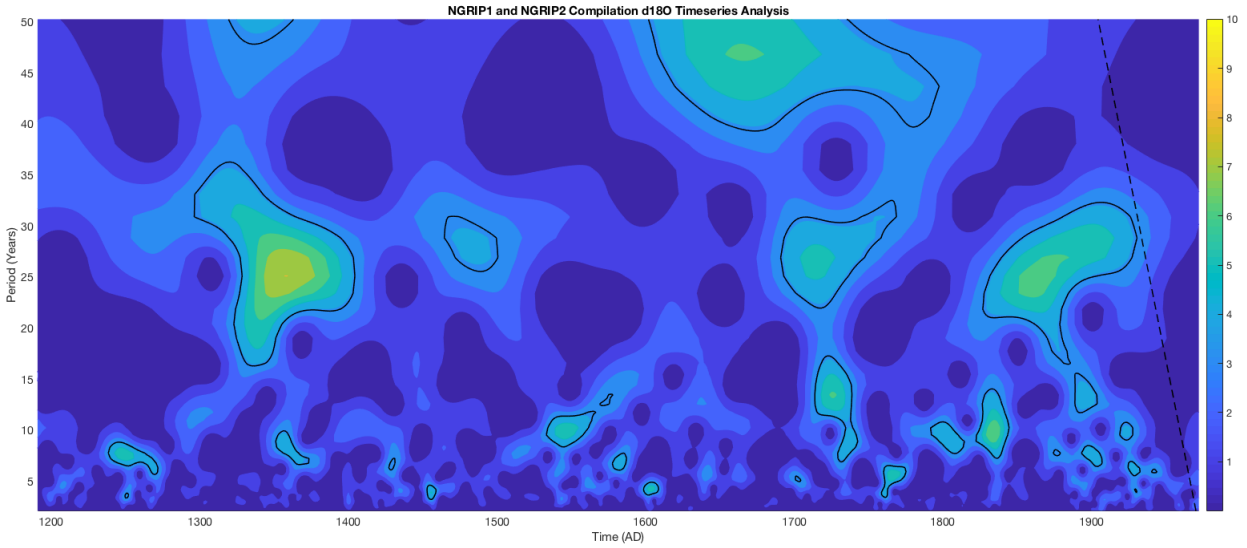

The tree ring wavelet analysis (Figure 6.37) indicates that there are strong signals in the tree ring record during strong La Niña years and/or very strong El Niño events. There

are numerous statistically significant 3-7 year signals, in particular between 1496A.D. to 1504A.D. and 1524A.D. to 1536A.D. These coincide with very strong El Niño years in 1525 and 1526, followed by strong to extreme La Niña years from 1528-1535A.D. (Gergis and Fowler, 2009).

Figure 6.37: Wavelet plot for tree ring oxygen isotopes 1200-2012 A.D.

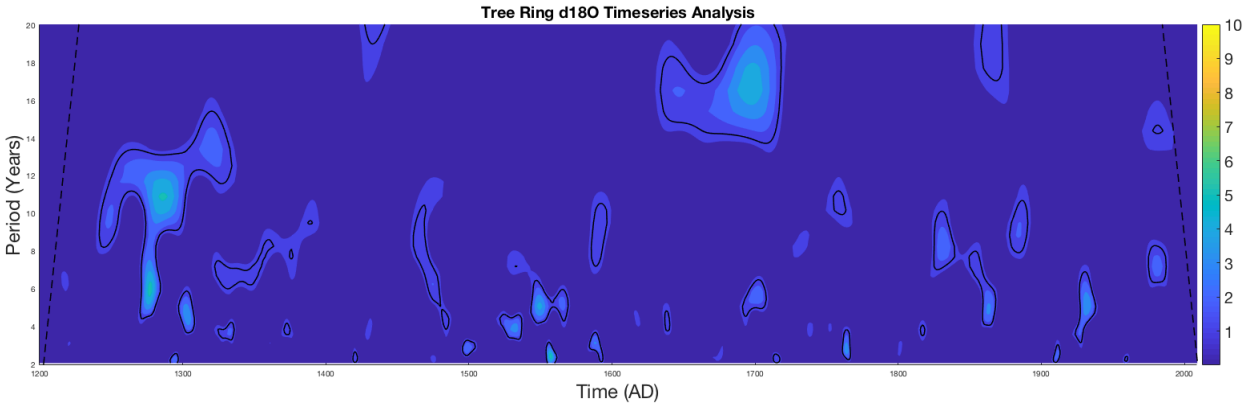

The NGRIP wavelet results from 2 to 20 year periodicity are shown in Figure 6.38. The region with the strongest power was at 1840A.D. with a 7-14 year periodicity. There are several 3-7 year regions consistent with an El Niño Southern Oscillation influence. These occurred at around 1250A.D., 1420A.D., 1450A.D., 1590A.D., 1600A.D., 1700A.D., 1760A.D. and 1950A.D. Despite both tree ring and NGRIP results showing influences from the same teleconnections, they do not appear have a concurrent influence.

Figure 6.38: Wavelet plot for ice core oxygen isotopes 1200-1973 A.D.

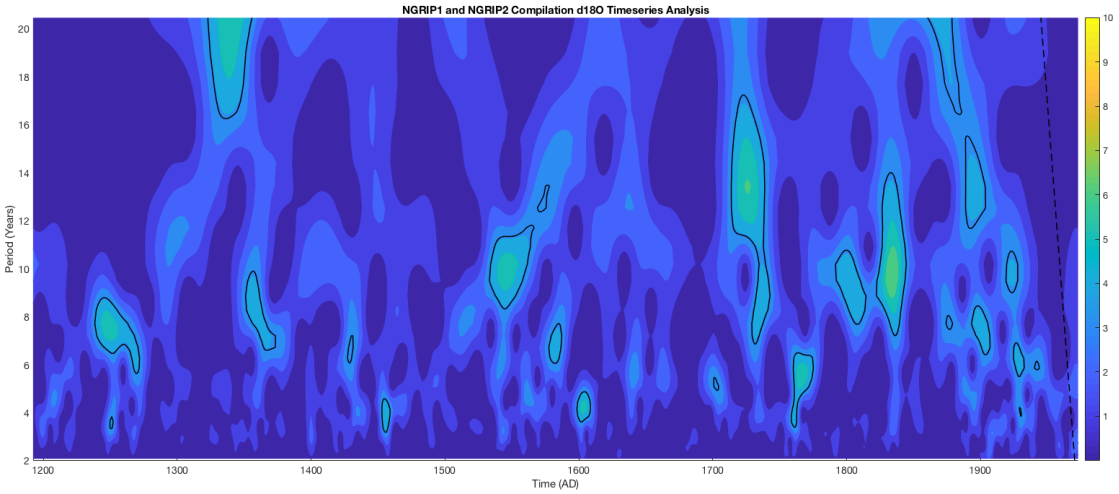

The cross wavelet and wavelet coherence plots (Figures 6.39, 6.40, 6.41 and 6.42) were produced using software provided by Grinsted et al. (2004) within Matlab. The cone of influence (COI) is shown as lighter shading and the thick black contour line shows the 5% significance level against red noise. The COI indicates where the edge effects may have an influence. The in-phase relationships are shown by arrows pointing right, anti-phase shown by left pointing arrows, and arrows that point straight down indicate a 90°lead in the second time series (the second dataset in the plot title). The cross wavelet plot indicates regions in which the two time series show high common power, within the time frequency space.

The cross wavelet plot in Figure 6.39 shows several regions of high common power. The region with the highest periodicity, from 34-66 years, was centred at 1300A.D. with a 90°lead between the two time series. Again, this coincides with the phase shift of the NAO from predominately positive to negative conditions. A region of recurring 20-32 year periodicity stretched from 1260-1500A.D., shifting between in-phased, 90°NGRIP

lead and anti-phased. There were two regions of anti-phase high common power of approximately 48 year periodicity centred at around 1640A.D. and 1810A.D. Just prior to 1900A.D. there was a 90°tree ring lag with a 16-32 year periodicity. Regions indicating a anti-phased shorter periodicity of approximately 7-9 years occurred at around 1250A.D., 1590A.D. and 1830A.D. In-phase regions with a periodicity of 2-9 year are indicated at 1265A.D., 1360A.D., 1600A.D., 1890A.D. and 1920A.D.; and a periodicity of 10-13 years are indicated at around 1300A.D. and 1720A.D.

These dates are consistent with the occurence of a negative phase of the AMO from 1890A.D. to 1920A.D., which shifted to a positive phase from 1925A.D. to 1960A.D. (Sutton et al., 2018), as well as a positive phase of the NAO from 1920A.D. to 1930A.D. (Hurrell and Loon, 1997; Visbeck et al., 2001).

Figure 6.39: Cross wavelet plot of tree rings and NGRIP compilation from 1200-1973 A.D.

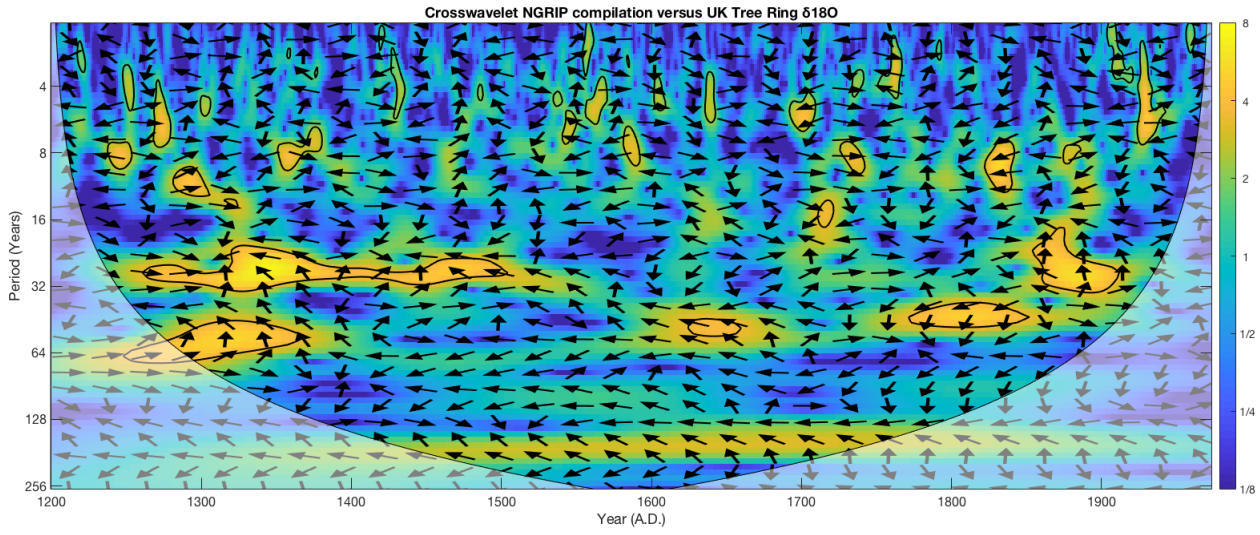

The three wavelet coherence plots (Figures 6.40, 6.41 and 6.42) indicate regions in which two time series covary without necessarily having high power, within the time

frequency space. Figure 6.40 shows strong regions of covariance between the NGRIP and tree ring records. There are regions with a NGRIP 90°lead at 1-2 year and 4-16 year periodicities just prior to 1500A.D., at a 16-32 year periodicity centred at 1900A.D., and a 32-60 year periodicity centred at 1350A.D. There was a strong region with a tree ring 90°led relationship at around 1650A.D., with a 3-8 year periodicity. There are two strong in phased regions, the first with a 8-16 year periodicity at approximately 1300A.D. and the second with a 6-12 year periodicity from approximately 1700-1730A.D. Finally, there are numerous significant anti-phased regions of strong power, with:

- 1-4 year periodicity at 1570A.D.,
- 1-2 year periodicity at 1930A.D.,
- 2-3 year periodicity at 1420A.D.,
- 4 year periodicity 1900-1910A.D.,
- 4-8 year periodicity at 1700A.D.,
- 5-9 year periodicity at 1230A.D.,
- 7-9 year periodicity at 1600A.D.,
- 8-16 year periodicity at 1840A.D., and
- 30 year periodicity at 1510A.D.

The NAO was in a positive phase from 1900-1915A.D., and a negative phase from 1930-1970 according to Hurrell and Loon (1997) and Visbeck et al. (2001).

Figure 6.40: Wavelet coherence plot of tree rings and NGRIP compilation from 1200-1973 A.D.

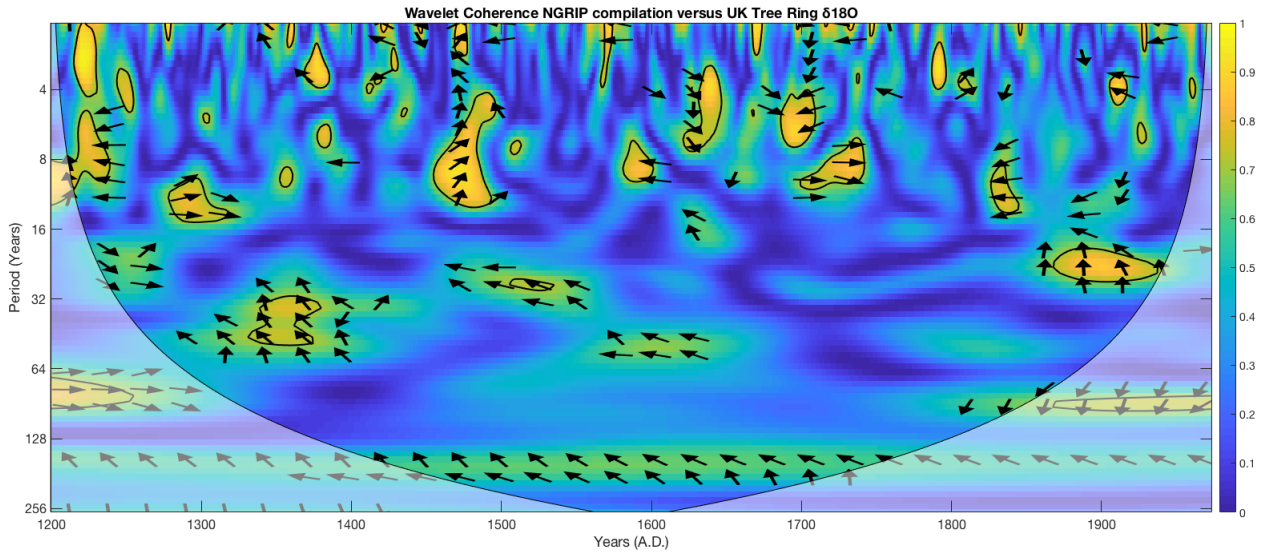

The wavelet coherence plot for the comparison of the UK historic temperatures compared to the tree ring δ^{18}O values is shown in Figure 6.41. There are four in-phase regions of significance at a 1-4 year periodicity during the years around 1910-1915, 1920, 1930 and 1960. These periods showing in-phased relationships are consistent with the general agreement of the two records shown in the earlier Figure 6.24. There is also a region of anti-phased covariance with an approximate periodicity of 18 years from 1930-1945A.D.

Figure 6.41: Wavelet coherence Pplot of UK historic temperatures versus tree rings from 1901-1973 A.D.

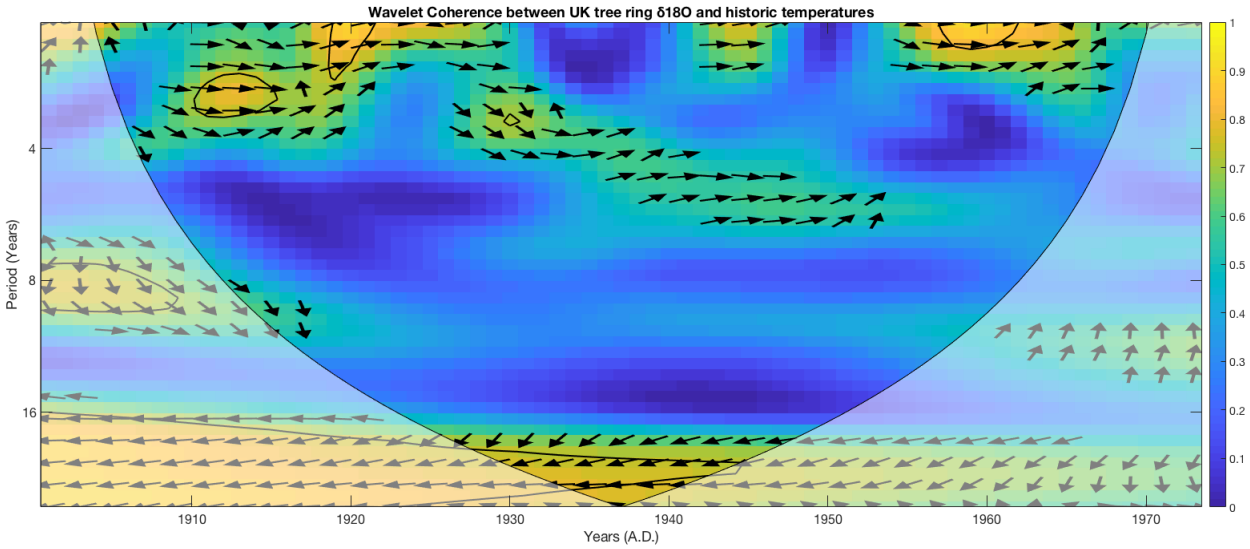

Figure 6.42 shows the wavelet coherence between the Greenland historic temperatures from Figure 6.26, and the NGRIP compilation data over the period from 1901-1973A.D. Within Figure 6.26 there appeared to be good cohesion between the peaks and troughs from 1920-1950A.D. Figure 6.42 shows that these two time series do covary during this time, at a period of approximately 3-8 years. The relationship during this time period appears to primarily consist of an in-phase to 90° historic temperature lead. The two other regions of significance show an in phase relationship at the 3 and 1-3 year period, centred around 1920A.D. as well as between 1935-1940A.D. respectively.

Figure 6.42: Wavelet coherence plot of Greenland historic temperatures versus NGRIP compilation from 1901-1973 A.D.

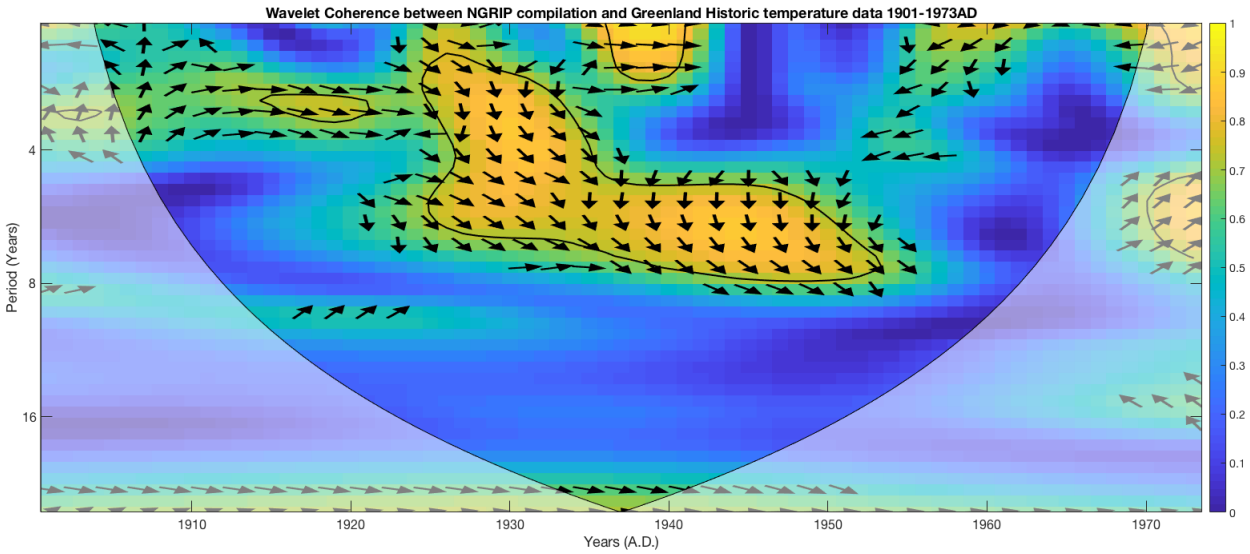

6.2 Discussion

This chapter explores a new high-resolution NGRIP2 ice core and a new master dataset of tree rings from the United Kingdom. These comparisons were conducted in order to determine whether the terrestrial tree ring records and the atmospheric NGRIP2 ice core record both show common climate influences. It also attempted to confirm whether the presence of the Little Ice Age and the Medieval Climate Anomaly is reflected in both these terrestrial and atmospheric isotope archives.

The comparison in Figure 6.3 between the existing ice core records within current literature clearly show the continental and altitude effect, similar to the results of the horse hair comparison. The century average comparisons found that the low δ^{18}O values occurred at 2000A.D. within the tree rings and values peaked during 1500A.D. within both

the tree ring and GRIP records. However, the NGRIP compilation showed the A.D. high to have occurred in 1900A.D., and the lowest δ^{18}O values from 200-500A.D. The GRIP core also showed the lowest δ^{18}O values from 100-500A.D. A 1400 A.D. peak in δ^{18}O within the NGRIP record was contrary to what is expected during the LIA. High δ^{18}O value peaks also occurred within the NGRIP record at 1200B.C., 900B.C., 300B.C. and 0A.D., with sharp rising values from 1600A.D.-1900A.D. in both the NGRIP and GRIP datasets, consistent with an anthropogenic influence. There appeared to be a delay between the increased δ^{18}O values of the 1400A.D. peak in NGRIP and the 1500A.D. peak in GRIP and tree rings. Finally, the results of the NGRIP2 century averages, specifically the lower values in the 6th century A.D. also show a potential influence of the 536-660A.D. Late Antique Ice Age (Büntgen et al., 2016).

1300A.D. was shown to be a key change point within the century averages and the alignment between the NGRIP and tree ring records. The tables in Section 6.1.7 showed that the NGRIP and GRIP records had lower minimum values, lower maximum values in the GRIP and tree rings, as well as lower means in the NGRIP and tree ring records during the Little Ice Age.

Looking into the moving average results, the increasing trend becomes more apparent in the NGRIP record from 1700-1973A.D., albeit with the hiatus from 1800-1850A.D. Within the 100 year moving average data, NGRIP showed the increasing trend from just prior to 1700A.D. The tree ring dataset showed two δ^{18}O peaks from approximately 1500-1575A.D. and 1675-1750A.D. Finally, all three records show an increase from 1600-1700A.D., with the GRIP and tree ring data showing a subsequent decline from 1700-1800A.D. and rise in values from 1800-1900A.D., although this pattern is dampened within the tree ring data.

Within the additional core comparisons, the highest mean values [least depleted], as expected, were shown at lower latitudes or coastal locations of Greenland. These included the Agassiz A79, Renland, and DYE3 cores. δ^{18}O values were most depleted in ^{18}O at the summit of the Greenland ice sheet, with a sharp longitudinal depletion gradient showing the strong continental effect, and an additional latitudinal influence with the continuation of lower δ^{18}O toward the northern-most coastline.

The 20 year running mean totals for the tree ring source water δ^{18}O against NGRIP δ^{18}O demonstrated that the relationship between these two time series is well aligned for the first 300 years. However, there were three large antiphased deviations in the NGRIP core at 1300A.D., just prior to 1400A.D., and just after 1450A.D. The records appeared to be antiphased again until approximately 1850A.D.

The results of the wavelet coherence analysis have shown that there are regions of strong common power within the NGRIP and tree ring datasets, as well as covariance without high power. The strongest region of common power between the two records had a 34-66 year periodicity at around 1300A.D., and had a 90°NGRIP lead. Regions of high common power and longer periodicities include 16-32 years at 1900A.D., 20-32 years at 1260-1500A.D., 48 years at 1640A.D. and 1810A.D. Regions of strong common power occurred more commonly as an in-phase relationship, although covariance more commonly occurred as an anti-phased relationship.

The comparison of the NGRIP and tree ring records showed that high common power, as well as covariance without high common power, occurred at 2-9 and 7-9 year periodicities over numerous dates. These results align with the 3-5 and 6-10 year cyclicity of ENSO cycles in the Pacific Ocean and North Atlantic Oscillation cycles in the Atlantic. The cross wavelet analysis showed 16-32, 20-32 and 48 year cyclicity, and the

individual NGRIP and tree ring wavelet analyses showed regions of high power at 20-40 and 50-80 year periodicities. These results reflect the Pacific Decadal Oscillation periodicity from 20-30 years and 50-70 years and Atlantic Multi-decadal Oscillation cycles from 50-90 years. Additionally, the 6-12 and 8-16 year periodicities seen within the NGRIP and tree ring cross wavelet analysis, as well as the two pulses of 25 year periodicity within the tree ring wavelet analysis reflect the 13-15 and 24-29 year solar cycles discussed by Miyahara et al. (2004).

There were several periods of high power and covariance, especially around 1300A.D., within the wavelet analysis, which coincided with shifts in the NAO, AMO and to a lesser degree, ENSO. As this was a key transitional period within the NAO, and likely also for the AMO, these results highlight the influence of the north Atlantic climate drivers on both the Greenland ice core and the United Kingdom tree ring records.

In summary, the high common power and covariance results, at periodicities of the same scale as the ENSO, NAO, AMO and PDO cycles, indicate a common influence from climate teleconnections and solar forcing within the terrestrial and atmospheric δ^{18}O values. The 1400A.D. peak in NGRIP followed by a 1500A.D. peak in tree ring values, confirmed by the dataset relationship results of the cross wavelet and wavelet coherence plots, also indicate that the larger scale climate teleconnections have an influence on Greenland prior to the eastern Atlantic [U.K.].

The results of this chapter have demonstrated that the presence of the Little Ice Age and the Medieval Climate Anomaly in both the terrestrial and atmospheric records is more clearly seen within the minimum δ^{18}O values. It has also shown that the NGRIP and tree ring records covary at an ENSO, NAO and AMO timescale.

7. Conclusions

This thesis has examined changes within oxygen isotope measurements of horse hair samples over time in order to explore the relationship with seasonal fluctuations in atmospheric conditions. This study specifically explored how changes in δ^{18}O values in horse hair directly reflect regional changes.

It has done this by examining relevant literature and scientific theory in Chapter 2 and exploring the background ecology, climate and geographical features of the study locations in Chapter 3. Chapter 4 demonstrated the methodologies used for the analysis of the three datasets. Chapter 5 and 6 presented and discussed the findings for the horse hair data, as well as the ice core and tree ring data, respectively. This chapter draws together the conclusions for this thesis by discussing the statistical uncertainties associated with comparing multiple climate proxy datasets [Section 7.1], suggesting avenues for further research and potential applications for this interdisciplinary research project

[Section 7.2], as well as highlighting the main findings from this thesis in the final Section 7.3.

7.1 Statistical uncertainty

When comparing complex datasets it is important to understand the statistical uncertainties associated with the analysis conducted.

The potential for intra-hair sequential change in growth rate may have an effect on the timing comparisons of the horse hair results in Chapter 5. The horse hairs were plotted against the median dates, which were extrapolated from the individual growth rates. Small changes in growth rate along the length of the hair could potentially cause errors in the date assignment of samples toward the tail end of the hair (dates furthest from the sampling date). Any small errors in the starting growth rate could also sequentially compound the inaccuracy of date assignments toward the tail end samples.

When considering the results of the horse hair sample accuracy examination, testing the homogenised samples of the *Rama* hair, the values shown have a maximum sampling error of $<0.5‰$. Examinations of multiple hairs over multiple sampling excursions, from single individuals (including *Robbie*, *Fudge*, *Gem*, *Silver* and *Jódís*) show that there is significant variation when sequentially analysing single hairs. However, when this noise is smoothed or normalised, examination of seasonal trends, meteorological influences and climate extreme events within the hair is possible. However, normalising the data using z-scores reduces internal variation, as a substitute method to using triplicate analysis.

The sampling sites and the pony breeds used in this study provide additional information to the increasing network of isotopic horse hair data. A comparison of these breeds with those already studied in Burnik Šturm et al. (2015) improves understanding of the intra-species variation within the δ^{18}O values of horse hair.

A key recommendation for future analysis of sequential horse hair for climatological comparison is the consistent and sole use of a hair compound standard, especially when comparing across analysis sets. Benzoic acid was not sufficient for comparisons between different hairs and sample runs. After the realisation of the profound impact of USGS42 inclusion, the widely varying averages were separated into two populations for further analysis in this study.

7.2 Applications

The purpose of this study was to compare the use of oxygen isotope analysis within different environmental archives across temporal and spatial scales. This study has interdisciplinary implications for the fields of archaeology, climatology, geography, physics, chemistry and geology. Each of these fields of research utilise and analysis isotope values for a range of purposes including climatological and dietary information.

In regards to further archaeological application, the study of oxygen isotopes in horse hairs have shown that it is possible to identify seasonal fluctuations within sequential samples. The comparable amplitudes of the meteoric water and the horse hair δ^{18}O also suggest a strong influence of drinking water on the keratin δ^{18}O. It is possible that these results can be used to further examine the implications of seasonal events in the archaeological record, through the analysis of human or other mammal hair values.

For example, the season that an individual died, or moved to a distinct dietary area, could be pinpointed. The results also showed the influence of rainfall and minimum temperatures. This has further potential application for identifying extreme cold or rainfall events, for the supplementation of historic meteorological records.

If a database were developed to record and cross-analyse temporally and spatially grouped δ^{18}O values of horse hair or keratin samples, similar to the dendrochronological process, it may be possible to use horse hair data such as this as a climate proxy, to supplement existing meteorological data. In locations with sparse historical data, it may provide enough information to assist the training of statistical climate forecasting systems and improve climate mitigation strategies.

Further examinations into the potential effects of temperature on horse hair growth would be beneficial; exploring whether northern horse breeds naturally have faster growing hair in order to account for harsher climates.

The Little Ice Age and Medieval Climate Anomaly were both periods that consisted of climate extremes, with subsequent ecological implications. Although this research did not show clear differentiation between the LIA, MCA and the intervening periods, within all statistical descriptives, there was evidence of the impact within the minimum temperatures, as well as evidence of a delay in the recording of climate teleconnection signals between Greenland and the United Kingdom. The results of this thesis indicate that more comparative research is required into the presence and timing of climate fluctuations within different local and regional proxy records of increasing complexity.

7.3 Conclusion

Although the horse hair results did not wholly support the expected effect of a latitudinal gradient on the oxygen isotope values, the results reflected the pattern of UK groundwater isotope distribution. The rainfall amount effect is expressed through south-westerly air masses moving over the United Kingdom, bringing high rainfall over the western coast and Exmoor. This causes increased depletion of δ^{18}O values toward the interior of the United Kingdom and the Oxfordshire region, and can be seen within the results of the horse hair comparison. Similar values for the Oxfordshire and Shetland hair, indicates a similar effect of latitude and rainfall amount. The increase in latitude displayed decreased values in Shetland and Iceland compared to Exmoor, however the impact of decreased rainfall amount in Oxfordshire manifested in similar values between Oxfordshire and the Shetland Islands. As revealed in the horse hair results, analysis of existing ice core records within the current literature found that the highest mean values [least depleted], were seen at lower latitudes or coastal locations of Greenland. δ^{18}O values were most depleted in ^{18}O at the summit of the Greenland ice sheet, with a sharp longitudinal depletion gradient suggesting a strong continental effect, and an additional latitudinal influence with the continuation of lower δ^{18}O toward the northern-most coastline.

Comparing the meteorological amplitudes against horse hair δ^{18}O, the temperature amplitudes are similar in magnitude to the hair amplitudes. It it clear from the response within the δ^{18}O of hair that there is a significant influence from the rainfall amount and seasonal temperature changes, which is consistent with basic isotopic theory and existing literature. The ice core comparison to historic temperatures showed similar offset to the modern difference between the ice sheet and coastal temperatures. The compar-

ison between tree ring isotopes can be interpreted as showing a similar amplitude to the historic temperatures, but with a slight dampening in regards to lower peaks values. Comparisons and correlation coefficient analysis of the tree ring and ice core values show good a negative relationship, with smaller amplitudes within the tree ring δ^{18}O results. This supports the hypothesis that oxygen isotopes show a common component within increasingly complex palaeoclimate records, albeit at different amplitudes and with an increased dampening effect.

Results of the fast Fourier transform analysis on the looped horse hair data demonstrated strong seasonal cycles in every hair. These results support and augment the findings of the amplitude comparison for the examination of the seasonal signals within biological δ^{18}O values in horse hair. Similarly, the high common power and covariance results of the ice core and tree ring δ^{18}O wavelet analysis, at periodicities of the same scale as the ENSO, NAO, AMO and PDO cycles, indicate a common influence from climate teleconnections and solar forcing within the terrestrial and atmospheric δ^{18}O values.

The results of the cross wavelet and wavelet coherence; with the delay between the 1400A.D. peak in NGRIP and 1500A.D. peak in tree ring values, indicates that Greenland experiences the influence of climate drivers such as the NAO and AMO at different temporal or spatial scales to the eastern Atlantic [U.K.]. As the greatest European impact from the AMO occurs during summer and the AO has a strong relationship with mean summer SST, these oscillations have a greater impact during the tree growing season and may therefore have had more of an influence on tree ring δ^{18}O values. However, the NAO impacts are primarily shown during the winter months, so might have a greater impact on the δ^{18}O ice core record in Greenland.

The 2 year and 3 year introduced lead times also showed similarities between the Green-

land and United Kingdom climates, within the atmospheric and terrestrial oxygen isotope records, though delayed within the tree ring dataset. This may be a reflection of link found by Gamiz-Fortis et al. (2011) between European land surface temperatures and Greenland SSTs up to 5 years prior. Alternatively, it could be that high resolution comparisons between regional proxy records of differing complexity may need to be chronologically adjusted to account for the climatological and biological delays.

A division was apparent when comparing the hair growth rate calculations in the northern and southern locations. The growth rates at the two northern horse locations [Iceland and Shetland Islands] had an average of 0.067cm/day. The two southern locations in Exmoor and Oxfordshire had a calculated average growth rate of 0.054cm/day. The growth rate calculations also suggested that differences are observed within the growth rates of different hairs of the same individual. The presence of so many confounding factors, such as this hair growth fluctuation, has suggested that it is the variation of the δ^{18}O values in horse hair that are important for this type of analysis, rather than the absolute values.

An interesting result of this research is that the horse hair analysis suggested that the minimum temperatures are a key indicator of change. The horse hair δ^{18}O results showed the Exmoor, Oxfordshire and Shetland Island values to be in the same statistical population. The winter minimum temperatures showed only a 0.9°difference between these locations, although there was a 3.7°difference from the Icelandic minimum temperature. These results indicated a relationship between winter minimum temperatures and horse hair δ^{18}O.

This research has examined the overarching question of how oxygen isotopic ratios are recorded among palaeoenvironmental archives with different levels of fractionation

complexity. It examined how δ^{18}O is affected by climate, and can therefore be used to reconstruct palaeoclimate. This was conducted using two case studies: firstly exploring how climate signals in ice core and tree ring records affect oxygen isotope values, during historical periods of extreme climate variability; and secondly, examining the relationship of oxygen isotopes within horse hair to latitude and climate. The purpose of these case studies is to enable researchers to improve comparisons of climate data from different environmental records; learn more about the mechanisms of past climate changes; and subsequently to enhance what is known about possible future climate changes.

The investigation of the latitudinal comparison of δ^{18}O values within horse hair is unique, as is the examination of the subsequent relationship between those δ^{18}O values and local meteorological variables. Horses are useful for this type of analysis because of their wide geographic and temporal range, and the strong relationship in the data to precipitation. This thesis suggests and confirms that there is still potential to use horse hair δ^{18}O for climate extremes and seasonality comparisons, although there needs to be further research into an accurate and timely method for estimating the intra-hair growth rate changes for each individual horse.

By bringing together analysis of increasingly complex palaeoenvironmental proxies, this thesis critically evaluates δ^{18}O measurements within atmospheric and terrestrial systems, across geographical transitions; as well as contribute to a greater understanding of the utilisation of oxygen isotope data for seasonal climate analysis. Ultimately, this thesis aimed to improve what is known about the relationship between oxygen isotopic ratios, geography and climate, as well as meteorological variables such as air temperature and rainfall. It consequently has the potential to contribute to future development of important new methodologies in relation to understanding changes in climate.

References

Allison, G.B., Gat, J.R. and Leaney, F.W.J. (1985). The relationship between deuterium and oxygen-18 delta values in leaf water. Chemical Geology: Isotope Geoscience Section, 58, pp. 145-156.

Ambrose, S. and Norr L. (1993). Experimental evidence for the relationship of the carbon isotope ratios of whole diet and dietary protein to those of bone collagen and carbonate. Lambert, J.B. and Grupe G. (ed.). Prehistoric human bone: archaeology at the molecular level. Berlin: Springer-Verlag. pp. 1-37.

Anderson, W.T., Bernasconi, S.M., McKenzie, J.A., Saurer, M. and Schweingruber, F. (2002). Model evaluation for reconstructing the oxygen isotopic composition in precipitation from tree ring cellulose over the last century. Chemical Geology: Isotope Geoscience Section, 182, pp. 121-137.

Andrews, J.T. (2005). Late Quaternary marine sediment studies of the Iceland shelf,

paleoceanography and land/ice sheet/ocean interactions. Caseldine, C., Russell, A., Hardardottir, J. and Knudsen, O. (eds.), Iceland Modern processes and past environments. London: Elsevier, 5(24).

Araguas, L., Danesi, P., Froehlich, K. and Rozanski, K. (1996). Global monitoring of the isotopic composition of precipitation. Journal of Radioanalytical and Nuclear Chemistry, Articles, 205(2), pp.189-200. [online] Available at: http://www.akademiai.com/doi/abs/10.1007/BF02039404.

Árnason, T. and Bjarnason, T. (1994). Growth and size of Icelandic toelter horses. Livestock Production Science, Abstracts, 40(1), pp. 79.

Axford, Y., Andresen, C.S., Andrews, J.T., Belt, S.T., Geirsdóttir, A., Massé, G., Miller, G.H., Ólafsdóttir, S. and Vare, L.L. (2011). Do paleoclimate proxies agree? A test comparing 19 late Holocene climate and sea-ice reconstructions from Icelandic marine and lake sediments. Journal of Quaternary Science, 26(6), pp. 645-656.

Ayliffe, L., Cerling, T., Robinson, T., West, A., Sponheimer, M., Passey, B., Hammer, J., Roeder, B., Dearing, M. and Ehleringer, J. (2004). Turnover of carbon isotopes in tail hair and breath CO 2 of horses fed an isotopically varied diet. Oecologia, 139(1), pp. 11-22. [online] Available at: http://www.ncbi.nlm.nih.gov/pubmed/14730442.

Baez, J.C., Gimeno, L., Gomez-Gesteira, M., Ferri-Yanez, F. and Real, R. (2013). Combined effects of the North Atlantic Oscillation and the Arctic Oscillation on sea surface temperature in the Alboran Sea. PLoS ONE, 8(4), pp. 1-9.

Baker, A.J. (2014). Lagrangian modelling of precipitation and speleothem proxy oxygen isotope systematics in the East Asian Summer Monsoon region. Durham the-

ses, Durham University. [online] Available at: http://etheses.dur.ac.uk/11460/.

Baker, S. (ed.), Davy, D., Dent, A., Webb, J. and Webber, J. (2000). The Exmoor pony handbook of the Exmoor Pony Society. Dulverton, Somerset: The Exmoor Pony Society, 72, pp. 41-45.

Baldini, L.M., McDermott, F., Foley, A.M. and Baldini, J.U.L. (2008). Spatial variability in the European winter precipitation δ^{18}O-NAO relationship: Implications for reconstructing NAO-mode climate variability in the Holocene. Geophysical Research Letters, 35, pp. 1-6.

Bampton, M., Kelley, A., Kelley, J., Jones, M. and Bigelow, G. (2017). Little Ice Age catastrophic storms and the destruction of a Shetland Island community. Journal of Archaeological Science, 87, pp. 17-29.

Barbour, M.M., Walcroft, A.S. and Farquhar, G.D. (2002). Seasonal variation in δ^{13}C and δ^{18}O of cellulose from growth rings of *Pinus radiata*. Plant, Cell and Environment, 25, pp. 1483-1499.

Beranova, R. and Kysely, J. (2012). Relationships between the North Atlantic Oscillation index and temperatures in Europe in global climate models. Studia Geophysica et Geodaetica, 57, pp. 138-153.

Bhushan, B. (2008). Nanoscale characterization of human hair and hair conditioners. Progress in Materials Science, 53, pp. 585-710.

Bierkens, M., Dolman, A. and Troch, P. (2008). Climate and the hydrological cycle. Wallingford: International Association of Hydrological Sciences.

Birchall, J., O'Connell, T.C., Heaton, T.H.E. and Hedges, R.E.M (2005). Hydrogen isotope ratios in animal body protein reflect tropic level. Journal of Animal Ecology, 74, pp. 877-881.

Block, R. (1939). The composition of keratins: The amino acid composition of hair, wool, horn, and other eukeratins. Journal of Biological Chemistry, 128, pp. 181-186.

Bony, S., Risi, C. and Vimeux, F. (2008). Influence of convective processes on the isotopic composition (δ^{18}O and δ D) of precipitation and water vapor in the tropics: 1. radiative-convective equilibrium and tropical ocean-global atmosphere-coupled ocean-atmosphere response experiment (TOGA-COARE) simulations. Journal of Geophysical Research: Atmospheres, pp. 113.

Bowen, G.J., Revenaugh, J. (2003). Interpolating the isotopic composition of modern meteoric precipitation. Water Resources Research, 39. [online] Available: `http://wateriso.eas.purdue.edu/waterisotopes/media/PDFs/2003WR002086.pdf`.

Bowen, G.J., Chesson, L., Nielson, K., Cerling, T.E. and Ehleringer, J.R. (2005a). Treatment methods for the determination of δ^{2}H and δ^{18}O of hair keratin by continuous-flow isotope-ratio mass spectrometry. Rapid Communications in Mass Spectrometry, 19(17), pp. 2371-2378.

Bowen, G.J., Wassenaar, L.I., Hobson, K.A. (2005). Global application of stable hydrogen and oxygen isotopes to wildlife forensics. Oecologia, 143, pp. 337-348.

Bowen, G., Ehleringer, J., Chesson, L., Thompson, A., Podlesak, D. and Cerling, T. (2009). Dietary and physiological controls on the hydrogen and oxygen isotope ratios of hair from mid-20th century indigenous populations. American Journal of Physical

Anthropology, 139(4), pp. 494-504. [online] Available at: http://www.ncbi.nlm.nih.gov/pubmed/19235792.

Brinkmann, L. Gerken, M. and Riek, A. (2012). Adaptation strategies to seasonal changes in environmental conditions of a domesticated horse breed, the Shetland pony (*Equus ferus caballus*). Journal of Experimental Biology, 215, pp. 1061-1068.

Brutsaert, W. (1982). Evaporation into the atmosphere: theory, history, and applications. Springer Science Business Media, Dordrecht.

Bryant, D. and Froelich, P.N. (1995). A model of oxygen isotope fractionation in body water of large mammals. Geochimica et Cosmochimica Acta, 59, pp. 4523-4537.

Büntgen, U., Myglan, V.S., Ljungqvist, F.C., McCormick, M., Di Cosmo, N., Sigl, M., Jungclaus, J., Wagner, S., Krusic, P.J., Esper, J., Kaplan, J.O., de Vaan, M.A.C., Luterbacher, J., Wacker, L., Tegel, W. and Kirdyanov, A.V. (2016). Cooling and societal change during the Late Antique Little Ice Age from 536 to around 660A.D. Nature Geoscience, 9, pp. 231-236.

Burk, R.L. and Stuiver, M. (1981). Oxygen isotope ratios in trees reflect mean annual temperature and humidity. Science, 211 (4489), pp. 1417-1419.

Burnik Šturm, M., Pukazhenthi, B., Reed, D., Ganbaatar, O., Sušnik, S., Haymerle, A., Voigt, C. and Kaczensky, P. (2015). A protocol to correct for intra- and interspecific variation in tail hair growth to align isotope signatures of segmentally cut tail hair to a common time line. Rapid Communications in Mass Spectrometry, 29(11), pp. 1047-1054.

Burton, S.H. (1978). Exmoor. 3rd Edition. Robert Hale Ltd., London. Printed and bound in Great Britain by Redwood Burn Limited Trowbridge and Esher.

Cerling, T.E., Hart, J.A. and Hart, T.B. (2004). Stable isotope ecology in the Ituri forest. Oecologia, 138, pp. 5-12.

Cerling, T., Wittemyer, G., Rasmussen, H., Vollrath, F., Cerling, C., Robinson, T. and Douglas-Hamilton, I. (2006). Stable isotopes in elephant hair document migration patterns and diet changes. Proceedings of the National Academy of Sciences, 103(2), pp. 371-373.

Cerling, T.E., Ayliffe, L.K., Dearing, M.D., Ehleringer, J.R., Passey, B.H., Podlesak, D.W., Torregrossa, A. and West, A.G. (2007). Determining biological tissue turnover using stable isotopes: The reaction progress variable. Oecologia, 151(2), pp. 175-189.

Chafik, L. (2012). The response of the circulation in the Faroe-Shetland Channel to the North Atlantic oscillation. Tellus, Series A, Dynamic meteorology and oceanography, 64 (18423), pp. 1-12.

Chen, G., Schnyder, H. and Auerswald, K. (2017). Model explanation of the seasonal variation of δ^{18}O in cow (*Box taurus*) hair under temperate conditions. Scientific Reports, 7(320), pp. 1-15.

Chenet, M., Roussel, E., Jomelli, V. and Grancher, D. (2010). Asynchronous Little Ice Age glacial maximum extent in southeast Iceland. Geomorphology, 114, pp. 253-260.

Chu, V.W. (2014). Greenland ice sheet hydrology: A review. Progress in Physical Geography, 38 (1), pp. 19-54.

Climate.gov (2016). Forensic meteorology solves the mystery of record snows | NOAA Climate.gov. [online] Available at: `https://www.climate.gov/news-features`

/understanding-climate/forensic-meteorology-solves-mystery-record-snows.

Cole, J.E., Rind, D., Webb, R.S., Jouzel, J. and Healy, R. (1999). Climatic controls on interannual variability of precipitation δ^{18}O: Simulated influence of temperature, precipitation amount, and vapor source region. Journal of Geophysical Research: Atmospheres, 104, pp. 259-267.

Cooley, J.W., Lewis, P.A.W. and Welch, P.D. (1969). The fast Fourier transform and its applications. IEEE Transactions on Education, 12(1), pp. 27-34.

Coplen, T.B. (1988). Normalization of oxygen and hydrogen isotope data. Chemical Geology (Isotope Geoscience Section), 72, pp. 293-297.

Coplen, T.B. (1994). Reporting of stable hydrogen, carbon, and oxygen isotopic abundances. International Union of Pure and Applied Chemistry, 66 (2), pp. 273-276.

Coplen, T.B. (2011). Guidelines and recommended terms for expression of stable-isotope-ratio and gas-ratio measurement results. Rapid Communications in Mass Spectrometry, 25, pp. 2538-2560.

Cryan, P.M., Bogan, M.A., Rye, R.O., Landis, G.P. and Kester, C.L. (2004). Stable hydrogen isotope analysis of bat hair as evidence for seasonal molt and long-distance migration. Journal of Mammalogy, 85, pp. 995-1001.

Csank, A.Z., Fortier, D. and Leavitt, S.W. (2013). Annually resolved temperature reconstructions from a late PlioceneâĂŞearly Pleistocene polar forest on Bylot Island, Canada. Palaeogeography, Palaeoclimatology, Palaeoecology, 369, pp. 313âĂŞ322.

Dansgaard, W. (1964). Stable isotopes in precipitation. Tellus, 16 (4), pp. 436-468.

Dansgaard, W., Johnsen, S.J., Clausen, H.B. and Gundestrup, M. (1973). Stable isotope glaciology. Meddelelser om Gronland, 197(2), pp. 1-53.

Dansgaard, W., Johnsen, S.J., Clausen, H.B., Dahl-Jensen, D., Gundestrup, N.S., Hammer, C.U., Hvidberg, C.S., Steffensen, J.P., Sveinbjórnsdottir, A.E., Jouzel, J. and Bond, G. (1993). Evidence for general instability of past climate from a 250 kyr ice core record. Nature. [online] Available at: http://jonah.org/journal%5C_club/03%5C_supplement/a%5C_1993%5C_dansgaard%5C_original%5C_do%5C_record.pdf.

Darling, W. and Talbot, J. (2003). The O and H stable isotope composition of freshwaters in the British Isles. 1. Rainfall Hydrology Earth System Science, 7(2), pp. 163-181.

Darling, W.G. (2004). Hydrological factors in the interpretation of stable isotopic proxy data present and past: a European perspective. Quaternary Science Reviews 23.7-8, pp. 743-770. [online] Available at: http://linkinghub.elsevier.com/retrieve/pii/S0277379104000149.

Deedrick, D.W. and Koch, S.L. (2004). Microscopy of hair part 1: A practical guide and manual for human hairs. Forensic Science Communications, 6(1). [online] Available at: https://archives.fbi.gov/archives/about-us/lab/forensic-science-communications/fsc/jan2004/research/2004.

DeNiro, M.J. and Epstein, S. (1978). Influence of diet on the distribution of carbon isotopes in animals. Geochimica et Cosmochimica Acta, 42(5), pp. 495-506.

Dezileau, L., Sabatier, P., Blanchemanche, P., Joly, B., Swingedouw, D., Cassou, C., Castaings, J., Martinez, P. and Von Grafenstein, U. (2011). Intense storm activ-

ity during the Little Ice Age on the French Mediterranean coast. Palaeogeography, Palaeoclimatology, Palaeoecology, 299, pp. 289-297.

DMI: Danish Meteorological Institute (2016). Greenland: DMI. [online] Available at: https://www.dmi.dk/en/klima/klimaet-frem-til-i-dag/groenland/.

Dongmann, G., Nürnberg, H.W., Förstel, H. and Wagener, K. (1974). On the enrichment of $H_2^{18}O$ in the leaves of transpiring plants. Radiation and Environmental Biophysics, 11(1), pp. 41-52.

Drake, B.L. (2017). Changes in North Atlantic Oscillation drove population migrations and the collapse of the western Roman empire. Nature: Scientific Reports, 7(1227), pp.1-7.

Duffy, J.E., McCarroll, D., Barnes, A., Bronk Ramsey, C., Davies, D., Loader, N.J., Miles, D. and Young, G.H.F. (2017). Short-lived juvenile effects observed in stable carbon and oxygen isotopes of UK oak trees and historic building timbers. Chemical Geology, 472, pp.1-7.

Dunnett, M. (2001). The diagnostic potential of equine hair: a comparative review of hair analysis for assessing nutritional status, environmental poisoning, and drug use and abuse. pp. 85-106.

Edwards, T.W.D., Hammarlund, D., Newton, B.W., Sjolte, J., Linderson, H., Sturm, C., St. Amour, N.A., Bailey, J.N.-L. and Nilsson, A.L. (2017). Seasonal variability in Northern Hemisphere atmospheric circulation during the Medieval Climate Anomaly and the Little Ice Age. Quaternary Science Reviews, 165, pp. 102-110.

Ehleringer, J., Bowen, G., Chesson, L., West, A., Podlesak, D. and Cerling, T. (2008). Hydrogen and oxygen isotope ratios in human hair are related to geography. Pro-

ceedings of the National Academy of Sciences, 105(8), pp. 2788-2793. [online] Available at: http://www.pnas.org/content/105/8/2788.short.

Elemental Microanalysis (2010). Technical report - EML reference materials for IRMS. [online] Available at: https://www.elementalmicroanalysis.com/product_list.php?sub=Isotope-Reference-Materials&category=124&menu=6.

Ellsworth, P.V. (2012). Oxygen isotope signature of cellulose: Advances as a climate proxy. Doctor of Philosophy. University of Miami

Eltahir, E.A.B. and Bras, R.L. (1996). Precipitation recycling. Reviews of Geophysics, 34, pp. 367-378.

Enfield, D.B. and Cid-Serrano, L. (2010). Secular and multidecadal warmings in the North Atlantic and their relationships with major hurricane activity. International Journal of Climatology, 30, pp. 174-184.

Esper, J., Frank, D.C., Timonen, M., Zorita, E., Wilson, R.J.S., Luterbacher, J., Holzkámper, S., Fischer, N., Wagner, S., Nievergelt, D., Verstege, A. and Búntgen, U. (2012). Orbital forcing of tree-ring data. Nature Climate Change, 2, pp. 862-866.

Esri (2017). ArcGIS: World Topographic Map. [online] Available at: http://www.arcgis.com/home/item.html?id=30e5fe3149c34df1ba922e6f5bbf808f.

Field, R.D. (2010). Observed and modelled controls on precipitation d18O over Europe: From local temperature to the Northern Annular Mode. Journal of Geophysical Research, 115, pp. 1-14.

Flanagan, L.B., Comstock, J.P. and Ehleringer, J.R. (1991). Comparison of modelled

and observed environmental influences on the stable oxygen and hydrogen isotope composition of leaf water in Phaseolus vulgaris L. Plant Physiology, 96, pp. 588-596.

Fricke, H.C., Clyde, W.C. and O'Neil, J.R. (1998). Intra-tooth variations in δ^{18}O (PO4) of mammalian tooth enamel as a record of seasonal variations in continental climate variables. Geochimica et Cosmochimica Acta, 62(11), pp 1839-1850.

Froehlich, K., Gibson, J.J. and Aggarwal, P. (2002). Deuterium excess in precipitation and its climatological significance. International Atomic Energy Agency, pp. 1-23. [online] Available at: https://inis.iaea.org/search/search.aspx?orig_q=RN:34017972.

Fugal, D. (2009). Conceptual wavelets in digital signal processing. San Diego, California: Space and Signals Technologies LLC Publishing.

Gallardo, C., Gil, V., Hagel, E., Tejeda, C. and de Castro, M. (2013). Assessment of climate change in Europe from an ensemble of regional climate models by the use of Kóppen-Trewartha classification. International Journal of Climatology, 33, pp. 2157-2166.

Gamiz-Fortis, S.R., Esteban-Parra, M.J., Pozo-Vazquez, D. and Castro-Diez, Y. (2011). Variability of the monthly European temperature and its association with the Atlantic sea-surface temperature from interannual to multidecadal scales. International Journal of climatology, 31, pp. 2115-2140.

García-Suárez, A., Butler, C. and Baillie, M. (2009). Climate signal in tree-ring chronologies in a temperate climate: A multi-species approach. Dendrochronologia, 27(3), pp. 183-198.

Garrison, T. ed. (2007). 9: Circulation of the ocean. Oceanography: An invitation to

marine science, 6th edition Belmont CA: Thomson Brooks/Cole, pp. 235.

Gat, J.R., Airey, P.L. (2006). Stable water isotopes in the atmosphere biosphere lithosphere interface: Scaling-up from the local to continental scale, under humid and dry conditions. Global Planetary Change, 51, pp. 25-33.

Geyfman, M., Plikus, M.V., Treffeisen, E., Andersen, B. and Paus, R. (2015). Resting no more: re-defining telogen, the maintenance stage of the hair growth cycle. Biological Reviews, 90, pp. 1179-1196.

Geos, F. (2001). Wind and wave frequency distributions for sites around the British Isles. Offshore technology report 2001/030. Southampton Oceanography Centre. Health & Safety Executive. Norwich, United Kingdom.

Gergis, J.L. and Fowler, A.M. (2009). A history of ENSO events since A.D. 1525: implications for future climate change. Climatic Change, 92, pp. 343-387.

Gfy.ku.dk. (2016). NGRIP - English version. [online] Available at: `http://www.gfy.ku.dk/~www-glac/ngrip/index_eng.htm`.

Gkinis, V., Simonsen, S.B., Buchardt, S.L., White, J.W C. and Vinther, B.M. (2014). Water isotope diffusion rates from the NorthGRIP ice core for the last 16,000 years - Glaciological and paleoclimatic implications. Earth and Planetary Science Letters, 405, pp. 132-141.

Golledge, N.R., Finlayson, A., Bradwell, T. and Everest, J.D. (2008). The last glaciation of Shetland, North Atlantic. Physical Geography, 90A (1), pp. 37-53.

Gonfiantini, R., Gratziu, S., Tongiorgi, E., 1965. Oxygen isotopic composition of water in leaves, in: Isotopes and radiation in soil-plant-nutrition studies. International

Atomic Energy Commission, Vienna, pp. 405-410.

Grinsted, A., Moore, J.C. and Jevrejeva S. (2004). Application of the cross wavelet transform and wavelet coherence to geophysical time series, Nonlinear Processes in Geophysics, 11 (5/6), pp. 561-566. [online] Available at: http://www.glaciology.net/Home/PDFs/Announcements/Application-of-the-cross-wavelet-transform-and-wavelet-coherence-to-geophysical-time-series.

Guillevic, M., Bazin, L., Landais, A., Kindler, P., Orsi, A., Masson-Delmotte, V., Blunier, T., Bucahrdt, S.L., Capron, E., Leuenberger, M., Martinerie, P., Prie, F. and Vinther, B.M. (2013). Spatial gradients of temperature, accumulation and δ^{18}O-ice in Greenland over a series of Dansgaard-Oeschger events. Climate of the Past, 9, pp. 1029-1051 .

Gundmundsson, A. and Andrew, R.E.B. (2007). Mechanical interaction between active volcanoes in Iceland. Geophysical Research Letters, 34, L10310.

Hahn, C.J. and Warren, S.G. (1999). Extended edited synoptic cloud reports from ships and land stations over the globe, 1952-1996. Environmental Sciences Division, US Department of Energy, Oak Ridge, Tennessee. [online] Available at: http://cdiac.ess-dive.lbl.gov/epubs/ndp/ndp026c/ndp026c.html.

Hanna, E., Fettweis, X., Mernild, S.H., Cappelen, J., Ribergaard, M.H., Shuman, C.A., Steffen, K., Wood, L. and Mote, T.L. (2013). Atmospheric and oceanic climate forcing of the exceptional Greenland ice sheet surface melt in summer 2012. International Journal of Climatology, 34, pp. 1022-1037.

Hare, P.E., Fogel, M.L., Stafford, T.W., Mitchell, A.D. and Hoering, T.C. (1991). The isotopic composition of carbon and nitrogen in individual amino acids isolated from

modern and fossil proteins. Journal of Archaeological Science, 18, pp. 277-292.

Harris, I.C. and Jones, P.D. (2017). CRU TS4.01: Climatic Research Unit (CRU) Time-Series (TS) version 4.01 of high-resolution gridded data of month-by-month variation in climate (Jan. 1901- Dec. 2016). Centre for Environmental Data Analysis. [online] Available at: http://dx.doi.org/10.5285/58a8802721c94c66ae45c3baa4d814d0.

Harrison, S., Rowan, A.V., Glasser, N.F., Knight, J., Plummer, M.A. and Mills, S.C. (2014). Little Ice Age glaciers in Britain: Glacier-climate modelling in the Cairngorm Mountains. The Holocene, 24 (2), pp. 135-140.

Hass, H.C. (1996). Northern Europe climate variations during late Holocene: evidence from marine Skagerrak. Palaeogeography, Palaeoclimatology, Palaoecology, 123, pp. 121-145.

Helliker, B., Ehleringer, J. (2002). Differential 18O enrichment of leaf cellulose in C3 versus C4 grasses. Functional Plant Biology, 29, pp. 435-442.

Hénaux, V., Powell, L.A., Hobson, K.A., Nielsen, C.K. and LaRue, M.A. (2011). Tracking large carnivore dispersal using isotopic clues in claws: an application to cougars across the Great Plains. Methods in Ecology and Evolution, 2. Available: http://dx.doi.org/10.1111/j.2041-210X.2011.00107.x.

Herget, J. (2005). Reconstruction of Pleistocene ice-dammed lake outburst floods in the Altai Mountains, Siberia. The Geological Society of America Inc., Boulder, Colorado.

Hobson, K.A. (2005). Stable isotopes and the determination of avian migratory connectivity and seasonal interactions. The Auk, 122, pp. 1037-1048.

Hobson, K.A and Wassenaar, L.I. (2008). Tracking animal migration with stable isotopes. Hobson K.A. and Wassenaar L.I., (ed.). London, UK: Academic Press, pp. 143.

Hodson, A. (1997). The Shetland pony: Allen breed series. London, UK: Allen and Company.

Hoefs, J. (2009). Stable Isotope Geochemistry. Berlin: Springer-Verlag.

Hoffmann, G. and Jouzel, J. (2001). Deuterium excess record from central Greenland over the last millennium Hints of a North Atlantic signal during the Little Ice Age century, 106, pp. 265-274.

Holmquist, J.R., Booth, R.K. and MacDonald, G.M. (2016). Boreal peatland water table depth and carbon accumulation during the Holocene Thermal Maximum, Roman Warm Period, and Medieval Climate Anomaly. Palaeogeography, Palaeoclimatology, Palaeoecology, 444, pp. 15-27.

Hook, B.A., Halfar, J., Gedalof, Z., Bollmann, J. and Schulze, D.J. (2015). Stable isotope paleoclimatology of the earliest Eocene using kimberlite-hosted mummified wood from the Canadian Subarctic. Biogeosciences, 12, pp. 5899-5914.

Hoppe, K.A. (2006). Correlation between the oxygen isotope ratio of North American bison teeth and local waters: Implication for paleoclimatic reconstructions. Earth and Planetary Science Letters, 244(1-2), pp. 408-417.

House, J. (1870). Geography of Oxfordshire. Lawson, W. (ed.). Collins' County Geographies, London, UK.

Hubálek, Z. (2016). The North Atlantic Oscillation system and plant phenology. Inter-

national Journal of Biometeorology, 60, pp. 749-756.

Hurrell, J.W. and Loon, H.V. (1997). Decadal variations in climate associated with the North Atlantic Oscillation. Climatic Change, 36, pp. 301-326.

Hurrell, J.W., Kushnir, Y. and Visbeck, M. (2001). The North Atlantic Oscillation. Science, 291 (5504), pp. 603-605.

Hvidberg, C.S., Steffensen, J.P., Clausen, H.B., Shoji, H. and Kipfstuhl, J. (2002). The NorthGRIP ice-core logging procedure: description and evaluation. Annals of Glaciology, 35, pp. 5-8.

IAEA/WMO (2018). Global network of isotopes in precipitation. The GNIP database. [online] Available at: `https://nucleus.iaea.org/wiser`.

IBM Corporation (2013). IBM SPSS statistics for Windows, version 22.0. Armonk, NY: IBM Corporation,

Iceandclimate.nbi.ku.dk. (2016). The central Greenland ice cores - University of Copenhagen. [online] Available at: `http://www.iceandclimate.nbi.ku.dk/research/drill_analysing/history_drilling/central_ice_cores/`.

Innera, M., Petersen, A.D., Desjardinst, D.R., Steficekt, B.A., Rosser, E.J. and Schott, H.C. (2013). Comparison of hair follicle histology between horses with pituitary pars intermedia dysfunction and excessive hair growth and normal aged horses. Veterinary Dermatology, 24, pp. 212-217.

Jardine, T.D. and Cunjak, R.A. (2005). Analytical error in stable isotope ecology. Oecologia, 144, pp. 528-533.

Jeffrey, A. (2016). Exploring palaeoaridity using stable oxygen and carbon isotopes in

small mammal teeth: a case study from two Late Pleistocene archaeological cave sites in Morocco, North Africa. Doctor of Philosophy. University of Oxford.

Jenkins, G.J., Perry, M.C. and Prior, M.J. (2008). The climate of the United Kingdom and recent trends. Met Office Hadley Centre, Exeter, UK. [online] Available at: www.ukcip.org.uk.

Jiang, H., Seidenkrantz, M.S., Knudsen, K.L. and Eiríksson, J. (2002). Late-Holocene summer sea-surface temperatures based on a diatom record from the north Icelandic shelf. The Holocene, 12(2), pp. 137-147.

Johnsen, S.J. (1977). Stable isotope homogenization of polar firn and ice. In Proceedings of Symposium on Isotopes and Impurities in Snow and Ice, I.U.G.G. XVI, General Assembly, Grenoble. 1975. pp. 210-219. Washington D.C.

Johnsen, S.J., Dansgaard, W. and White, J.W.C. (1989). The origin of Arctic precipitation under present and glacial conditions. Tellus, 41B, pp. 452-468.

Johnsen, S.J. (1999). GRIP oxygen isotopes. PANGAEA, [online] Available at: https://doi.org/10.1594/PANGAEA.55091.

Johnsen, S.J., Clausen, H.B., Jouzel, J., Schwander, J., Sveinbjörbsdóttir, A.E. and White, J. (1999). Stable isotope records from Greenland deep ice cores: The climate signal and the role of diffusion. NATO ASI Series, 156, pp. 89-107.

Johnsen, S.J., Clausen, H.B., Cuffey, K.M., Hoffmann, G., Schwander, J. and Creyts, T. (2000). Diffusion of stable isotopes in polar firn and ice: the isotope effect in firn diffusion, in Physics of Ice Core Records. pp. 121-140, Sapporo.

Johnsen, S., Dahl-Jensen, D., Gundestrup, N., Steffensen, J., Clausen, H., Miller, H.,

Masson-Delmotte, V., Sveinbörnsdottir, A. and White, J. (2001). Oxygen isotope and palaeotemperature records from six Greenland ice-core stations: Camp Century, Dye-3, GRIP, GISP2, Renland and NorthGRIP. J. Quaternary Sci., 16(4), pp. 299-307.

Jones, R.J., Ludlow, M.M., Troughton, J.H. and Blunt, C.G. (1981). Changes in natural carbon isotope ratio of the hair from steers fed diets of C4, C3, C4 species in sequence. Search, 12, pp. 85-87.

Jones, P.D. (1994). Hemispheric surface air temperature variations: a reanalysis and update to 1993. Journal of Climate, 7, pp. 1794-1802.

Jones, P.D., Jonsson, T. and Wheeler, D. (1997). Extension to the North Atlantic Oscillation using early instrumental pressure observations from Gibraltar and South-west Iceland. International Journal of Climatology, 17, pp. 1433-1450.

Jones, P.D. and Moberg A. (2003). Hemispheric and large-scale surface air temperature variations: an extensive revision and an update to 2001. Journal of Climate, 16, pp. 206-223.

Jones, M.D., Leng, M.J., Arrowsmith, C., Deuchars, C., Hodgson, J. and Dawson, T. (2007). Local δ^{18}O and δ^{2}H variability in UK rainfall. Hydrology and Earth System Sciences Discussions, 4, pp. 2403-2423.

Jones, T.R., White, J.W.C., Steig, E.J., Vaughn, B.H., Morris, V., Gkinis, V., Markle, B.R. and Schoenemann, S.W. (2017). Improved methodologies for continuous-flow analysis of stable water isotopes in ice cores. Atmospheric Measurement Techniques, 10, pp. 617-632.

Jónsson, S. and Valdimarsson, H. (2005). Chapter 4: Recent developments in oceano-

graphic research in Icelandic waters. Caseldine, C., Russell, A., Hardardóttir, J. and Knudsen, Ó. (ed.). Iceland - Modern Processes and Past Environments, Developments in Quaternary Science 5. Elsevier, Amsterdam-Boston-Heidelberg-London, pp. 79-92.

Jouzel, J., Koster, R.D., Suozzo, R.J. and Russell, G.L. (1994). Stable water isotope behavior during the last glacial maximum: A general circulation model analysis. Journal of Geophysical Research, 99, pp. 25791-25801,

Katzenberg, M.A. and Krouse, H.R. (1989). Application of stable isotope variation in human tissue to problems in identification. Canadian Society of Forensic Science, 22, pp. 7-19.

Kaufman, D.S., Schneider, D.P., McKay, N.P., Ammann, C.M., Bradley, R.S., Briffa, K.R., Miller, G.H., Otto-Bliesner, B.L., Overpeck, J.T. and Vinther, B.M. (2009). Arctic lakes 2k project members recent warming reverses long-term Arctic cooling. Science, 325, pp. 1236-1239.

Kendall, C. and Caldwell, E.A. (1998). Chapter 2: Fundamentals of Isotope Geochemistry. pp. 51-86.

Kendall, C. and McDonnell, J.J. (1998). Isotope Tracers in Catchment Hydrology. 1st ed., Amsterdam: Elsevier Science pp. 60.

Kirsanow, K. and Tuross, N. (2011). Oxygen and hydrogen isotopes in rodent tissues: Impact of diet, water and ontogeny. Palaeogeography, Palaeoclimatology, Palaeoecology, 310, pp.9-16.

Kobashi, T., Shindell, D.T., Kodera, K., Box, J.E., Nakaegawa, T. and Kawamura, K. (2013). On the origin of multidecadal to centennial Greenland temperature anomalies

over the past 800 yr. Climate of the Past, 9, pp. 583-596.

Kobashi, T. Menviel, L., Jeltsch-Thómmes, A., Vinther, B.M., Box, J.E., Muscheler, R., Nakaegawa, T., Pfister, P.L., Döring, M., Leuenberger, M., Wanner, H. and Ohmura, A. (2017). Volcanic influence on centennial to millennial Holocene Greenland temperature change. Scientific Reports, 7(1441), pp. 1-10.

Koch, P.L. (1998). Isotopic reconstruction of past continental environments. Annual Review of Earth Planetary Science, 26, pp. 573-613.

Koch, P.L., Michener, R. and Lajtha, K. (2007). Isotopic study of the biology of modern and fossil vertebrates. Stable Isotopes in Ecology and Environmental Science, 2, pp. 99-154.

Kraniauskas, P. (1994). A plain man's guide to the FFT. IEEE Signal Processing Magazine, 11(2), pp. 24-35.

Krause, K. and Foitzik, K. (2006). Biology of the hair follicle: The basics. Seminars in Cutaneous Medicine and Surgery, 25, pp. 2-10.

Krigbaum, J., Berger, M.H., Daegling, D.J. and McGraw, W.S. (2013). Stable isotope canopy effects for sympatric monkeys at Taï Forest, Côte d'Ivoire. Biology Letters, 9, 20130466.

Kunz, M., Seifert, B. and Trüeb, R.M. (2009). Seasonality of hair shedding in healthy women complaining of hair loss. Dermatology, 219(2), pp. 105-110.

Lai, C. and Ehleringer, J.R. (2011). Deuterium excess reveals diurnal sources of water vapor in forest air. Oecologia, 165(1), pp. 213-223.

Lamb, H.H. (1995). Climate, history and the modern world, 2nd edition. Routledge,

London, UK.

Larsen, D.J., Geirsdóttir, A. and Miller, G.H. (2015). Precise chronology of Little Ice Age expansion and repetitive surges of Langjökull, central Iceland. Geology, 43(2), pp. 167-170.

Lau, K. and Weng, H. (1995). Climate signal detection using wavelet transform: How to make a time series sing. Bulletin of the American Meteorological Society, 76(12), pp. 2391-2402.

LeBeau, M.A., Montgomery, M.A., Brewer, J.D. (2011). The role of variations in growth rate and sample collection on interpreting results of segmental analyses of hair. Forensic Science International, 210, pp. 110-116.

Lee-Thorp, J., Likius, A., Mackaye, H.T., Vignaud, P., Sponheimer, M. and Brunet, M. (2012). Isotopic evidence for an early shift to C4 resources by Pliocene hominins in Chad. PNAS, 109 (50), pp. 20369-20372.

Levin, N.E., Cerling, T.E., Passey, B.H., Harris, J.M. and Ehleringer, J.R. (2006). A stable isotope aridity index for terrestrial environments. Proceedings of the National Academy of Sciences, 103, pp. 11201-11205.

Lindbäck, K. (2015). Hydrology and Bed Topography of the Greenland Ice Sheet. Last known surroundings. Digital Comprehensive Summaries of Uppsala Dissertations from the Faculty of Science and Technology, 1265. PhD. Uppsala University.

Loader, N.J., Robertson, I., Barker, A.C., Switsur, V.R. and Waterhouse, J.S. (1997). An improved technique for the batch processing of small wholewood samples to α-cellulose. Chemical Geology, 136, pp. 313-317.

Loftus, E., Roberts, P. and Lee-Thorp, J.A. (2016). An isotopic generation: four decades of stable isotope analysis in African archaeology. Azania: Archaeological Research in Africa, 51(1), pp. 88-114.

Long, A.J., Woodroffe, S.A., Milne, G.A., Bryant, C.L., Simpson, M.J.R. and Wake, L.M. (2012). Relative sea-level change in Greenland during the last 700 years and ice sheet response to the Little Ice Age. Earth and Planetary Science Letters, 315-216, pp. 76-85.

Mann, M.E., Zhang, Z., Rutherford, S., Bradley, R.S., Hughes, M.K., Shindell, D., Ammann, C., Faluvegi, G. and Ni, F. (2009). Global signatures and dynamical origins of the Little Ice Age and Medieval Climate Anomaly. Science, 326, pp. 1256-1259.

Mant, M., Nagel, A. and Prowse, T. (2016). Investigating residential history using stable hydrogen and oxygen isotopes of human hair and drinking water. Journal of Forensic Sciences, 61(4), pp. 884-891.

Mantua, N.J. and Hare, S.R. (2002). The Pacific Decadal Oscillation. Journal of Oceanography, 58 (1), pp. 35-44.

Maraun, D. and Kurths J. (2004). Cross wavelet analysis: significance testing and pitfalls. Nonlinear Processes in Geophysics, 11, pp. 505-514.

Marshall, J., Johnson, H. and Goodman, J. (2001). A study of the interaction of the North Atlantic Oscillation with ocean circulation. Journal of Climate, 14, pp. 1399-1421.

Marshall, J. and Plumb, R.A. (2007). Atmosphere, ocean and climate dynamics : An introductory text. Elsevier Science, ProQuest Ebook Central. [online] Available at: https://ebookcentral.proquest.com/lib/oxford/detail.action?

docID=534996.

McCarroll, D. and Loader, N. (2004). Stable isotopes in tree rings. Quaternary Science Reviews, 23 (7-8), pp. 771-801.[online] Available at: http://linkinghub.elsevier.com/retrieve/pii/S0277379104000150.

McConnell, J., Lamorey, G., Lambert, S. and Taylor, K. (2002). Continuous ice-core chemical analyses using inductively coupled plasma mass spectrometry. Environmental Science & Technology, 36(1), pp. 7-11.

McConnell, J., Maselli, O., Sigl, M., Vallelonga, P., Neumann, T., Anschútz, H., Bales, R., Curran, M., Das, S., Edwards, R., Kipfstuhl, S., Layman, L. and Thomas, E. (2014). Antarctic-wide array of high-resolution ice core records reveals pervasive lead pollution began in 1889 and persists today. Sci. Rep., 4. pp. 4-7.

McConnell, J.R., Wilson, A.I., Stohl, A., Arienzo, M.M., Chellman, N.J., Eckhardt, S., Thompson, E.M., Pollard, A.M. and Steffensen, J.P. (2018). Lead pollution recorded in Greenland ice indicates European emissions tracked plagues, wars, and imperial expansion during antiquity. Proceedings of the National Academy of Sciences, 115(22), pp. 5726-5731.

McGowan, H.A., Marx, S.K., Denholm, J., Soderholm, J. and Kamber, B.S. (2009). Reconstructing annual inflows to the headwater catchments of Murray river, Australia, using the Pacific Decadal Oscillation. Geophysical Research Letters, 36.

McKinley, M. (2017). Anatomy and physiology: An integrative approach. Just the facts 101: Textbook key facts, 1st edition. Content Technologies, Inc.

Meier-Augenstein, W. (2009). Stable isotope forensics. Chichester: John Wiley & Sons.

Merlivat, L. (1978). Molecular diffusivities of $H_2^{16}O$, $HD^{16}O$, and $H_2^{18}O$ in gases. Journal of Chemical Physics, 69, pp. 2864-2871.

Mernild, S.H., Seidenkrantz, M.-S., Chylek, P., Liston, G.E. and Hasholt, B. (2011). Climate-driven fluctuations in freshwater flux to Sermilik Fjord, East Greenland, during the last 4000 years. The Holocene, 22(2), pp. 155-164.

Míček, T. and Schrenk, H.J. (1994). Icelandic ponies. Sunburst Books, London.

Miettinen, A., Divine, D.V., Husum, K., Koç, N. and Jennings, A. (2015). Exceptional ocean surface conditions on the SE Greenland shelf during the Medieval Climate Anomaly. Paleoceanography, 30, pp. 1657-1674.

Minson, D.J., Ludlow, M.M. and Troughton, J.H. (1975). Differences in natural carbon isotope ratios of milk and hair from cattle grazing tropical and temperature pastures. Nature, 256 (5518), pp. 602.

Miyahara, H., Masuda, K., Muraki, Y., Furuzawa, H., Menjo, H. and Nakamura, T. (2004). Cyclicity of solar activity during the Maunder Minimum deduced from radiocarbon content. Solar Physics, 224 (1-2), pp. 317-322.

Mitchell, T.D. and Jones, P.D. (2005). An improved method of constructing a database of monthly climate observations and associated high-resolution grids. International Journal of Climatology, 25, pp. 693-712.

Moberg, A., Sonechkin, D.M., Holmgren, K., Datsenko, N.M., and Karlen, W. (2005). Highly variable Northern Hemisphere temperatures reconstructed from low- and high-resolution proxy data. Nature, 433, pp. 613-617.

Mook, W.G. (2006). Introduction to isotope hydrology: Stable and radioactive isotopes

of hydrogen, oxygen and carbon. Balkema Proceedings and Monographs in Engineering, Water and Earth Science. London: Taylor & Francis Group. pp. 6-17.

Montagna, W. and Ellis, R. (ed.). (1958). The biology of hair growth. Academic Press Inc., New York.

Mudie, P.J., Rochon, A., Prins, M.A., Soenajo, D., Troelstra, S.R., Levac, E., Scott, D.B., Roncaglia, L. and Kuijpers, A. (2006): Late Pleistocene-Holocene marine geology of Nares Strait Region: Palaeoceanography from foraminifera and dinoflagellate cysts, sedimentology and stable isotopes. Polarforschung, 74, pp. 169-83.

Muir, T.S. (1915) The physical geography of Iceland. Scottish Geographical Magazine, 31(5), pp. 254-257.

Nakagawa, A., Kitagawa, A., Asami, M., Nakamura, K., Schoeller, D.A., Slater, R., Minagawa, M. and Kaplan, I.R. (1985). Evaluation of isotope ratio (IR) mass spectrometry for the study of drug metabolism. Biomedical Mass Spectrometry, 12, pp. 502-506.

National Hydrological Monitoring Programme (2017). Hydrological summary for the United Kingdom: September 2017. Centre for Ecology and Hydrology and the British Geological Survey. [online] Available at: `http://www.hydoutuk.net/archive/`.

New, M., Hulme, M. and Jones, P.D. (2000). Representing twentieth century space-time climate variability. Part 2: development of 1901-96 monthly grids of terrestrial surface climate. Journal of Climate, 13, pp. 2217-2238.

North Greenland Ice Core Project (NGRIP) members (2004). High-resolution record of Northern Hemisphere climate extending into the last interglacial period. Nature,

431, pp. 147-151.

Notendur.hi.is. (2016). Climate in Iceland. [online] Available at: https://notendur.hi.is/oi/climate_in_iceland.htm.

O'Connell, T. (1996). The isotopic relationship between diet and body proteins: implications for the study of diet in archaeology. PhD. University of Oxford.

O'Connell, T.C., Hedges, R.E.M., Healey, M.A. and Simpson, A.H.R.W. (2001). Isotopic comparison of hair, nail and bone: Modern analyses. Journal of Archaeological Science, 28, pp. 1247-1255.

O'Dell, A.C. and Walton, K. (1962). Regions of the British Isles: The highlands and islands of Scotland. Published by Thomas Nelson and Sons Ltd. Printed in Great Britain by Robert Cunningham and Sons Ltd, Alva. Chapter 15 - The Islands, pp. 314-316.

O'Grady, S.P., Wende, A.R., Remien, C.H., Valenzuela, L.O., Enright, L.E., Chesson, L.A., Abel, E.D., Cerling, T.E. and Ehleringer, J.R. (2010). Aberrant water homeostasis detected by stable isotope analysis. Public Library of Science ONE, 5(7), pp. 1-7.

O'Grady, S., Valenzuela, L., Remien, C., Enright, L., Jorgensen, M., Kaplan, J., Wagner, J., Cerling, T. and Ehleringer, J. (2012). Hydrogen and oxygen isotope ratios in body water and hair: modeling isotope dynamics in nonhuman primates. American Journal of Primatology, 74, pp. 651-660.

Oerlemans, J. (2005). Extracting a climate signal from 169 glacier records. Science, 308(5722), pp. 675-677.

Ogilvie, A.E.J. (2005). Local knowledge and travellers' tales: A selection of climatic observations in Iceland. Rose, J. Caseldine, C., Russell, J., and Knudsen, Ó. (ed.). Iceland - Modern Processes and Past Environments, Developments in Quaternary Science 5. Elsevier, Amsterdam-Boston-Heidelberg-London, pp. 257-287.

Ogilvie, A. and Jónsson, T. (2001). "Little Ice Age" research: A perspective from Iceland. Climatic Change, 48 (1), pp. 9-52.

Ólafsdóttir, K.B., Geirsdóttir, A., Miller, G.H. and Larsen, D.J. (2013). Evolution of NAO and AMO strength and cyclicity derived from a 3-ka varve-thickness record from Iceland. Quaternary Science Reviews, 69, pp. 142-154.

Olsen, J., Anderson, N.J. and Knudsen, M.F. (2012). Variability of the North Atlantic Oscillation over the past 5,200 years. Nature Geoscience, 5, pp. 808-812.

Ortega, P., Lehner, F., Swingedouw, D., Masson-Delmotte, V., Raible, C.C, Casado, M. and Yiou, P. (2015). A model-tested North Atlantic Oscillation reconstruction for the past millennium. Nature, 523, pp. 71-74.

Pang, H., He, Y., Zhang, Z., Lu, A. and Gu, J. (2004). The origin of summer monsoon rainfall at New Delhi by deuterium excess. Hydrology and Earth System Science, 8(1), pp.115-118. [online] Available at: `http://www.hydrol-earth-syst-sci.net/8/115/2004/`.

Pate, F.D. and Anson, T.J. (2008). Stable nitrogen isotope values in arid-land kangaroos correlated with mean annual rainfall: Potential as a palaeoclimatic indicator. International Journal of Osteoarchaeology, 18(3), pp. 317-326.

Pearson, P.N. (2012). Oxygen isotopes in foraminifera: Overview and historical review. The Paleontological Society Papers, 18, pp. 1-38.

Pellegrini, M., Pouncett, J., Jay, M., Pearson, M.P. and Richards, M.P. (2016). Tooth enamel oxygen "isoscapes" show a high degree of human mobility in prehistoric Britain. Scientific Reports, 6, pp. 1-9.

Persson, A. (1998). How do we understand the Coriolis Force? Bulletin of the American Meteorological Society, pp. 1373.

Peterson, T.C., Vose, R., Schmoyer, R. and Razuvaev, V. (1998). Global Historical Climatology Network (GHCN) quality control of monthly temperature data. International Journal of Climatology, 18, pp. 1169-1179.

Pfahl, S. and Sodemann, H. (2014). What controls deuterium excess in global precipitation. Climate of the Past, 10(2), pp. 771-781. [online] Available at: http://www.clim-past.net/10/771/2014/.

Picarro, Inc. (2012). Picarro L2130-i δD/δ^{18}O ultra high-precision isotopic water analyzer datasheet. [online] Available at https://www.picarro.com/products_solutions/peripherals/for_h2o/continuous_water_sampler.

Pietsch, S.J., Hobson, K.A., Wassenaar, L.I. and Tütken, T. (2011). Tracking cats: problems with placing feline carnivores on δ^{18}O, δD isoscapes. Public Library of Science ONE, 6(9), pp. 1-11.

Podlesak, D., Torregrossa, A., Ehleringer, J., Dearing, M., Passey, B. and Cerling, T. (2008). Turnover of oxygen and hydrogen isotopes in the body water, CO2, hair, and enamel of a small mammal. Geochimica et Cosmochimica Acta, 72(1), pp. 19-35.

Polikar, R. (1996). The wavelet tutorial, 2nd edition, Rowan University Department of Electrical and Computer Engineering, New Jersey, [online] Available at: http://users.rowan.edu/~polikar/WAVELETS/WTtutorial.html.

Polikar, R. (1999). The story of wavelets. Mastorackis, N., ed., Physics and Modern Topics in Mechanical and Electrical Engineering, World Scientific and Engineering Press, pp. 192-197.

Prokoph, A. and El Bilali, H. (2008). Cross-wavelet analysis: A tool for detection of relationships between Paleoclimate Proxy Records. Mathematical Geosciences, 40, pp. 575-586.

R Core Team (2013). R: A language and environment for statistical computing. R Foundation for Statistical Computing, Vienna, Austria.

Remien, C.H., Adler, F.R., Chesson, L.A., Valenzuela, L.O., Ehleringer, J.R. and Cerling, T.E. (2014). Deconvolution of isotope signals from bundles of multiple hairs. Oecologia, 175(3), pp. 781-789.

Reynard, L.M. and Hedges, R.E.M. (2008). Stable hydrogen isotopes of bone collagen in palaeodietary and palaeoenvironmental reconstruction. Journal of Archaeological Science, 35, pp. 1934-1942.

Reynolds-Henne, C.E., Siegwolf, R.T.W, Treydte, K.S., Esper, J., Henne, S. and Saurer, M. (2007). Temporal stability of climate-isotope relationships in tree rings of oak and pine (Ticino, Switzerland). Global Biogeochemical Cycles, 21, pp. 1-12.

Risi, C., Bony, S. and Vimeux, F. (2008). Influence of convective processes on the isotopic composition (δ^{18}O and δD) of precipitation and water vapor in the tropics: 2. Physical interpretation of the amount effect. Journal of Geophysical Research: Atmospheres, 113.

Roberts, P., Fernandes, R., Craig, O. E., Larsen, T., Lucquin, A., Swift, J. A. and Zech, J. (2018). Calling all archaeologists: guidelines for terminology, methodology, data

handling, and reporting when undertaking and reviewing stable isotope applications in archaeology. Rapid Communications in Mass Spectrometry, 32 (5), pp. 361-372.

Roberts, P. (2016). Fruits of the forest: Human stable isotope ecology and rainforest adaptations in Late Pleistocene and Holocene Sri Lanka. PhD. University of Oxford.

Roden, J.S., Lin, G. and Ehleringer, J.R. (2000). A mechanistic model for interpretation of hydrogen and oxygen isotope ratios in tree-ring cellulose. Geochimica et Cosmochimica Acta, 64, pp. 21-35.

Rozanski, K. (2005). Isotopes in atmospheric moisture. *In* Aggarwal, P.K., Gat, J.R. and Froehlich, K.F.O (ed.) Isotopes in the Water Cycle: Past, Present and Future of a Developing Science. Springer, Dordrecht, The Netherlands, pp. 291-302.

Rozanski, K. Araguás-Araguás, L. and Gonfiantini, R. (1992). Relation between long-term trends of Oxygen-18 isotope composition of precipitation and climate. Science, 258, pp.981-985.

Rozanski, K. Araguás-Araguás, L. and Gonfiantini, R. (1993). Isotopic patterns in modern global precipitation. Swart, P.K., Lohmann, K.C., McKenzie, J. and Savin, S. (ed.) Climate change in continental isotopic records. Geophysical Monograph, 78. American Geophysical Union, Washington DC. pp. 1-36.

Rydval, M., Gunnarson, B.E., Loader, N.J., Cook, E.R., Druckenbrod, D.L. and Wilson, R. (2017). Spatial reconstruction of Scottish summer temperatures from tree rings. International Journal of Climatology, 37, pp. 1540-1556.

Saurer, M., Aellen K. and Siegwolf R. (1997). Correlating δ^{13}C and δ^{18}O in cellulose of trees. Plant, Cell and Environment, 20, pp. 1543-1550.

Saurer, M., Cherubini, P. and Siegwolf, R. (2000). Oxygen isotopes in tree rings of *Abies alba*: The climatic significance of interdecadal variations. Journal of Geophysical Research, 105, pp. 12461-12470.

Saurer, S. (2003). The influence of climate on the oxygen isotopes in tree rings. Isotopes in Environmental and Health Studies, 39(2), pp. 105-112.

Saurer, M., Cherubini, P., Reynolds-Henne, C.E., Treydte, K.S., Anderson, W.T. and Siegwolf, R.T.W. (2008). An investigation of the common signal in tree ring stable isotope chronologies at temperate sites. Journal of Geophysical Research, 113, pp. 1-11.

Saurer, M., Kress, A., Leuenberger, M., Rinne, K.T., Treydte, K.S. and Siegwolf, R.T.W. (2012). Influence of atmospheric circulation patterns on the oxygen isotope ratio of tree rings in the Alpine region. Journal of Geophysical Research, 117, pp. 1-12.

Schmunk, R. (2018). Panoply. New York, USA: NASA Goddard Institute for Space Studies.

Schulting, R.J., Snoeck, C., Begley, I., Brookes, S., Bazaliiskii, V.I., Ramsey, C.B. and Weber, A. (2018). Using δ^2H in human bone collagen to correct for freshwater ^{14}C reservoir offsets: A pilot study from Shamanka II, Lake Baikal, southern Siberia. Radiocarbon, 60(5), pp. 1521-1532.

Sdwebx.worldbank.org (2018). Downscaled data download. [online] Available at: `http://sdwebx.worldbank.org/climateportal/index.cfm?page=downscaled_data_download&menu=historical`.

Seidenkrantz, M.-S., Aagaard-Sorensen, S., Sulsbrück, H., Kuijpers, A., Jensen, K.G. and Kunzendorf, H. (2007). Hydrography and climate of the last 4400 years in a SW

Greenland fjord: implications for Labrador Sea palaeoceanography. The Holocene, 17(3), pp. 387-401.

Seierstad, I.K., Abbott, P. M., Bigler, M., Blunier, T., Bourne, A. J., Brook, E., Buchardt, S.L., Buizert, C., Clausen, H.B., Cook, E., Dahl-Jensen, D., Davies, S.M., Guillevic, M., Johnsen, S.J., Pedersen, D.S., Popp, T.J., Rasmussen, S.O., Severinghaus, J.P., Svensson, A. and Vinther, B. M (2014). Consistently dated records from the Greenland GRIP, GISP2 and NGRIP ice cores for the past 104 ka reveal regional millennial-scale δ^{18}O gradients with possible Heinrich event imprint. Quaternary Science Reviews, 106, pp. 29-46.

Sharp, Z. and Cerling, T. (1998). Fossil isotope records of seasonal climate and ecology: straight from the horse's mouth. Geology, 26, pp. 219-222.

Sharp, Z., Atudorei, V., Panarello, H., Fernández, J. and Douthitt, C. (2003). Hydrogen isotope systematics of hair: archeological and forensic applications. Journal of Archaeological Science, 30(12), pp.1709-1716. [online] Available at: `http://linkinghub.elsevier.com/retrieve/pii/S0305440303000712`.

Sharp, Z. (2007). Principles of stable isotope geochemistry. Pearson Education, Upper Saddle River.

Sheshshayee, M.S., Bindumadhava, H., Ramesh, R., Prasad, T.G., Lakshminarayana, M.R. and Udayakumar, M. (2005). Oxygen isotope enrichment (δ^{18}O) as a measure of time-averaged transpiration rate. Journal of Experimental Botany, 56, pp. 3033-3039.

Sidorova, O., Siegwolf, R., Myglan, V., Ovchinnikov, D., Shishov, V., Helle, G., Loader, N. and Saurer, M. (2013). The application of tree-rings and stable isotopes for re-

constructions of climate conditions in the Russian Altai. Climatic Change, 120(1-2), pp. 153-167. [online] Available at: http://link.springer.com/10.1007/s10584-013-0805-5.

Sigl, M., Winstrup, M., McConnell, J.R., Welten, K.C., Plunkett, G., Ludlow, F., Büntgen, U., Caffee, M., Chellman, N., Dahl-Jensen, D., Fischer, H., Kipfstuhl, S., Kostick, C., Maselli, O.J., Mekhaldi, F., Mulvaney, R., Muscheler, R., Pasteris, D.R., Pilcher, J.R., Salzer, M., Sch upbach, S., Steffensen, J.P., Vinther, B.M. and Woodruff, T.E. (2015). Timing and climate forcing of volcanic eruptions for the past 2,500 years. Nature, 523, pp. 543-549.

Sponheimer, M., Lee-Thorp, J., de Ruiter, D., Codron, D., Codron, J., Baugh, A.T. and Thackeray, F. (2005). Hominins, sedges, and termites: new carbon isotope data from the Sterkfontein valley and Kruger National Park. Journal of Human Evolution, 48 (3), pp. 301-312.

Stevens, R.E. and Hedges, R.E.M (2004). Carbon and nitrogen stable isotope analysis of northwest European horse bone and tooth collagen, 40,000BP-present: Palaeoclimatic interpretations. Quaternary Science Reviews, 23, pp. 977-991.

Stótter, J., Wastl, M., Caseldine, C. and Häberle, T. (1999). Holocene palaeoclimatic reconstruction in northern Iceland: Approaches and results. Quaternary Science Reviews, 18, pp. 457-474.

Summerfield, M.A. (1991). Global geomorphology: An introduction to the study of landforms. Pearson: Prentice Hall, Harlow.

Sutton, R.T., McCarthy, G.D., Robson, J., Sinha, B., Archibald, A.T. and Gray, L.J. (2018). Atlantic multidecadal variability and the U.K. ACSIS program. American

Meteorological Society, BAMS, pp. 415-425.

Thorburn, P.J. and Mensforth, L.J. (1993). Sampling water from alfalfa (*Medicago sativa*) for analysis of stable isotopes of water. Communications in Soil Science and Plant Analysis, 24(5-6), pp.549-557.

Tieszen, L.L. and Boutton, T.W. (1988). Stable carbon isotopes in terrestrial ecosystem research. In: Rundel, P.W., Ehleringer, J.R. and Nagy, K.A. (ed.). Stable isotopes in ecological research. Berlin and New York: Springer-Verlag. pp. 167-195.

Tieszen, L.L., Boutton, T.W., Tesdahl, K.G. and Slade, N.A. (1983). Fractionation and turnover of stable carbon isotopes in animal tissues: Implications for δ^{13}C analysis of diet. Oecologia, 57(1-2), pp. 32-37.

Tieszen, L.L. and Fagre, T. (1993). Effect of diet quality and composition on the isotopic composition of respiratory CO2, bone collagen, bioapatite, and soft tissues. In: Lambert, J.B. and Grupe, G. (ed.). Prehistoric human bone: archaeology at the molecular level. Berlin: Springer-Verlag. pp. 121-155.

Torrence, C. and Compo, G.P. (1998). A practical guide to wavelet analysis. Bulletin of the American Meteorological Society, 79 (1), pp. 61-78.

Treydte, K., Boda, S., Pannatier, E.G., Fonti, P., Frank, D., Ullrich, B., Saurer, M., Siegwolf, R., Battipaglia, G., Werner, W. and Gessler, A. (2014). Seasonal transfer of oxygen isotopes from precipitation and soil to the tree ring: source water versus needle water enrichment. New Phytologist, 202, pp. 772-783.

Trigo, R.M., Osborn, T.J. and Corte-Real, J.M. (2002). The North Atlantic Oscillation influence on Europe: climate impacts and associated physical mechanisms. Climate Research, 20, pp. 9-17

Trouet, V., Esper, J., Graham, N.E., Baker, A., Scourse, J.D. and Frank, D.C. (2009). Persistent positive North Atlantic Oscillation mode dominated the Medieval Climate Anomaly. Science, 324(5923), pp. 78-80.

Tribbia, J. (1991). 9: The rudimentary theory of atmospheric teleconnections associated with ENSO. Glantz, M., Katz, R. and Nicholls, N. ed., Teleconnections linking worldwide climate anomalies: scientific basis and societal impact. Cambridge: Cambridge University Press.

Tsonis, A.A., Hunt, A.G. and Elsner, J.B. (2002). On the relation between ENSO and global climate change. Meteorology and Atmospheric Physics, 84, pp. 229-242.

UK Meteorological Office (2011). Fact sheet No.7 - Climate of southwest England, National Meteorological Library and Archive. [online] Available at: http://www.metoffice.gov.uk/learning/library/factsheets.

UK Meteorological Office (2016a). Lerwick climate information - Met Office. [online] Available at: http://www.metoffice.gov.uk/public/weather/climate/gfxnjyxk4.

UK Meteorological Office (2016b). Liscombe climate information - Met Office. [online] Available at: http://www.metoffice.gov.uk/public/weather/climate/gcj6tuher.

UK Oak Project (2019). UK Oak Project - Swansea University. [online] Available at: https://www.oak-research.co.uk.

United States Geological Survey (2011a). Report of stable isotopic composition: Reference material USGS40. 40, pp. 1-3.

United States Geological Survey (2011b). Report of stable isotopic composition: Reference material USGS41. 41, pp. 1-3.

United States Geological Survey (2011c). Report of stable isotopic composition: Reference material USGS42. 42, pp. 1-4.

United States Geological Survey (2011d). Report of stable Isotopic composition: Reference material USGS43. 43, pp. 1-4.

Vallack, H., Loader, N.J., Young, G., McCarroll, D. and Brown, D. (2016). Stable oxygen isotopes in Irish oaks: potential for reconstructing local and regional climate. Irish Geography, 49(2), pp. 55-70.

van Dam, J. and Reichart, G. (2009). Oxygen and carbon isotope signatures in late Neogene horse teeth from Spain and application as temperature and seasonality proxies. Palaeogeography, Palaeoclimatology, Palaeoecology, 274(1-2), pp. 64-81.

Venegas, S. (2001). Statistical methods for signal detection in climate. Danish Center for Earth System Science (DCESS) Report 2. Copenhagen, Denmark: Niels Bohr Institute for Astronomy, Physics and Geophysics.

Vinther, B. (2006). Greenland and North Atlantic climatic conditions during the Holocene - as seen in high resolution stable isotope data from Greenland ice cores.. PhD Dissertation. Niels Bohr Institute University of Copenhagen.

Vinther, B., Johnsen, S., Andersen, K., Clausen, H. and Hansen, A. (2003). NAO signal recorded in the stable isotopes of Greenland ice cores. Geophys. Res. Lett., 30(7). [online] Available at: `http://doi.wiley.com/10.1029/2002GL016193`.

Vinther, B.M., Andersen, K.K., Jones, P.D., Briffa, K.R. and Cappelen J. (2006). Ex-

tending Greenland temperature records into the late 18th Century. Journal of Geophysical Researd, 111 (D11105), pp. 1-13.

Vinther, B.M., Clausen, H.B., Fisher, D.A., Koerner, R.M., Johnsen, S.J., Andersen, K.K., Dahl-Jensen, D., Rasmussen, S.O., Steffensen, J.P. and Svensson, A.M. (2008). Synchronizing ice cores from the Renland and Agassiz ice caps to the Greenland ice core chronology. Journal of Geophysical Research, 113, pp. 1-10.

Vinther, B.M., Jones, P.D., Briffa, K.R., Clausen, H.B., Andersen, K.K., Dahl-Jensen, D. and Johnsen S.J. (2010). Climatic signals in multiple highly resolved stable isotope records from Greenland. Quaternary Science Reviews, 29, pp. 522-538.

Visbeck, M.H., Hurrell, J.W., Polvani, L. and Cullen, H.M. (2001). The North Atlantic Oscillation: Past, present, and future. PNAS, 98(23), pp.12876-12877.

Walker, M., Björck, S. and Lowe, J. (2001). Integration of ice core, marine and terrestrial records (INTIMATE) from around the North Atlantic region. Quaternary Science Reviews, 20(11), pp. 1169-1174.

Walker, G.R. and Richardson, S.B. (1991). The use of stable isotopes of water in characterizing the source of water in vegetation. Chemical Geology: Isotope Geoscience Section, 94, pp. 145-158.

Wallace, J. and Hobbs, P. (2006). Atmospheric Science: An introductory survey, 2nd edition. Academic Press, Elsevier.

Wang, T., Surge, D. and Walker, K.J. (2013). Seasonal climate change across the Roman Warm Period/Vandal Minimum transition using isotope sclerochronology in archaeological shells and otoliths, southwest Florida, USA. Quaternary International, 308-209, pp. 230-241.

Weißbach, S., Wegner, A., Opel, T., Oerter, H., Vinther, B.M. and Kipfstuhl, S. (2016). Spatial and temporal oxygen isotope variability in northern Greenland - implications for a new climate record over the past millennium. Climate of the Past, 12, pp. 171-188.

Welp, L.R., Keeling, R.F., Meijer, H.A.J., Bollenbacher, A.F., Piper, S.C., Yoshimura, K., Francey, R.J., Allison, C.E and Wahlen M. (2011). Interannual variability in the oxygen isotopes of atmospheric CO2 driven by El Niño. Nature, 477, pp. 579-582

West, A.G., Ayliffe, L.K. and Cerling, T.E. (2004). Short term diet changes revealed using stable carbon isotopes in horse tail hair. Functional Ecology, pp. 616-624. [online] Available at: http://onlinelibrary.wiley.com/doi/10.1111/j.0269-8463.2004.00862.x/full.

West, J.B., Bowen, G.J., Dawson, T.E., Tu, K.P. (2009). Isoscapes: Understanding movement, pattern, and process on earth through isotope mapping. New York: Springer Verlag, 487.

Woodborne, S., Hall, G., Robertson, I., Patrut, A., Rouault, M., Loader, N. and Hofmeyr, M. (2015). A 1000-year carbon isotope rainfall proxy record from South African Baobab trees (Adansonia digitata L.). Public Library of Science ONE, 10(5), pp. 124-202. [online] Available at: http://dx.plos.org/10.1371/journal.pone.0124202.

Woollings, T., Hannachi, A., Hoskins, B. and Turner, A. (2010). A regime view of the North Atlantic Oscillation and its response to anthropogenic forcing. Journal of Climate, 23, pp. 1291-1307.

Yakir, D. (1992). Variations in the natural abundance of oxygen-18 and deuterium in

plant carbohydrates. Plant, Cell & Environment, 15, pp. 1005-1020.

Yakir, D., Berry, J., Giles, L. and Osmond, C.B. (1994). Isotopic heterogeneity of water in transpiring leaves: identification of the component that controls the δ^{18}O of atmospheric O2 and CO2. Plant, Cell & Environment, 17, pp. 73-80.

Yakir, D., 1998. Oxygen-18 in leaf water: a crossroad for plant- associated isotopic signals. Griffiths, H. (ed.), Stable Isotopes: The Integration of Biological, Ecological and Geochemical Processes. Bios Scientific, Oxford, pp. 147-168.

Young, G.H.F., Loader, N.J., McCarroll, D., Bale, R.J., Demmler, J.C., Miles, D., Nayling, N.T., Rinner, K.T., Robertson, I., Watts, C., Whitney, M. (2015). Oxygen stable isotope ratios from British oak treeâĂŘrings provide a strong and consistent record of past changes in summer rainfall. Climate Dynamics.

Zhai, X., Johnson, H.L. and Marshall, D.P. (2014). A simple model of the response of the Atlantic to the North Atlantic Oscillation. Journal of Climate, 27, pp. 4052-4069.

Zazzo, A., Cerling, T., Ehleringer, J., Moloney, A., Monahan, F. and Schmidt, O. (2015). Isotopic composition of sheep wool records seasonality of climate and diet. Rapid Communications in Mass Spectrometry, 29(15), pp. 1357-1369. [online] Available at: `http://www.ncbi.nlm.nih.gov/pubmed/26147475`.